

PAUL CHRISTIAN

# Polymer Thin Films by initiated Chemical Vapor Deposition

From Proton Conduction to the Encapsulation of  
Pharmaceuticals

## DOCTORAL THESIS

For obtaining the academic degree of  
Doktor der technischen Wissenschaften

Doctoral Program in Engineering Sciences  
Doctoral School Physics



Graz University of Technology

Supervisor:

ASS.PROF. DR. ANNA MARIA COCLITE  
Institute of Solid State Physics  
Graz University of Technology

Graz, January 31, 2018

Paul Christian: *Polymer Thin Films by initiated Chemical Vapor Deposition*, From Proton Conduction to the Encapsulation of Pharmaceuticals, © January 31, 2018



*To Carina.*



## **AFFIDAVIT**

I declare that I have authored this thesis independently, that I have not used other than the declared sources/resources, and that I have explicitly indicated all material which has been quoted either literally or by content from the sources used. The text document uploaded to TUGRAZonline is identical to the present doctoral thesis.

---

Date

---

Signature



# Abstract

---

In this thesis, vapor-phase synthesized polymer thin films are explored in the context of ion-exchange membranes and drug delivery systems. Both applications can greatly benefit from the usage of this versatile class of materials as polymers provide resistance to various chemicals, are typically cheap in production and light in weight while also offering significant mechanical strength. However, common solution processing routes can easily become a limiting factor when delicate substances (such as pharmaceuticals) are involved or when polymers with various functionalities are required. A solvent-free alternative is the polymerization by initiated Chemical Vapor Deposition (iCVD). In iCVD, all the reactants are delivered from the vapor-phase so that even the most delicate substrates can be coated conformally. Also, copolymers with tailored properties can easily be obtained as the use of a common solvent is not required. This makes iCVD particularly interesting for the synthesis of ion-exchange membranes and for the encapsulation of pharmaceuticals. At first, preparation of polymer electrolyte membranes by iCVD has been studied. For this, copolymers of 1H,1H,2H,2H-perfluorodecyl acrylate and methacrylic acid have been synthesized and key material properties, such as chemical and physical stability, morphology and structure, were then evaluated. While showing promising properties at first, thermal stability issues were soon discovered to be a limiting factor for fuel cell application. To avoid these shortcomings, also the preparation of sulfonated copolymers was attempted by iCVD, which required a post-deposition modification. While studies are still at a very early stage, the resulting material seems very promising in terms of ionic conductivity. In regard to pharmaceutical applications, iCVD polymers were explored for drug encapsulation. For instance, thin hydrogel encapsulation was able to suppress drug crystallization even at elevated temperatures while a hydrophobic coating enhanced crystallization instead. In another study, the mesh size of an iCVD hydrogel coating was varied by adjusting the cross-linker content, which, in turn, translated into a tunable release behavior of thin indomethacin films. The studies presented within this thesis show some of the distinct advantages of iCVD and will hopefully foster further interest in this intriguing technique and its potential applications.



# Kurzfassung

---

Diese Arbeit behandelt die Herstellung von Polymerdünnschichten mittels Gasphasenabscheidung für den Einsatz als Ionenaustauschmembranen und in pharmazeutischen Anwendungen. Beide Anwendungen können stark von der Verwendung dieser vielseitigen Materialien profitieren, da Polymere Beständigkeit gegen verschiedenste Chemikalien bieten, typischerweise billig in der Herstellung sind und bei geringem Gewicht ausgeprägte mechanische Festigkeit aufweisen. Herkömmliche Flüssigphasen-Synthese kann jedoch leicht zu einem limitierenden Faktor werden, insbesondere wenn empfindliche Substanzen (wie Pharmazeutika) beteiligt sind oder wenn Polymere mit verschiedenen Funktionalitäten benötigt werden. Eine lösungsmittelfreie Alternative ist die Polymerisation mittels *initiated Chemical Vapor Deposition* (iCVD). In iCVD werden alle Reaktanten in der Gasphase prozessiert, so dass auch die empfindlichsten Oberflächen konform beschichtet werden können. Auch Copolymere mit maßgeschneiderten Eigenschaften können leicht erzielt werden, da die Verwendung eines gemeinsamen Lösungsmittels nicht erforderlich ist. Dies macht iCVD besonders interessant für die Synthese von Ionenaustauschmembranen und für die Beschichtung von Pharmazeutika. Zunächst wurde die Herstellung von Polymerelektrolytmembranen mittels iCVD untersucht. Dazu wurden Copolymere aus 1H, 1H, 2H, 2H-Perfluordecylacrylat und Methacrylsäure synthetisiert und wichtige Materialeigenschaften, wie chemische und physische Stabilität, Morphologie und Struktur, untersucht. Während diese Materialien anfangs vielversprechende Eigenschaften aufzeigten, wurden dann jedoch thermische Stabilitätsprobleme als begrenzende Faktoren festgestellt, welche einen Einsatz in Brennstoffzellen praktisch unmöglich machen. Um diese Nachteile zu vermeiden, wurde auch die Herstellung von sulfonierten Copolymeren mittels iCVD versucht, was eine weitere Modifizierung nach der Synthese nötig machte. Während Studien noch in einem sehr frühen Stadium sind, scheint das resultierende Material hinsichtlich der Ionenleitfähigkeit sehr vielversprechend zu sein. Im Hinblick auf pharmazeutische Anwendungen wurden iCVD-Polymere als Beschichtung von Arzneimitteln evaluiert. Zum Beispiel war eine dünne Hydrogel-Beschichtung in der Lage, die Wirkstoffkristallisation sogar bei erhöhten Temperaturen zu unterdrücken, während eine hydrophobe Beschichtung stattdessen die Kristallisation verstärkte. In einer weiteren Studie wurde die Maschenweite von iCVD-Hydrogel-Beschichtungen verändert, indem der Vernetzungsgrad im Polymer variiert wurde, was

wiederum zu einem abstimmbaren Freisetzungverhalten von dünnen Indomethacinfilmen führte. Die in dieser Arbeit vorgestellten Studien zeigen einige der besonderen Vorteile von iCVD und werden hoffentlich weiteres Interesse an dieser faszinierenden Technik und ihren möglichen Anwendungen wecken.



# Acknowledgements

---

Firstly, I would like to express my sincere gratitude to my supervisor Anna Maria Coclite. Not only did she provide me with the freedom to explore a wide variety of topics within this thesis but also provided the necessary support whenever needed. With her passion for research, always eager to attempt new concepts and to push the level of what is currently possible, she was truly an inspiring supervisor.

I am most grateful to Oliver Werzer, who sparked my interest in scientific research in the first place and taught me so many different things. Being my co-supervisor during my Master's thesis, he became my closest scientific collaborator in the last three years, never ceasing to provide input and support. Thank you so much for everything!

I am deeply indebted and uttermost grateful to Prof. Karen Gleason for giving me the chance to work in her lab at MIT. Always truly interested in my ongoing work and taking the time to discuss experimental progress in great detail, she provided me with new insights and invaluable advice. Thank you so much for making this great experience possible!

To all the members of the G-Lab at MIT: Andong Liu, Minghui Wang, Junjie Zhao, Priya Moni, Xiaoxue Wang, Do Han Kim and Edward Gleason. Thank you for the great time in and outside of the lab!

I am grateful to former and current members of the Coclite Group and to the members of the *k*-room, in particular to Andrew Jones, Martin Tazreiter, Stephan Tumphart, Paul Salzmann, to our Post-doc Alberto Perrotta as well as to my PhD colleagues Stefan Pachmajer, Katrin Unger and Julian Pilz. Special gratitude goes to fellow PhD candidate Fabian Muralter, who provided valuable comments on this thesis.

I am most grateful to Christian Röthel, who is not only a colleague but also one of my dearest and closest friends. From joint exercises during our physics degree to night-shifts at synchrotrons and eventually to our first common publication you have always been a true friend.

I am also most thankful to Gernot Kraberger. With his cheerful and most knowledgeable character, he provided both fun and valuable insights whenever one or the other was required. Thank you for being a dear friend!

To my parents, for their unconditional, never ceasing love and support: Thank you so much!



# Contents

---

1	INTRODUCTION	1
1.1	References . . . . .	2
<b>I</b>	<b>FUNDAMENTALS AND METHODS</b>	<b>5</b>
2	POLYMERS	7
2.1	Polymer electrolyte membranes . . . . .	9
2.1.1	Proton transport mechanisms . . . . .	11
2.2	Polymers in pharmaceutical applications . . . . .	12
2.2.1	Drug release from polymer systems . . . . .	13
2.3	References . . . . .	15
3	POLYMER SYNTHESIS	21
3.1	Step-wise polymerization . . . . .	21
3.2	Kinetics . . . . .	22
3.3	Radical chain polymerization . . . . .	24
3.3.1	Radical initiation . . . . .	25
3.3.2	Propagation . . . . .	26
3.3.3	Termination . . . . .	27
3.3.4	Step and chain polymerization in comparison . . . . .	28
3.4	Copolymerization . . . . .	29
3.5	initiated Chemical Vapor Deposition . . . . .	30
3.5.1	Initiator . . . . .	32
3.5.2	Monomer vapor pressure and surface fraction . . . . .	34
3.6	References . . . . .	35
4	POLYMER ANALYSIS	39
4.1	Chemical analysis by FTIR . . . . .	39
4.1.1	Copolymer analysis . . . . .	39
4.1.2	Fineman-Ross analysis . . . . .	42
4.2	Spectroscopic ellipsometry . . . . .	42
4.2.1	Data modeling . . . . .	44
4.2.2	In situ measurements . . . . .	46
4.3	Electrochemical impedance spectroscopy . . . . .	47
4.4	References . . . . .	50
<b>II</b>	<b>PROTON CONDUCTIVE POLYMERS</b>	<b>53</b>
5	VAPOR-PHASE-SYNTHESIZED FLUOROACRYLATE POLYMER THIN FILMS	55
5.1	Preface . . . . .	55
5.2	Abstract . . . . .	56
5.3	Introduction . . . . .	56
5.4	Experimental . . . . .	57
5.5	Results and Discussion . . . . .	59

5.6	Conclusion . . . . .	70
5.7	Acknowledgements . . . . .	70
5.8	References . . . . .	71
5.9	Supporting Information . . . . .	73
6	THERMAL STUDIES ON PROTON CONDUCTIVE COPOLYMER THIN FILMS	75
6.1	Preface . . . . .	75
6.2	Abstract . . . . .	76
6.3	Introduction . . . . .	76
6.4	Experimental details . . . . .	77
6.5	Results and discussion . . . . .	79
6.5.1	Chemical stability by FT-IR . . . . .	79
6.5.2	Temperature-dependent ellipsometry . . . . .	81
6.5.3	Water stability . . . . .	85
6.6	Conclusion . . . . .	87
6.7	Acknowledgment . . . . .	88
6.8	References . . . . .	88
7	SULFONATED POLYMER ELECTROLYTE THIN FILMS FROM ICVD	91
7.1	Preface . . . . .	91
7.2	Abstract . . . . .	92
7.3	Introduction . . . . .	92
7.4	Methods . . . . .	94
7.5	Results and discussion . . . . .	96
7.6	Conclusion . . . . .	106
7.7	References . . . . .	107
	<b>III DIRECT COATING OF PHARMACEUTICALS BY ICVD</b>	<b>109</b>
8	POLYMER ENCAPSULATION OF AN AMORPHOUS PHARMACEUTICAL BY ICVD	111
8.1	Preface . . . . .	111
8.2	Abstract . . . . .	112
8.3	Introduction . . . . .	112
8.4	Materials and Methods . . . . .	115
8.5	Results . . . . .	117
8.6	Discussion . . . . .	124
8.7	Conclusion . . . . .	127
8.8	Author Information . . . . .	128
8.9	Acknowledgments . . . . .	128
8.10	References . . . . .	128
8.11	Supporting Information . . . . .	132
9	WRINKLE FORMATION IN A POLYMERIC DRUG COATING DEPOSITED VIA ICVD	135
9.1	Preface . . . . .	135
9.2	Abstract . . . . .	136
9.3	Introduction . . . . .	136

9.4	Materials and methods . . . . .	138
9.5	Results and discussion . . . . .	140
9.6	Conclusion . . . . .	148
9.7	Acknowledgements . . . . .	149
9.8	References . . . . .	149
9.9	Supporting Information . . . . .	152
10	CONTROLLING INDOMETHACIN RELEASE THROUGH VAPOR-PHASE DEPOSITED HYDROGEL FILMS	153
10.1	Preface . . . . .	153
10.2	Abstract . . . . .	153
10.3	Main text . . . . .	154
10.4	Results . . . . .	156
10.5	Methods . . . . .	170
10.6	Acknowledgment . . . . .	171
10.7	Author contributions . . . . .	172
10.8	References . . . . .	172
10.9	Supporting Information . . . . .	176
11	CONCLUSION AND OUTLOOK	181

# Acronyms

---

AFM	Atomic force microscopy
API	Active pharmaceutical ingredient
EDX	Energy-dispersive X-ray spectroscopy
EGDMA	Ethylene glycol dimethacrylate
EW	Equivalent weight
DEGDVE	Di(ethylene glycol) divinyl ether
DVB	Divinylbenzene
EIS	Electrochemical impedance spectroscopy
GMA	Glycidyl methacrylate
FTIR	Fourier-transform infrared spectroscopy
HEMA	(Hydroxyethyl)methacrylate
iCVD	initiated Chemical Vapor Deposition
IUPAC	International Union of Pure and Applied Chemistry
MAA	Methacrylic acid
oCVD	oxidative Chemical Vapor Deposition
PE	Polyethylene
PET	Polyethylene terephthalate
PEM	Polymer electrolyte membrane
PFBSF	Perfluorobutane sulfonyl fluoride
PFDA	1 <i>H</i> ,1 <i>H</i> ,2 <i>H</i> ,2 <i>H</i> -Perfluorodecyl acrylate
PFOSF	Perfluorooctane sulfonyl fluoride
PP	Polypropylene
PTFE	Polytetrafluoroethylene
PVC	Polyvinyl chloride
s-PEEK	sulfonated polyether ether ketone

TAPO Di-*tert*-amyl peroxide

TBPO Di-*tert*-butyl peroxide

XPS X-ray photoelectron spectroscopy

XRD X-ray diffraction





# Introduction

---

With a global annual production capacity of 322 million tons,<sup>1</sup> plastics are not only a major economic factor but also a crucial material in various applications. While in everyday usage the term *polymer* is still strongly associated with (and synonymously used to) the term *plastic*, synthetic polymers have long surpassed their sole function as a packaging material.<sup>2</sup> Today, polymers are employed in a plethora of different applications, both industrial and consumer-related; they are being used in pipes, insulation, clothing, protective equipment (e. g., helmets) and heart valve replacements, among many other applications.<sup>3-5</sup> Moreover, natural polymers such as silk and cellulose (the main component of wood/paper) have been employed for many centuries.<sup>6</sup>

Tailored polymer compositions allow for a huge variety of material properties, ranging from flexible to rigid, from insulating to conductive, from amorphous to (liquid-)crystalline and also specific stimuli-responsiveness can be included (e. g., temperature-, pH- or light-responsiveness).<sup>7-9</sup>

Due to the versatile nature of polymeric materials, their application is not just limited to large-scale industrial usage. The rise of affordable small-scale 3D printers allows small businesses and private persons alike to make use of polymeric materials on an unprecedented scale; individual reproduction of spare parts, artistic usage and even complex prototype development have all become accessible this way.

However, not all polymers are that easily processable and, depending on the employed monomer(s), synthesis can be a challenging task. This is especially true for the synthesis of copolymers comprising opposing functionalities (e. g., hydrophilic/hydrophobic) or when conformal coatings on delicate substrates are desired.

In this context, initiated Chemical Vapor Deposition (iCVD) can be a powerful and versatile tool to synthesize polymers directly on even the most delicate substrates, such as pharmaceuticals or paper.<sup>10,11</sup> This technique relies on polymerization from the gas phase, thus avoiding common issues encountered in solution synthesis. A plethora of different chemistries is available for iCVD and copolymers can easily be obtained without the need of a common solvent. These unique features make iCVD particularly appealing for the two research topics covered within this thesis: (a) the synthesis of polymer electrolytes and (b) the preparation of thin polymer films for pharmaceutical applications.

The thesis itself is structured into three parts, with Part I providing a brief introduction to polymers in general, to their synthesis and to the main experimental characterization methods used. This is followed by parts dedicated to the findings of this thesis.

Part II focuses on the versatility of iCVD, which is exploited for the synthesis of proton conductive polymers. Earlier work had already demonstrated the ability of the iCVD technique to successfully synthesize copolymer membranes of methacrylic acid (MAA) and a perfluorinated compound (1*H*,1*H*,2*H*,2*H*-Perfluorodecyl acrylate, PFDA), showing promising ionic conductivity at ambient temperature.<sup>12,13</sup> As fuel cells usually operate at elevated temperatures of  $\sim 80^\circ\text{C}$  or above, it is crucial to study the thermal properties of such materials. For this, polymers of varying compositions were synthesized by iCVD and subjected to thermal analysis by *in situ* ellipsometry. This way, thermal expansion as well as thermal transitions could be monitored and be related to the polymer composition. A more detailed study was also carried out on polymers containing just PFDA, as this highly hydrophobic material is of particular interest for steam condensers.<sup>14,15</sup> The effect of cross-linking on the thermal stability of PFDA polymers was explored while monitoring the changes in the surface energy by means of water contact angle measurements. To conclude the topic of vapor deposited proton conductors, a sulfonated polymer was successfully synthesized by iCVD. Preliminary data of this material show promising proton conductivity values, encouraging further research into this material.

Part III focuses then on the ability of iCVD to synthesize polymers directly on delicate substrates. This major strength of the iCVD technique is explored in the framework of polymer coatings for pharmaceutical substances. Initially, the focus was on providing protective coatings for thin, amorphous drug formulations. For this, different polymer compositions were tested on the model drug system clotrimazole. By X-ray diffraction experiments, the crystallization of the drug was monitored while being subjected to heat treatment. During the preparation of iCVD polymers on the thin drug films, wrinkle formation was observed in the coatings. In a separate study, this effect has been explored in more detail. Finally, the release behavior of the drug indomethacin was investigated in a thin film reservoir system as a function of the polymer mesh size of the iCVD hydrogel coating.

## 1.1 References

- (1) PlasticsEurope *Plastics – the Facts 2016*; PlasticsEurope (Association of Plastics Manufacturers in Europe), EPRO (European Association of Plastics Recycling, and Recovery Organisations), 2016, 38.

- (2) M. Vert, Y. Doi, K.-H. Hellwich, M. Hess, P. Hodge, P. Kubisa, M. Rinaudo, and F. Schué *Pure and Applied Chemistry* **2012**, *84*, 377–410, DOI: 10.1351/PAC-REC-10-12-04.
- (3) G. G. Odian, *Principles of polymerization*, 4th edition; Wiley: 2004; 812 pp.
- (4) K. Modjarrad and S. Ebnesajjad, *Handbook of Polymer Applications in Medicine and Medical Devices*; Elsevier: 2013; 365 pp.
- (5) A. Srinivasan and S. Bandyopadhyay, *Advances in Polymer Materials and Technology*, 1st edition; CRC Press: Boca Raton, 2016; 824 pp.
- (6) O. Olatunji, *Natural Polymers: Industry Techniques and Applications*; Springer: 2015; 372 pp.
- (7) C. d. l. Heras Alarcón, S. Pennadam, and C. Alexander *Chemical Society Reviews* **2005**, *34*, 276–285, DOI: 10.1039/B406727D.
- (8) G. G. Wallace, P. R. Teasdale, G. M. Spinks, and L. A. P. Kane-Maguire, *Conductive Electroactive Polymers: Intelligent Polymer Systems, Third Edition*, 3rd edition; CRC Press: Boca Raton, 2008; 263 pp.
- (9) D. W. v. Krevelen and K. T. Nijenhuis, *Properties of Polymers, Fourth Edition: Their Correlation with Chemical Structure; their Numerical Estimation and Prediction from Additive Group Contributions*, 4th edition; Elsevier Science: Amsterdam, 2009; 1030 pp.
- (10) K. K. S. Lau and K. K. Gleason *Surface and Coatings Technology* **2007**, *201*, 9189–9194, DOI: 10.1016/j.surfcoat.2007.04.045.
- (11) S. G. Im, D. Kusters, W. Choi, S. H. Baxamusa, M. C. M. van de Sanden, and K. K. Gleason *ACS Nano* **2008**, *2*, 1959–1967, DOI: 10.1021/nn800380e.
- (12) A. M. Coclite, P. Lund, R. Di Mundo, and F. Palumbo *Polymer* **2013**, *54*, 24–30, DOI: 10.1016/j.polymer.2012.11.004.
- (13) C. Ranacher, R. Resel, P. Moni, B. Cermenek, V. Hacker, and A. M. Coclite *Macromolecules* **2015**, *48*, 6177–6185, DOI: 10.1021/acs.macromol.5b01145.
- (14) A. T. Paxson, J. L. Yagüe, K. K. Gleason, and K. K. Varanasi *Advanced Materials* **2014**, *26*, 418–423, DOI: 10.1002/adma.201303065.
- (15) DropWise Technologies Corp. *Technology* URL: <http://www.drop-wise.com/technology-1/> (accessed 01/22/2018).



## Part I

### FUNDAMENTALS AND METHODS

This part provides some background information on polymers in general, on their synthesis and on the main experimental characterization methods used within this work.



# Polymers

The term *polymer* (Greek, “poly·mer”, literally meaning *many parts*) denotes a class of materials which is characterized by the repetition of single, covalently linked units.<sup>1</sup> The International Union of Pure and Applied Chemistry (IUPAC) defines the following two terms in this context:

## IUPAC definitions

**Polymer.** Substance composed of macromolecules.

**Macromolecule.** A molecule of high relative molecular mass, the structure of which essentially comprises the multiple repetition of units derived, actually or conceptually, from molecules of low relative molecular mass.

Source: [2]

In the most simple case, a polymer consists of multiple repetitions of a single structural unit type. The number of repeating units  $n$  is thereby large enough so that material properties are (more or less) independent of the chain length. This is in contrast to *oligomers*, which usually feature a much smaller number of repeating units. A single unit is then called *monomer*, which is also the original building block in polymer synthesis.<sup>2</sup> This is also reflected in the nomenclature of polymers: in many cases, just the preposition “*poly*” is added to the monomer name when referring to the polymerized form.<sup>†</sup>

While the chemistry of a polymer is inferred from its constituting monomer units, another important characteristic is its molecular mass (i. e. the number of repeating units). This quantity is typically stated as the number-average molar mass  $M_n$  of a polymer, which calculates as

$$M_n = \frac{\sum_{i=1}^n n_i m_i}{\sum_{i=1}^n n_i} . \quad (2.1)$$

Here,  $n_i$  denotes the number of molecules with mass  $m_i$ . Accordingly, the mass-average molar mass  $M_w$  is then defined by<sup>‡</sup>

$$M_w = \frac{\sum_{i=1}^n n_i m_i^2}{\sum_{i=1}^n n_i m_i} . \quad (2.2)$$

<sup>†</sup> For example, a polymer derived from styrene is called poly(styrene).

<sup>‡</sup> The index  $w$  stands for *weight*, a term widely used for historic reasons but should generally be avoided when referring to *mass*.

Given the definitions in Equations (2.1) and (2.2), it is clear that an increased molecular mass will contribute more strongly to the mass-average molar mass than to the number-average one. If a polymer is *monodisperse*, meaning that different chains have all the same number of repeating units,  $M_w$  equals  $M_n$ . However, polymers will usually be *polydisperse* systems, meaning that molecular masses will not have a defined value but rather follow a broad distribution. This is reflected in the fraction  $M_w/M_n$ , which measures the degree of polydispersity.<sup>3</sup>

For synthetic polymers, usually two main polymer classes are distinguished: If the polymer repeating unit is made of just a single monomer type, it is referred to as *homopolymer*. On the other hand, if two or more different monomer types are present, the resulting polymer is labeled a *copolymer*.<sup>4</sup> In Figure 2.1, a schematic representation of the four main copolymer types is provided. Depending on how the two different monomer types are arranged within the polymer chain, one distinguishes random, alternating, block and graft copolymers. In general, the reactivity of the involved monomers and the synthesis procedure will determine which of the different copolymer types is formed. In Section 3.4, synthesis of such copolymer structures will be discussed in more detail.

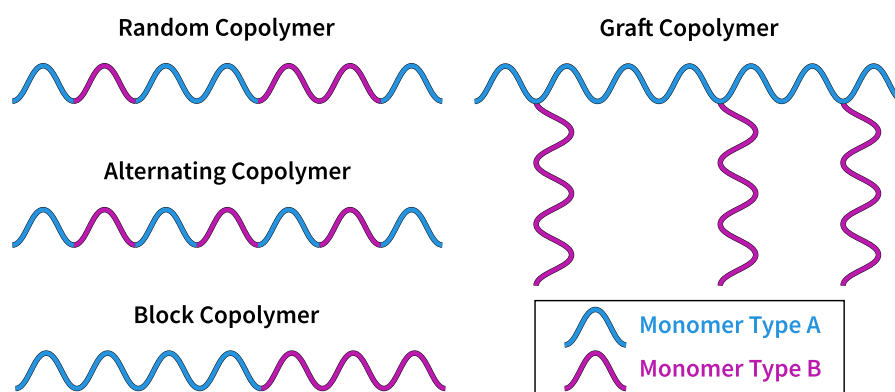


Figure 2.1: Graphical representation of the four main copolymer types differentiated in literature.

Due to the wide range of chemistries and processing techniques that are available for polymer synthesis, a large variety of properties and functions can be covered by this class of materials. This is why polymers are utilized in a plethora of different applications, ranging from simple packaging materials to highly sophisticated thermal insulation solutions for spacecrafts.<sup>5</sup> In the following sections, two specific applications of polymeric materials are discussed as they are related to the research carried out within the framework of this thesis. The first topic is focused on polymer electrolyte membranes, which are integral components in fuel cell systems. The second topic summarizes some examples of polymers employed in pharmaceutical applications.



## 2.1 Polymer electrolyte membranes

Polymer electrolyte membranes (PEMs) are materials that facilitate selectively ionic (mostly *protonic*) charge transport, which makes them particularly interesting for fuel cell applications.<sup>6–8</sup> However, PEMs are also employed in other systems, such as biofuel cells,<sup>9</sup> solid supercapacitors,<sup>10</sup> dye-sensitized solar cells<sup>11</sup> or in pharmaceutical applications.<sup>12</sup> Apart from exhibiting high ionic conductivities, these materials are often required to withstand elevated temperatures as well as harsh chemical environments, especially when employed in fuel cells.<sup>8,13</sup> For this, membranes are often composed of fluorinated compounds providing the necessary stability. The ionic conductivity derives from the acid groups present in the polymer structure. When hydrated, protons dissociate from the acid groups and are transferred to the surrounding media, generating mobile charge carriers.<sup>14</sup>

In Figure 2.2, a schematic representation of a polymer electrolyte fuel cell is provided. The PEM is positioned between two electrodes through which working gases, for example hydrogen and oxygen, are flown. In an ideal scenario, no gas cross-over occurs and the gases can only react with each other when the fuel (e. g., hydrogen) is catalytically oxidized at the anode (Equation (2.3)). The positively charged ions are then transported through the PEM, which does not allow for electron passage. Instead, electrons have to move through the electrical wires, establishing an electric current.

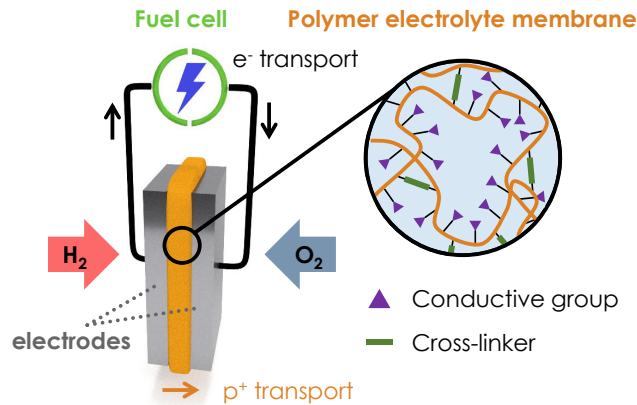


Figure 2.2: Schematic drawing of the membrane-electrode assembly in a PEM fuel cell. The polymer membrane usually consists of groups providing structural stability (e. g., cross-linker, fluorinated groups) and groups facilitating ionic charge transfer when hydrated (usually acids such as sulfonic acid). Figure reproduced with permission from ref. [15]. Copyright ©2017 Paul Christian



A highly hydrated state is also required as the solvation process of a single sulfonic acid group involves about four water molecules.<sup>22</sup> For a well-hydrated electrolyte, around 20 water molecules are present per  $\text{SO}_3^-$  group.<sup>23</sup> While most PEMs incorporate strong acid groups (mostly sulfonic acid) into the polymer matrix, also polymer electrolytes based on carboxylic<sup>6</sup> or on phosphonic<sup>24</sup> functionalities have been demonstrated.

Apart from fluorinated PEMs, also hydrocarbon-based polymer electrolyte membranes have seen increased interest in recent years.<sup>14,25</sup> These materials are often based on the sulfonation of polymers with an aromatic backbone, which provides the necessary thermal and chemical stability. For instance, poly(styrene sulfonic acid) or sulfonated polyether ether ketone (s-PEEK) have successfully been demonstrated, with s-PEEK showing conductivities of about 100 mS/cm above 100 °C.<sup>26,27</sup>

### 2.1.1 Proton transport mechanisms

In a polymer electrolyte membrane, proton transport can occur by three different mechanisms: a) hopping (Grotthuss) mechanism, b) vehicular mechanism or c) direct transport.

*Hopping mechanism.* In this mechanism, an excess proton is transported in water by *hopping* from one water molecule to the next.<sup>28</sup> In Figure 2.3, the transfer of a proton along two other water molecules by tunneling via hydrogen bonding is depicted. This mechanism is also referred to as *Grotthuss mechanism*, named after Theodor von Grotthuss, who first proposed this type of charge transfer in 1806.<sup>29</sup>

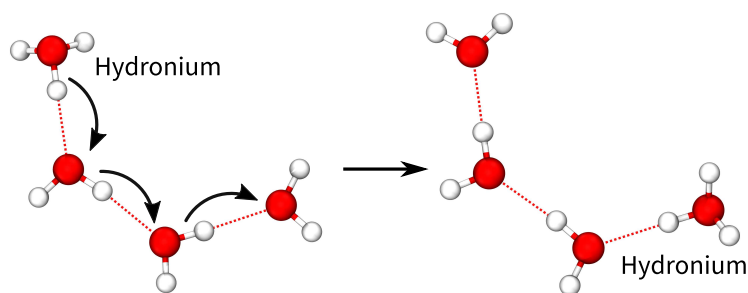


Figure 2.3: Representation of proton transport by the hopping mechanism (Grotthuss). The proton moves from its initial position on the hydronium molecule to neighboring water molecules via the hydrogen bonds.

For the solvation of the hydronium ion ( $\text{H}_3\text{O}^+$ ) in water, the two most well-known structures are the *Zundel* and the *Eigen cation* ( $\text{H}_5\text{O}_2^+$  and  $\text{H}_9\text{O}_4^+$  complexes, respectively). While the Zundel state describes

the delocalization of the proton between two water molecules, the Eigen cation corresponds to a hydronium ion which is strongly solvated by three surrounding water molecules. From *ab initio* molecular dynamics simulations, it has been inferred that proton conduction proceeds by a transition between Eigen (dominant form) and Zundel states (as an intermediate), so that the solvation structure rather than the ions themselves are moving.<sup>30,31</sup>

*Vehicular mechanism.* In contrast to the hopping mechanism, this type of transport describes the diffusive transport of the proton-solvent molecule complex (e. g., the hydronium ion). As strong hydrogen bonding is absent, this mechanism is typically characterized by lower proton mobility. Typically, both water and protons diffuse at similar rate.<sup>28</sup>

*Direct transport.* Another possible charge transport mechanism is the cooperative rearrangement of groups. Mobile polymer chains can pass a positively charged ion on to a neighboring chain, for example by side-chain movements. This requires the polymer to be in an un-ordered state, meaning that this mechanism will only be encountered at temperatures above the glass transition point.<sup>32</sup>

As the number of available charge carriers is depending on the solvation state of the acid groups, increased humidity (i. e. water content in the membrane) as well as increased temperature usually will lead to an increase in conductivity. While the hopping mechanism typically dominates at lower temperatures and highly solvated states, charge transport is mostly facilitated by the vehicular mechanism at elevated temperatures and/or low hydration states.<sup>28,33,34</sup>

## 2.2 Polymers in pharmaceutical applications

In pharmaceutical technology, polymers are primarily employed in three different ways: either as implantable networks, as carrier systems or as polymer-drug conjugates.<sup>35</sup> While also naturally-derived polymers see some application in pharmaceutical formulation (e. g., chitosan<sup>36,37</sup> or cellulose<sup>38,39</sup>), the use of synthetic polymers is often preferable due to them being more predictable in their properties and because they carry less risk of immunogenicity.<sup>40</sup>

Polymers can be used as protective coatings, forming reservoir systems in which the active pharmaceutical ingredient (API) is enclosed within an outer polymer layer.<sup>41,42</sup> Or they can act as scaffolds in which the drug is loaded and preserved in a dispersed state. The addition of the polymer can help in various ways, for example by preserving the solid state of the drug, by enhancing the solubility (and thus bioavailability) or by providing controlled release.<sup>43,44</sup> Hydrogels are a special case of matrix-type systems as they also store the API within

their structure.<sup>45,46</sup> However, the release mechanism is based on the swelling of the hydrogel in an aqueous environment and will depend on the polymer mesh size.<sup>47</sup>

With polymer systems, also active targeting can be achieved. By use of stimuli-responsive polymers (e. g., temperature- or pH-responsive polymers), the release behavior can be adjusted so that API liberation occurs only within certain environments. For instance, pH-responsiveness can be utilized to target specific parts of the gastrointestinal tract, as pH-values increase progressively from the stomach on.<sup>48</sup>

Conventionally, polymer-based drug delivery systems are prepared in solution, for which a variety of different methods are available.<sup>49</sup> Often, this requires multiple processing steps and can be quite laborious. In addition, solution processing might interfere with certain properties of the drug, such as the desired solid state.

For this reason, vapor-phase synthesis of polymeric drug coatings are particularly interesting as they do not require any solvents. While conventional Chemical Vapor Deposition methods are not well suited due to their high operating temperatures, the gentle conditions used in initiated Chemical Vapor Deposition pose little limitation and polymeric API coatings have already successfully been demonstrated.<sup>50,51</sup>

The addition of a polymer to the formulation will also affect the release behavior. In API-polymer systems, drug release proceeds either by degradation/erosion/disintegration of the polymer host matrix or by diffusion of the drug.<sup>52,53</sup> In the following section, some background on the mathematical modeling of diffusive drug release is provided.

### 2.2.1 Drug release from polymer systems

Here, a brief overview on some of the mathematical models commonly used to describe drug release behavior from polymeric systems is presented. For a more detailed introduction and a comprehensive overview of the topic, several well-written reviews can be found in literature.<sup>54-57</sup>

Often, drug release proceeds by mere mass-diffusion from polymer systems. In these cases, the release behavior is usually described by Fick's laws of diffusion. Fick's second law of diffusion describes the spatial change in concentration over time due to diffusion as

$$\frac{\partial c}{\partial t} = D \nabla^2 c, \quad (2.6)$$

with  $c$  being the concentration per volume. The diffusion coefficient is denoted by  $D$  and can be approximated with the Stokes-Einstein equation<sup>58</sup> by

$$D = \frac{k_B T}{6\pi\eta r_H} \quad (2.7)$$

with  $k_B$  being the Boltzmann constant,  $T$  being the temperature,  $\eta$  being the dynamic viscosity and  $r_H$  being the hydrodynamic radius of the drug.

Depending on the geometry of the system, this will result in different expressions for the release behavior. For instance, in case of thin matrix films, the cumulative absolute amount of drug released at time  $t$ , denoted by  $M_t$ , is given by<sup>55</sup>

$$\frac{M_t}{M_\infty} = 1 - \frac{8}{\pi^2} \sum_{n=0}^{\infty} \frac{1}{(2n+1)^2} \exp\left\{ \frac{-D(2n+1)^2 \pi^2 t}{L^2} \right\}. \quad (2.8)$$

The drug amount of full release is  $M_\infty$ , and  $L$  is the thickness of the film. For a partial release, Equation (2.8) can be approximated by

$$\frac{M_t}{M_\infty} = 4\sqrt{\frac{Dt}{\pi L^2}} \quad \text{for} \quad \frac{M_t}{M_\infty} < 0.6 \quad (2.9)$$

Among the various models, the semi-empirical equations of *Peppas*<sup>59</sup> and *Higuchi*<sup>60</sup> are probably the most commonly applied ones.

*Peppas equation.* This equation can typically be applied as an approximation to Fickian diffusion for times where drug release is not yet exceeding 60% of the full release. The cumulative absolute amount of drug released at time  $t$ ,  $M_t$ , is given by

$$\frac{M_t}{M_\infty} = kt^n, \quad (2.10)$$

with  $M_\infty$  being the total drug amount (full release). The constant  $k$  is related to the geometry of the system and the drug diffusivity, while  $n$  denotes the release exponent. From a fit to the experimental data, the type of diffusion can readily be determined by the parameter  $n$ . For a slab geometry,  $n = 0.5$  indicates Fickian transport while  $n = 1$  implies a Case II transport. For values in between, anomalous transport occurs.<sup>54</sup>

*Higuchi equation.* For a non-swelling, non-eroding polymer system, drug release behavior can be modeled by

$$\frac{M_t}{A} = \sqrt{D(2c_0 - c_s)c_s t}. \quad (2.11)$$

Here,  $A$  is the exposed surface area,  $D$  is the drug diffusivity in the polymer, while  $c_0$  and  $c_s$  denote the initial drug concentration and the drug solubility in the polymer, respectively.

When analyzing experimental release data, particular care has to be taken that all the prerequisites for a certain model are fulfilled. Different geometries of the same drug system (e. g., slab, spherical, cylindrical) will require different mathematical treatment and can greatly bias the results when neglected.

## 2.3 References

- (1) F. A. Bettelheim, W. H. Brown, M. K. Campbell, S. O. Farrell, and O. Torres, *Introduction to Organic and Biochemistry*, 8 edition; Brooks Cole: Belmont, CA, 2012; 704 pp.
- (2) A. D. Jenkins, P. Kratochvíl, R. F. T. Stepto, and U. W. Suter *Pure and Applied Chemistry* **2009**, *68*, 2287–2311, DOI: 10.1351/pac199668122287.
- (3) *Colloid Science: Principles, Methods and Applications*, 1 edition; Cosgrove, T., Ed.; Wiley-Blackwell: Oxford, UK ; Ames, Iowa, 2005, 304 pp.
- (4) A. Rudin and P. Choi, *The Elements of Polymer Science and Engineering*; Academic Press: 2012; 584 pp.
- (5) V. E. Skurat In *Encyclopedia of Aerospace Engineering*, DOI: 10.1002/9780470686652.eae236.pub2; John Wiley & Sons, Ltd: 2010.
- (6) V. Mehta and J. S. Cooper *Journal of Power Sources* **2003**, *114*, 32–53, DOI: 10.1016/S0378-7753(02)00542-6.
- (7) V. Neburchilov, J. Martin, H. Wang, and J. Zhang *Journal of Power Sources* **2007**, *169*, 221–238, DOI: 10.1016/j.jpowsour.2007.03.044.
- (8) S. J. Peighambaroust, S. Rowshanzamir, and M. Amjadi *International Journal of Hydrogen Energy* **2010**, *35*, 9349–9384, DOI: 10.1016/j.ijhydene.2010.05.017.
- (9) L. Zhang, M. Zhou, D. Wen, L. Bai, B. Lou, and S. Dong *Biosensors and Bioelectronics* **2012**, *35*, 155–159, DOI: 10.1016/j.bios.2012.02.035.
- (10) H. Gao and K. Lian *RSC Advances* **2014**, *4*, 33091–33113, DOI: 10.1039/C4RA05151C.
- (11) J. N. De Freitas, J. E. Benedetti, F. S. Freitas, A. F. Nogueira, and M. A. De Paoli In *Polymer Electrolytes*; Woodhead Publishing Series in Electronic and Optical Materials, DOI: 10.1533/9781845699772.2.381; Woodhead Publishing: 2010, 381.
- (12) R. J. Latham, R. G. Linford, and W. S. Schlindwein *Ionics* **2003**, *9*, 41–46, DOI: 10.1007/BF02376535.
- (13) J. Wu, X. Z. Yuan, J. J. Martin, H. Wang, J. Zhang, J. Shen, S. Wu, and W. Merida *Journal of Power Sources* **2008**, *184*, 104–119, DOI: 10.1016/j.jpowsour.2008.06.006.
- (14) M. A. Hickner, H. Ghassemi, Y. S. Kim, B. R. Einsla, and J. E. McGrath *Chemical Reviews* **2004**, *104*, 4587–4612, DOI: 10.1021/cr020711a.

- (15) P. Christian, *Oxidative and initiated Chemical Vapor Deposition for the Synthesis of Sulfonated Polymer Electrolyte Membranes*; Marshall Plan Scholarship Papers: 2017.
- (16) R. O'Hayre, S.-W. Cha, W. Colella, and F. B. Prinz, *Fuel Cell Fundamentals*, 3rd edition; Wiley: Hoboken, N.J, 2016; 580 pp.
- (17) H. Pu, *Polymers for PEM Fuel Cells*; John Wiley & Sons: 2014; 428 pp.
- (18) K. A. Mauritz and R. B. Moore *Chemical Reviews* **2004**, *104*, 4535–4586, DOI: 10.1021/cr0207123.
- (19) A. K. Sahu, S. Pitchumani, P. Sridhar, and A. K. Shukla *Bulletin of Materials Science* **2009**, *32*, 285–294, DOI: 10.1007/s12034-009-0042-8.
- (20) The Chemours Company *Nafion N115, N117, N1110 - Product Information*, 2016.
- (21) P. Colomban, *Proton Conductors: Solids, Membranes and Gels - Materials and Devices*; Cambridge University Press: 1992; 618 pp.
- (22) M. Maréchal, J. L. Souquet, J. Guindet, and J. Y. Sanchez *Electrochemistry Communications* **2007**, *9*, 1023–1028, DOI: 10.1016/j.elecom.2006.12.021.
- (23) J. Larminie, A. Dicks, J. Larminie, and A. Dicks In *Fuel Cell Systems Explained*, DOI: 10.1002/9781118878330.ch4; John Wiley & Sons, Ltd,: 2003, 67.
- (24) H. Steininger, M. Schuster, K. D. Kreuer, A. Kaltbeitzel, B. Bingöl, W. H. Meyer, S. Schauff, G. Brunklaus, J. Maier, and H. W. Spiess *Physical Chemistry Chemical Physics* **2007**, *9*, 1764–1773, DOI: 10.1039/B618686F.
- (25) M. Rikukawa and K. Sanui *Progress in Polymer Science* **2000**, *25*, 1463–1502, DOI: 10.1016/S0079-6700(00)00032-0.
- (26) S. M. J. Zaidi, S. D. Mikhailenko, G. P. Robertson, M. D. Guiver, and S. Kaliaguine *Journal of Membrane Science* **2000**, *173*, 17–34, DOI: 10.1016/S0376-7388(00)00345-8.
- (27) J. M. Serpico, S. G. Ehrenberg, J. J. Fontanella, X. Jiao, D. Perahia, K. A. McGrady, E. H. Sanders, G. E. Kellogg, and G. E. Wnek *Macromolecules* **2002**, *35*, 5916–5921, DOI: 10.1021/ma020251n.
- (28) J. Zhang, H. Zhang, J. Wu, and J. Zhang In *Pem Fuel Cell Testing and Diagnosis*, Zhang, J., Zhang, H., Wu, J., and Zhang, J., Eds.; Elsevier: Amsterdam, 2013, 143.
- (29) T. von Grothuss *Annales de Chimie* **1806**, *22*.
- (30) M. Tuckerman, K. Laasonen, M. Sprik, and M. Parrinello *The Journal of Physical Chemistry* **1995**, *99*, 5749–5752, DOI: 10.1021/j100016a003.



- (31) A. A. Hassanali, J. Cuny, V. Verdolino, and M. Parrinello *Phil. Trans. R. Soc. A* **2014**, 372, 20120482, DOI: 10.1098/rsta.2012.0482.
- (32) F. Gray and M. Armand In *Handbook of Battery Materials*, Daniel, C. and Besenhard, J. O., Eds., DOI: 10.1002/9783527637188.ch18; Wiley-VCH Verlag GmbH & Co. KGaA: 2011, 627.
- (33) K.-D. Kreuer, S. J. Paddison, E. Spohr, and M. Schuster *Chemical Reviews* **2004**, 104, 4637–4678, DOI: 10.1021/cr020715f.
- (34) J. Kopasz and C. Mittelsteadt In *Fuel Cells : Data, Facts and Figures*, Stolten, D., Samsun, R. C., and Garland, N., Eds., DOI: 10.1002/9783527693924.ch10; Wiley-VCH Verlag GmbH & Co. KGaA.: 2016, 99.
- (35) P. R. Wardwell and R. A. Bader In *Engineering Polymer Systems for Improved Drug Delivery*, Bader, R. A. and Putnam, D. A., Eds., DOI: 10.1002/9781118747896.ch2; John Wiley & Sons, Inc.: 2013, 29.
- (36) S. A. Agnihotri, N. N. Mallikarjuna, and T. M. Aminabhavi *Journal of Controlled Release* **2004**, 100, 5–28, DOI: 10.1016/j.jconrel.2004.08.010.
- (37) N. Bhattarai, J. Gunn, and M. Zhang *Advanced Drug Delivery Reviews* **2010**, 62, 83–99, DOI: 10.1016/j.addr.2009.07.019.
- (38) K. J. Edgar *Cellulose* **2007**, 14, 49–64, DOI: 10.1007/s10570-006-9087-7.
- (39) M. C. I. Mohd Amin, N. Ahmad, N. Halib, and I. Ahmad *Carbohydrate Polymers* **2012**, 88, 465–473, DOI: 10.1016/j.carbpol.2011.12.022.
- (40) M. Skiles and J. Blanchette In *Engineering Polymer Systems for Improved Drug Delivery*, Bader, R. A. and Putnam, D. A., Eds., DOI: 10.1002/9781118747896.ch8; John Wiley & Sons, Inc.: 2013, 227.
- (41) A. Ahmed, C. Bonner, and T. A. Desai *Journal of Controlled Release* **2002**, 81, 291–306, DOI: 10.1016/S0168-3659(02)00074-3.
- (42) W.-W. Yang and E. Pierstorff *Journal of Laboratory Automation* **2012**, 17, 50–58, DOI: 10.1177/2211068211428189.
- (43) R. G. Strickley *Pharmaceutical Research* **2004**, 21, 201–230, DOI: 10.1023/B:PHAM.0000016235.32639.23.
- (44) E. Bouyer, G. Mekhloufi, V. Rosilio, J.-L. Grossiord, and F. Agnely *International Journal of Pharmaceutics* **2012**, 436, 359–378, DOI: 10.1016/j.ijpharm.2012.06.052.

- (45) R. K. Bose and K. K. S. Lau *Chemical Vapor Deposition* **2009**, *15*, 150–155, DOI: 10.1002/cvde.200806748.
- (46) G. G. de Lima, D. Kanwar, D. Macken, L. Geever, D. M. Devine, and M. J. Nugent In *Handbook of Polymers for Pharmaceutical Technologies*, Thakur, V. K. and Thakur, n. K., Eds., DOI: 10.1002/9781119041559.ch1; John Wiley & Sons, Inc.: 2015, 1.
- (47) C. S. Brazel and N. A. Peppas *Polymer* **1999**, *40*, 3383–3398, DOI: 10.1016/S0032-3861(98)00546-1.
- (48) M. Ashford and J. Fell *Journal of Drug Targeting* **1994**, *2*, 241–257, DOI: 10.3109/10611869408996806.
- (49) C. E. Mora-Huertas, H. Fessi, and A. Elaissari *International Journal of Pharmaceutics* **2010**, *385*, 113–142, DOI: 10.1016/j.ijpharm.2009.10.018.
- (50) S. J. P. McInnes, E. J. Szili, S. A. Al-Bataineh, J. Xu, M. E. Alf, K. K. Gleason, R. D. Short, and N. H. Voelcker *ACS Applied Materials & Interfaces* **2012**, *4*, 3566–3574, DOI: 10.1021/am300621k.
- (51) S. J. P. McInnes, E. J. Szili, S. A. Al-Bataineh, R. B. Vasani, J. Xu, M. E. Alf, K. K. Gleason, R. D. Short, and N. H. Voelcker *Langmuir* **2016**, *32*, 301–308, DOI: 10.1021/acs.langmuir.5b03794.
- (52) K. M. Shakesheff In *Handbook of Biodegradable Polymers*, Lendlein, A. and Sisson, A., Eds., DOI: 10.1002/9783527635818.ch15; Wiley-VCH Verlag GmbH & Co. KGaA: 2011, 363.
- (53) J. W. McGinity, J. C. DiNunzio, and J. M. Keen In *Engineering Polymer Systems for Improved Drug Delivery*, Bader, R. A. and Putnam, D. A., Eds., DOI: 10.1002/9781118747896.ch9; John Wiley & Sons, Inc.: 2013, 283.
- (54) P. Costa and J. M. Sousa Lobo *European Journal of Pharmaceutical Sciences* **2001**, *13*, 123–133, DOI: 10.1016/S0928-0987(01)00095-1.
- (55) J. Siepmann and F. Siepmann *International Journal of Pharmaceutics* **2008**, *364*, 328–343, DOI: 10.1016/j.ijpharm.2008.09.004.
- (56) J. Siepmann and N. A. Peppas *Advanced Drug Delivery Reviews* **2012**, *64*, Supplement, 163–174, DOI: 10.1016/j.addr.2012.09.028.
- (57) R. A. Bader In *Engineering Polymer Systems for Improved Drug Delivery*, Bader, R. A. and Putnam, D. A., Eds., DOI: 10.1002/9781118747896.ch1; John Wiley & Sons, Inc.: 2013, 1.
- (58) A. Einstein *Annalen der Physik* **1905**, *322*, 549–560, DOI: 10.1002/andp.19053220806.

- (59) P. L. Ritger and N. A. Peppas *Journal of Controlled Release* **1987**, 5, 23–36, DOI: 10.1016/0168-3659(87)90034-4.
- (60) T. Higuchi *Journal of Pharmaceutical Sciences* **1963**, 52, 1145–1149, DOI: 10.1002/jps.2600521210.

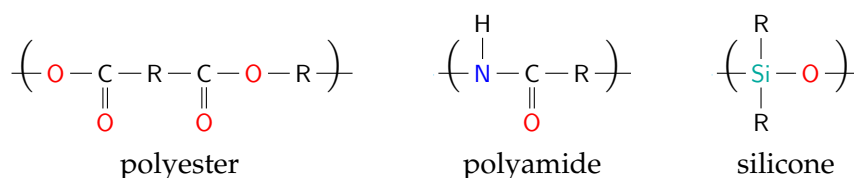


# Polymer synthesis

In this chapter, an introduction to polymer synthesis by free-radical polymerization is provided. While (from a commercial viewpoint) this mechanism is arguably the most important one, also step-wise polymerization will be briefly discussed as another important mechanism. The last section focuses then on the transition from solution-based radical polymerization to one from the vapor-phase. The corresponding technique is called initiated Chemical Vapor Deposition, which is the main (polymer) synthesis method employed in this thesis. More exhaustive reviews of the topics presented here and a more general introduction to polymerization can be found in literature.<sup>1-4</sup>

## 3.1 Step-wise polymerization

Step-wise polymerization is a concept describing the polymerization of monomers by a reaction of their functional groups. The most important polymer types synthesized by step-wise polymerization are polyesters, polyamides and silicones, among others.<sup>5</sup> Their structural formulas are depicted in Scheme 3.2.



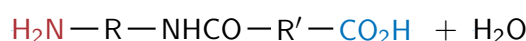
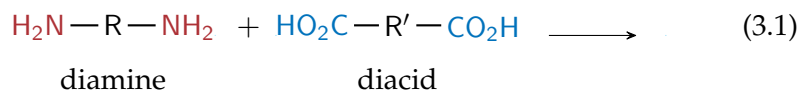
Scheme 3.2: Basic structural formulas of polymers commonly synthesized by step-wise polymerization.

In Figure 3.1, a simple graphical representation of such a step-wise polymerization reaction is provided. Monomers are readily reacting with each other in a statistical manner, initially forming dimers, then trimers and so on. As reaction time elapses, longer oligomers are formed, eventually resulting in long polymer chains (thus the name *step-wise polymerization*). In turn, this also means that high molecular weight polymers will only be obtained towards the end of the reaction.<sup>1</sup>

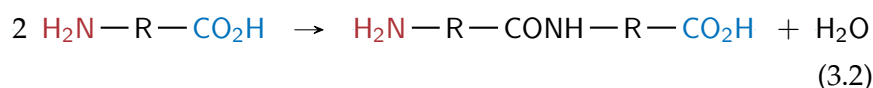
In order for the polymerization to proceed, the involved monomers need to be bi- or multifunctional.<sup>†</sup> Further, step-growth polymeriza-

<sup>†</sup> This refers to number of functional groups per molecule.

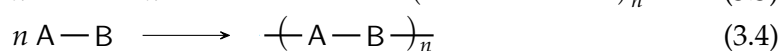
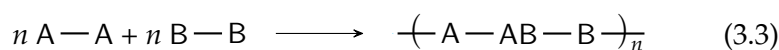
tion reactions can be classified by the type of monomer(s) employed. If only one monomer type is utilized, it has to contain at least two different types of functional groups (e. g., monomers of type  $A-R-B$ , with  $A$  and  $B$  being functional groups). Alternatively, one can also employ two different monomers, each one exhibiting only a single type of functional group (e. g.,  $A-R-A$  and  $B-R-B$ ). An example is the synthesis of polyamide by step-growth polymerization, which can either be facilitated by reacting diamines with diacids



or by the use of amino acids



In general, such reactions can be expressed by the following two equations:<sup>1</sup>



While these equations describe the polymerization in a rather general fashion, in practice often an external catalyst is used in addition to enhance the polymerization reaction. An example is the synthesis of poly(*p*-phenylene oxide) from 2,6-dimethylphenol by oxidative coupling, which proceeds only in the presence of a CuCl-pyridine catalyst.<sup>6,7</sup>

### 3.2 Kinetics

For the uncatalyzed step-wise polymerization reaction of two compounds, the reaction rate will be of second-order (third-order overall) and can be expressed as

$$-\frac{d[A]}{d\tau} = k[A^2][B], \quad (3.5)$$

with  $\tau$  denoting time and  $k$  being the rate constant.<sup>8</sup>  $[A]$  and  $[B]$  are the concentration of reactants with functionality  $A$  and  $B$ , respectively. For cases where concentrations  $[A]$  and  $[B]$  are approximately equal,<sup>†</sup> one can express Equation (3.5) as

$$-\frac{d[A]}{[A]^3} = kd\tau. \quad (3.6)$$

<sup>†</sup> This is true when polymers with high molecular weight should be obtained.

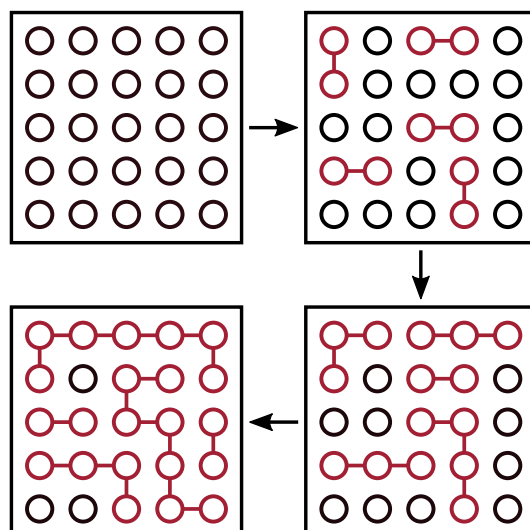


Figure 3.1: Schematic representation of a step-wise polymerization reaction, showing different stages in time. Open circles represent single monomer units, colored circles connected by strokes represent chemically linked species. Please note that the regular monomer arrangement is only chosen for visual clarity.

An integration of this equation for times  $\tau = 0$  to  $\tau = t$  yields

$$2kt = \frac{1}{[A_t]^2} - \frac{1}{[A_0]^2}. \quad (3.7)$$

Usually, Equation (3.7) is expressed in terms of  $p(t)$ , which is the fraction of functional groups reacted at time  $t$ .<sup>5</sup> With  $A_t = A_0(1 - p)$ , Equation (3.7) becomes

$$2A_0^2kt = \frac{1}{(1 - p)^2} - 1. \quad (3.8)$$

Accordingly, the degree of polymerization  $\overline{DP}$  is then described by<sup>†</sup>

$$\overline{DP} = \frac{A_0}{A_t} = \frac{1}{1 - p}. \quad (3.9)$$

From statistical considerations,<sup>5</sup> one obtains the following expressions for number- ( $M_N$ ) and weight-average molecular weight ( $M_W$ ) of a molecule containing  $m$  units:

$$M_N = \frac{m}{1 - p} \quad (3.10)$$

$$M_W = \frac{m(1 + p)}{1 - p} \quad (3.11)$$

<sup>†</sup> This is the so-called Carothers equation, found by Wallace Hume Carothers, the inventor of nylon.<sup>9</sup>

Only when the fraction conversion  $p$  is close to unity, application-relevant (i. e. high) molecular weights are obtained. For the polydispersity index  $\mathbb{D}_M$ , one obtains

$$\mathbb{D}_M \equiv \frac{\overline{M}_W}{\overline{M}_N} = 1 + p. \quad (3.12)$$

This means that for  $p = 1$ ,  $\mathbb{D}$  is limited to 2. If an external catalyst is present (i. e. polymerization reaction is of first order for the functional groups present), Equation (3.5) has to be modified:

$$-\frac{d[A]}{d\tau} = k[A][B] \quad (3.13)$$

Accordingly, a different expression is obtained for the rate equation:

$$\overline{DP} = [A_0]kt + 1 \quad (3.14)$$

### 3.3 Radical chain polymerization

Chain polymerization is a technique in which unsaturated monomers<sup>†</sup> are gradually attached to active sites of growing polymer chains, thus facilitating growth.<sup>1</sup> The technique is widely employed in the synthesis of common polymers such as polyethylene (PE), polypropylene (PP) and polyvinyl chloride (PVC). Polymers synthesized this way account for about 80 % of everyday polymers.<sup>2</sup>

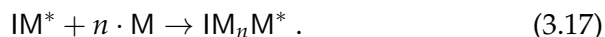
A key difference between step-wise and chain polymerization is the presence of an initiator in the latter. The initiator  $I$  is used to produce (re-)active species  $I^*$



which can either be radicals or ionic species (cationic/anionic). These active species can then react with suitable monomer(s)  $M$ , initiating the chain polymerization:



This also transfers the reactive center to the monomer, denoted by  $IM^*$ . The radical propagates then by successive monomer attachment, facilitating chain growth (until appropriately terminated):



For polymerization to occur, monomers must be at least *bifunctional* (i. e. the monomer can be linked to two or more molecules for a given reaction mechanism). This functionality can be obtained by either opening of a double bond (1), of a ring (2) or by co-reactive functional groups (3).<sup>3</sup> In the following, only reactions based on mechanism (1) will be considered.

<sup>†</sup> Those are compounds with carbon-carbon double or triple bonds.



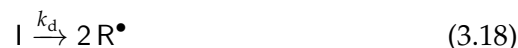
It should be noted that reactions (3.15) to (3.17) will usually occur simultaneously during polymerization in bulk as initiation/termination steps are separated neither spatially nor in time. Instead, radicals are perpetually, albeit randomly, generated and will activate/terminate in a statistical manner, leading to a rather broad distribution in the polymerization degree. If a narrower distribution is desired, an adapted technique such as *living radical polymerization* can be employed.<sup>10-12</sup> While several variants of this technique exist, their working principle relies on the suppression of termination reactions of a growing chain. A more detailed description can be found in literature.<sup>13-15</sup>

However, from the considerations above, three different stages can be identified in the growth of a single chain: *initiation*, *propagation* and *termination*. In the following sections, these individual reaction steps are discussed in the framework of *radical chain polymerization*, i. e. when the reactive species are radicals  $R^\bullet$ .

### 3.3.1 Radical initiation

Radicals are neutral chemical species (except for the case of *radical ions*) which possess an unpaired electron.<sup>16</sup> This results in a partially filled orbital, making them highly reactive. They can facilitate the polymerization of almost any vinyl group via opening of the carbon-carbon  $\pi$ -bond because resonance stabilization of the propagating reactive centers is rarely affected by the substituting groups.<sup>1</sup>

The initiation of a radical chain polymerization reaction consists of two steps. First, radicals are generated by dissociation of a so-called initiator molecule  $I$ , which exhibits a labile bond (often a peroxide bond, i. e. O–O) in its structure. For a certain temperature/pressure, the dissociation reaction



will occur at a characteristic rate constant  $k_d$ . Depending on how the dissociation energy is provided to the molecule, three initiation mechanisms are usually differentiated: thermal-, photo- and redox initiations.<sup>2</sup>

Initiator dissociation follows in general a first-order Arrhenius-behavior described by

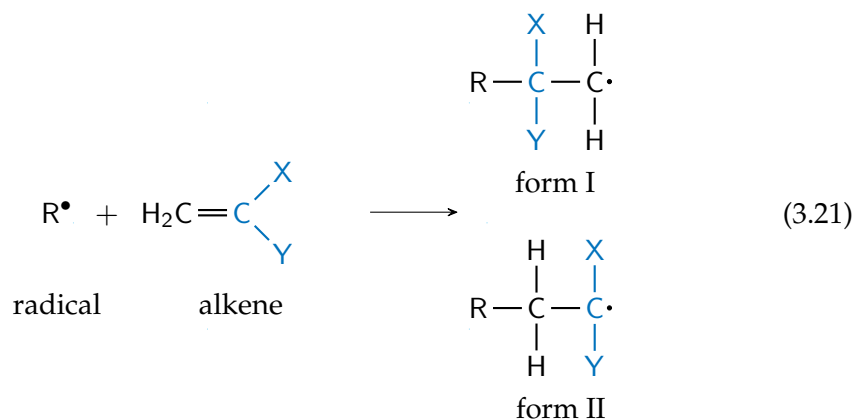
$$k_d = A \cdot e^{-E_a/RT}, \quad (3.19)$$

with  $k_d$  denoting the rate constant,  $A$  being a pre-exponential constant (*frequency factor*),  $E_a$  being the activation energy (for dissociation of the labile initiator bond) and  $R$  and  $T$  being the universal gas constant and reaction temperature, respectively.<sup>1</sup> The factor  $A$  accounts empirically for the number of transition attempts per time unit (thus the name *frequency factor*) and is often reported as  $\log_{10} A$  in literature. While it should be noted that this factor is also a function of temperature ( $A \propto T^n$ , with  $0.5 < n < 1$ ),<sup>17</sup> its effect on the rate constant is usually negligible as often only the order of magnitude is experimentally

accessible for  $A$ . Another important parameter is the initiator half-life, which is related to the rate constant  $k_d$  by

$$\tau_{1/2} = \ln(2)/k_d. \quad (3.20)$$

When a radical attacks the vinyl bond of either a mono- ( $X = H$ ) or a 1,1-disubstituted alkene, this results in the formation of one of two possible structures:<sup>1,2</sup>



The existence of the two different structures will influence how subsequent monomer units can be attached to the growing polymer chain (discussed further in Section 3.3.2). However, it should be noted that form II is far more stable than form I as the radical is stabilized by resonance effects of the substituent(s) at this position.<sup>1</sup>

In general, the initiation reaction can be represented by



with  $M$  denoting a single monomer (the index denotes the number of units) and  $k_i$  being the corresponding rate constant.

From Equation (3.18), the rate of radical generation can be expressed as

$$d[\text{R}^\bullet]/dt = 2 \cdot k_d [I]. \quad (3.23)$$

The square brackets of  $[I]$  denote the total initiator concentration in the system. The rate of initiation  $r_{\text{ini}}$  is then obtained by accounting for the *initiator efficiency*  $f$ , which leads to<sup>1</sup>

$$r_{\text{ini}} = 2 \cdot f \cdot k_d [I]. \quad (3.24)$$

The factor  $f$  accounts for the fact that not for every generated radical a polymerization reaction will be initiated and thus,  $f \leq 1$ .

### 3.3.2 Propagation

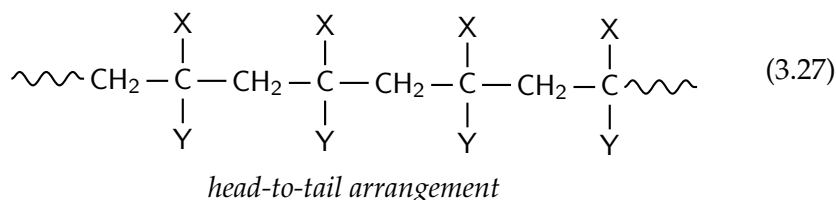
Chain growth proceeds by successive monomer addition to the new radical center formed by the initiation reaction (Equation (3.22)):



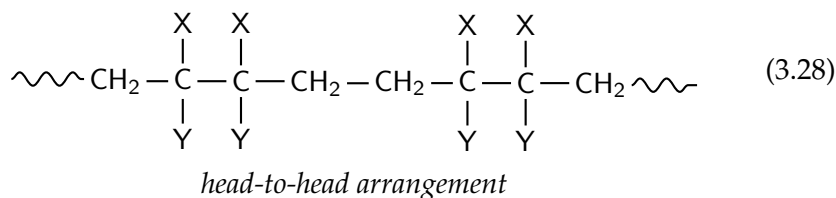
In general, the propagation reaction step can be expressed as



with  $k_p$  being the rate constant of propagation. As two types of radical centers can be formed in the initiation reaction (*cf.* Equation (3.21)), two propagation modes are possible. If successive monomer addition and initiation reaction proceed alike, this leads to the formation of a *head-to-tail arrangement*:<sup>2</sup>



Alternatively, if monomer addition proceeds by alternating between the two modes of Equation (3.21), this results in a *head-to-head arrangement*:<sup>2</sup>



However, usually the *head-to-tail* arrangement predominates greatly as the *head-to-head* fraction does not exceed a few percent for most vinyl monomers. The reason for this large difference is steric hindrance by the often bulky substituents, limiting the approach of a radical, as well as the resonance stabilization provided to the radical by most substituents.<sup>1,18</sup> An exception to this behavior are monomers with small substituents or ones which do not provide much resonance stabilization, e. g. fluorine. For instance, *head-to-head* fractions of ~5% are found in poly(vinylidene fluoride).<sup>19</sup>

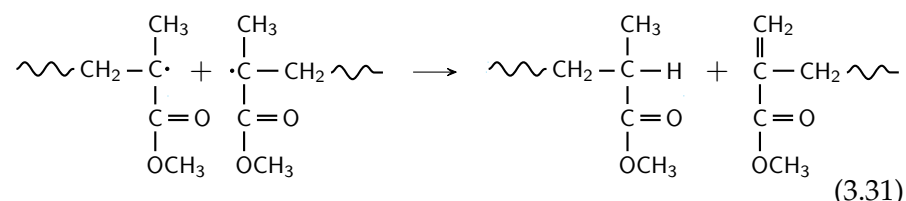
### 3.3.3 Termination

The final step in radical polymerization is the termination step, in which an actively growing chain loses its ability to grow further. In principle, this is facilitated by recombination of the active chain with either another radical or with another growing chain.<sup>3</sup> The corresponding reaction equations are thus

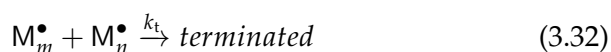


For some monomers, also termination by *disproportion* is possible. In this mechanism, a hydrogen atom is transferred from one active chain

to the other, terminating both chains and creating a new vinyl bond in the hydrogen-donating one.<sup>18</sup> Exemplary, this is depicted here for poly(methyl methacrylate):



Often, a combination of the different termination processes will occur so that the termination rate constant  $k_t$  will be the sum of all the involved termination modes:



### 3.3.4 Step and chain polymerization in comparison

The differences in the reaction mechanisms of step and chain growth polymerization do not only require different processing conditions and/or monomers, they are also reflected in the properties of the resulting polymers. In Table 3.1, some key differences between chain and step-wise polymerization are listed.

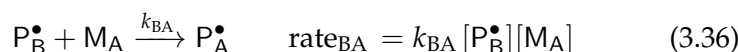
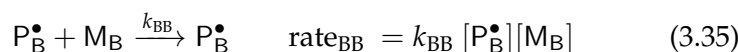
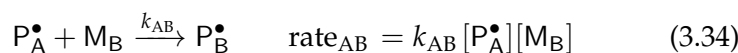
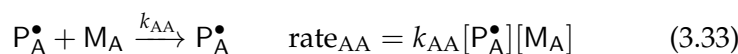
Table 3.1: Characteristic properties of chain polymerization and step polymerization in comparison. Table is based on ref. [2].

	Chain polymerization	Step polymerization
Mol. mass	High	initially low, changes over time
Reactivity	only active species and monomer can react	any two monomers can react
Species	monomers, oligomers, polymers and growing chains coexist for $t > t_0$	$t_0$ : monomers $> t_0$ : growing chain $t_{\text{final}}$ : high $M_w$ polymer
Reaction duration	short	long
Temperature	low	high

### 3.4 Copolymerization

Copolymerization is an important tool to alter various properties of a polymer by incorporating other monomers into its structure. For instance, cross-linkers<sup>†</sup> can provide additional (mechanical) stability, incorporation of hydrophilic groups can improve aqueous solubility and the addition of functional groups will allow for further modifications such as by addition reactions.<sup>20-22</sup>

In the framework of radical chain polymerization, copolymerization differs from the mechanisms described in Section 3.3 in the way chain growth by radical propagation proceeds. When two types of monomers ( $M_A$  and  $M_B$ ) are present during polymerization, the addition step of Equation (3.26) has to be replaced by four possible reactions:



Here,  $P_i$  stands for a growing polymer chain of any length with an end-group of species  $i$  and  $k_{XY}$  denotes the reaction constant for the transition from end-group species  $X$  to species  $Y$ . The expressions placed in square brackets refer to the total concentration of the respective compounds.<sup>3</sup>

From the rate equations 3.33 to 3.36, a simple expression, relating the monomer fraction in the polymer  $F_i$  to the monomer fraction present in the reaction feed  $f_i$ , can be derived:

$$F_A = \frac{r_A f_A^2 + f_A f_B}{r_A f_A^2 + 2f_A f_B + r_B f_B^2} \quad (3.37)$$

Here,  $r_i$  denotes the reactivity ratio of monomer  $i$  ( $r_A = k_{AA}/k_{AB}$  and  $r_B = k_{BB}/k_{BA}$ , respectively) and  $F_B = 1 - F_A$ . For a full derivation, please refer to ref. [3].

The reactivity ratios  $r_i$  of monomers involved in the copolymerization will also determine the structure of the resulting copolymer. For instance, if reactivity ratios are much smaller than one, attachment of the same species to a growing chain is greatly suppressed and a perfectly alternating copolymer results. In Table 3.2, an overview of the different cases is provided. A graphical representation of the different copolymer structures is provided in Figure 2.1.

<sup>†</sup> A cross-linker is a monomer with two reactive groups, meaning it can attach onto two different polymer chains during polymerization, effectively "linking" them together.

Table 3.2: Resulting copolymer structures for various reactivity ratio combinations of monomers A and B. Table is based on ref. [3].

$r_A$	$r_B$	$r_A \cdot r_B$	Copolymer structure
$r_A = 1/r_B$	$r_B = 1/r_A$	1	(ideal) random
$\ll 1$	$\ll 1$	$\rightarrow 0$	alternating
$> 1$	$> 1$	$> 1$	block copolymer
$\gg 1$	$< 1$	$< 1$	$\sim$ homopolymer of A
$< 1$	$\gg 1$	$< 1$	$\sim$ homopolymer of B
$\gg 1$	$\gg 1$	$\gg 1$	mixture of homopolymers A & B

### 3.5 initiated Chemical Vapor Deposition

In principle, polymer synthesis by initiated Chemical Vapor Deposition (iCVD) is following the steps of conventional radical polymerization in solution (as described in Section 3.3), with the exception that all the reagents are delivered from the vapor phase.<sup>4,23,24</sup> A typical iCVD setup is depicted schematically in Figure 3.2. Monomers enter the vacuum chamber through a heated mixing line, with flow controllers (or needle valves) adjusting the individual flow rates. To ease evaporation, monomer jars are also heated (typically to temperatures between 40 and 90 °C). The initiator enters the chamber through a separate line, kept at ambient temperature, to avoid premature (thermal) decomposition of the labile compound. In the chamber, a resistively heated filament is located suspended above the substrate stage. The stage is usually water cooled/heated so that temperatures between 10 and 60 °C can be set. The system is evacuated by a roughening pump.

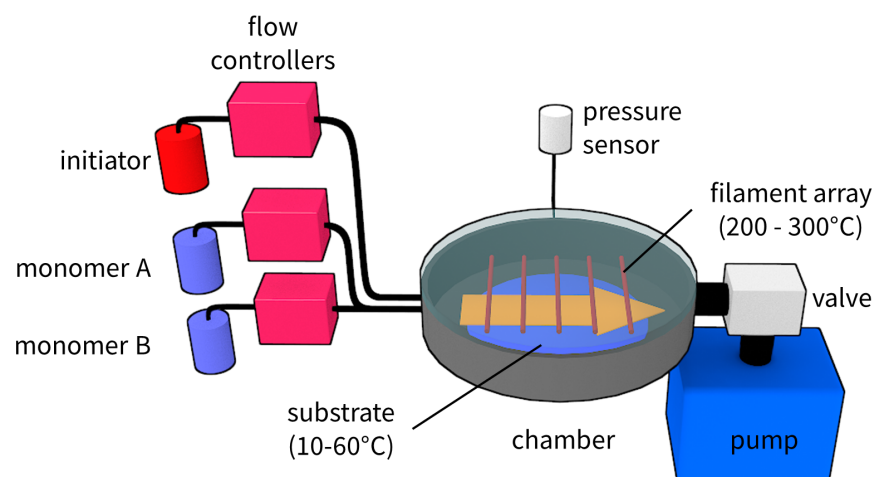


Figure 3.2: Schematic drawing of an iCVD system.

During deposition, a constant pressure is set in the chamber by use of a positional valve. Typically, pressures in the range between 5 to 130 Pa are used.

In Figure 3.3a, the reaction steps of iCVD polymerization are schematically depicted. Radicals are formed by thermal decomposition of an initiator (usually a peroxide) at a heated filament. These radicals can then attack vinyl bonds of monomers adsorbed at a substrate surface and, by subsequent monomer attachment, chain growth proceeds until terminated. The reaction equations for this mechanism are summarized in Figure 3.3b. As all the polymerization reactions occur at the substrate interface, this allows for the deposition of conformal coatings even on porous substrates or on surface structures with high aspect ratios.<sup>25,26</sup>

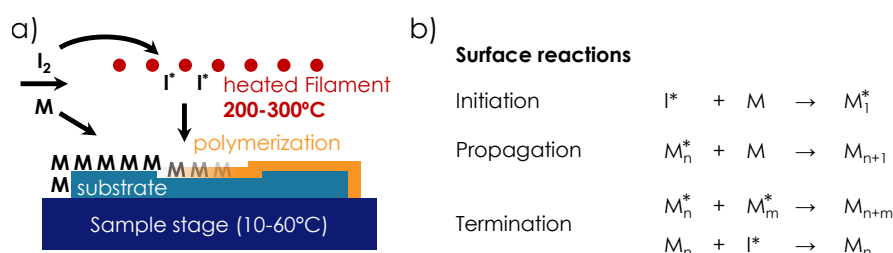


Figure 3.3: Schematic cross-sectional drawing of an iCVD chamber. Figure reproduced with permission from ref. [27]. Copyright ©2017 Paul Christian

While there are several experimental parameters which influence an iCVD deposition (e. g., filament and substrate temperatures, monomer flow rates or working pressure), they can ultimately be related to two governing parameters: the radical type and the surface fractions of the reactants. In the following, some theoretical and experimental considerations on these parameters are provided.

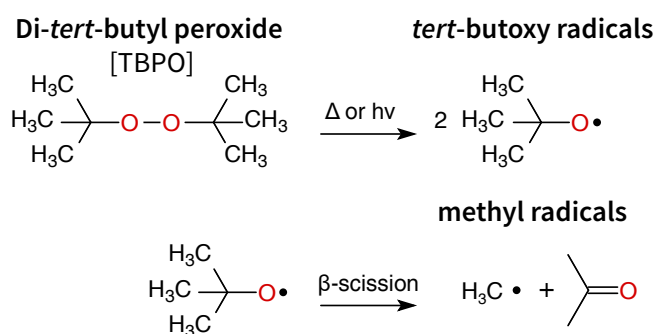
In iCVD, polymerization proceeds in analogy to the Eley-Rideal mechanism<sup>28</sup> so that the monomer surface concentration is determining the sticking probability of the initiator radicals.<sup>29</sup> This means that only the surface concentration of radicals ( $[I^*]$ ) and monomer ( $[M]$ ) have to be considered in the polymerization reaction. This behavior is also reflected in the deposition rate  $r_{\text{dep}}$ , which is given by

$$r_{\text{dep}} \sim k_{\text{dep}} [I^*] [M]. \quad (3.38)$$

Here,  $k_{\text{dep}}$  denotes the rate constant of the deposition. In general, the rate constant will follow an Arrhenius law (cf. Equation (3.19)) as a function of (substrate) temperature  $T_{\text{sub}}$ .

### 3.5.1 Initiator

The initiator most commonly employed in iCVD is Di-*tert*-butyl peroxide (TBPO).<sup>4</sup> By activation (e. g. thermally), the peroxide bond can selectively be broken, leading to the formation of radicals.<sup>30</sup> Two principal radical formation paths exist for TBPO, schematically depicted in Scheme 3.3. Given that sufficient energy is provided, TBPO will first decompose yielding *tert*-butoxyl radicals. The averaged activation energy for TBPO decomposition in gas-phase is  $(158.9 \pm 3.0) \text{ kJmol}^{-1}$ , with the averaged frequency factor  $A$  being  $10^{(15.6 \pm 0.4)} \text{ s}^{-1}$ .<sup>31,32</sup> From the activation energy and the frequency factor, TBPO half-lives<sup>†</sup> can be determined as a function of temperature according to Equation (3.20), with the results being visualized in Figure 3.4. At 150 °C, the TBPO half-life is approximately  $(120 \pm 8) \text{ min}$ , meaning that only a few radicals are formed at any given moment. If the temperature is increased to 200 °C instead, the half-life is drastically reduced to about  $(1.0 \pm 0.2) \text{ min}$ . In an iCVD process, this is generally the (filament) temperature at which polymerization reactions start to proceed at reasonable deposition rates ( $\sim 1 \text{ nm/min}$ ).



Scheme 3.3: Structural formula of TBPO and reaction pathways for radical formation by activation (e. g. thermally) and  $\beta$ -scission.<sup>33</sup>

The *tert*-butoxyl radicals can further undergo a  $\beta$ -scission reaction of the C–C bond, which results in the formation of methyl radicals. The occurrence of two different radical species has some relevance in iCVD processes; while methyl radicals dominate at filament temperatures above 270 °C, *tert*-butoxyl radicals are primarily formed at lower temperatures.<sup>34</sup> This difference is thought to cause different growth behaviors in liquid-crystalline fluoro-polymers as the filament temperature is varied in the iCVD process.<sup>35</sup>

Another interesting aspect is the fact that *tert*-butoxyl radicals are good hydrogen abstractors and will rarely initiate chain growth directly when employed in solution. Instead, they will abstract hydrogen atoms from solvent molecules, which in turn initiate the

<sup>†</sup> The time required to reduce a quantity to half of its starting value.



polymerization.<sup>36</sup> While solvents are not present in iCVD, hydrogen abstraction can still lead to a branching of the growing polymer chains.<sup>33</sup>

The range of activation energies reported for the  $\beta$ -scission of the C–C bond in *tert*-butoxyl radicals is  $50.5 - 64 \text{ kJmol}^{-1}$ , with  $A$  varying between  $10^{12.9}$  and  $10^{14.0 \pm 0.3} \text{ s}^{-1}$ .<sup>37–39</sup> At first it may seem surprising that despite their low activation energy, methyl radicals via  $\beta$ -scission are only observed at relatively high filament temperatures in iCVD.<sup>34</sup> However, the reported values represent the high pressure limiting constants (valid approximately at standard atmosphere and above). Interestingly, the  $\beta$ -scission of *tert*-butoxyl radicals shows a pressure dependence; at lower pressures, the frequency factor is a function of the pressure and a fall-off in the decay parameter  $k$  results.<sup>38,40</sup> As iCVD processes are usually performed well below the high pressure limit ( $p_{\text{iCVD}} < 140 \text{ Pa}$ ), this might explain the apparent discrepancy between theory and experiment.

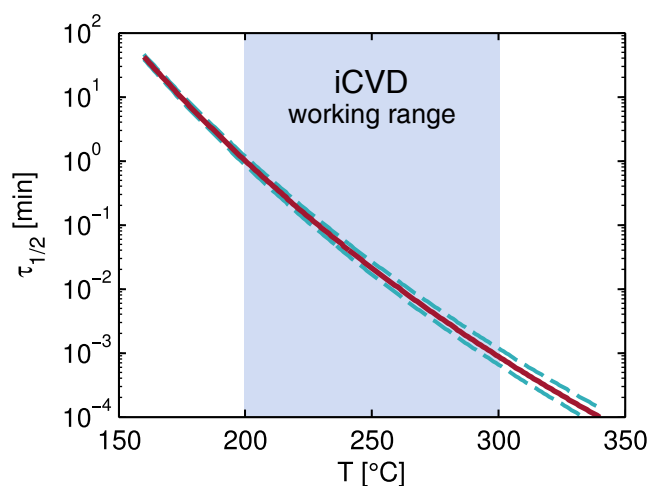


Figure 3.4: Half-life of TBPO as a function of temperature as determined from Equation (3.20). The dashed lines represent the error margins. The temperature-region typically employed in iCVD processes is highlighted in blue.

Besides TBPO, other initiators that have been used in iCVD are Di-*tert*-amyl peroxide (TAPO)<sup>23</sup>, hexafluoropropylene oxide (HFPO),<sup>41</sup> perfluorooctane sulfonyl fluoride (PFOSF)<sup>42</sup> and perfluorobutane sulfonyl fluoride (PFBSF).<sup>43</sup> The latter three are employed in the iCVD synthesis of polytetrafluoroethylene (PTFE) films. While HFPO can act both as initiator and monomer, iCVD polymerization is greatly enhanced when either PFOSF or PFBSF is utilized as a dedicated initiator.<sup>4</sup>

### 3.5.2 Monomer vapor pressure and surface fraction

As iCVD polymerization is a surface reaction in which all the reactants are supplied from the vapor phase, control over monomer adsorption rates is key to the process. However, the monomer fraction available for polymerization is not inherently known in iCVD as reactants are continuously supplied to the system. This is in contrast to solution-based techniques for which monomer fraction(s) are usually exactly known (e. g., by individual weight of the reactants prior to mixing).

In iCVD, the monomer surface concentration is depending on adsorption from the vapor phase. Such adsorption can often be treated in the framework of the *Brunauer-Emmett-Teller* (BET) theory,<sup>44</sup> which extends Langmuir theory<sup>45</sup> to multilayer adsorption. The adsorbed volume  $V_{\text{ad}}$  is then given by

$$V_{\text{ad}} = \frac{c \cdot V_{\text{m}} \cdot (p_{\text{m}}/p_{\text{m,sat}})}{(1 - p_{\text{m}}/p_{\text{m,sat}}) [1 - (1 - c) (P_{\text{m}}/p_{\text{m,sat}})]}, \quad (3.39)$$

with  $V_{\text{m}}$  denoting the volume of an adsorbed monolayer and with  $p_{\text{m}}$  and  $p_{\text{m,sat}}$  being monomer partial and saturation pressure, respectively.<sup>44</sup> The BET constant  $c$  is related to the difference in adsorption heat between the first layer  $E_{\text{mono}}$  and subsequent layers  $E_{\text{L}}$  by

$$c = \exp\left(\frac{E_{\text{mono}} - E_{\text{L}}}{R \cdot T}\right). \quad (3.40)$$

In the Henry's law limit ( $p_{\text{m}} \ll p_{\text{m,sat}}$ ), the zeroth order Taylor expansion of Equation (3.39) yields a linear adsorption isotherm

$$V_{\text{ad}} \Big|_{p_{\text{m}} \ll p_{\text{m,sat}}} \sim c \cdot V_{\text{m}} \cdot \frac{p_{\text{m}}}{p_{\text{m,sat}}}, \quad (3.41)$$

meaning that the  $p_{\text{m}}/p_{\text{m,sat}}$  ratio is an approximate measure of the monomer concentration adsorbed on a surface (i. e. the monomer concentration available for polymerization).<sup>23</sup> Thus, the monomer surface concentration  $[\text{M}]$  can be approximated by

$$[\text{M}] \Big|_{p_{\text{m}} \ll p_{\text{m,sat}}} \sim \frac{p_{\text{m}}}{p_{\text{m,sat}}}. \quad (3.42)$$

The validity of this approximation is supported by experimental findings of Lau *et al.*<sup>23,46</sup> and is usually applicable for  $p_{\text{m}}/p_{\text{m,sat}} < 0.3$ , which is well within standard iCVD operating conditions. Both deposition rate and molecular mass show an increase with an increasing surface monomer concentration.<sup>46</sup>

For given experimental conditions, the monomer partial pressure is then given by the monomer to total flow ratio  $Q_{\text{m}}/Q_{\text{total}}$  times the chamber pressure  $p_{\text{chamber}}$ :

$$p_{\text{m}} = \frac{Q_{\text{m}}}{Q_{\text{total}}} \cdot p_{\text{chamber}} \quad (3.43)$$

The saturation pressure, on the other hand, is a function of temperature and is best determined experimentally for each operating temperature (i. e. substrate temperature in iCVD). However, collecting data at various temperatures for every monomer might not always be feasible or possible. In such cases it is often sufficient to extrapolate the vapor pressure by use of either the Clausius-Clapeyron relation or the Antoine equation.<sup>47,48</sup> The former approach is widely used in the iCVD community as it requires only the knowledge of the vapor pressure  $p_1$  at temperature  $T_1$  (e. g., the boiling point, where the vapor pressure equals ambient pressure) and the latent heat of vaporization  $\Delta H_{\text{vap}}$  of a monomer. From this, any other pair  $(p_2, T_2)$  along the binodal curve can be determined by

$$\ln \frac{p_1}{p_2} = -\frac{\Delta H_{\text{vap}}}{R} \cdot \left( \frac{1}{T_1} - \frac{1}{T_2} \right). \quad (3.44)$$

However, the  $\Delta H_{\text{vap}}$  will not be constant over a wide temperature range so that large deviations might result from this extrapolation.

The Antoine equation, on the other hand, is better suited to (*semi-*) empirically describe the vapor pressure as a function of temperature. Given that Antoine parameters  $A$ ,  $B$ ,  $C$  are known for a certain compound, the vapor pressure at temperature  $T$  can be calculated by

$$\log_{10} p = A - \frac{B}{C + T}. \quad (3.45)$$

The Antoine parameters are usually only valid within a certain pressure regime and different sets might be necessary to describe the full range between critical and triple point. It should also be noted that particular attention has to be paid to the units of the constants/physical quantities. Due to the distinct nature of the Antoine parameters (for example,  $A$  has units ten to the power of pressure), one has to specify which units are used for pressure and temperature. Typically, pressure is stated either in millimeter of mercury or in bar while temperature is mostly given in Kelvin.

The surface fraction of monomer species  $i$  is then given by

$$f_i = \frac{[M_i]}{\sum_i [M_i]}. \quad (3.46)$$

### 3.6 References

- (1) G. G. Odian, *Principles of polymerization*, 4th edition; Wiley: 2004; 812 pp.
- (2) W.-F. Su, *Principles of Polymer Design and Synthesis*; Springer Science & Business Media: 2013; 314 pp.
- (3) A. Rudin and P. Choi, *The Elements of Polymer Science and Engineering*; Academic Press: 2012; 584 pp.

- (4) K. K. Gleason, *CVD Polymers: Fabrication of Organic Surfaces and Devices*; John Wiley & Sons: Weinheim, Germany, 2015; 484 pp.
- (5) C. E. Carraher Jr., *Polymer Chemistry - An Introduction*; Marcel Dekker, Inc.: New York, USA, 1996; Vol. Fourth Edition; 688 pp.
- (6) A. S. Hay, H. S. Blanchard, G. F. Endres, and J. W. Eustance *Journal of the American Chemical Society* **1959**, *81*, 6335–6336, DOI: 10.1021/ja01532a062.
- (7) A. S. Hay *Journal of Polymer Science Part A: Polymer Chemistry* **1998**, *36*, 505–517, DOI: 10.1002/(SICI)1099-0518(199803)36:4<505::AID-POLA1>3.0.CO;2-O.
- (8) P. J. Flory, *Principles of Polymer Chemistry*; The George Fisher Baker Non-Resident Lectureship in Chemistry at Cornell University; Cornell University Press: Ithaca, NY, 1953; 688 pp.
- (9) M. E. Hermes, *Enough for One Lifetime: Wallace Carothers, Inventor of Nylon*; Chemical Heritage Foundation: Washington, D.C., 1996; 345 pp.
- (10) M. K. Georges, R. P. N. Veregin, P. M. Kazmaier, and G. K. Hamer *Macromolecules* **1993**, *26*, 2987–2988, DOI: 10.1021/ma00063a054.
- (11) M. Kato, M. Kamigaito, M. Sawamoto, and T. Higashimura *Macromolecules* **1995**, *28*, 1721–1723, DOI: 10.1021/ma00109a056.
- (12) J. Chiefari, Y. K. (Chong, F. Ercole, J. Krstina, J. Jeffery, T. P. T. Le, R. T. A. Mayadunne, G. F. Meijs, C. L. Moad, G. Moad, E. Rizzardo, and S. H. Thang *Macromolecules* **1998**, *31*, 5559–5562, DOI: 10.1021/ma9804951.
- (13) O. W. Webster *Science* **1991**, *251*, 887–893.
- (14) K. Matyjaszewski and J. Xia *Chemical Reviews* **2001**, *101*, 2921–2990, DOI: 10.1021/cr940534g.
- (15) W. A. Braunecker and K. Matyjaszewski *Progress in Polymer Science* **2007**, *32*, 93–146, DOI: 10.1016/j.progpolymsci.2006.11.002.
- (16) P. Muller *Pure and Applied Chemistry* **2009**, *66*, 1077–1184, DOI: 10.1351/pac199466051077.
- (17) J. M. Criado, L. A. Pérez-Maqueda, and P. E. Sánchez-Jiménez *Journal of Thermal Analysis and Calorimetry* **2005**, *82*, 671–675, DOI: 10.1007/s10973-005-0948-3.
- (18) W.-F. Su In *Principles of Polymer Design and Synthesis*; Lecture Notes in Chemistry, DOI: 10.1007/978-3-642-38730-2\_7; Springer, Berlin, Heidelberg: 2013, 137.
- (19) J. B. Lando and W. W. Doll *Journal of Macromolecular Science, Part B* **1968**, *2*, 205–218, DOI: 10.1080/00222346808212449.

- (20) K. C. Taylor and H. A. Nasr-El-Din *Journal of Petroleum Science and Engineering* **1998**, *19*, 265–280, DOI: 10.1016/S0920-4105(97)00048-X.
- (21) R. Al-Itry, K. Lamnawar, and A. Maazouz *Polymer Degradation and Stability* **2012**, *97*, 1898–1914, DOI: 10.1016/j.polyimdegradstab.2012.06.028.
- (22) Y. Buchmüller, A. Wokaun, and L. Gubler *Fuel Cells* **2013**, *13*, 1177–1185, DOI: 10.1002/face.201300144.
- (23) K. K. S. Lau and K. K. Gleason *Macromolecules* **2006**, *39*, 3688–3694, DOI: 10.1021/ma0601619.
- (24) A. M. Coclite, R. M. Howden, D. C. Borrelli, C. D. Petruczok, R. Yang, J. L. Yagüe, A. Ugur, N. Chen, S. Lee, W. J. Jo, A. Liu, X. Wang, and K. K. Gleason *Advanced Materials* **2013**, *25*, 5392–5423, DOI: 10.1002/adma.201301878.
- (25) M. Gupta, V. Kapur, N. M. Pinkerton, and K. K. Gleason *Chemistry of Materials* **2008**, *20*, 1646–1651, DOI: 10.1021/cm702810j.
- (26) H. G. Pryce Lewis, N. P. Bansal, A. J. White, and E. S. Handy *Thin Solid Films* **2009**, *517*, 3551–3554, DOI: 10.1016/j.tsf.2009.01.114.
- (27) P. Christian, *Oxidative and initiated Chemical Vapor Deposition for the Synthesis of Sulfonated Polymer Electrolyte Membranes*; Marshall Plan Scholarship Papers: 2017.
- (28) K. W. Kolasinski In *Surface Science*, DOI: 10.1002/9781119941798.ch3; John Wiley & Sons, Ltd: 2012, 115.
- (29) S. H. Baxamusa and K. K. Gleason *Chemical Vapor Deposition* **2008**, *14*, 313–318, DOI: 10.1002/cvde.200806713.
- (30) N. A. Milas and D. M. Surgenor *Journal of the American Chemical Society* **1946**, *68*, 205–208, DOI: 10.1021/ja01206a017.
- (31) L. F. R. Cafferata and C. J. Manzione *Journal of Chromatographic Science* **2001**, *39*, 45–48, DOI: 10.1093/chromsci/39.2.45.
- (32) Y.-S. Duh, C.-S. Kao, and W.-L. W. Lee *Journal of Thermal Analysis and Calorimetry* **2017**, *127*, 1071–1087, DOI: 10.1007/s10973-016-5859-y.
- (33) P. G. Mekarbane and B. J. Tabner *Macromolecules* **1999**, *32*, 3620–3625, DOI: 10.1021/ma981917+.
- (34) G. Ozaydin-Ince and K. K. Gleason *Journal of Vacuum Science & Technology A* **2009**, *27*, 1135–1143, DOI: 10.1116/1.3168553.
- (35) A. M. Coclite, Y. Shi, and K. K. Gleason *Advanced Functional Materials* **2012**, *22*, 2167–2176, DOI: 10.1002/adfm.201103035.

- (36) D. Bednarek, G. Moad, E. Rizzardo, and D. H. Solomon *Macromolecules* **1988**, *21*, 1522–1528, DOI: 10.1021/ma00183a050.
- (37) M. Weber and H. Fischer *Journal of the American Chemical Society* **1999**, *121*, 7381–7388, DOI: 10.1021/ja990837y.
- (38) C. Fittschen, H. Hippler, and B. Viskolcz *Physical Chemistry Chemical Physics* **2000**, *2*, 1677–1683, DOI: 10.1039/B0000090.
- (39) M. Buback, M. Kling, and S. Schmatz *Zeitschrift für Physikalische Chemie* **2005**, *219*, 1205–1222, DOI: 10.1524/zpch.2005.219.9.1205.
- (40) M. Blitz, M. J. Pilling, S. H. Robertson, and P. W. Seakins *Physical Chemistry Chemical Physics* **1999**, *1*, 73–80, DOI: 10.1039/A806524A.
- (41) S. J. Limb, C. B. Labelle, K. K. Gleason, D. J. Edell, and E. F. Gleason *Applied Physics Letters* **1996**, *68*, 2810–2812, DOI: 10.1063/1.116332.
- (42) H. G. Pryce Lewis, J. A. Caulfield, and K. K. Gleason *Langmuir* **2001**, *17*, 7652–7655, DOI: 10.1021/la0104929.
- (43) K. K. S. Lau and K. K. Gleason *Surface and Coatings Technology* **2007**, *201*, 9189–9194, DOI: 10.1016/j.surfcoat.2007.04.045.
- (44) S. Brunauer, P. H. Emmett, and E. Teller *Journal of the American Chemical Society* **1938**, *60*, 309–319, DOI: 10.1021/ja01269a023.
- (45) I. Langmuir *Journal of the American Chemical Society* **1918**, *40*, 1361–1403, DOI: 10.1021/ja02242a004.
- (46) K. K. S. Lau and K. K. Gleason *Macromolecules* **2006**, *39*, 3695–3703, DOI: 10.1021/ma0601621.
- (47) B. Linder, *Thermodynamics and Introductory Statistical Mechanics*, 1 edition; Wiley-Interscience: Hoboken, N.J, 2004; 232 pp.
- (48) J. Gmehling, B. Kolbe, M. Kleiber, and J. Rarey, *Chemical Thermodynamics: for Process Simulation*; Wiley-VCH: Weinheim, 2012; 760 pp.

# Polymer analysis

---

The following chapter provides a brief introduction to the experimental techniques mainly employed within this thesis. While the presented methods have a broad applicability in general, measurement principles and data analysis are specifically discussed in the context of thin polymeric films. The chapter starts with a discussion of chemical analysis by Fourier-transform infrared spectroscopy (FTIR). This is followed by sections on spectroscopic ellipsometry, which allows the characterization of thickness/optical properties. Also, the study of dynamic behaviors (such as swelling and thermal transitions) with this technique is discussed. The chapter is completed by a brief discussion of electrochemical impedance spectroscopy, a powerful tool for coating performance analysis and for the characterization of electrical properties.

## 4.1 Chemical analysis by FTIR

Fourier-transform infrared spectroscopy (FTIR) is a powerful technique utilized in the investigation of the infrared absorption/transmission properties of a material. Usually, the mid-infrared region ( $\sim 4000 - 400 \text{ cm}^{-1}$ ) is explored in such an experiment, where fundamental vibrations can be attributed to the corresponding rotational/vibrational structure of the material.

### 4.1.1 Copolymer analysis

The composition of copolymers is often the defining property when material characteristics are experimentally assessed and obtaining compositional data is thus crucial for the analysis of such films. Standard techniques for such analysis include FTIR, various mass spectrometry techniques, X-ray photoelectron spectroscopy (XPS) and energy-dispersive X-ray spectroscopy (EDX).<sup>1-5</sup> Among these techniques, FTIR is a reliable, relatively inexpensive (both time- and cost-wise) technique.<sup>6</sup>

In FTIR analysis, the most common approach relies on the identification of characteristic vibrations in the experimental spectra which can be assigned uniquely to a single monomer species. By comparing peak heights and/or areas, the composition can be determined. While this method works reasonably well for some systems, it has

several limitations. Signal strength depends not only on the relative amount of a component and single peak analysis (especially when performed manually) is strongly dependent on the baseline correction applied. For iCVD films, it has been demonstrated that FTIR spectra of copolymers can often be approximated sufficiently-well as a linear combination of the homo-polymer spectra, weighted by their respective fractions.<sup>7</sup> This allows for a larger part of the spectrum to be included in the compositional analysis, reducing ambiguity.

The description relies on the Bouguer-Lambert-Beer law, which describes the decrease in radiant power as a function of thickness in transmission.<sup>6</sup> For a system of  $N + 1$  layers (substrate with  $N$  layers atop), the radiant power of the outgoing light  $I(\bar{\nu})$  is described by

$$I(\bar{\nu}) = I_0(\bar{\nu})10^{-\sum_{i=1}^{N+1} A_i(\bar{\nu})d_i}, \quad (4.1)$$

with  $I_0(\bar{\nu})$  being the radiant power of the incoming light and  $A_i(\bar{\nu})$  and  $d_i$  being the absorbance per unit length and the thickness of layer  $i$ , respectively. When the FTIR spectrum of the substrate (usually a silicon wafer) can be measured independently, signal from the (polymer) films remain:

$$\frac{I(\bar{\nu})}{I_{\text{sub}}} = 10^{-\sum_{i=1}^N A_i(\bar{\nu})d_i}. \quad (4.2)$$

Rearranging Equation (4.2), one obtains the absorbance spectrum  $A(\bar{\nu})$  of the polymer system:

$$A(\bar{\nu}) = -\log_{10} \frac{I(\bar{\nu})}{I_{\text{sub}}} = \sum_{i=1}^N A_i(\bar{\nu})d_i \quad (4.3)$$

While this equation describes the absorbance spectrum of  $N$  separated layers, Equation (4.3) also holds for a system in which layers are (physically) intermixed (under the assumption of constant volume). In turn, this means that the volume fraction  $F_i$  of component  $i$  in a mixture can be determined by

$$F_i = \frac{d_i}{d} \quad \text{with} \quad \sum_{i=1}^N F_i = 1 \quad \text{and} \quad d = \sum_{i=1}^N d_i. \quad (4.4)$$

This equation can not only be used for mixtures but also in cases where independent absorbance spectra can be assumed for the different monomers constituting the copolymer film. While this will usually be not the case for the full FTIR spectrum, the data evaluation can be restricted to a range where this assumption is fulfilled. In Figure 4.1, the model is graphically represented in the case of a copolymer film, which is treated as a combination of two homopolymer films, with their respective thicknesses accounting for their volume fractions. For a more detailed description of this approach, please refer to ref. [7].

In Figure 4.2, analysis of a p(EGDMA-HEMA) copolymer by this method is provided as an example. As can be seen from the fit, the



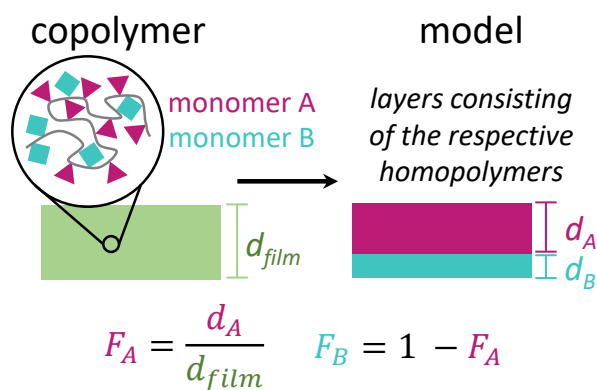


Figure 4.1: Graphical representation of the model assumed in the compositional analysis of copolymer FTIR data.

method is able to reproduce the experimental spectrum reasonably well in the range  $2000 - 1200 \text{ cm}^{-1}$  by a linear combination of the homopolymer spectra. From this, the HEMA and EGDMA fractions are determined to be 85 % and 15 %, respectively. It should be noted that this method also comes with several limitations and good agreement between fit and experimental data will not always be obtained. Also, it should be emphasized that this method will not necessarily result in an absolute quantification. However, it strongly reduces ambiguity usually introduced by manual evaluation and increases reproducibility.

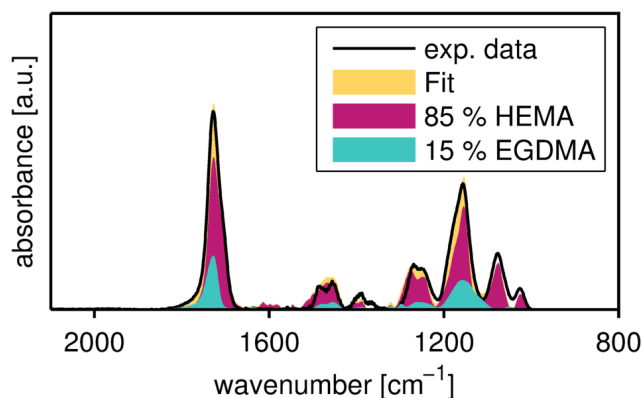


Figure 4.2: Copolymer analysis by direct calibration: experimental FTIR data of a  $\sim 200 \text{ nm}$  p(EGDMA-HEMA) film are treated as a linear combination of the respective homopolymer spectra. The fit parameters are the copolymer fractions (i. e. the weights assigned to the homopolymer spectra), from which a HEMA content of 85 % is determined.

### 4.1.2 Fineman-Ross analysis

Determining the compositions of copolymers is advisable in general but is particularly important when analyzing the reactivity ratios of the involved copolymers. Such analysis will also reveal the nature of the copolymer structure, as detailed in Section 3.4. This way one can also distinguish between the formation of a polymer mixture (i. e. monomers polymerize to homopolymers independently) and the synthesis of a *true* copolymer.

In principle, one can use the copolymer equation presented in Equation (3.37) to determine the reactivity ratios  $r_A$  and  $r_B$  from experimental data. A common strategy is the linearization of this equation, as presented by Fineman and Ross.<sup>8</sup>

#### Fineman-Ross equation

$$\underbrace{\frac{f_A(2F_A - 1)}{(1 - f_A)F_A}}_y = \underbrace{\frac{f_A^2(1 - F_A)}{(1 - f_A)^2F_A}}_x r_A - r_B \quad (4.5)$$

While the Fineman-Ross equation is an (algebraic) correct treatment of the copolymer equation, its evaluation by ordinary least-squares fitting is statistically not correct. The values of both dependent and independent variables (i. e.  $y$  and  $x$  in Equation (4.5), respectively) exhibit uncertainties, which violates the requirements for least-squares fitting.<sup>9</sup> Also, different values are obtained for the reactivity ratios  $r_x$  depending on which monomer is declared as compound A.

A statistically correct method called *error in variables method* (EVN) has been presented by Tidwell and Mortimer<sup>10</sup>. A software implementation has been presented by O'Driscoll and Reilly.<sup>11,12</sup> Also, parameter estimation by a Monte Carlo approach has been reported.<sup>13</sup> Despite these problems, the Fineman-Ross method is still widely applied in copolymer analysis, but care has to be taken when utilizing/referring to reactivity ratios from literature.

## 4.2 Spectroscopic ellipsometry

Spectroscopic ellipsometry is an optical technique in which changes in polarization are measured as a function of wavelength when linearly polarized light is reflected from a surface.<sup>14</sup> By modeling the experimental data, information on thickness, roughness and the optical properties of thin films can be gained.

In Figure 4.3, a schematic representation of an ellipsometric measurement is provided. Incoming, linearly polarized light is reflected from a surface at an angle  $\Phi_0$ . The incoming wave is propagating with an electric field vector  $\vec{E}_i$ , which experiences a phase- and amplitude

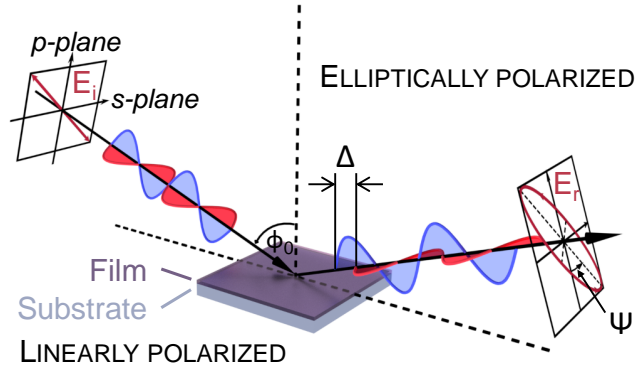


Figure 4.3: Schematic representation of an ellipsometric measurement. Incoming, linearly-polarized light is reflected from a sample under incident angle  $\Phi_0$ . This results in a phase shift  $\Delta$  and a change in the amplitude ratio  $\Psi$  for the reflected light, both being registered at a detector (not depicted).

change when interacting with the surface. The reflected light propagates with an electric field vector  $\vec{E}_r$ , experiencing a phase difference  $\Delta$  between the reflected  $s$ - and  $p$ -polarized light:

$$\Delta = \delta_{r,p} - \delta_{r,s} \quad (4.6)$$

The Fresnel coefficients  $r$  for  $s$ - and  $p$ -polarized light are given by the ratio between the electric field vector of reflected and incident light:<sup>14</sup>

$$r_p = \frac{E_{r,p}}{E_{i,p}} = \frac{n_t \cos(\theta_i) - n_i \cos(\theta_t)}{n_t \cos(\theta_i) + n_i \cos(\theta_t)} \quad (4.7)$$

$$r_s = \frac{E_{r,s}}{E_{i,s}} = \frac{n_i \cos(\theta_i) - n_t \cos(\theta_t)}{n_i \cos(\theta_i) + n_t \cos(\theta_t)} \quad (4.8)$$

The index  $i$  denotes the medium of the incident wave, with index  $t$  denoting the second medium. The refractive index is denoted by  $n$  and the angle of incidence by  $\theta$ . From this, the amplitude ratio  $\Psi$  is determined by

$$\tan \Psi = \left| \frac{r_p}{r_s} \right|. \quad (4.9)$$

The complex reflectance ratio  $\rho$  is then given by the so-called *Fundamental Equation of Ellipsometry*:<sup>14</sup>

$$\rho = \frac{r_p}{r_s} = \tan \Psi \exp(i\Delta) \quad (4.10)$$

In spectroscopic ellipsometry, the quantities  $\Delta$  and  $\Psi$  are measured as a function of wavelength, from which then the optical properties of the sample can be determined. In *variable angle spectroscopic ellipsometry* (VASE), data are collected also at various angles  $\Phi_0$  (typically, at

$\Phi_0 = 65, 70$  and  $75^\circ$ ). In Figure 4.4, exemplary VASE data of a transparent organic film, supported on a silicon substrate, are provided. The fringe in  $\Psi$  stems from optical interference, with position and number of fringes being related to the film thickness. From a fit to the data, the (initially) unknown properties of the organic layer are determined (see inset). In the following section, the models most commonly employed in the analysis of ellipsometric data will be briefly presented.

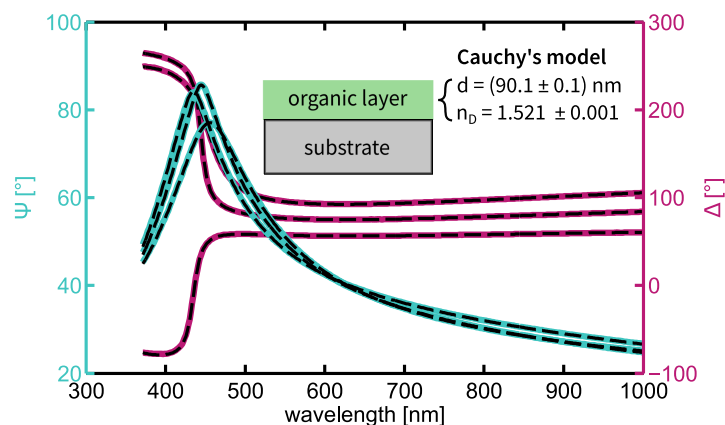


Figure 4.4: Exemplary experimental data from an spectroscopic ellipsometry measurement of an organic film on a silicon substrate. The phase and amplitude differences  $\Delta$  and the  $\Psi$  are plotted as function of wavelength for three incidence angles ( $60, 65$  and  $75^\circ$ ). The data is fitted (dashed lines) with the optical model shown in the inset, yielding thickness  $d$  and refractive index  $n_D$ .

#### 4.2.1 Data modeling

In order to obtain (quantitative) information from an ellipsometric measurement, a proper optical model has to be constructed. To fit Equation (4.10), the optical properties of the materials involved have to be either known or modeled instead. For this, either the complex refractive index  $\tilde{n}$  or the relative permittivity  $\epsilon$  is used:

$$\tilde{n} = n - ik \quad (4.11)$$

$$\epsilon = \epsilon_1 - i\epsilon_2 \quad \text{with} \quad \epsilon = \tilde{n}^2 \quad (4.12)$$

Here,  $k$  is the extinction coefficient and  $\epsilon_1$  and  $\epsilon_2$  are real and complex part of the permittivity. If all the optical parameters are known for a certain sample, just the layer thicknesses remain unknown and thus can easily be obtained from a fit to the experimental data. A helpful collection of optical constants for various materials can be found online at the *refractive index* database.<sup>15</sup>

However, often also the optical constants will be part of the model because tabulated values do not exist at all or because the optical properties of thin films are different from those of the bulk (which are typically known). In such instances, the (empirical) Cauchy's equation (cf. Equation (4.13)) is a very useful model, describing the refractive index  $n$  of a transparent material as a function of wavelength  $\lambda$  by coefficients  $A$ ,  $B$  and  $C$ .<sup>14</sup>

**Cauchy's equation with Urbach absorption term**

$$n(\lambda) = A + \frac{B}{\lambda^2} + \frac{C}{\lambda^4} \quad (4.13)$$

$$k(\lambda) = k_0 \cdot \exp\left(\frac{hc}{\lambda E_U} - \frac{E_g}{E_U}\right) \quad (4.14)$$

If some absorption is present, this model can be extended by an Urbach absorption term according to Equation (4.14). Here,  $E_U$  is the Urbach energy,  $k_0$  is the absorption amplitude and  $E_g$  is the band gap.<sup>16,17</sup> It should be noted that Equations (4.13) and (4.14) are not Kramers-Kronig consistent and *physically* correct results cannot be expected.<sup>14</sup> Nevertheless, above's equations can serve as an adequate model in cases where absorption effects are present but not dominant.

When dealing with *fully* transparent films,<sup>†</sup> better results are often obtained when employing the Sellmeier instead of the Cauchy model.<sup>14</sup>

**Sellmeier equation**

$$n(\lambda) = \left( \epsilon(\infty) + \frac{A_1 \lambda^2}{\lambda^2 - B_1} + \frac{A_2 \lambda^2}{\lambda^2 - B_2} \right)^{1/2} \quad (4.15)$$

However, in all these models perfect conditions are assumed, i. e. sharp interfaces, no roughness or no interpenetration between layers. However, imperfections are often encountered in practice and have to be accounted for in the data analysis. For all the cases mentioned so-far, effective media approximations can be used. These are models which describe the optical properties of materials in which two (different) phases are present. For example, a mixture between ambient (air) and thin film can be utilized to account for the presence of a surface roughness. The two most-commonly used models to describe the relative permittivity  $\epsilon$  of an effective media are *Maxwell Garnett* (MG)<sup>18</sup>

**Maxwell Garnett**

$$\frac{\epsilon - \epsilon_a}{\epsilon + 2\epsilon_a} = (1 - f_a) \frac{\epsilon_b - \epsilon_a}{\epsilon_b + 2\epsilon_a} \quad (4.16)$$

<sup>†</sup> i. e., absorption is negligible in the wavelength range of interest

and the *Effective Media Approximation* (EMA):<sup>19</sup>

**Effective Media Approximation**

$$f_a \frac{\epsilon_a - \epsilon}{\epsilon_a + 2\epsilon} + (1 - f_a) \frac{\epsilon_b - \epsilon}{\epsilon_b + 2\epsilon} = 0 \quad (4.17)$$

Here,  $\epsilon_a$  and  $\epsilon_b$  are the relative permittivity of phases A and B, respectively. The factor  $f_a$  denotes the probability to find  $\epsilon_a$  in a spherical space within the media. In Figure 4.5, the different assumptions between the two models are depicted. In the MG model, the total fraction  $f_a$  of phase A is surrounded entirely by phase B, which means that the permittivity of the effective media changes depending on which material is defined as sub-phase A. In the EMA model, on the other hand, the probability to find phases A and B within a spherical volume is described. Therefore, it can easily be extended to the general case of  $n$  intermixed phases:<sup>14,19</sup>

$$\sum_{i=1}^n f_i \frac{\epsilon_i - \epsilon}{\epsilon_i + 2\epsilon} = 0 \quad (4.18)$$

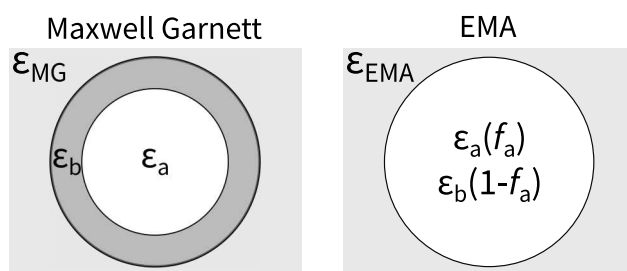


Figure 4.5: Graphical representation of the two effective medium theories commonly employed: Maxwell Garnett (left) and *effective media approximation* EMA (right). Figure is based on ref. [14].

#### 4.2.2 In situ measurements

A major advantage of ellipsometry over other techniques (such as X-ray reflectivity) is how fast data can be acquired. A standard measurement at fixed incidence angle requires a few seconds at most, thus allowing also the study of dynamic behaviors such as *in situ* growth,<sup>20,21</sup> glass transitions<sup>22,23</sup> or swelling.<sup>24,25</sup> It should be noted that swelling studies can also be performed with media different than water. Moreover, samples can not only be characterized when fully immersed but also when exposed to vapors (e. g., humidity).

### 4.3 Electrochemical impedance spectroscopy

Electrochemical impedance spectroscopy (EIS) is a powerful tool for the characterization of electrochemical properties of materials employed in applications such as batteries, fuel cells or for corrosion protection.<sup>26–28</sup>

In EIS, a periodic electrical signal is applied to the measurement system and its response is recorded at different frequencies. Depending on whether the applied signal has a constant voltage or a constant current amplitude, the measurement is labeled either *potentiostatic* or *galvanostatic*.<sup>29–31</sup> While data from both modes are often equivalent, the former is recommended for high-impedance systems and the latter for battery testing.<sup>32</sup> Usually, a sinusoidal signal is applied to the system so that voltage  $U$  and current  $I$  will be of form

$$U(t) = U_0 \cos(\omega t) \quad (4.19)$$

$$I(t) = I_0 \cos(\omega t + \theta), \quad (4.20)$$

with  $\omega$  being the angular frequency and  $\theta$  being the phase shift between the voltage and current response.  $U_0$  and  $I_0$  denote the voltage and the current amplitude, respectively. The impedance of the system  $Z$  is then defined as the ratio between voltage and current signal and will in general be a function of (angular) frequency:

$$Z(t) = \frac{U(t)}{I(t)} = Z_0 \frac{\cos(\omega t)}{\cos(\omega t + \theta)} \quad \text{with} \quad Z_0 = \frac{U_0}{I_0} \quad (4.21)$$

Expressing Equation (4.21) in the frequency domain ( $\omega$ ) via a Laplace transform, one obtains

$$Z(\omega) = Z_0 \exp(j\theta) = Z_0(\cos(\theta) + j \sin(\theta)). \quad (4.22)$$

Here,  $j$  denotes the imaginary unit. From Equation (4.22) it is also evident that the impedance can be separated into a real  $Z_r$  and a complex  $Z_j$  component


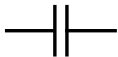



$$Z(\omega) = Z_r + jZ_j, \quad (4.23)$$

which, in turn, leads to two common types of graphical representation for impedance data: the Nyquist and the Bode plot. The former is a representation of  $-Z_j$  as a function of  $Z_r$ , while the latter represents both quantities as a function of frequency.<sup>31</sup>

The interpretation of impedance spectroscopy data relies then on modeling the experimental response by an equivalent circuit. For this, several electrical components can be used. In Table 4.1, an overview of components frequently used in EIS analysis is provided.

While capacitive effects are dominating the impedance behavior at high frequencies, resistive effects account for the low frequency response. In addition, double layer formation and diffusion processes

Table 4.1: Electrical elements and their corresponding impedance expression as well as the electronic symbols.<sup>29–31</sup> The *constant phase element* is abbreviated as “CPE”.

$R / \Omega$	... resistance		
$C / F$	... capacitance		
$L / H$	... inductance		
$Q_0 / s^n \cdot \Omega^{-1}$	... admittance ( $1/ z $ ) at $\omega = 1 \text{ rad s}^{-1}$		
$n$	... CPE exponent		
$A_W / \Omega \cdot s^{-1/2}$	... Warburg coefficient		
Element	Electronic symbol	Impedance	
Resistor		$Z = R$	(4.24)
Capacitor		$Z = j \cdot \frac{1}{\omega \cdot C}$	(4.25)
Inductor		$Z = j \cdot \omega \cdot L$	(4.26)
CPE		$Z = \frac{1}{Q_0 \cdot \omega^n} e^{-\frac{\pi}{2}nj}$	(4.27)
Warburg impedance		$Z = \frac{A_W}{\sqrt{\omega}} + \frac{A_W}{j \cdot \sqrt{\omega}}$	(4.28)

are often encountered in EIS measurements. To model such behavior, empirical elements are often used. For instance, double layers can often be described by the *constant phase element* (CPE), which represents an imperfect capacitor. Likewise, diffusion processes can often be modeled by a *Warburg element*.<sup>30</sup>

Usually, equivalent circuits will contain multiple elements to account for several interfaces/processes that are present in a measurement system. When two electrical components are connected in series, the total impedance is

$$Z_{\text{total}} = Z_1 + Z_2, \quad (4.29)$$

while a parallel connection yields

$$Z_{\text{total}} = \frac{Z_1 \cdot Z_2}{Z_1 + Z_2}. \quad (4.30)$$

In Figure 4.6, impedance responses commonly encountered in EIS are depicted in Nyquist representation along the corresponding equivalent circuits. However, caution has to be taken when constructing an equivalent circuit; just because a good match between model and experimental data is achieved, this does not validate the model as an adequate description of the experimental system at hand.



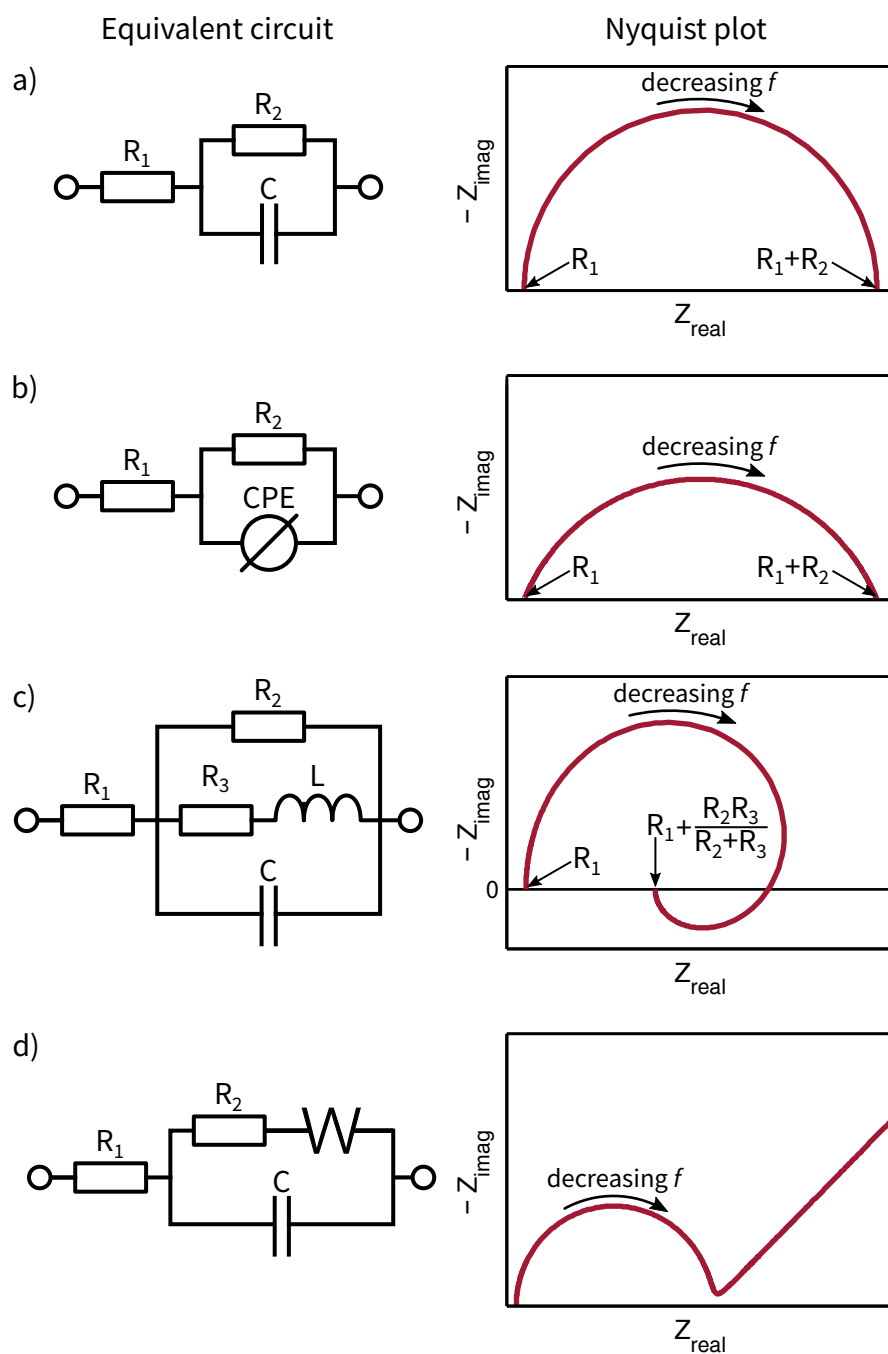


Figure 4.6: Selected data types commonly encountered in the analysis of electrochemical impedance spectroscopy data. Equivalent circuits are provided on the left, with the corresponding impedance data depicted on the right side in Nyquist representation. Data are plotted on equally scaled axes for a correct representation.

#### 4.4 References

- (1) R. Abate, A. Ballistreri, G. Montaudo, D. Garozzo, G. Impallomeni, G. Critchley, and K. Tanaka *Rapid Communications in Mass Spectrometry* **1993**, *7*, 1033–1036, DOI: 10.1002/rcm.1290071113.
- (2) C. M. Kassis, J. K. Steehler, D. E. Betts, Z. Guan, T. J. Romack, J. M. DeSimone, and R. W. Linton *Macromolecules* **1996**, *29*, 3247–3254, DOI: 10.1021/ma951782x.
- (3) A. Glidle, M. J. Swann, C. S. Hadyoon, L. Cui, J. Davis, K. S. Ryder, and J. M. Cooper *Journal of Electron Spectroscopy and Related Phenomena* **2001**, *121*, 131–148, DOI: 10.1016/S0368-2048(01)00331-0.
- (4) H. Ling and L. Junyan *Journal of Fluorine Chemistry* **2008**, *129*, 590–597, DOI: 10.1016/j.jfluchem.2008.04.007.
- (5) B. Nowacki, E. R. deAzevedo, and L. Akcelrud *Polymer Testing* **2011**, *30*, 342–347, DOI: 10.1016/j.polymertesting.2011.02.003.
- (6) P. R. Griffiths and J. A. D. Haseth, *Fourier Transform Infrared Spectrometry*; John Wiley & Sons: 2007; 556 pp.
- (7) M. Tazreiter, P. Christian, R. Schennach, T. Grießer, and A. M. Coclite *Analytical Methods* **2017**, *9*, 5266–5273, DOI: 10.1039/C7AY01748K.
- (8) M. Fineman and S. D. Ross *Journal of Polymer Science* **1950**, *5*, 259–262, DOI: 10.1002/pol.1950.120050210.
- (9) C. Hagiopol, *Copolymerization: Toward a Systematic Approach*; Springer Science & Business Media: 1999; 238 pp.
- (10) P. W. Tidwell and G. A. Mortimer *Journal of Polymer Science Part A: General Papers* **1965**, *3*, 369–387, DOI: 10.1002/pol.1965.100030137.
- (11) K. F. O'Driscoll and P. M. Reilly *Makromolekulare Chemie. Macromolecular Symposia* **1987**, *10-11*, 355–374, DOI: 10.1002/masy.19870100118.
- (12) M. Dube, R. A. Sanayei, A. Penlidis, K. F. O'Driscoll, and P. M. Reilly *Journal of Polymer Science Part A: Polymer Chemistry* **1991**, *29*, 703–708, DOI: 10.1002/pola.1991.080290512.
- (13) D. Zaldívar, G. Fuentes, D. Monett, C. Peniche, R. W. Arcís, A. Soto, and J. San Román *Polímeros* **1999**, *9*, 35–40, DOI: 10.1590/S0104-14281999000100005.
- (14) H. Fujiwara, *Spectroscopic Ellipsometry: Principles and Applications*, 1 edition; Wiley: Chichester, England ; Hoboken, NJ, 2007; 392 pp.

- (15) M. N. Polyanskiy *Refractive index database* URL: <https://refractiveindex.info> (accessed 01/11/2018).
- (16) F. Urbach *Physical Review* **1953**, *92*, 1324–1324, DOI: 10.1103/PhysRev.92.1324.
- (17) J. D. Dow and D. Redfield *Physical Review B* **1972**, *5*, 594–610, DOI: 10.1103/PhysRevB.5.594.
- (18) D. E. Aspnes, J. B. Theeten, and F. Hottier *Physical Review B* **1979**, *20*, 3292–3302, DOI: 10.1103/PhysRevB.20.3292.
- (19) D. a. G. Bruggeman *Annalen der Physik* **1935**, *416*, 636–664, DOI: 10.1002/andp.19354160705.
- (20) M. A. Hopper, R. A. Clarke, and L. Young *Journal of The Electrochemical Society* **1975**, *122*, 1216–1222, DOI: 10.1149/1.2134428.
- (21) E. Langereis, S. B. S. Heil, H. C. M. Knoop, W. Keuning, M. C. M. v. d. Sanden, and W. M. M. Kessels *Journal of Physics D: Applied Physics* **2009**, *42*, 073001, DOI: 10.1088/0022-3727/42/7/073001.
- (22) S. Kawana and R. A. L. Jones *Physical Review E* **2001**, *63*, 021501, DOI: 10.1103/PhysRevE.63.021501.
- (23) G. Vignaud, M. S. Chebil, J. K. Bal, N. Delorme, T. Beuvier, Y. Grohens, and A. Gibaud *Langmuir* **2014**, *30*, 11599–11608, DOI: 10.1021/la501639z.
- (24) R. Toomey, D. Freidank, and J. Rühle *Macromolecules* **2004**, *37*, 882–887, DOI: 10.1021/ma034737v.
- (25) W. Ogieglo, H. Wormeester, K.-J. Eichhorn, M. Wessling, and N. E. Benes *Progress in Polymer Science* **2015**, *42*, 42–78, DOI: 10.1016/j.progpolymsci.2014.09.004.
- (26) F. Mansfeld *Journal of Applied Electrochemistry* **1995**, *25*, 187–202, DOI: 10.1007/BF00262955.
- (27) U. Tröltzsch, O. Kanoun, and H.-R. Tränkler *Electrochimica Acta* **2006**, *51*, 1664–1672, DOI: 10.1016/j.electacta.2005.02.148.
- (28) R.-X. Dong, S.-Y. Shen, H.-W. Chen, C.-C. Wang, P.-T. Shih, C.-T. Liu, R. Vittal, J.-J. Lin, and K.-C. Ho *Journal of Materials Chemistry A* **2013**, *1*, 8471–8478, DOI: 10.1039/C3TA11331K.
- (29) E. Barsoukov and J. R. Macdonald, *Impedance Spectroscopy: Theory, Experiment, and Applications*; John Wiley & Sons: 2005; 616 pp.
- (30) M. E. Orazem and B. Tribollet, *Electrochemical Impedance Spectroscopy*, DOI: 10.1002/9780470381588.fmatter; John Wiley & Sons, Inc.: 2008.

- (31) A. Lasia, *Electrochemical Impedance Spectroscopy and its Applications*, 2014 edition; Springer: New York, 2014; 367 pp.
- (32) Gamry *EIS - Potentiostatic or Galvanostatic Mode* URL: <https://www.gamry.com/application-notes/EIS/eis-potentiostatic-galvanostatic-mode/> (accessed 02/02/2018).

## Part II

### PROTON CONDUCTIVE POLYMERS

This section explores the properties of proton conductive polymers synthesized by iCVD. Different chemistries are evaluated for improved proton conductivities and the thermal behavior of the polymers is studied *in situ*. The results are reproduced from their respective peer-reviewed publications and have been reformatted to fit the format of this thesis.



# Vapor-phase-synthesized Fluoroacrylate Polymer Thin Films: Thermal Stability and Structural Properties



BEILSTEIN JOURNAL OF NANOTECHNOLOGY

## Vapor-phase-synthesized fluoroacrylate polymer thin films: thermal stability and structural properties

Paul Christian and Anna Maria Coclite\*

Full Research Paper

Open Access

Address:  
Institute of Solid State Physics, Graz University of Technology, 8010  
Graz, Austria

Email:  
Anna Maria Coclite - anna.coclite@tugraz.at

\* Corresponding author

Keywords:  
EGDMA; iCVD; in situ; PFDA; spectroscopic ellipsometry;  
temperature dependent; X-ray diffraction

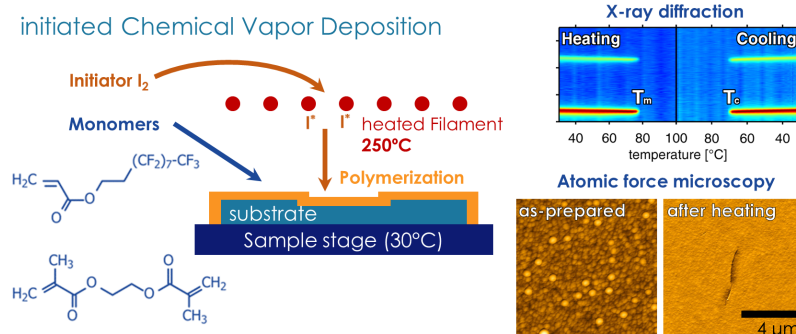
*Beilstein J. Nanotechnol.* 2017, 8, 933–942.  
doi:10.3762/bjnano.8.95

Received: 17 January 2017  
Accepted: 05 April 2017  
Published: 26 April 2017

This article is part of the Thematic Series "Vapor-based polymers: from films to nanostructures".

Guest Editors: M. Koenig and J. Lahann

© 2017 Christian and Coclite; licensee Beilstein-Institut.  
License and terms: see end of document.



## 5.1 Preface

This work was conducted at Graz University of Technology. The author of this thesis performed sample preparation, characterization as well as data evaluation and also wrote the manuscript. Anna Maria Coclite supervised the project and provided support in the manuscript preparation. The following text and its illustrations are identical to the published work<sup>1</sup> and are reproduced with permission.

- (1) P. Christian and A. M. Coclite *Beilstein Journal of Nanotechnology* 2017, 8, 933–942, DOI: 10.3762/bjnano.8.95.

## 5.2 Abstract

In this study, the thermal, chemical and structural stability of 1*H*,1*H*,2*H*, 2*H*-perfluorodecyl acrylate polymers (p-PFDA) synthesized by initiated chemical vapor deposition (iCVD) were investigated. PFDA polymers are known for their interesting crystalline aggregation into a lamellar structure that induces super-hydrophobicity and oleophobicity. Nevertheless, when considering applications which involve chemical, mechanical and thermal stresses, it is important to know the limits under which the crystalline aggregation and the resulting polymer properties are stable. For this, chemical, morphological and structural properties upon multiple heating/cooling cycles were investigated both for linear PFDA polymers and for differently strong cross-linked alterations thereof. Heat treatment leaves the chemical composition of the linear PFDA polymers largely unchanged, while a more ordered crystalline structure with smoother morphology is observed. At the same time, the hydrophobicity and the integrity of the polymer deteriorate upon heating. The integrity and hydrophobicity of cross-linked p-PFDA films was preserved likely because of the lack of internal strain due to the coexistence of both crystalline and amorphous phases. The possibility to finely tune the degree of crosslinking can therefore expand the application portfolio in which PFDA polymers can be utilized.

## 5.3 Introduction

Fluoropolymers, such as polytetrafluoroethylene, are interesting for a variety of different applications due to their low surface energy. The resultant hydrophobic and oleophobic surfaces are used as biocompatible surfaces<sup>1</sup>, antifouling coatings<sup>2</sup>, and as low dielectric constant materials<sup>3</sup> for microelectronics. Perfluoroacrylates are particularly appealing for such applications, as they combine the hydrophobic properties of the fluorinated pendant groups with easy processability due to an unsaturated acrylate group, allowing for mild processing conditions. One of the greatest limitations to the long-term stability of perfluoroacrylate-based technologies are mechanical, thermal and chemical stresses on the materials<sup>4-7</sup>.

Some super-hydrophobic and oleophobic surfaces based on perfluoroacrylates were previously prepared by initiated chemical vapor deposition (iCVD)<sup>8</sup>. The iCVD technique allows polymerization of the fluorinated monomers, while the chemical structure of the precursor(s) remains intact. Therefore, ultrathin (<100 nm) perfluoropolymers can be easily deposited with high control over the chemistry<sup>9</sup> and crystalline structure<sup>10</sup> of the resulting coatings. Different from other thin film polymer deposition techniques, iCVD takes place in a completely dry environment, eliminating the tedious need of dis-



solving the fluoropolymers. In addition, it also allows the chemical structure of the monomers to be retained at high deposition rates, especially when compared with pulsed plasma deposition techniques<sup>11</sup>. The mechanism of polymerization by iCVD mirrors that of radical polymerization in solution<sup>12</sup>. An initiator molecule is thermally decomposed into radicals by a filament heated to 250-300 °C. The radicals of the initiator selectively react with the vinyl bonds of monomer species absorbed on the substrate, initiating the polymerization. For this, the substrate is typically held below 60 °C. Chain growth then proceeds on the substrate surface until terminated by another initiator radical or another initiator-monomer fragment.

The mechanical and chemical robustness of iCVD perfluoropolymers at elevated temperature has not yet been investigated. The aim of this study is to identify the limits of the thermal and mechanical stability of the 1*H*,1*H*,2*H*,2*H*-perfluorodecyl acrylate polymer (p-PFDA), and in order to enhance its durability, the copolymerization with ethylene glycol dimethacrylate (EGDMA) as a cross-linker is evaluated (the monomers are depicted in Figure 1). EGDMA is a diester with no free hydrophilic groups, which offers low viscosity, flexibility and high cross-link density in various polymer applications. Differently cross-linked p-PFDA films deposited by iCVD were previously studied, albeit with a somewhat different scope<sup>13</sup>. In contrast to the other cross-linkers that have been studied in combination with perfluoropolymers (e.g., divinylbenzene (DVB)), EGDMA has a higher conversion rate, which results in a very low percentage of unreacted vinyl bonds after the deposition. It has been demonstrated that only after annealing, the perfluorinated films were strongly cross-linked by DVB resulting in films that showed low hysteresis between advancing and receding contact angle<sup>14</sup>. The advantage of cross-linking with EGDMA is the elimination of the annealing step, resulting in a cross-linked film already in the as-deposited form. The thermal stability of the thin films was evaluated by ellipsometry, Fourier transform infrared spectroscopy and X-ray diffraction. In situ ellipsometric studies allow the monitoring of the evolution of the thickness and optical constants of the materials during the heating ramp. This is particularly suitable for evidencing thermal transitions in thin films with thickness ranging from a few micrometers to monolayers<sup>15,16</sup>.

## 5.4 Experimental

The monomer precursor 1*H*,1*H*,2*H*,2*H*-perfluorodecyl acrylate (PFDA, purity 97%), the cross-linking agent ethylene glycol dimethacrylate (EGDMA, purity 98%) and the initiator *tert*-butyl peroxide (TBPO, purity 98%) were purchased from Sigma-Aldrich (Germany) and used without further purification. p-PFDA films with different degrees of cross-linking were prepared by initiated chemical vapor

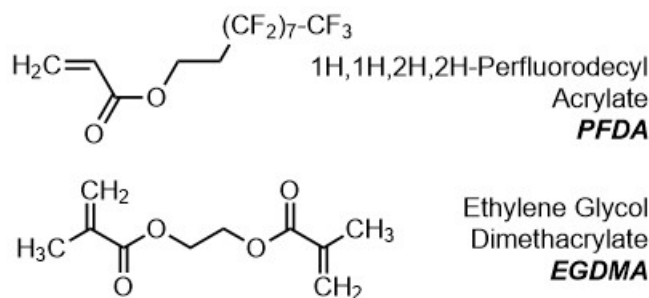


Figure 5.1: Molecular structure of the monomers PFDA and EGDMA.

deposition (iCVD). The average thickness of the as-deposited polymer films was  $(350 \pm 50)$  nm. Detailed information on the actual processing conditions are provided in Supporting Information 5.9, while a full description of the setup can be found in a previous publication<sup>17</sup>. As substrates, silicon wafers with a native oxide layer (thickness 1.7 nm) were used after being cut into  $2 \times 2$  cm pieces.

Fourier transform infrared spectroscopy (FTIR) was performed on a Bruker IFS 66v/s spectrometer in transmission mode, with all the data being converted to absorption spectra by the OPUS software. The data are automatically baseline corrected by a custom routine written in R, utilizing the algorithms provided in the baseline package<sup>18</sup>.

Specular X-ray diffraction (XRD) patterns were recorded on a PANalytical Empyrean diffractometer. The system is equipped with a copper sealed tube ( $\lambda = 0.154$  nm), a Göbbel mirror, various slits and a PIXcel<sup>3D</sup> solid state detector. All data were recorded using the same setup and are represented in the scattering vector ( $q_z$ ) notation, whereby  $q_z = 4\pi \cdot \sin(\Theta)/\lambda$ . The index  $z$  indicates that only net planes parallel to the substrate surface were probed in the experiment (specular scan). *In situ*, temperature-dependent XRD studies were performed with a DHS900 heating stage attachment (Anton-Paar, Austria), using a heating rate of  $2^\circ\text{C}/\text{min}$ . The integration time was set to one minute, meaning that a temperature resolution of  $2^\circ\text{C}$  could be achieved. Atomic force micrographs were taken in noncontact mode on a Nanosurf easyScan 2, equipped with a PPP-NCLR-10 cantilever (NanoWorld AG, Switzerland). The data are corrected for artifacts with the freely available software package Gwyddion<sup>19</sup>.

The water contact angle (WCA) of the polymer films was determined by the static sessile drop method on a CAM200 contact angle analyzer (KSV Instruments, Finland). Each sample was probed on five different spots, using a droplet volume of  $4 \mu\text{L}$ .

*In situ* temperature-dependent spectroscopic ellipsometry measurements were performed on a Woollam M-2000 ellipsometer (J.A. Woollam Co., USA), equipped with a THMS600 temperature stage (Linkam, UK) under nitrogen atmosphere. The samples were investigated in the temperature range between  $10$  and  $150^\circ\text{C}$  at a

heating/cooling rate of 5 °C/min, with a hold time of 5 min between steps. Prior to the measurement, the samples were equilibrated by three subsequent heating and cooling cycles. The optical data were recorded every second at an incidence angle of 75° in the wavelength range of 370 to 1000 nm. The ellipsometric data were modeled using the CompleteEASE<sup>®</sup> software by a three-layer system consisting of the silicon substrate, the interfacial oxide layer and the transparent top layer. The wavelength- and temperature-dependent refractive indices of silicon and oxide were taken from literature<sup>20</sup>, whereas Cauchy's equation was utilized in modeling the polymer film. A nonlinear least squares fit of the experimental data with this model yields the optical constants and thickness of the polymer layers.

## 5.5 Results and Discussion

### Chemical composition

The retention of chemical functionality and the degree of cross-linking for the different samples were evaluated by FTIR spectroscopy. In Figure 5.2, the spectra of the as-prepared samples are depicted (solid lines), where the data are normalized with the polymer layer thickness (i.e., with the sampled volume). Starting with the spectrum of p-PFDA, several characteristic absorption peaks are noted. In the fingerprint region (1500-500 cm<sup>-1</sup>), the skeletal vibrations of the CH<sub>x</sub> and CF<sub>x</sub> groups are visible, most prominently featuring the symmetric and antisymmetric stretch of the CF<sub>2</sub> groups at 1251 and 1206 cm<sup>-1</sup>, respectively. In addition, a strong absorption peak is observed at 1740 cm<sup>-1</sup>, stemming from the C=O stretching of the ester groups. Upon cross-linking, this peak increases in intensity as EGDMA has twice the number of C=O groups relative to PFDA. In the fingerprint region, the signal of the CF<sub>x</sub> groups decreases with increased cross-linking, eventually resulting in two distinct peaks of C–O stretching at 1257 and 1158 cm<sup>-1</sup> for p-EGDMA. Additional peaks in the regions of 1480–1450 cm<sup>-1</sup> and 3000–2800 cm<sup>-1</sup> in the spectra of the cross-linked polymers are attributed to deformation and stretching vibrations of the CH<sub>x</sub> groups, respectively. Interestingly, a small peak at 1638 cm<sup>-1</sup> is noted to appear exclusively for p-EGDMA, which is characteristic for C=C stretching<sup>21</sup>. This implies that the polymerization of the cross-linker is not completely facilitated as some unreacted vinyl bonds remained in the polymer. Nevertheless, this peak is absent for all other spectra, thus the fraction of unreacted monomer species (in the limit of the experiment) is likely small. This means that the postdeposition annealing steps are superfluous, which is a clear advantage over other cross-linkers such as divinylbenzene; for the latter, iCVD copolymerization with PFDA resulted only in minor conversion rates, necessitating a time-consuming thermal conversion after deposition<sup>14</sup>.

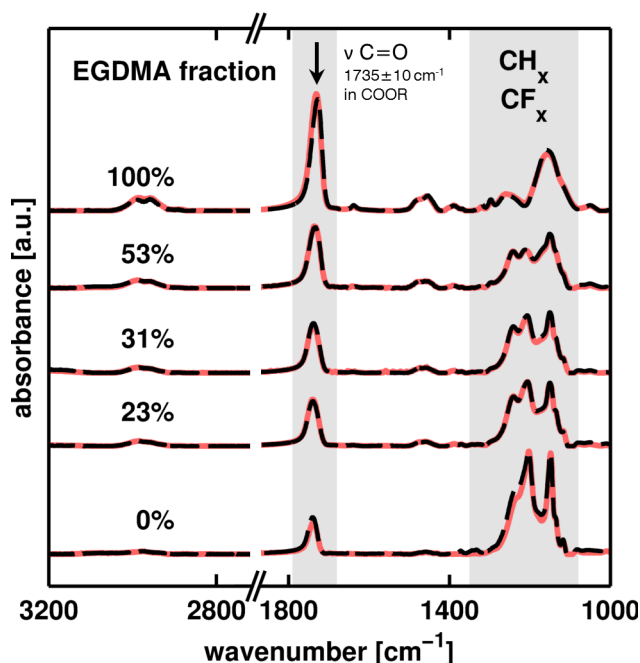


Figure 5.2: FTIR spectra of p-PFDA films with different EGDMA crosslinker ratios in the as-prepared state (dashed line) and after heat-treatment (solid line). The signal intensity is normalized by the film thickness. Data are shifted on the  $y$ -axis for clarity.

To evaluate the degree of cross-linking, each spectrum is treated as a linear combination of the spectra of the p-EGDMA and PFDA homopolymers, each weighted with a factor accounting for its fraction. By a linear fit of these factors, the composition is then obtained (see labels of the spectra in Figure 5.2).

After repeated heating of such samples to 150 °C under nitrogen atmosphere, the chemical composition of the polymers remained unchanged (dashed lines in Figure 5.2). This means that both p-PFDA and cross-linked alterations thereof are chemically stable in the investigated temperature range, within the detection limits of the FTIR spectroscopy measurement.

### Surface morphology and wettability

The impact of the cross-linker on the surface morphology of p-PFDA films was investigated by atomic force microscopy (AFM) for the as-prepared and heat-treated samples (see Figure 5.3). For pristine p-PFDA films, the surface consists of randomly distributed spherical aggregations, forming a hillocklike structure. This is also reflected by the root mean square roughness ( $\sigma$ ) of the surface, which was 23.7 nm. The mean radius of the spherical structures is about 200 nm, as determined from the autocorrelation length of the micrograph.

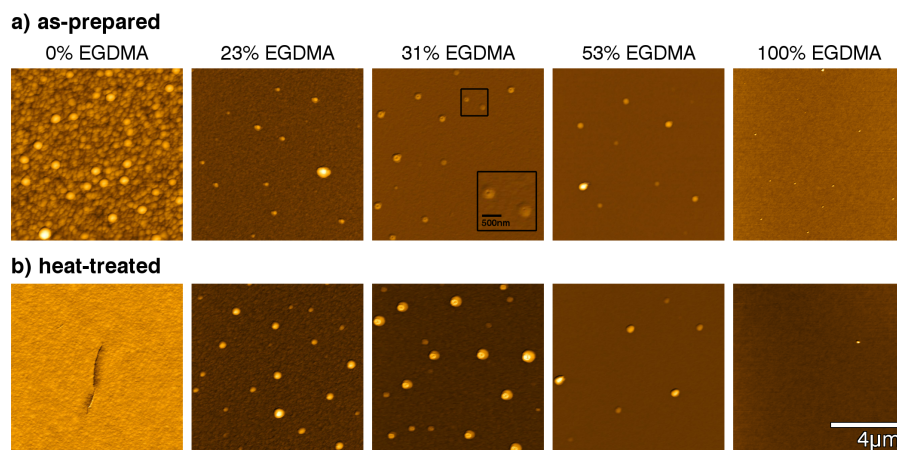


Figure 5.3: AFM height micrographs of as-prepared (a) and heat-treated (b) p-PFDA films with different degrees of EGDMA cross-linking. The data are represented on individual color scales for clarity.

Upon addition of EGDMA, the surface morphology is drastically changed. The hillock-like structure of pure p-PFDA is reduced to a few aggregated clusters, interrupting the otherwise smooth polymer film. Except for these grains, the layer's root mean square roughness is below 2 nm, indicating a rather smooth coating of the silicon wafer (roughness below 1 nm). This morphology persists as the EGDMA content increases, suggesting that the transition from spherical aggregations to a smooth coating occurs already at small additions of crosslinker. For the p-EGDMA film, no surface aggregations are observed and a smooth coating results (roughness below 1 nm). The absence of spherical structures in p-EGDMA and the close resemblance to the morphology of p-PFDA films suggest that these aggregations are in fact just due to the PFDA units, as shown also in previous works<sup>12,14</sup>. An interesting detail is observed in the AFM scan of a sample containing 31 % EGDMA (third image from left in Figure 5.3a). Small notches are noted for all the grains, extending twenty to thirty nanometers into the film (a more detailed view is shown in the inset). Possibly, these structures are the result of the degassing of unpolymerized monomer units, which are "buried" within the film during deposition. However, this behavior does not occur for the other samples (or is at least not observable in the respective AFM scans) and is uncharacteristic for iCVD polymers in general. Therefore, it is assumed that such structures are specific for this very sample and not characteristic for this particular EGDMA concentration.

After repeated heating of these polymer films to 150 °C, changes in surface morphology were recorded by AFM (Figure 5.3b). For the p-

PFDA films, a completely different surface morphology results. The spherical aggregates in the as-prepared polymer are completely absent and a relatively smooth surface results instead. The morphology is still reminiscent of the hillock-like structures but on a much smaller scale; the roughness decreases to below 2 nm, comparable to that of cross-linked surfaces. However, multiple cracks have formed in the polymer film, extending several micrometers in the lateral direction (an example is shown in Figure 5.3, see Supporting Information 5.9, Figure S5.9 for larger scales). The line profiles of these cracks reveal a penetration depth of approximately 20 nm, which means that they are limited to the interfacial area (the film thickness is approximately 350 nm). For cross-linked films, the temperature treatment results in no observable changes, indicating good stability towards temperature variation in the investigated range.

Changes in the surface morphology and chemistry also affect the wettability, as evidenced by a decreasing water contact angle (WCA) upon EGDMA addition to the polymer (Figure 5.4a). While the PFDA homopolymer forms a highly hydrophobic surface with a WCA of  $(138 \pm 2)^\circ$ , a linear decrease results as the fraction of EGDMA cross-linker is gradually increased. The intercept with the y-axis was one of the fit parameters and the fit result,  $139^\circ$ , falls within the error range of the physical measurement of the water contact angle of the PFDA homopolymer. For the EGDMA homopolymer, a WCA of  $(69 \pm 1)^\circ$  was ultimately observed. The change in wettability stems from the (relative) increase of carbonyl groups upon addition of EGDMA, which turns the polymer more hydrophilic. Similar to the morphological changes discussed above, heat treatment predominantly affects the water contact angle of the PFDA homopolymer. A decrease of the WCA to  $(121 \pm 1)^\circ$  results, while the cross-linked polymers show little to no change, independent of the degree of cross-linking. PFDA homopolymer, while only minor changes are noted for cross-linked alterations. Despite the formation of cracks, a pronounced decrease in the  $\sigma_{RMS}$  value was observed for the PFDA homopolymer, resulting in a much smoother film. This suggests that the initial WCA of the p-PFDA films stems in fact from a combination of hydrophobicity by the perfluorinated groups and the high surface roughness present in the as-prepared films. On the other hand, the effect of elevated temperature shows no or only a negligible effect on the morphology and chemical composition of cross-linked polymers (in the investigated range). This means that after deposition, these compositions are already closer to equilibrium so that less internal strain occurs. In turn, this makes these films less prone to rupture formation or surface rearrangement upon exposure to elevated temperatures. The data also show that in thermally annealed films, a water contact angle of approximately  $120^\circ$  can be maintained up to EGDMA fractions of

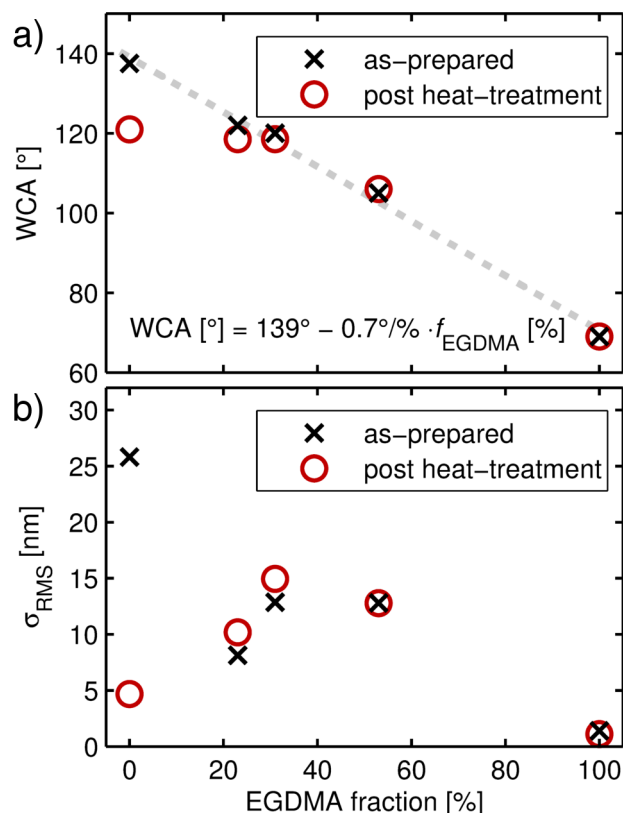


Figure 5.4: Water contact angle (WCA) (a) and root mean square surface roughness ( $\sigma_{RMS}$ ) (b) of p-PFDA films with different degrees of EGDMA cross-linking, as determined by the static sessile drop method and from AFM, respectively. The  $\sigma_{RMS}$  values were calculated from the  $50 \times 50 \mu\text{m}^2$  AFM micrograph areas presented in Supporting Information 5.9, Figure S5.9. For the as-prepared films, a linear relationship between the contact angle and the cross-linker ratio is found (dashed line). Error bars have been omitted for clarity as the standard deviation of the WCA was less than two degrees.

40 %, indicating a surface composition dominated by the fluorinated groups of the PDFA portion.

### Structural characterization

The distinct features of pure p-PFDA films and cross-linked alterations thereof are not only limited to the interface but are rather the result of differences in the bulk of the thin films. This is evident from the specular X-ray diffraction data of the as-prepared films, as depicted in Figure 5.5a. Pristine p-PFDA exhibits a low intensity peak at  $q_z = 3.88 \text{ nm}^{-1}$ , meaning that this film is (at least partially) crystalline. This peak is characteristic for the hexagonal packing of the

fluorinated pendant chains into a bilayer structure of distance  $d = (3.18 \pm 0.02) \text{ nm}$  (corresponding to a scattering vector  $q_z = 1.98 \text{ nm}^{-1}$ ) [4]. Thus, the Bragg peak in Figure 5.5a is identified as the 002 reflection of this lamellar packing (data depicting the 001 reflection is provided in Supporting Information 5.9, Figure S5.10). Additionally, the data show a preferred orientation of the lamella that is parallel to the substrate surface, as other reflections are absent in the spectra (measured up to  $q_z = 20 \text{ nm}^{-1}$ ).

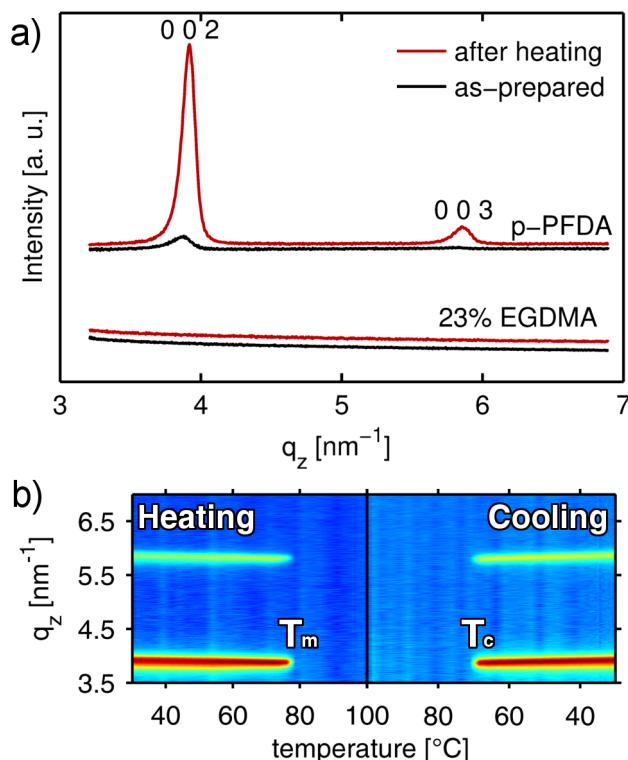


Figure 5.5: (a) Specular X-ray diffraction patterns of a p-PFDA film and a cross-linked alteration thereof with 23% EGDMA content in the as-prepared state and after heating to 150 °C. For clarity, data are shifted along the  $y$ -axis (intensity). (b) Temperature-dependent *in situ* X-ray diffraction measurements of crystalline p-PFDA at a rate of 2 °C/min, with  $T_m$  and  $T_c$  denoting the onset of melting and of crystallization at 76 and 69 °C, respectively.

A very different behavior results as the PFDA polymer is crosslinked by the addition of EGDMA to the iCVD process. The crystalline features of the PFDA homopolymer are absent in the cross-linked alterations, independent of the tested EGDMA fraction (thus, only the sample with the lowest EGDMA content is shown). The cross-linked polymers lack a defined repeating unit due to the random nature of the chain interconnects, which constitute a steric hindrance for chain rearrangement, thus limiting the formation of any long-range order.



The structural difference between the PFDA homopolymer and its cross-linked alterations most likely accounts for their distinct thermal response in terms of morphology (see the AFM data in Figure 5.3), while the chemistry remains unaffected by the heat treatment (see the FTIR data in Figure 5.2). After heating to 150 °C and cooling back to ambient, the cross-linked polymers do not show any change in the XRD pattern, while the 002 Bragg reflection of the PFDA homopolymer displays a strong increase in intensity. In addition, a further (higher order) reflection of the lamellar structure emerges at  $q_z = 5.86 \text{ nm}^{-1}$ , corresponding to the 003 plane. This behavior suggests that thermal treatment greatly improves crystallinity and/or mosaicity of the PFDA homopolymer, but does not lead to the formation of crystalline domains in the cross-linked films. Likely, with a lower cross-linker fraction, some degree of crystallinity might be preserved.

To gain further insight into the thermally induced structural changes of p-PFDA films, *in situ* X-ray diffraction experiments were performed. In Figure 5.5b, the specular diffraction pattern of the PFDA homopolymer is depicted in a pseudo-color representation as a function of temperature. The data features most prominently the positions of the 002 and 003 Bragg reflections, which display a shift towards lower  $q$ -values (and thus larger lattice distances) upon temperature increase, corresponding to thermal expansion of the unit cell. At  $(76 \pm 2) \text{ }^\circ\text{C}$ , a sudden decrease in the diffracted intensity is then observed, denoting the melting point of the lamella. As the temperature is further increased to 100 °C, no change is observed in the diffraction pattern, that is, the polymer remains in the amorphous state. Upon cooling, recrystallization occurs at  $(69 \pm 2) \text{ }^\circ\text{C}$ . Once they have emerged, these Bragg peaks display little variation in intensity as a function of temperature, suggesting that the polymer side-chains assume the final lamella arrangement within the resolution of the experiment (2 °C/min). On the other hand, a more pronounced shift of the Bragg peak positions towards higher  $q$ -values is noted upon cooling.

To quantify the thermal expansion/contraction of the p-PFDA unit cell, the coefficients of linear thermal expansion (CTEs) both for heating ( $\alpha_{\text{heating}}$ ) and cooling ( $\alpha_{\text{cooling}}$ ) are determined from the data. In general, the CTE is defined as

$$\alpha = \frac{1}{L_0} \frac{dL}{dT}, \quad (5.1)$$

with  $dL/dT$  denoting the rate of change in thickness with temperature, normalized by an initial thickness  $L_0$  (for this work,  $L_0$  refers to the length at 25 °C). From a linear fit to the data in Figure 5.5b, the linear CTEs are determined to be  $\alpha_{\text{heating}} = (2.18 \pm 0.05) \cdot 10^{-4} \text{ K}^{-1}$  and  $\alpha_{\text{cooling}} = (3.2 \pm 0.1) \cdot 10^{-4} \text{ K}^{-1}$ . The difference between the CTEs of the heating and the cooling run indicates that the sample has not yet reached an equilibrium state, which is expected for an as-prepared

sample. Upon recrystallization under cooling, the Bragg peaks are slightly shifted towards higher  $q$ -values (see Figure 5.5a,b); the bilayer distance is reduced with respect to the as-prepared state and minor relaxation has occurred in the p-PFDA unit cell. While this difference diminishes in subsequent runs, an increasing peak intensity is still observed after the third run (data not shown).

While X-ray diffraction techniques are perfectly suited to follow structural processes in crystalline materials, their application to amorphous materials is less favorable. To also provide some insight into the amorphous, cross-linked p-(PFDA-co-EGDMA) films, *in situ* spectroscopic ellipsometry was utilized. In Figure 5.6, the evolution of the film thickness (normalized to the thickness at 25 °C) is depicted as a function of temperature, as determined from ellipsometry data. After several equilibration cycles (as described in the Experimental section), a reversible behavior is recorded. Figure 5.6a shows a typical measurement for a PFDA homopolymer for a heating and a cooling run. The data features most notably a first-order phase transition, with the onsets at 73 and 71 °C, determined by linear fits to the data. These points correspond to melting, and respectively, crystallization of the lamella. These thermal transition points are in reasonable agreement with those determined from the X-ray diffraction experiment ( $76 \pm 2$  and  $(69 \pm 2)$  °C). The difference is attributed to general sensitivity and temperature resolution differences between these two techniques. While in the X-ray diffraction experiment a resolution of only 2 °C is achieved, the ellipsometric measurement features a ten-times better temperature resolution. In addition, ellipsometry allows even very minor changes in film thickness to be monitored without the need of long integration times.

Above and below the transition point, the data features the thermal expansion of the p-PFDA film. The observed changes do not depend on whether the experiment is performed while heating or cooling, hinting at a reversible behavior. This also means that no thickness loss occurs during the experiment. As this behavior was noted for all the samples (within this temperature regime), only cooling runs are considered from here on.

When EGDMA is added to the polymer, a different behavior was revealed (Figure 5.6b). A strong thermal transition, as observed for the PDFDA homopolymer, is absent. This is expected as X-ray diffraction scans did not show any crystalline fraction (Figure 5.5a). Instead, the data evidence a gradual decrease in the thermal expansion as the EGDMA content increases. In addition, the thermal expansion features a slight curvature, indicating a thermal transition.

To investigate this in more detail, changes in film thickness and in refractive index are depicted together in Figure 5.7 as a function of temperature. For a EGDMA fraction of 23 % (Figure 5.7a), a thermal transition at  $T = (61 \pm 5)$  °C is evidenced by the intersection of

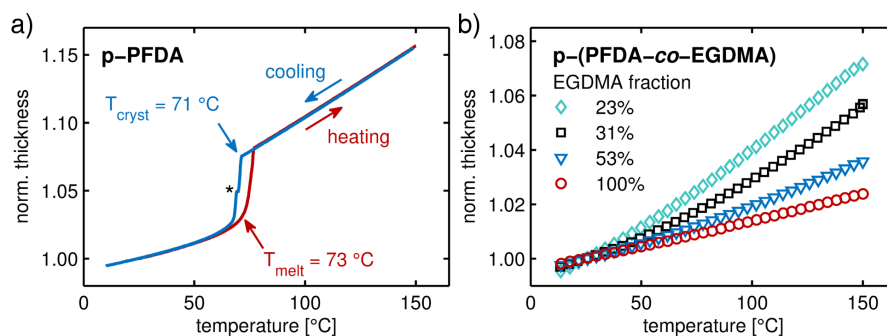


Figure 5.6: *In situ* spectroscopic ellipsometry data depicting film thickness evolution as a function of temperature for a PFDA homopolymer (a) and for samples containing different degrees of EGDMA cross-linking (b). The heating/cooling rates were 5 °C/min and data are normalized to the thickness at 25 °C. The data in (b) has been reduced for clarity and only cooling runs are shown. Please note that the discontinuity in (a) is an artifact and has been marked by an asterisk.

two linear fits to the data. With an increasing EGDMA content, this thermal transition shifts to higher temperatures but also becomes less pronounced (Figure 5.7b,c). Finally, for the EGDMA homopolymer, no transition is observable. While the thermal expansion decreases with increasing EGDMA content, the opposite behavior is noted in the refractive index. Interestingly, this shift in the refractive index (at ambient temperature) shows a linear behavior with the EGDMA fraction and could thus be used to determine the copolymer ratio. The obtained ratios are in good agreement with those determined from FTIR measurements (within a few percent). It is worth noting that another feasible way to evidence such transitions is to determine the thermal expansion coefficient at each temperature by numerical differentiation<sup>22</sup>. This procedure results in comparable transition points (data not shown) but is very sensitive to noise in the fit/measurement. Thus, measurements should then be performed under stationary (isothermal) conditions for each temperature.

The origin of the thermal transitions could not be unambiguously identified. While crystalline fractions and first-order phase transitions were (in the limit of the experiments) not evident in the present data, the position of the thermal transitions suggests a relation to the crystalline packing present in the PFDA homopolymer. Likely, the thermal transition originates from a collective movement of the perfluorinated PFDA sidechains upon temperature increase. Compared to the liquid-crystalline state, the energy barrier for such chain movement is lowered as lattice energy is absent. This is in agreement with the sample containing 23% EGDMA, which exhibited the lowest transition

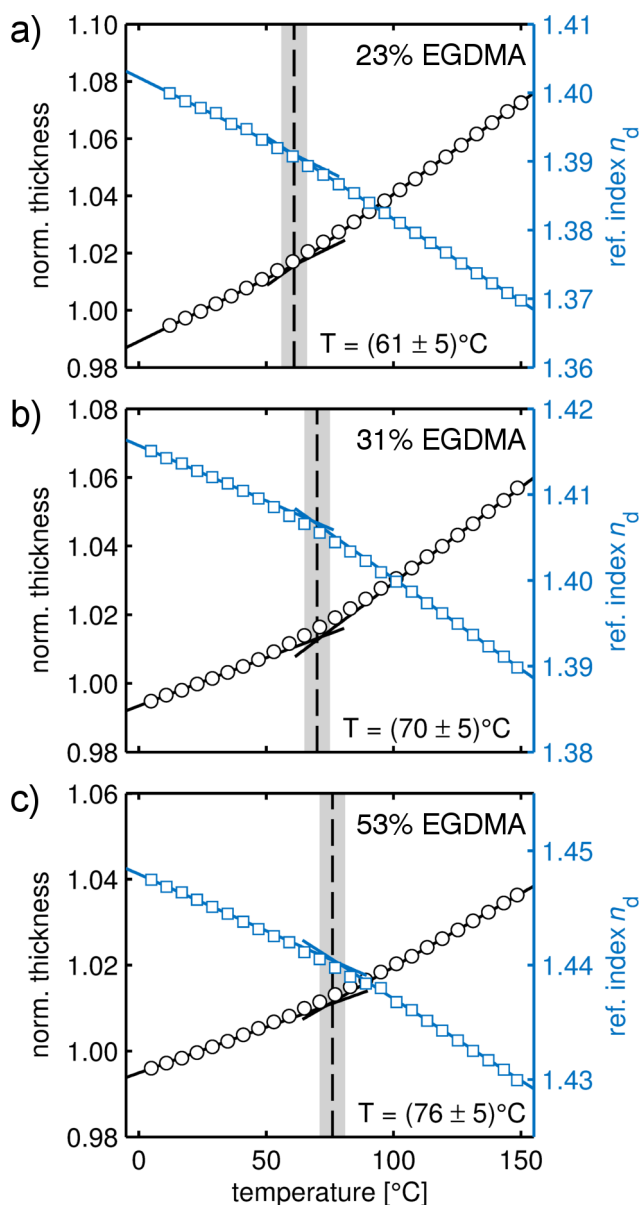


Figure 5.7: Normalized film thickness and the refractive index  $n_D$  (at  $\lambda = 589.3\text{ nm}$ ) as a function of the temperature for p-(PFDA-co-EGDMA) films with (a) 23% EGDMA, (b) 31% EGDMA, and (c) 53% EGDMA content. From the intersection of the linear functions fitted to the data, the thermal transitions are evidenced. The corresponding transition temperatures are annotated in the graph. The shaded area represents the error bar.

point at  $T = (61 \pm 5)^\circ\text{C}$ . With stronger cross-linking, the mobility of the fluoroalkyl groups is lowered, thus yielding a shift to higher temperatures while also yielding weaker transitions in general.

There are also several reports in literature which mention a glass transition in the EGDMA homopolymer, located between 130–140 °C<sup>23,24</sup>. However, such a transition is not evident in the present data. While thin films typically do show a different behavior compared to bulk materials, a film thickness greater than 100 nm (such as the ones used in this study) is often found in agreement with the bulk<sup>25,26</sup>.

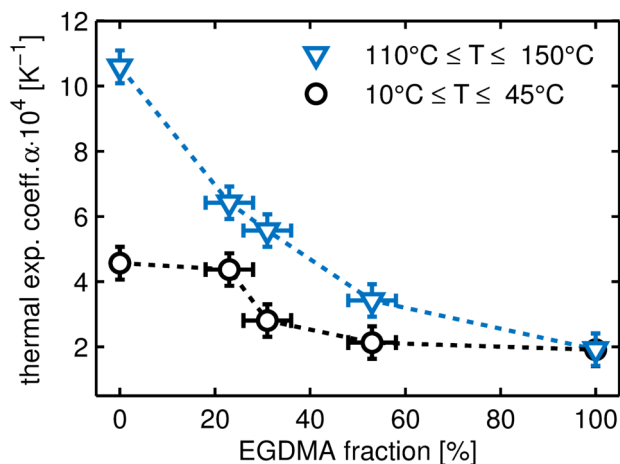


Figure 5.8: Coefficient of linear thermal expansion,  $\alpha$ , as a function of EGDMA cross-linker fraction for various p-(PFDA-co-EGDMA) films in two temperature regions. The data points are interconnected by dashed lines as a guide to the eye.

In addition, CTEs are determined for regions in which changes in film thickness depend linearly on temperature. Figure 5.8 displays the change in thermal expansion coefficients as a function of EGDMA content in the regions below and above the thermal transition points (10–45 °C and 110–150 °C, respectively). Below the melting point, the PFDA homopolymer exhibits the highest thermal expansion coefficient of the systems. As EGDMA cross-linker is added to the polymer, the CTEs decrease and the difference between CTEs above and below the thermal transition also decreases until it is fully absent for the p-EGDMA homopolymer. This behavior reflects the fact that thermal transitions become weaker with increasing EGDMA content and are fully absent for the p-EGDMA homopolymer (in the investigated temperature range). As the WCA (i.e., the surface energy) displayed little dependence on the EGDMA content (below 40% fraction), this allows for the deposition of highly hydrophobic p-(PFDA-co-EGDMA) surfaces with control over the thermal expansion (and mechanical properties) being established by the cross-linker degree.

## 5.6 Conclusion

The morphological and structural properties of linear and crosslinked p-PFDA films deposited by iCVD were investigated with the aim of identifying the limit of thermal stress that these films can sustain before losing integrity. PFDA polymers have indeed shown very interesting properties in terms of repellence of oil and water, due to the formation of a crystalline lamellar structure between the PFDA chains. While this makes the p-PFDA highly suitable for a large variety of applications, it is interesting to know how these properties change with temperature oscillations that can occur during the everyday use of technologies based on this polymer.

The present study shows that the mechanical stability can be greatly improved by the addition of a cross-linker. When the linear p-PFDA was exposed to the heating cycles, the chemistry remained unchanged while the crystallinity of the films was largely improved and the morphological character of the surface became smoother. Nevertheless, the thermal stress caused some ruptures in the films and reduced the hydrophobic properties. EGDMA, added as a cross-linker, was shown to preserve the chemical stability and hydrophobicity of p-PFDA coatings while making the film more cohesive. The loss of the structural integrity in the PFDA homopolymer was attributed to the different thermal expansion coefficients of the crystalline and amorphous film portions, which caused tension in these films upon heating/cooling. The cross-linked films were fully amorphous, also upon heating, but had more stable hydrophobic properties and showed an increased crack resistance.

In addition, this study demonstrated that EGDMA is a feasible cross-linker for the synthesis of thermally stable hydrophobic polymers. While the ester groups can become a limiting factor at even higher temperatures, EGDMA offers unique advantages for applications below 150 °C. It outperforms previously employed reagents like DVB, allowing for faster deposition rates in the iCVD process and making postdeposition curing unnecessary, as high conversion rates are readily achieved.

The chosen deposition technique, iCVD, allows fine-tuning of the cross-linking ratio, different from other vapor-based deposition techniques (e.g., plasma-enhanced CVD). Therefore, depending on the application and on the desired polymer properties, one can choose to work in conditions that drive crystallinity and hydrophobicity or thermally stable surface properties instead.

## 5.7 Acknowledgements

The work was funded by the Austrian Science Fund (FWF) [Grant P26993]. The authors gratefully acknowledge Roland Resel for inter-

esting and helpful scientific discussions and for the use of the X-ray diffractometer.

## 5.8 References

- (1) E. Sarantopoulou, Z. Kollia, A. C. Cefalas, A. M. Douvas, M. Chatzichristidi, P. Argitis, and S. Kobe *Materials Science and Engineering: C* **2007**, *27*, 1191–1196, DOI: 10.1016/j.msec.2006.09.044.
- (2) D. L. Schmidt, R. F. Brady, K. Lam, D. C. Schmidt, and M. K. Chaudhury *Langmuir* **2004**, *20*, 2830–2836, DOI: 10.1021/la035385o.
- (3) F. He, Y. Gao, K. Jin, J. Wang, J. Sun, and Q. Fang *ACS Sustainable Chemistry & Engineering* **2016**, *4*, 4451–4456, DOI: 10.1021/acssuschemeng.6b01065.
- (4) K. Honda, M. Morita, H. Otsuka, and A. Takahara *Macromolecules* **2005**, *38*, 5699–5705, DOI: 10.1021/ma050394k.
- (5) A. Fujimori, R. Masuya, T. Masuko, E. Ito, M. Hara, K. Kanai, Y. Ouchi, K. Seki, and H. Nakahara *Polymers for Advanced Technologies* **2006**, *17*, 653–663, DOI: 10.1002/pat.790.
- (6) T. Kanashima, O. Maida, N. Kohma, M. Okumoto, M. Ueno, S. Kitai, M. Okuyama, H. Ohashi, and Y. Tamenori *Applied Surface Science* **2006**, *252*, 7774–7780, DOI: 10.1016/j.apsusc.2005.06.055.
- (7) Y. Yoo, J. B. You, W. Choi, and S. G. Im **2013**, *4*, 1664–1671, DOI: 10.1039/C2PY20963B.
- (8) A. M. Coclite, Y. Shi, and K. K. Gleason *Advanced Materials* **2012**, *24*, 4534–4539, DOI: 10.1002/adma.201200682.
- (9) M. Gupta and K. K. Gleason *Langmuir* **2006**, *22*, 10047–10052, DOI: 10.1021/la061904m.
- (10) A. M. Coclite, Y. Shi, and K. K. Gleason *Advanced Functional Materials* **2012**, *22*, 2167–2176, DOI: 10.1002/adfm.201103035.
- (11) A. Milella, R. Di Mundo, F. Palumbo, P. Favia, F. Fracassi, and R. d'Agostino *Plasma Processes and Polymers* **2009**, *6*, 460–466, DOI: 10.1002/ppap.200930011.
- (12) A. M. Coclite, R. M. Howden, D. C. Borrelli, C. D. Petruczok, R. Yang, J. L. Yagüe, A. Ugur, N. Chen, S. Lee, W. J. Jo, A. Liu, X. Wang, and K. K. Gleason *Advanced Materials* **2013**, *25*, 5392–5423, DOI: 10.1002/adma.201301878.

- (13) I. Vilaró, J. L. Yagüe, and S. Borrós *ACS Applied Materials & Interfaces* **2017**, *9*, 1057–1065, DOI: 10.1021/acsami.6b12119.
- (14) J. L. Yagüe and K. K. Gleason *Macromolecules* **2013**, *46*, 6548–6554, DOI: 10.1021/ma4010633.
- (15) G. Beaucage, R. Composto, and R. S. Stein *Journal of Polymer Science Part B: Polymer Physics* **1993**, *31*, 319–326, DOI: 10.1002/polb.1993.090310310.
- (16) J. L. Keddie, R. A. L. Jones, and R. A. Cory *EPL (Europhysics Letters)* **1994**, *27*, 59, DOI: 10.1209/0295-5075/27/1/011.
- (17) P. Christian, H. M. Ehmman, A. M. Coclite, and O. Werzer *ACS Applied Materials & Interfaces* **2016**, *8*, 21177–21184, DOI: 10.1021/acsami.6b06015.
- (18) K. H. Liland, B.-H. Mevik, and R. Canteri *baseline: Baseline Correction of Spectra. R package version 1.2-0*, 2015.
- (19) D. Nečas and P. Klapetek *Central European Journal of Physics* **2011**, *10*, 181–188, DOI: 10.2478/s11534-011-0096-2.
- (20) C. M. Herzinger, B. Johs, W. A. McGahan, J. A. Woollam, and W. Paulson *Journal of Applied Physics* **1998**, *83*, 3323–3336, DOI: 10.1063/1.367101.
- (21) P. Larkin, *Infrared and Raman Spectroscopy: Principles and Spectral Interpretation*; Elsevier: 2011; 239 pp.
- (22) S. Kawana and R. A. L. Jones *Physical Review E* **2001**, *63*, 021501, DOI: 10.1103/PhysRevE.63.021501.
- (23) S. Loshaek *Journal of Polymer Science* **1955**, *15*, 391–404, DOI: 10.1002/pol.1955.120158007.
- (24) K. Horie, A. Otagawa, M. Muraoka, and I. Mita *Journal of Polymer Science: Polymer Chemistry Edition* **1975**, *13*, 445–454, DOI: 10.1002/pol.1975.170130217.
- (25) J. L. Keddie, R. A. L. Jones, and R. A. Cory *Faraday Discussions* **1994**, *98*, 219–230, DOI: 10.1039/FD9949800219.
- (26) G. Vignaud, M. S. Chebil, J. K. Bal, N. Delorme, T. Beuvier, Y. Grohens, and A. Gibaud *Langmuir* **2014**, *30*, 11599–11608, DOI: 10.1021/la501639z.



## 5.9 Supporting Information

### iCVD DEPOSITION CONDITIONS

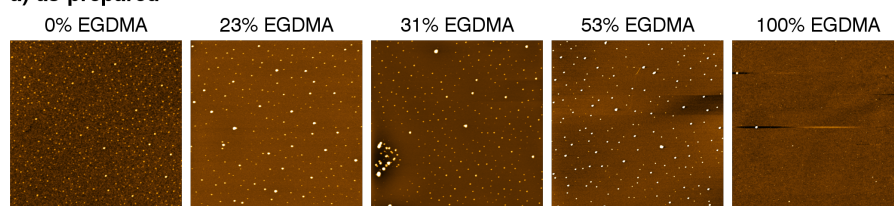
The following parameters were used in the synthesis of 1*H*,1*H*,2*H*,2*H*-perfluorodecyl acrylate (PFDA) and ethylene glycol dimethacrylate (EGDMA) copolymers by initiated Chemical Vapor Deposition (iCVD): The working pressure was set to 800 mTorr, the filament was heated to 250 °C and the substrate was held at 30 °C. For all the samples, an initiator flow rate of 0.6 sccm of tert-butyl peroxide was used. The PFDA and EGDMA flow rates are stated in Table S5.1. The total flow rate was controlled to 4.8 sccm by adjusting the Nitrogen patch flow accordingly.

Table S5.1: Flow rates of the PFDA monomer ( $F_{\text{PFDA}}$ ) and the crosslinker EGDMA ( $F_{\text{EGDMA}}$ ) employed in the iCVD polymerization.

	$F_{\text{PFDA}}$ [sccm]	$F_{\text{EGDMA}}$ [sccm]
p-PFDA	$0.15 \pm 0.01$	–
23 % EGDMA	$0.17 \pm 0.01$	$0.02 \pm 0.02$
31 % EGDMA	$0.20 \pm 0.01$	$0.05 \pm 0.02$
51 % EGDMA	$0.16 \pm 0.01$	$0.20 \pm 0.02$
p-EGDMA	–	$0.10 \pm 0.02$

### ATOMIC FORCE MICROSCOPY

#### a) as-prepared



#### b) heat-treated

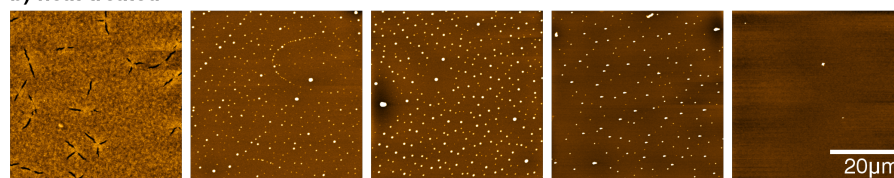


Figure S5.9: AFM micrographs of as-prepared (a) and heat-treated (b) p-PFDA films with different degrees of EGDMA cross-linking, depicting larger scales. The data are represented on individual color scales for clarity.

## X-RAY REFLECTIVITY MEASUREMENTS

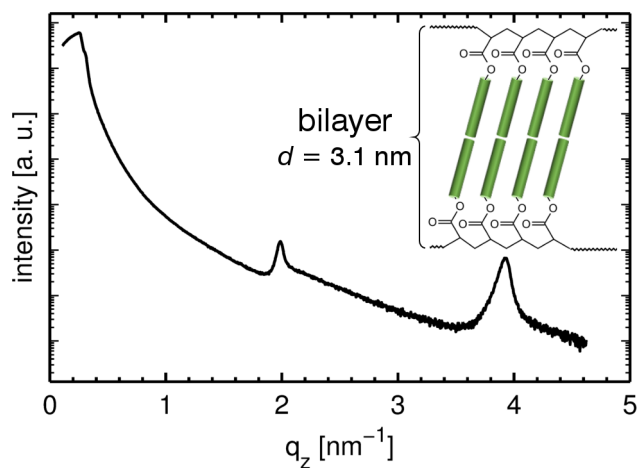


Figure S5.10: X-ray reflectivity data of an as-prepared p-PFDA film, exhibiting first and second order diffraction peaks corresponding to the bilayer packing of the perfluorinated groups. The inset shows a scheme of the p-PFDA lamellar structure, with the  $\text{CH}_2\text{CH}_2(\text{CF}_2)_7\text{CF}_3$  groups being represented by cylindrical rods.

# Thermal Studies on Proton Conductive Copolymer Thin Films based on Perfluoroacrylates synthesized by initiated Chemical Vapor Deposition

Thin Solid Films 635 (2017) 3–8



Contents lists available at ScienceDirect

Thin Solid Films

journal homepage: [www.elsevier.com/locate/tsf](http://www.elsevier.com/locate/tsf)



Thermal studies on proton conductive copolymer thin films based on perfluoroacrylates synthesized by initiated Chemical Vapor Deposition



Paul Christian, Anna Maria Coclite \*

Institute of Solid State Physics, NAWI Graz, Graz University of Technology, 8010 Graz, Austria

\* Corresponding author at: Institute of Solid State Physics, Petersgasse 16/III, 8010 Graz, Austria.  
E-mail address: [anna.coclite@tugraz.at](mailto:anna.coclite@tugraz.at) (A.M. Coclite).

## 6.1 Preface

This work was conducted at Graz University of Technology. The author of this thesis performed sample preparation, characterization as well as data evaluation and also wrote the manuscript. Anna Maria Coclite supervised the project and provided support in the manuscript preparation. The following text and its illustrations are identical to the published work<sup>1</sup> and are reproduced with permission.

- (1) P. Christian and A. M. Coclite *Thin Solid Films* **2017**, 635, 3–8, DOI: 10.1016/j.tsf.2017.01.023.

## 6.2 Abstract

The thermal properties of ion-conductive materials are crucial for their use in temperature-sensitive applications such as polymer electrolyte fuel cells. In this study, 1*H*,1*H*,2*H*,2*H*-perfluorodecyl acrylate and methacrylic acid (MAA) copolymers are synthesized by initiated Chemical Vapor Deposition. This method is a solvent-free thin film deposition technique, which allows for the preparation of polymers in distinct stoichiometric compositions. The chemical stability of the copolymers was investigated upon elevated temperatures along with other thermal properties. For this, experimental techniques such as infrared spectroscopy and ellipsometry were used. The data show that samples are chemically stable up to 150 °C, a point above which anhydride formation occurs, resulting in the loss of the conductive groups. A second order thermal transition was found at  $(95 \pm 5)$  °C for polymers containing 20 % MAA, which shifts towards higher temperatures as the MAA content increases. In addition, the water stability was tested. While the membranes show considerable water uptake (over 35 % at 60 % MAA content), mechanical stability is lacking, resulting in rupture formation and partial dissolution. A possible route to overcome this issue is found in crosslinking, with the addition of 15 % ethylene glycol dimethacrylate providing sufficient stability to the polymer.

## 6.3 Introduction

Membrane materials for application in polymer electrolyte membrane fuel cells (PEMFCs) compete not only for the highest proton conductivities, but have likewise to withstand elevated temperatures and a harsh chemical environment<sup>1</sup>. While some materials such as sulfonated poly(benzimidazole) or poly(arylene ether)s are able to match or even surpass the conductivity of Dupont's Nafion<sup>®</sup> – the prototypical, commercially available perfluoro-sulfonated ionomer – other requirements, such as hydrolytic stability, remain questionable<sup>2,3</sup>. In the search for easy-to-synthesize and cost-effective alternatives to Nafion, a plethora of different sulfonated compounds have been investigated<sup>4-6</sup>. But also other acid functionalities such as phosphonic<sup>7</sup> and carboxylic acid<sup>8</sup> have been explored for this purpose. Recently, promising conductivity values were reported for thin films of 1*H*,1*H*,2*H*,2*H*-Perfluorodecyl acrylate (PFDA) and methacrylic acid (MAA) copolymers, synthesized by initiated Chemical Vapor Deposition (iCVD)<sup>9,10</sup>. The iCVD process is a solvent-free technique, operating under mild vacuum conditions and at low substrate temperatures, allowing for conformal polymer deposition even on delicate substrates such as paper<sup>11</sup>, pharmaceuticals<sup>12</sup> or reverse osmosis membranes<sup>13</sup>. The process relies on the thermal decompo-

sition of an initiator (usually a peroxide) at a hot filament (typical temperatures between 200 and 300 °C), thus forming radicals. Monomer precursors, containing vinyl bonds, are delivered as vapors to the sample compartment, adsorbing at the temperature-controlled substrate surface (usually operated between 10 and 60 °C). Radicals from the vapor phase can then react with the vinyl bonds of the adsorbed monomer, turning the initiator-monomer complex into a radical. By further monomer attachment, polymerization is facilitated until chain growth is terminated by another radicalized chain or initiator radical. The selective nature of monomer/initiator interactions in iCVD allows full retention of chemical functionalities as opposed to other deposition techniques like plasma-enhanced Chemical Vapor Deposition, where the carboxylic acid moiety is only partially preserved<sup>14</sup>. In addition, the solvent-free synthesis of copolymers with opposing characteristics (e. g. hydrophilic/-phobic ones) by iCVD is advantageous when compared to standard solution polymerization, where a common solvent and/or multiple processing steps are required<sup>15</sup>. A more detailed description of the iCVD process and of the related fundamental reactions can be found in literature<sup>16,17</sup>.

In this study, the thermal properties of iCVD p(PFDA-*co*-MAA) films are investigated, both under N<sub>2</sub> atmosphere and when fully immersed into water. While the characterization of thermal properties by standard techniques is usually limited to the bulk, spectroscopic ellipsometry readily allows the investigation of materials with thicknesses ranging from a few micrometers down to monolayers. For instance, Beaucage *et al.* studied the glass transition and thermal expansion coefficient of a 300 nm thin polystyrene film by ellipsometry<sup>18</sup>. Another advantage of this technique is that it can be applied to other media than air so that also the swelling behavior of the polymer films can be studied *in-situ*. Fourier infrared spectroscopy (FT-IR) complements the thermal characterization, allowing insight into the chemical composition and stability of such membranes.

## 6.4 Experimental details

Radical co-polymerization of 1*H*,1*H*,2*H*,2*H*-Perfluorodecyl acrylate (PFDA, purity 97 %) and methacrylic acid (MAA, purity 99 %) was performed via initiated Chemical Vapor Deposition (iCVD) in a custom build reactor, using tert-butyl peroxide (TBPO, purity 98 %) as initiator. For some samples, ethylene glycol dimethacrylate (EGDMA, purity 98 %) was added to the process as a crosslinking agent. As substrates, silicon wafers with a native oxide layer (SIEGERTWAFER, Germany) were used. All the depositions were performed at a working pressure of 107 Pa, with initiator and PFDA flow rates being 0.6 and 0.3 sccm, respectively. The MAA flow rates were 2, 4 and 7 sccm for the individual samples. The total flowrate was held at 8 sccm

by adjusting the nitrogen patch flowrate accordingly. For the cross-linked samples, the PFDA flow was set to 0.2 sccm while various MAA/EGDMA flow ratios were tested. The filament was heated to 240 °C while the substrate temperature was held at 30 °C. The average layer thickness of the as-deposited polymer films was  $(220 \pm 40)$  nm. A detailed description of the experimental setup can be found in a recent publication<sup>12</sup>. For comparison, Nafion<sup>®</sup> 117 thin films (from solution, conc. 5 %) were prepared on  $2 \text{ cm}^2 \times 2 \text{ cm}^2$  silicon substrates by spin coating 100  $\mu\text{L}$  solution at a speed of 3000 rounds per minute, resulting in a layer thickness of approximately 220 nm. All materials (unless stated otherwise) were purchased from Sigma-Aldrich, Germany, and used without further treatment.

Transmission mode Fourier transform infrared spectroscopy (FT-IR) was performed on a Bruker IFS 66v/s spectrometer. All the data were converted to absorption spectra in the OPUS software and an automated baseline correction was performed by a custom software written in R, utilizing the algorithms provided in the baseline package<sup>19</sup>. Copolymer composition was determined by fitting the experimental data with a linear combination of the respective homopolymer spectra. The fitting parameters are the weighting factors of the homopolymer spectra, which account for their respective fraction in the copolymer.

Spectroscopic ellipsometry measurements were performed with an M-2000 ellipsometer (J.A. Woollam Co., USA) in reflection at an incident angle of 75°, recording optical data in the wavelength range of 370 to 1000 nm. The system was equipped with THMS600 temperature stage (Linkam, UK), allowing for in-situ temperature-dependent studies. Temperature studies were carried out under inert atmosphere, for which a constant Nitrogen flow was applied to the sample chamber. Prior to the measurements, samples were equilibrated by repeatedly cycling them in the (temperature) region of interest (for at least three times), with a hold time of 5 min in-between the cooling and heating cycle. While an irreversible thickness loss occurs during the first cycle(s), three repetitions were found sufficient to equilibrate the samples, i. e. further heating cycles were reversible (in the limit of the experiment). The experimental data were modeled with the CompleteEASE<sup>®</sup> software, using a three-layer system consisting of the silicon substrate, the interfacial oxide layer and the transparent (polymer) top layer. For the former two, temperature-dependent optical models were taken from literature<sup>20</sup>, whereas wavelength- and temperature-dependent refractive indices of the polymers were modeled by the Sellmeier equation. From a non-linear least squares fit of the experimental data, this model yields the optical constants and thicknesses of the polymer layers. For the swelling studies, a liquid cell attachment (J.A. Woollam Co., USA) was used. The data analysis follows the pro-

cedure described above, except for the use of water as the ambient medium in the model.

## 6.5 Results and discussion

To probe the influence of polymer composition on the thermal characteristics, p(PFDA-co-MAA) films, containing different fractions of MAA, were prepared by iCVD. The deposition rate was approximately 20 nm/min and did not change significantly as the MAA content was varied. After deposition, the film thicknesses and the chemical compositions were determined by ellipsometry and FT-IR spectroscopy, respectively. Subsequently, temperature-dependent measurements and swelling studies were carried out *in-situ* by ellipsometry and finally the chemical composition was reexamined.

### 6.5.1 Chemical stability by FT-IR

The retention of chemical moieties in the iCVD process and the chemical stability after temperature treatment were assessed by FT-IR spectroscopy. In Figure 6.1, FT-IR spectra of films in the as-prepared (dashed line) and in the post heat treatment state (solid line) are shown. Such spectra exhibit mainly two regions of interest. In the so-called fingerprint region, located between 800 and 1300  $\text{cm}^{-1}$ , the skeletal vibrations of the  $\text{CH}_x$  and  $\text{CF}_x$  groups are contained. Several different vibrations are overlapping in this region, making a clear distinction between the individual contributions of PFDA, respectively MAA, difficult. However, as the MAA fraction increases, a decrease in the pronounced peak at 1200  $\text{cm}^{-1}$  is noted. This peak is identified as the symmetric stretching of the  $\text{CF}_2$  groups<sup>21</sup>, meaning that the decrease in intensity is an indicator for the (relative) reduction of PFDA in the polymer. In the second region of interest, spanning from 1600 to 1800  $\text{cm}^{-1}$ , the strong stretching signals of the carbonyl groups overlap, resulting in a double peak, with maxima located at 1742 and 1706  $\text{cm}^{-1}$ . The former corresponds to a saturated acyclic ester, a group which is just present in the PFDA monomer. On the other hand, the second carbonyl peak exhibits a shift to lower wavenumbers, characteristic for a highly polar chemical environment. Thus, the latter is attributed to the  $-\text{COOH}$  group of the methacrylic acid. From the respective ratio of these peaks, the polymer composition is determined (within  $\pm 10\%$ ).

After repeatedly heating to 150  $^\circ\text{C}$ , the spectra show little change. Only minor deviations are noted in the data, which are due to small variations in the baseline of the original spectra, affecting mostly the curve shape at the peak tails. This, in turn, means that the chemical composition remains unaffected by temperatures below 150  $^\circ\text{C}$  (in the limit of the experiment). However, a further temperature increase

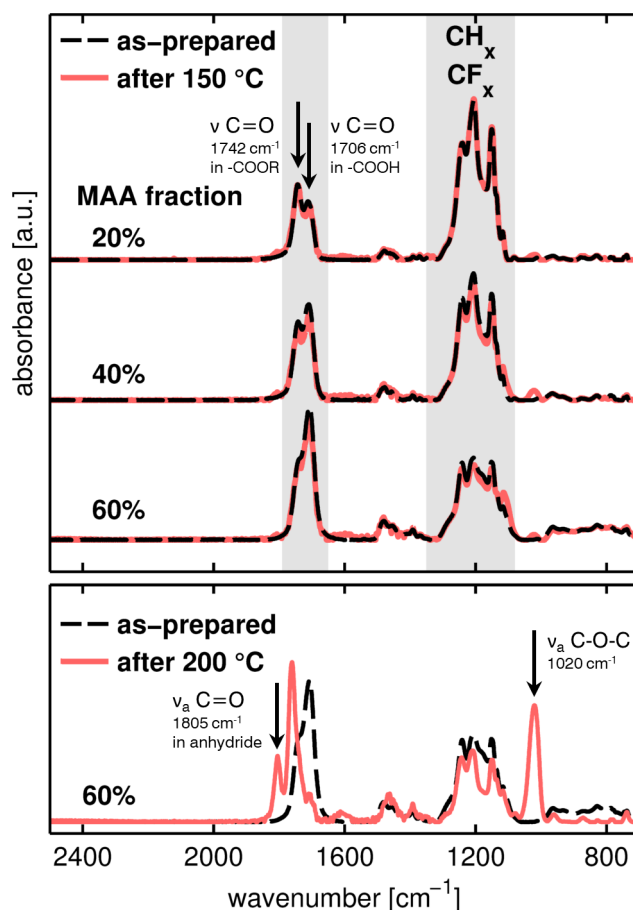
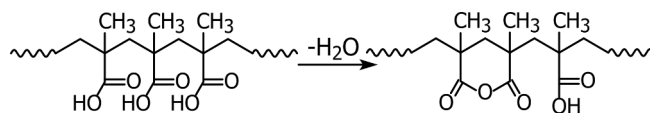


Figure 6.1: FT-IR spectra of p(PFDA-*co*-MAA) films in the as-prepared state and after being heated to 150 °C under N<sub>2</sub> atmosphere. The peaks of the ester groups (–COOR) and of the carboxylic acid groups (–COOH) are characteristic for PFDA and MAA, respectively. At the bottom, the spectra of a film containing 60% MAA are shown before and after heating to 200 °C. All data are normalized by the respective sample thicknesses.

strongly alters the spectra (see Figure 6.1, bottom graph). Most notably, two new peaks emerge (located at 1805 and 1020 cm<sup>–1</sup>) while the signal of the 1700 cm<sup>–1</sup> vibration is found greatly diminished. As the latter stems from the C=O vibration in the carboxylic acid, this suggests a chemical alteration of the MAA moiety. A possible explanation is cyclic anhydride formation, which comes at the loss of the –OH functionality and has previously been reported for pMAA after heating to 250 °C under air (see Scheme 6.1 for the reaction model)<sup>22</sup>. Indeed, the additional peaks can be identified as asymmetric vibration of C=O and C–O–C, respectively, characteristic for an organic acid anhydride.





Scheme 6.1: Reaction scheme for the anhydride formation in polymers containing methacrylic acid moieties.

While first signs of anhydride formation are also present in samples heated to 180 °C, only a small MAA fraction is yet affected (data not shown). However, further anhydride conversion is expected upon prolonged storage at this temperature. It should be noted that in the presence of oxygen, anhydride formation can readily occur also at lower temperatures.

### 6.5.2 Temperature-dependent ellipsometry

As samples are subjected to different temperatures, changes in the dielectric function/sample thicknesses are monitored by ellipsometry, evidencing thermal transitions as well as thermal expansion/contraction. In a first step, the thermal response of the benchmark Nafion<sup>®</sup> was measured in a temperature region between 25 and 150 °C (see Figure 6.2a). The data features most prominently a thermal transition at 101 °C, as determined from the point of intersection of two linear regression fits to the experimental data. This point is generally attributed to the glass transition of the Nafion<sup>®</sup> polymer matrix<sup>23,24</sup>.

The transition point is found slightly below the values reported in literature. This difference is attributed to fact that supported thin films rather than freestanding, bulk materials were used in this study. The reason for this was to allow better comparability between the thermal properties of Nafion<sup>®</sup> and that of supported, thin films deposited by iCVD.

There is only minor thermal expansion noted below the point of order-disorder rearrangement, as the Nafion<sup>®</sup> film thickness increases merely by 1 % from room temperature to 80 °C, the standard operating point of PEMFCs. This behavior is deemed favorable in terms of gas permittivity and membrane integrity, but also for the protonic transport.

In Figure 6.2b, film thicknesses of iCVD polymer films containing different fractions of MAA are shown as a function of temperature upon cooling from 150 °C to room temperature. The film thickness is found in a linear relation with temperature in the region below 75 °C, corresponding to thermal expansion, respectively contraction. As the MAA content is increased in the polymer, the slope of the thermal expansion is reduced. Above 75 °C, the temperature response deviates from a linear relation, hinting at a thermal transition. However, a pronounced thermal transition, as noted for Nafion, is absent in these

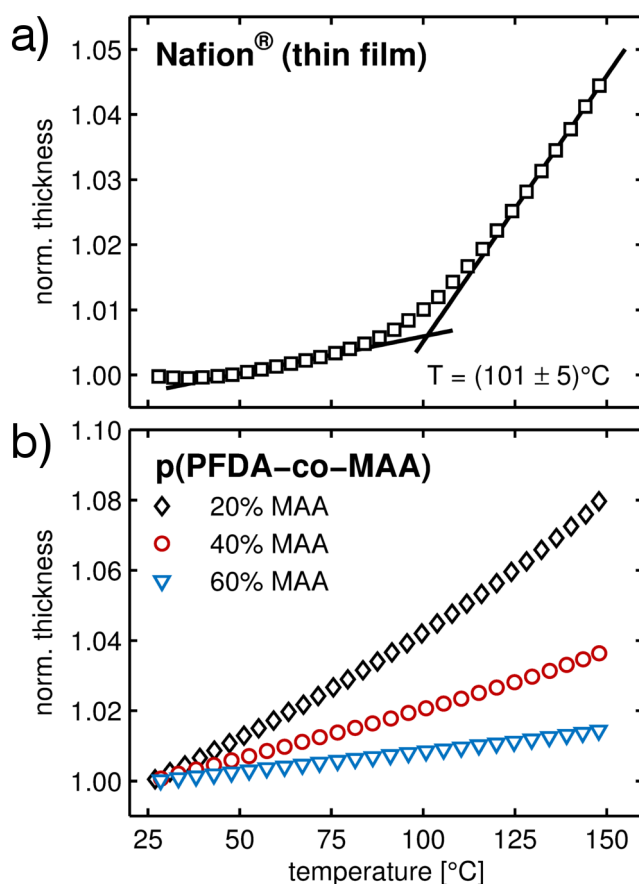


Figure 6.2: *In-situ* ellipsometric measurements of film thicknesses as function of temperature for a spin cast Nafion® film (a) and p(PFDA-co-MAA) polymers of varying MAA content (b). Data are reduced for clarity and are normalized to ambient thickness (26 °C). The cooling rates were 5 °C/min (a), respectively 40 °C/min (b).

data. To investigate this transition further, changes in both the film thickness as well as the refractive index  $n$  ( $\lambda = 589.3$  nm) were evaluated as function of the reciprocal temperature (see Figure 6.3). From this representation a thermally induced transition, though weak, is evidenced for polymers containing 20 and 40% MAA. With the increasing MAA content, the transition point shifts from 95 to 106 °C, which suggests an even higher transition for the sample containing 60% MAA. However, as the transitions are weak in general and too few data points can be collected at higher temperatures (the anhydride formation practically limits the experiment to 150 °C), this cannot be verified for the 60% MAA sample. The gradual rather than sudden change in the data indicates that this transition is of second-order, possibly a glass transition. A thermal study of the pMAA homopolymer reported a glass transition temperature  $T_g$  of 138 °C for a 106 nm

film, which would explain the shift of the transition to higher temperatures with increasing MAA content<sup>25</sup>. Different heating rates did not affect the observed behavior (5, 40 and 60 °C/min, data not shown). Interestingly, if films are heated above 150 °C (and thus, anhydride formation takes place), a much more pronounced transition, located at 124 °C, was observed (see Figure 6.3c). Possibly, the reduction of polar –OH groups during anhydride formation lowers also the steric hindrance for collective movement, thus yielding a stronger thermal response upon reaching the transition temperature<sup>26</sup>.

While data in Figure 6.2 were obtained upon cooling, it should be noted that the very same behavior persists upon heating. After the initial equilibration (as described in the experimental section), the sample thickness at room temperature is not anymore affected by the thermal history (for temperatures not exceeding 150 °C), indicating a fully reversible thermal response.

The reversible film expansion/contraction also allows for the determination of the thermal expansion coefficient, both in the regions before and after the thermal transition. The linear thermal expansion coefficient  $\alpha$  relates the changes in thickness  $L$  to the change in temperature  $T$  and some initial thickness  $L_0$  according to

$$\alpha = \frac{1}{L_0} \frac{dL}{dT}. \quad (6.1)$$

It should be noted that the ellipsometric measurement is only sensitive to changes in one dimension (i. e. in the film thickness). This means that only in the case of an isotropic material, this linear expansion coefficient is also directly related to the volumetric one. In Figure 6.4, the change of the thermal expansion coefficients with MAA fraction is depicted. The data show that for temperatures below 70 °C, small additions of MAA have little impact on the thermal expansion coefficient. However, after a critical MAA fraction is present initially, any further addition of the acid group to the PFDA homopolymer impacts directly the thermal response. On the other hand, it is also noted that the difference between the thermal expansion coefficients above and below the thermal transition region diminishes. This also reflects the fact that the thermal transitions become weaker at higher MAA contents, as noted already from the data in Figure 6.2. The observed behavior likely originates from the liquid-crystalline properties of the pPFDA homopolymer, which has been added to the graph for comparison. The perfluorinated pendant chains exhibit hexagonal closed-packing into bilayers, with the lamella orienting parallel to the substrate surface. The melting point of the lamella is at 75 °C<sup>27</sup>, which also explains the strong variation between the expansion coefficient below and above this transition. This preferential packing leads to a strong anisotropic response as the polymer chains gain additional mobility upon a temperature increase, thus yielding the highest thermal expansion coefficient of the polymers studied. How-

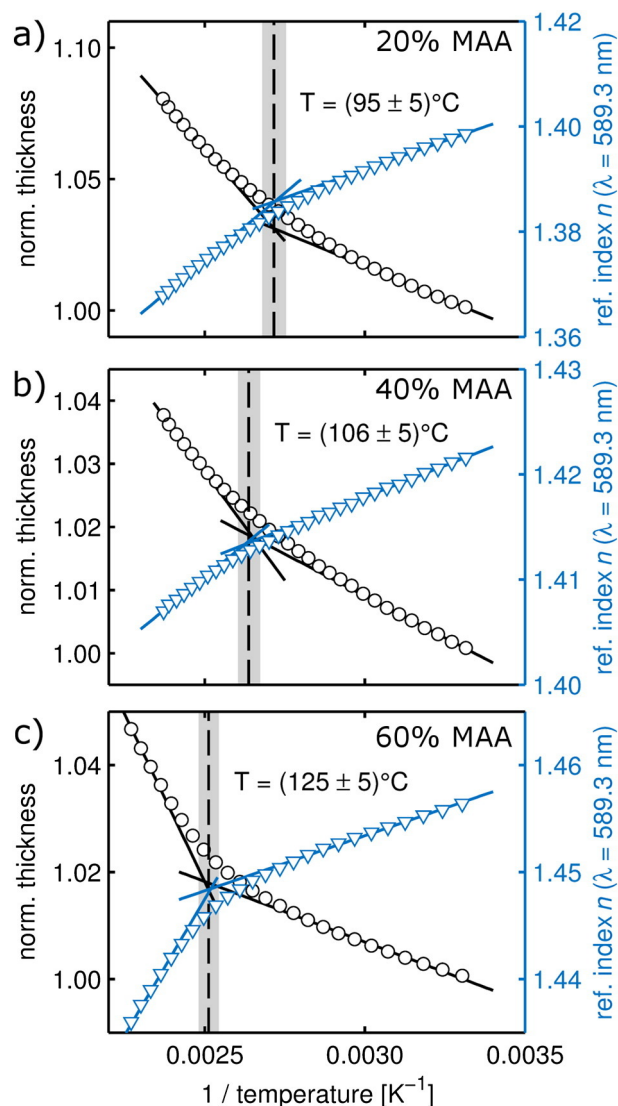


Figure 6.3: Film thickness ( $\circ$ ) and refractive index ( $\nabla$ ) data versus reciprocal temperature for p(PFDA-co-MAA) polymers with (a) 20%, (b) 40% and (c) 60% MAA content. The samples were heated to  $150^\circ\text{C}$  (a, b) and  $200^\circ\text{C}$  (c), respectively. Vertical, dashed lines represent the transition points as determined from the intersections of the linear regressions. The error is represented by the shaded area. Data are reduced for clarity and are normalized to ambient thickness ( $26^\circ\text{C}$ ). The cooling rate was  $5^\circ\text{C}/\text{min}$  for (a, b) and  $20^\circ\text{C}/\text{min}$  for (c).

ever, as shown previously<sup>10</sup>, the addition of MAA decrease crystallite size while also introducing more disordered regions, lowering the anisotropic character. In turn, this greatly lowers the thermal expansion coefficient. While all the copolymers studied in this work did not

show any crystallinity (in the limit of an X-ray diffraction experiment, data not shown), it is expected that lower MAA fractions still exhibit some degree of long range order. As the MAA content rises further, the polymer becomes fully amorphous, thus showing less and less dependence in its thermal response on a further MAA increase. This suggests that the observed thermal transitions are in fact related to relaxation processes of the pendent fluorinated sidechains, which might still exhibit some local ordering.

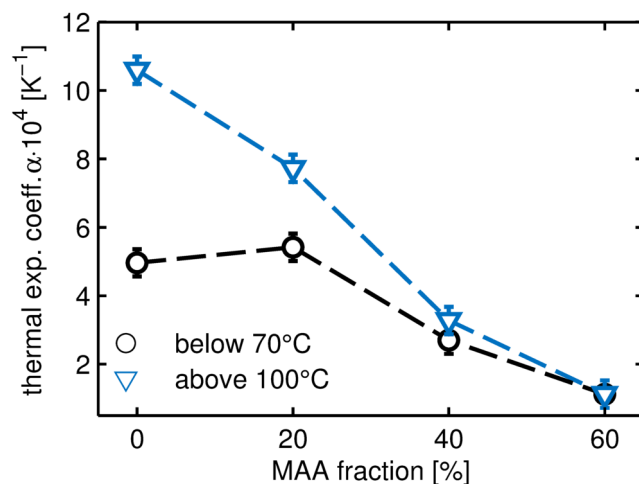


Figure 6.4: Variation of the linear thermal expansion coefficient as a function of MAA fraction present in the polymer. The coefficients were determined by linear regression of the temperature-dependent thickness data, for temperatures below 70 °C and above 100 °C. The error bars reflect just the uncertainty of the fit.

### 6.5.3 Water stability

The swelling behavior of the polymer films in water (held at 25 °C) is exemplarily shown in Figure 6.5 for samples containing 40 and 60 % MAA, respectively. Initially, the swelling proceeds rather fast in these films; within the first 10 min after the water addition, the thickness has already reached approximately 50 % of the total swelling for the 40 % MAA sample, respectively 70 % in the case of 60 % MAA. However, further swelling proceeds at a much slower speed so that an equilibrium state was still not reached for the 60 % MAA sample as the experiment was terminated after >1 h.

For many samples, the swelling data showed some initial thickness loss, indicating stability issues. This becomes even more prevalent when the water is heated to 50 °C. In the inset of Figure 6.5, an optical micrograph of a film with 60 % MAA is shown after this treat-

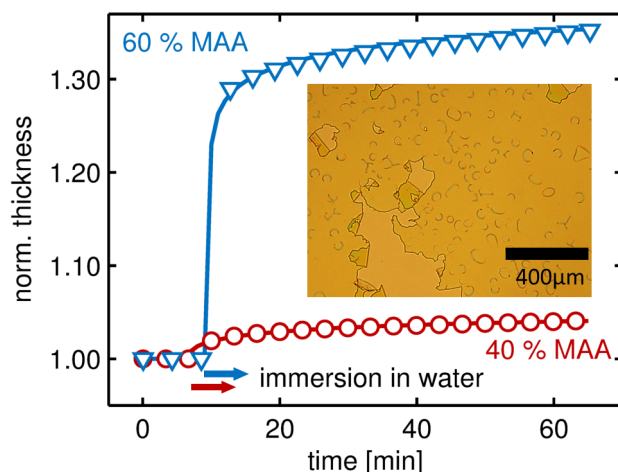


Figure 6.5: Swelling of p(PFDA-*co*-MAA) films after being immersed into 25 °C water at  $t = 0$  min, as determined from the optical model fitted to the ellipsometric data. Data are reduced for clarity and normalized to the initial sample thickness. The inset shows an optical micrograph of a polymer film with 60% MAA after heating the water to 50 °C. As a guide to the eye, sigmoid functions are fitted to the data (solid lines).

ment. After drying, the polymer film shows large ruptures and multiple smaller, encircled regions, where partial dissolution occurred. While the ruptures are mainly due to mechanical stress coming from the sealing ring of the liquid cell, the partial dissolution also indicates that likely the polydispersity is rather high, with the oligomeric portions then getting more easily dissolved.

In order to withstand these conditions, the potential application of a crosslinking agent was briefly investigated. The addition of EGDMA to the PFDA/MAA copolymer does not change the thermal properties in the investigated temperature range while also showing the same chemical stability (data not shown). While several crosslinker ratios were tested, a volume fraction of 15% was found sufficient to provide the necessary mechanical stability to avoid rupture formation and also to minimize dissolution (data not shown). For the overall water uptake, the addition of the EGDMA crosslinker is even beneficial, as shown in Figure 6.6. The increased amount of carbonyl groups at the reduction of the hydrophobic perfluorinated groups makes the overall polymer more hydrophilic, helping with the water uptake. Only at rather high MAA fractions (>50%), the crosslinker starts to have an adverse effect.

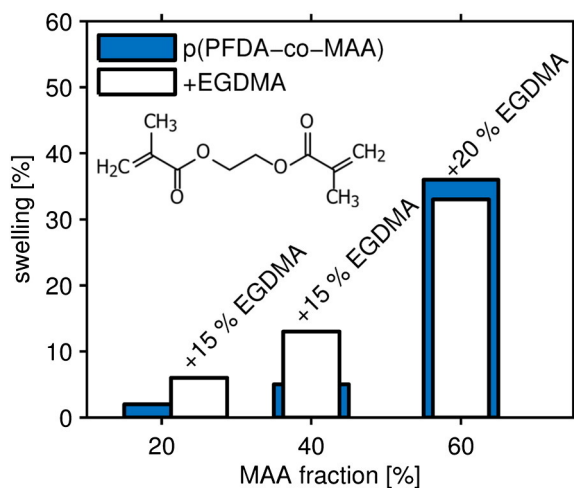


Figure 6.6: Bar plot representing the maximum swelling of p(PFDA-co-MAA) films in 25 °C water as determined from ellipsometric data. The MAA fractions are 20, 40 and 60%. In addition, the swelling behaviors of cross-linked p(PFDA-EGDMA-MAA) polymers with similar MAA fractions (25, 40, 60 °C) are shown. The structural formula of the cross-linker EGDMA is provided in the inset. For clarity, data of the latter are represented by smaller bars and the respective EGDMA fraction is annotated.

## 6.6 Conclusion

In this study, the thermal properties of p(PFDA-co-MAA) films were investigated in respect to the polymer composition. Synthesis by initiated Chemical Vapor Deposition allowed for the preparation of smooth polymer films with defined stoichiometric compositions. From spectroscopic ellipsometry data, thermal expansion and transitions of the polymers could be studied. At low contents of MAA, the copolymers exhibit the highest thermal expansion. Likely, this behavior stems from a remaining anisotropic character of the PFDA fraction, whose homopolymer is liquid-crystalline. A further increase of MAA in the polymer makes it more isotropic and in turn, also the thermal expansion is greatly reduced. The reduction of the thermal expansion coefficient with increasing MAA content is found to follow a linear relationship, after an initial amount of MAA is present. In addition, thermal transitions were noted in the polymers, located at  $(95 \pm 5)^\circ\text{C}$  for 20% MAA and at  $(106 \pm 5)^\circ\text{C}$  for 40% MAA, respectively. Possibly, these transitions are related to a relaxation process of the PFDA sidechains. However, the true nature of these transitions could not unambiguously be identified with the present data. Thermogravimetric analysis or thin-film differential scanning calorimetry might be feasible tools to further elucidate on this matter. Heating

the polymers up to 150 °C results in no change in the chemical functionality, as evidenced by FT-IR spectroscopy. However, exposing the polymer films to even higher temperatures resulted in the formation of anhydrides as adjacent methacrylic acid groups are being joined together. As this comes at the loss of the –OH functionalities, the ionic conductivity of such membranes will be greatly reduced. While chemical stability is provided up to temperatures of 150 °C under nitrogen atmosphere, other limitations are found in aqueous environment. At room temperature, samples exhibit swelling, with the degree of swelling increasing with the content of hydrophilic MAA. However, as water immersed samples are heated to 50 °C, partial dissolution and rupture formation occurs. A possible solution was found in the addition of a crosslinking agent, interconnecting polymer chains and thus providing higher mechanical stability already at an EGDMA content of 15 %.

## 6.7 Acknowledgment

The work was funded by the Austrian Science Fund (FWF) [Grant P26993-N19].

## 6.8 References

- (1) S. J. Peighambaroust, S. Rowshanzamir, and M. Amjadi *International Journal of Hydrogen Energy* **2010**, *35*, 9349–9384, DOI: 10.1016/j.ijhydene.2010.05.017.
- (2) J. Rozière and D. J. Jones *Annual Review of Materials Research* **2003**, *33*, 503–555, DOI: 10.1146/annurev.matsci.33.022702.154657.
- (3) M. A. Hickner, H. Ghassemi, Y. S. Kim, B. R. Einsla, and J. E. McGrath *Chemical Reviews* **2004**, *104*, 4587–4612, DOI: 10.1021/cr020711a.
- (4) N. Asano, M. Aoki, S. Suzuki, K. Miyatake, H. Uchida, and M. Watanabe *Journal of the American Chemical Society* **2006**, *128*, 1762–1769, DOI: 10.1021/ja0571491.
- (5) B. Bae, T. Yoda, K. Miyatake, H. Uchida, and M. Watanabe *Angewandte Chemie International Edition* **2010**, *49*, 317–320, DOI: 10.1002/anie.200905355.
- (6) S. Deng, M. K. Hassan, A. Nalawade, K. A. Perry, K. L. More, K. A. Mauritz, M. T. McDonnell, D. J. Keffer, and J. W. Mays *Polymer* **2015**, *77*, 208–217, DOI: 10.1016/j.polymer.2015.09.033.



- (7) H. Steininger, M. Schuster, K. D. Kreuer, A. Kaltbeitzel, B. Bingöl, W. H. Meyer, S. Schauff, G. Bruncklaus, J. Maier, and H. W. Spiess *Physical Chemistry Chemical Physics* **2007**, *9*, 1764–1773, DOI: 10.1039/B618686F.
- (8) V. Mehta and J. S. Cooper *Journal of Power Sources* **2003**, *114*, 32–53, DOI: 10.1016/S0378-7753(02)00542-6.
- (9) A. M. Coclite, P. Lund, R. Di Mundo, and F. Palumbo *Polymer* **2013**, *54*, 24–30, DOI: 10.1016/j.polymer.2012.11.004.
- (10) C. Ranacher, R. Resel, P. Moni, B. Cermenek, V. Hacker, and A. M. Coclite *Macromolecules* **2015**, *48*, 6177–6185, DOI: 10.1021/acs.macromol.5b01145.
- (11) K. K. S. Lau, Y. Mao, H. G. Pryce Lewis, S. K. Murthy, B. D. Olsen, L. S. Loo, and K. K. Gleason *Thin Solid Films* **2006**, *501*, 211–215, DOI: 10.1016/j.tsf.2005.07.208.
- (12) P. Christian, H. M. Ehmman, A. M. Coclite, and O. Werzer *ACS Applied Materials & Interfaces* **2016**, *8*, 21177–21184, DOI: 10.1021/acsmi.6b06015.
- (13) R. Yang, J. Xu, G. Ozaydin-Ince, S. Y. Wong, and K. K. Gleason *Chemistry of Materials* **2011**, *23*, 1263–1272, DOI: 10.1021/cm1031392.
- (14) G. Urstöger, R. Resel, G. Koller, and A. M. Coclite *Journal of Applied Physics* **2016**, *119*, 135307, DOI: 10.1063/1.4945578.
- (15) D. Poppe, H. Frey, K. D. Kreuer, A. Heinzl, and R. Mülhaupt *Macromolecules* **2002**, *35*, 7936–7941, DOI: 10.1021/ma012198t.
- (16) K. K. S. Lau and K. K. Gleason *Macromolecules* **2006**, *39*, 3695–3703, DOI: 10.1021/ma0601621.
- (17) A. M. Coclite, R. M. Howden, D. C. Borrelli, C. D. Petruczok, R. Yang, J. L. Yagüe, A. Ugur, N. Chen, S. Lee, W. J. Jo, A. Liu, X. Wang, and K. K. Gleason *Advanced Materials* **2013**, *25*, 5392–5423, DOI: 10.1002/adma.201301878.
- (18) G. Beaucage, R. Composto, and R. S. Stein *Journal of Polymer Science Part B: Polymer Physics* **1993**, *31*, 319–326, DOI: 10.1002/polb.1993.090310310.
- (19) K. H. Liland *MethodsX* **2015**, *2*, 135–140, DOI: 10.1016/j.mex.2015.02.009.
- (20) C. M. Herzinger, B. Johs, W. A. McGahan, J. A. Woollam, and W. Paulson *Journal of Applied Physics* **1998**, *83*, 3323–3336, DOI: 10.1063/1.367101.
- (21) D. Lin-Vien, N. B. Colthup, W. G. Fateley, and J. G. Grasselli, *The Handbook of Infrared and Raman Characteristic Frequencies of Organic Molecules*; Elsevier: 1991; 522 pp.

- (22) C. A. Fyfe and M. S. McKinnon *Macromolecules* **1986**, *19*, 1909–1912, DOI: 10.1021/ma00161a021.
- (23) T. Kyu and A. Eisenberg *Journal of Polymer Science: Polymer Symposia* **1984**, *71*, 203–219, DOI: 10.1002/polc.5070710119.
- (24) S. J. Osborn, M. K. Hassan, G. M. Divoux, D. W. Rhoades, K. A. Mauritz, and R. B. Moore *Macromolecules* **2007**, *40*, 3886–3890, DOI: 10.1021/ma062029e.
- (25) C. Sung, A. Vidyasagar, K. Hearn, and J. L. Lutkenhaus *Langmuir* **2012**, *28*, 8100–8109, DOI: 10.1021/la301300h.
- (26) J. Heijboer *International Journal of Polymeric Materials and Polymeric Biomaterials* **1977**, *6*, 11–37, DOI: 10.1080/00914037708075218.
- (27) K. Honda, M. Morita, H. Otsuka, and A. Takahara *Macromolecules* **2005**, *38*, 5699–5705, DOI: 10.1021/ma050394k.

# Sulfonated Polymer Electrolyte Thin Films from initiated Chemical Vapor Deposition

---

Paul Christian,<sup>¶,†</sup> Junjie Zhao,<sup>¶</sup> Minghui Wang,<sup>¶</sup> Priya Moni,<sup>¶</sup>  
Anna Maria Coclite<sup>†</sup> and Karen K. Gleason<sup>†,\*</sup>

<sup>¶</sup> Department of Chemical Engineering, Massachusetts Institute of Technology, Cambridge, MA 02139, USA

<sup>†</sup> Institute for Solid State Physics, NAWI Graz, Graz University of Technology, 8010 Graz, Austria

\* Corresponding author: kkgleasn@mit.edu

## 7.1 Preface

The following text and its illustrations are based on preliminary results gained on the sulfonation of vapor-phase deposited polymer films, which have been reported in a Marshall Plan Scholarship paper<sup>1</sup> written by the author of this thesis. The author performed the polymer synthesis by initiated Chemical Vapor Deposition, performed the sulfonation reaction and carried out the experimental characterization by FT-IR spectroscopy, scanning electron microscopy as well as electrochemical impedance spectroscopy. Junjie Zhao, Minghui Wang and Priya Moni assisted with the post-deposition sulfonation and provided valuable input on the synthesis in general. Anna Maria Coclite and Karen Gleason supervised the project.

- (1) P. Christian, *Oxidative and initiated Chemical Vapor Deposition for the Synthesis of Sulfonated Polymer Electrolyte Membranes*; Marshall Plan Scholarship Papers: 2017.

## 7.2 Abstract

In this study, initiated Chemical Vapor Deposition (iCVD), a solvent-free polymerization technique, was employed for the synthesis of polymer electrolyte membranes. poly(glycidyl methacrylate) [pGMA] films were successfully synthesized by iCVD and different cross-linkers and substrate materials were evaluated. Post-deposition sulfonation was explored to transfer samples into electrolytic materials. While delamination occurred from flat, rigid substrates like silicon, better adhesion was found on rough surfaces such as poly(ethylene terephthalate) or on porous substrates such as nylon. Apart from chemical and morphological characterizations, also preliminary data on the conductivity of such films was obtained. The results show promising material properties, with conductivities above  $\sigma > 10 \text{ mS/cm}$ . This motivates further studies of such vapor-synthesized, thin film polyelectrolyte membranes, in which also their implementation in applications such as biofuel cells or drug delivery is explored.

## 7.3 Introduction

Polymer electrolyte membranes (PEMs) are crucial components in applications like fuel cells (among others), facilitating selective (protonic) charge transport between the electrodes.<sup>1-3</sup> In addition to high protonic conductivities, these materials are required to withstand elevated temperatures as well as a harsh chemical environment.<sup>3,4</sup> These membranes are often composed of fluorinated parts providing the necessary stability and an acid group for ionic conductivity.<sup>5</sup> However, synthesis of such membranes is usually a tedious and costly process, especially as common solvents are often absent and process temperatures or interface control can become limiting factors.<sup>6,7</sup> Also, novel applications such as biofuel cells foster interest in alternative PEM concepts, often prepared directly on unconventional substrates such as paper.<sup>6</sup> The direct preparation of PEMs on more delicate supports puts additional restrictions on the synthesis processes, usually limiting the use of harsh chemical and thermal conditions. Conformal, low-temperature and solvent-free techniques could (at least) partially circumvent these issues while allowing the preparation of cheaper, better-performing and application-tailored polymers.

Among vapor-based polymerization techniques, initiated and oxidative Chemical Vapor Deposition (iCVD and oCVD, respectively) have emerged as promising candidates for PEM synthesis. Both techniques translate the richness and versatility of synthetic organic chemistry into vapor-based processes while still offering the advantages of a conventional liquid phase synthesis. The iCVD technique was already successfully utilized in the synthesis of a copolymer membrane of methacrylic acid and a perfluorinated compound, which showed

promising ionic conductivity at ambient temperature.<sup>8,9</sup> However, elevated temperatures led to a loss of mechanical stability, thus putting most practical applications (e. g., in fuel cells) in question. In addition, the (weak) carboxylic acid group tends to anhydride formation, which comes at the loss of its proton-donating functionality and renders the polymer useless as ionomer.<sup>10</sup> This motivates the use of different, stronger acid groups like sulfonic acid, which is also the conductive group in commercial Nafion, one of the most commonly employed membranes.<sup>11</sup> However, sulfonation cannot be done directly by the iCVD process which implies the need of a post-deposition modification. This can, for example, be achieved by the incorporation of aromatic phenyl rings into the copolymer, which can be sulfonated through electrophilic substitution.<sup>5</sup> Another option are ring-opening reactions of epoxide groups in which sulfonic acid groups are attached. Possible candidates are polymers incorporating glycidyl methacrylate (GMA). The post-deposition reaction can be carried out under relatively mild conditions (80°C, nitrogen atmosphere) in a water / isopropyl alcohol / sodium sulfite / sodium bisulfite mixture (weight ratio 77/10/10/3).<sup>12</sup> In Figure 7.1a, the reaction scheme is provided and in Figure 7.1b, the actual reaction setup is depicted.

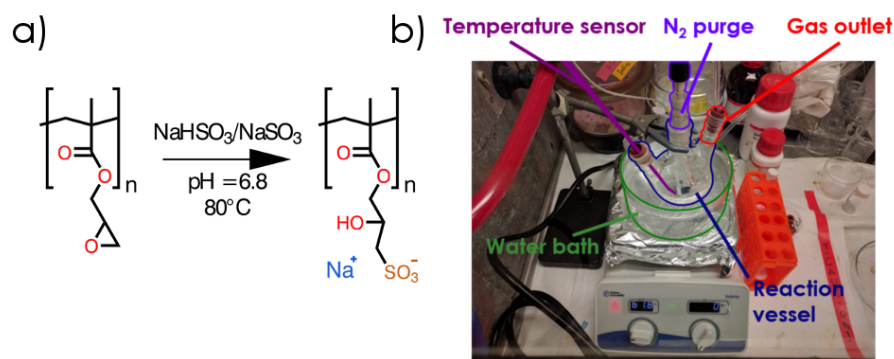


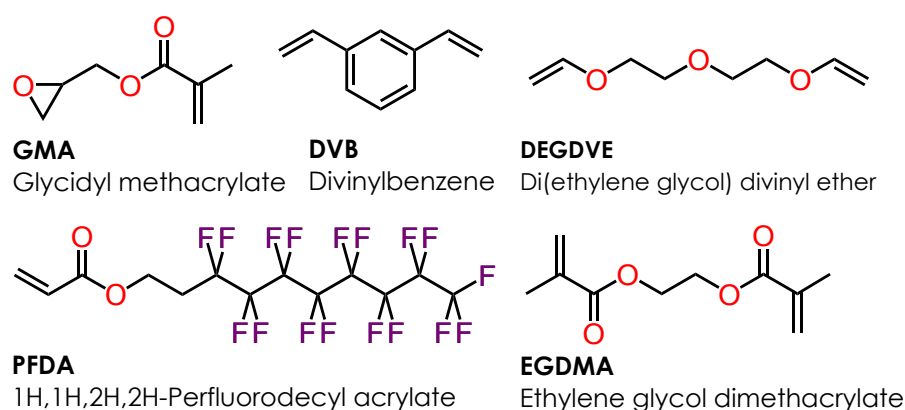
Figure 7.1: a) Reaction scheme depicting the ring opening sulfonation reaction of an epoxy group in a sodium sulfite/sodium bisulfite solution. b) Experimental sulfonation setup employing a three-neck round-bottom flask.

Previous work on this material relied on radiation-induced grafting of GMA onto various substrates and a subsequent sulfonation step.<sup>12,13</sup> By the use of the iCVD technique, this tedious effort can be avoided and preparation of stable membranes should be directly possible.<sup>14</sup>

In this study, initiated Chemical Vapor Depositions is evaluated for the synthesis of proton conductive membranes. For this, synthesis of various pGMA copolymers was attempted, with post-deposition sulfonation being used to introduce sulfonic acid functionalities to the starting materials. For this, different comonomers were evaluated, their structural formulas being depicted in Scheme 7.1. After synthe-

sis, key material properties were analyzed utilizing techniques such as Fourier transform infrared spectroscopy (FTIR) or electrochemical impedance spectroscopy (EIS). The FTIR technique allows for chemical and compositional analysis after polymer synthesis and was used to evidence post-deposition material modifications (i. e., sulfonation). Impedance spectroscopy, on the other hand, was utilized to probe the electro-chemical properties of the films, most importantly the ionic conductivity. Sample characterization is complimented by structural/morphological analysis by scanning electron microscopy (SEM), optical and atomic force microscopy (AFM). This variety of analytical techniques allows to probe distinct key material properties during the different stages of membrane preparation, allowing for synthesis adjustments to be made more directly.

### iCVD monomers



Scheme 7.1: Structural formulas of the monomers used in the polymer synthesis by iCVD. The structures are labeled by their respective abbreviations (given in bold, capital letters), with their common names being stated below.

## 7.4 Methods

Various copolymers of glycidyl methacrylate (GMA) were prepared by iCVD in a custom build reactor. For this, three different cross-linkers and one co-monomer were employed; divinylbenzene (DVB), Di(ethylene glycol) divinyl ether (DEGDVE), ethylene glycol dimethacrylate (EGDMA) and 1H,1H,2H,2H-Perfluorodecyl acrylate (PFDA), with their structural formulas being provided in Scheme 7.1. The monomers were evaporated at different temperatures and flown into the reactor through a heated mixing line (held at 90 °C). For this, GMA, EGDMA and DVB were heated to 60 °C, PDFDA to 70 °C and DEGDVE to 45 °C. The initiator, tert-butyl peroxide (TBPO), was then thermally decomposed at a resistively heated filament (Chromalloy O, Goodfellow). In order to obtain co-polymers with varying compositions,

the flow rates of the reactants were adjusted by needle valves. For the initiator, a constant flow rate of 1 sccm was used. The reactor chamber is connected to a rotary vane pump and an automated butterfly valve is used to maintain the selected pressure of  $(26.6 \pm 0.3)$  Pa during depositions. The substrate temperature was held at  $(40 \pm 2)$  °C by a heater/chiller system (NESLAB) for most of the depositions. Only for p(GMA-DVB) films, the substrates were held at  $(27 \pm 2)$  °C instead. All the chemicals were bought from Sigma-Aldrich.

As substrates, silicon wafers with a native oxide layer were used for most of the studies. For iCVD, samples were additionally prepared on commercial nylon membranes (Sterlitech, NY0214225, pore size  $0.20 \mu\text{m}$ ), poly(ethylene terephthalate) [PET] sheets or on porous Polytetrafluoroethylene membranes (PTFE, Goodfellow, pore size  $0.45 \mu\text{m}$ ).

Fourier Transform Infra-Red spectra (FTIR) were collected on a Nicolet is50 spectrophotometer, equipped with a MCT detector, at a resolution of  $4 \text{ cm}^{-1}$ . Samples were measured either in transmission or in an attenuated total reflection (ATR) configuration, depending on the substrate. Experimental data are converted to absorbance and were automatically baseline corrected utilizing a custom R routine, implementing the baseline package.<sup>15</sup>

Atomic force microscopy (AFM) images were collected in tapping mode on a Nanosurf Easyscan 2 instrument, equipped with a PPP-NCLR-10 cantilever (Nanosensors). Data are leveled and corrected for artifacts in the freely available software package Gwyddion.<sup>16</sup>

Scanning electron microscopy (SEM) images were recorded on a Hitachi TM3000 microscope, equipped with a Bruker Quantax 70 EDS detector. The acceleration voltage was either 5 kV or 15 kV, depending on the sample.

Electrochemical impedance spectroscopy (EIS) was performed on a Gamry Reference 600 potentiostat. Samples were characterized by four-point potentiostatic measurements. For this, samples were cut to size and inserted into a BekkTech BT-110 conductivity clamp. The clamp was then inserted into a sealed glass vessel, where it was exposed to a saturated water vapor atmosphere. Data were collected at 10 points per decade in the frequency range from 1 MHz to 0.1 Hz, applying an AC voltage of  $U_{\text{RMS}} = 10 \text{ mV}$ . The experimental data were fitted to an equivalent circuit model for the frequency range from 10 kHz to 1 Hz, with data points close to the grid frequency (50 Hz) being removed prior evaluation. From the measured resistance  $R$ , the conductivity  $\sigma$  is then calculated according to  $\sigma = l/(R \cdot w \cdot h)$ , with  $l$  denoting electrode spacing and  $w$ ,  $h$  being sample width and height (= thickness), respectively.

## 7.5 Results and discussion

In a first step, GMA-containing polymer films were synthesized by iCVD on silicon substrates. Unless stated otherwise, films were usually deposited with a thickness of one micrometer. While the chosen film thickness is still well below that of commercial membranes (typically several tens of micrometers), it demonstrates that thicker films can also be prepared by iCVD. Further, proton transport properties can more reliably be analyzed for thicker films. To add (physical) stability to the polymers, DEGDVE was employed as a cross-linker in the polymerization. The resulting films were analyzed by FTIR, an example is shown in Figure 7.2. The data demonstrate the successful polymerization of GMA by iCVD, matching the reference spectrum of pGMA almost exactly. This means that full functionality is being retained throughout the process and that vinyl bond conversion efficiency is high (as vinyl peaks, typically observed around 1630 and 990  $\text{cm}^{-1}$ , are absent in the spectrum).<sup>17</sup> This means that monomer inclusion is likely low and also that both vinyl bonds of the cross-linker units are polymerized. However, this exact match with the pGMA homopolymer spectrum also evidences an issue. Due to the absence of chemical groups unique to the cross-linker, the co-polymer composition cannot be determined from the FTIR data.

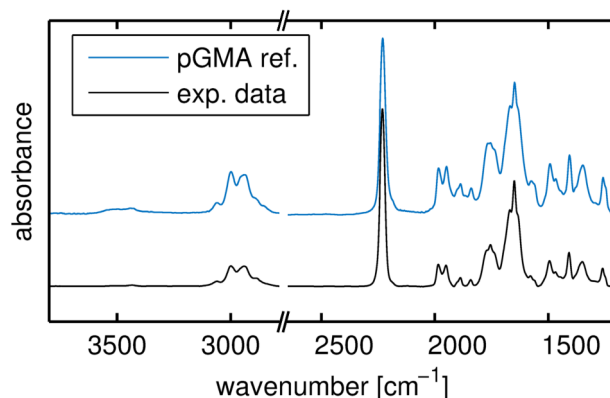


Figure 7.2: Experimental FTIR spectrum of an as-prepared p(GMA-DEGDVE) polymer film (bottom) along the reference pattern of pGMA, taken from a Thermo Scientific™ FTIR database (top). Data are shifted for clarity.

In a next step, the p(GMA-DEGDVE) films were sulfonated in solution according to the procedure described in the introduction. In Figure 7.3, exemplary results for post-sulfonation polymer films are shown. The sample has been exposed to the reactant solution for six hours while being held at 70 °C. During the reaction, the polymer film had delaminated, an issue commonly encountered in the sulfonation process. While as-prepared films cover smoothly the silicon wafer surface, films would delaminate and fragment during the sulfonation



(compare the photographs in Figure 7.3a). Picking up larger fragments and drying them on a silicon support, further analysis was possible. An AFM micrograph (in Figure 7.3b) reveals a rough surface area ( $\sigma_{\text{RMS}} = (13 \pm 1) \text{ nm}$ , which is in stark contrast to the smooth surface of as-prepared films (roughness approx. 1 nm, data not shown).

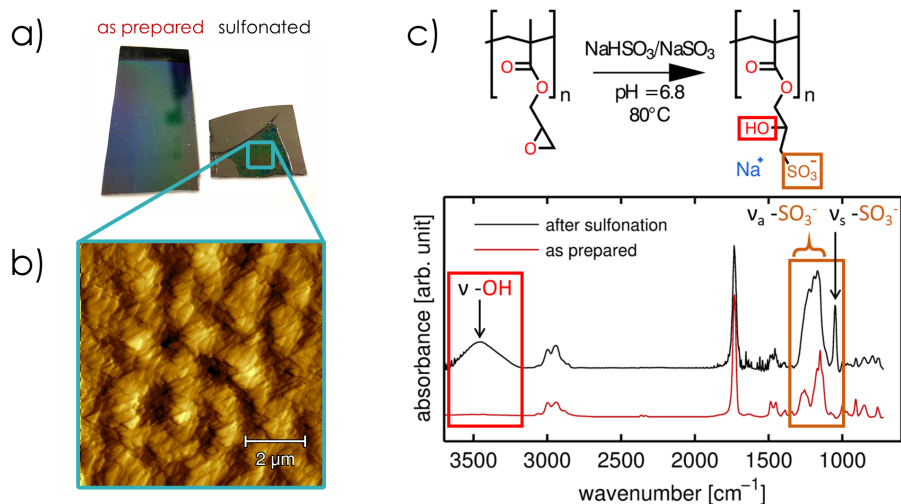


Figure 7.3: a) Photographs of an as-prepared p(GMA-DEGDVE) film on a silicon substrate and a delaminated piece after sulfonation (supported on silicon). b) AFM micrograph of the sulfonated polymer piece. c) Scheme depicting the chemical modification of GMA during sulfonation (top) and FTIR spectra of the two samples (bottom), evidencing differences in chemical composition after the solution treatment. Data are shifted for clarity.

Film delamination and the changed surface structure indicate already that some modification has occurred in the film, which is confirmed in the chemical analysis by FTIR (Figure 7.3c). The experimental spectra before and after sulfonation show clear differences in the fingerprint regions ( $1500\text{--}500 \text{ cm}^{-1}$ ) and in the  $-\text{OH}$  stretch regions ( $3600\text{--}3100 \text{ cm}^{-1}$ ). Post-sulfonation, the spectrum features peaks characteristic for sulfonate groups, located at  $1193$  and  $1047 \text{ cm}^{-1}$ , as well as a broad absorption peak at  $3446 \text{ cm}^{-1}$ , attributed to the formation of hydroxide groups.<sup>18</sup> A comparison with the reaction scheme (Figure 7.3c, top) shows that the occurrence of these groups is associated with a successful opening of the epoxide so that the sodium salt of the sulfonic acid is then attached in a nucleophilic attack. While this means that iCVD-deposited GMA polymers can successfully be sulfonated, film delamination and subsequent fragmentation pose a serious challenge for any practical application. For this reason, one has to understand the occurrence of delamination first. From the experimental data, the change in hydrophilicity during sulfonation is identified as the most probable cause; as the sulfonic acid salt attaches, polymers

become strongly hydrophilic and thus start swelling in the sulfonation medium, which in turn causes stress at the polymer/substrate interface. The rigid silicon substrate does not support the strong expansion of the polymer during swelling and thus, delamination occurs. It should be noted that, in principle, delamination could also be due to a too low cross-linking degree. For polymers deposited by iCVD, stable films are usually obtained at cross-linker fractions of about 10% or above. However, varying monomer to cross-linker flow rates did not result in any stable films during sulfonation, while the same films were found stable in water at the same temperatures (data not shown). However, as DEGDVE content could not be determined from FTIR data, no conclusive assessment of the cross-linker fraction could be made (however, successful cross-linking is evident from improved stability in water). Therefore, the following section will provide some examples of other co-monomers tested as well as other strategies to limit delamination during the sulfonation.

**GMA-polymers with different co-monomers.** A major advantage of the iCVD technique over other polymerization techniques is how easily polymers with different co-monomers can be synthesized, as the need for common solvents is absent. As it was not possible to detect DEGDVE fractions from FTIR data and film delamination remained a critical issue independent of the tested deposition parameters, different co-monomers were investigated instead. For this, two other cross-linkers, DVB and EGDMA, as well as PFDA, a perfluorinated co-monomer, were tested. As their chemistry shows at least some differences to GMA (*cf.* Scheme 7.1), their volume fraction can more easily be assessed from FTIR data. Selected examples are provided in Figure 7.4, where experimental data are evaluated as a linear combination of the homopolymer spectra, weighted by their respective fraction and normalized by the sample thickness. From a fit to the data, the composition is then evaluated. For GMA co-polymers with PFDA and EGDMA, reasonably good agreement is achieved (*cf.* Figure 7.4a,c,d). The fits match closely the experimental data and different GMA content can be distinguished (*cf.* Figure 7.4c,d). While this treatment can also be applied to p(GMA-DVB) polymers (*cf.* Figure 7.4b), the spectra show strong deviations from the fit in the fingerprint region (marked by an asterisk in the plot). The assumptions of little interaction between the co-monomers does not hold in this case and the co-polymer gives rise to additional absorption peaks. However, when the evaluated data range is reduced to the region of C–H stretch above  $2800\text{ cm}^{-1}$ , polymer composition can still be determined by this routine. A more detailed description of this method and its limitations can be found in literature.<sup>19</sup>

While changing the co-monomer in the GMA films did allow for an easier compositional analysis, structural damage and delamination during sulfonation remained critical issues. Exemplary, optical micro-

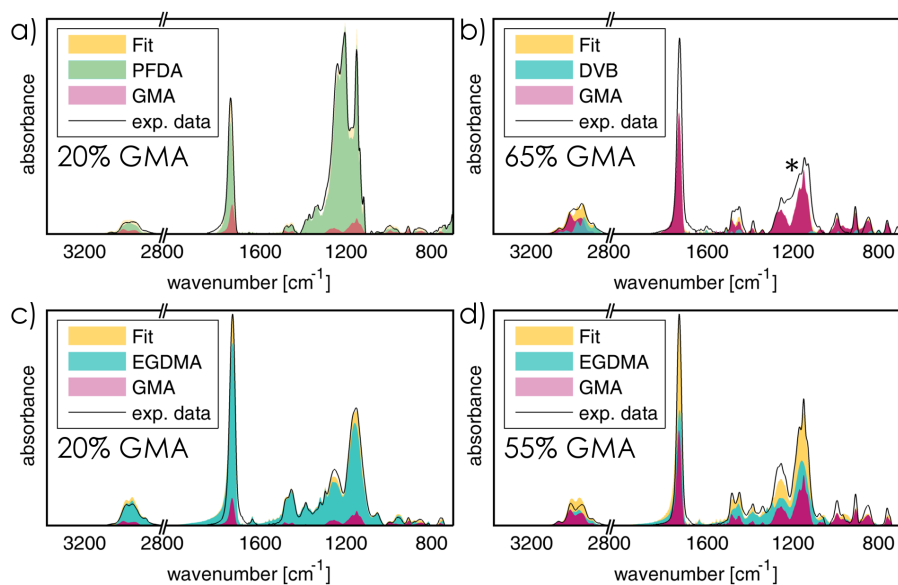


Figure 7.4: Exemplary FTIR spectra of different GMA copolymers: a) p(GMA-PFDA), b) p(GMA-DVB) and c,d) p(GMA-EGDMA) films with different GMA content. For compositional analysis, experimental data are fitted by a linear combination of the respective homopolymer spectra. In case of the p(GMA-DVB) films, deviations from this model are noted (marked by an asterisk, see text for a more detailed explanation). Please note that so-determined volume fractions will have an absolute error of about 10 %, as there is a high degree of freedom in the baseline corrections.

graphs of a p(GMA-PDFA) film and a p(GMA-DVB) film, after being exposed to the sulfonation solution, are shown in Figure 7.5a and b, respectively. Despite the high PFDA content (> 90 %), ruptures and partial delamination occurred. For this reason, PFDA was not further considered. Likewise, DVB co-polymers were severely affected by the sulfonation process (Figure 7.5b). However, in contrast to PFDA, these samples exhibit a behavior more similar to that of p(GMA-DEGDVE) films. Interestingly, defined patterns are also noted on the samples, possibly hinting at the occurrence of phase separation in these films. Likewise, EGDMA films exhibit comparable behavior but also do not limit delamination (data not shown). While all the tested cross-linker seem to be feasible per se, altered chemistry does not limit delamination and thus, other strategies were evaluated instead.

**Nylon and PET substrates.** While different cross-linkers, polymer compositions and also grafting was explored as possible ways to limit film delamination from silicon substrates during sulfonation, none of the evaluated strategies did result in a significant improvement. Therefore, also different substrates were evaluated for the preparation

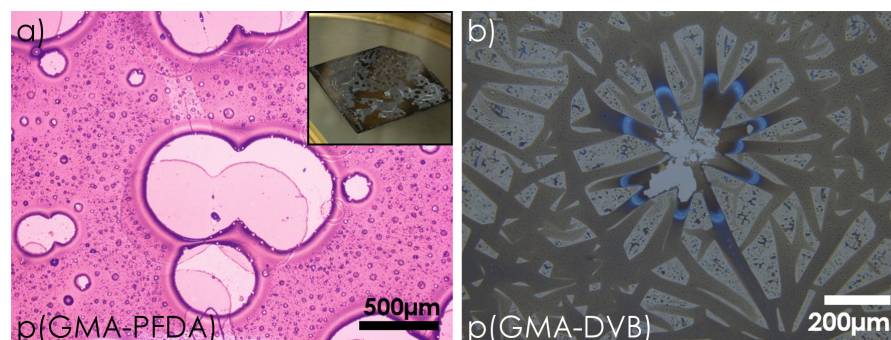


Figure 7.5: Optical microscopy images of samples after sulfonation: a) p(GMA-PFDA) film with little GMA content (< 10%), the inset depicting the entire sample. b) p(GMA-DVB) film with 60% GMA content.

of sulfonated PEMs by iCVD. Two porous (nylon and PTFE) and a non-porous substrate (PET) were employed in the film preparation. From a material characterization point of view, the PET substrate offers the advantage of being more accessible to most of the analytical techniques employed in this study. Most importantly, FTIR analysis can be performed in this case by using the surface-sensitive ATR configuration. As this requires substrate and polymer to be separated by a sharp interface, porous substrates are not well suited. For this reason, chemical analysis was performed exclusively on samples prepared on PET substrates. However, the porous substrates provide better stability to the iCVD polymers due to their larger surface area. Also, the porosity of the substrates eases water uptake, a possible advantage in the conductivity measurements.

Films prepared on either of these flexible substrates showed improved stability of the iCVD films during sulfonation. Exemplarily, FTIR data of p(GMA-DEGDVE) samples are provided in Figure 7.6a, evidencing the differences in the measured spectra depending on the substrate choice (silicon or PET). Despite having an iCVD layer of about  $1.5\ \mu\text{m}$  atop, the substrate is also partially sampled in the ATR measurement. However, the differences do not significantly alter the overall pattern and the iCVD polymer is easily recognized. After being kept in the sulfonation solution for 8 hours at  $75\ ^\circ\text{C}$ , the film remained attached to the substrate surface and FTIR data evidence the successful conversion of the GMA groups (compare Figure 7.6b with the data in Figure 7.4c). While it should be noted that some samples also delaminated from PET (mostly when handled in a highly swollen state, e. g. during rinsing), overall stability was significantly improved in comparison to samples prepared on silicon.

In another step, the transfer of the acid salt to sulfonic acid was tested. For this, samples were stored in one molar sulfuric acid for 8 hours, which should lead to a hydrolysis reaction. As exposure to

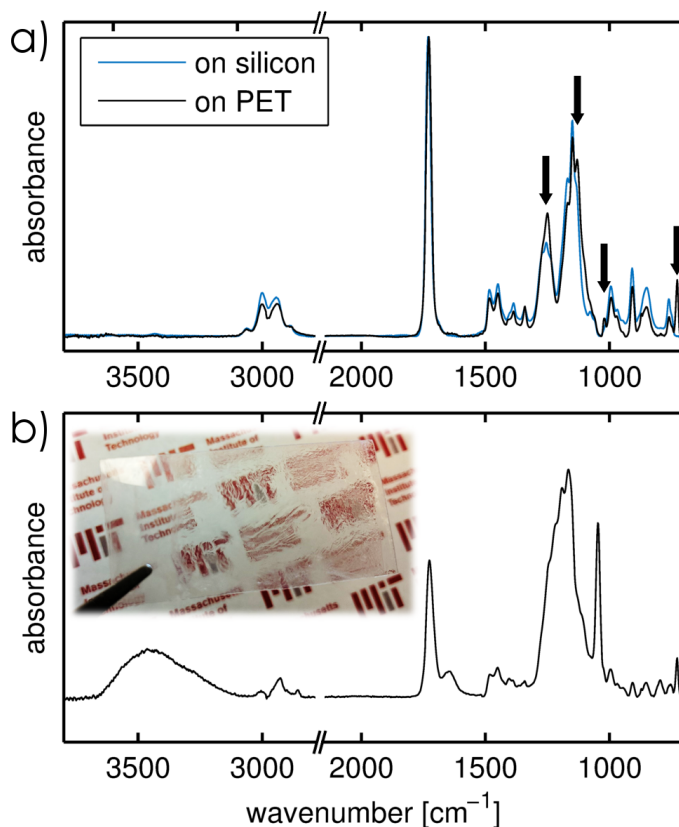


Figure 7.6: a) FTIR spectra of as-prepared p(GMA-DEGDVE), prepared either on a silicon or on a PET substrate. The data are collected in transmission for silicon and in ATR configuration for PET. Arrows mark absorption peaks stemming from the PET substrate. b) FTIR ATR spectrum of a sulfonated p(GMA-DEGDVE) sample on a PET substrate (8 hours at 75 °C). The inset depicts a photograph of the sample in the swollen state. While the left side of the transparent PET substrate has been left uncoated, strong wrinkling of the swollen iCVD polymer, covering the right part of the substrate, results in the image being blurred out. Data have been baseline and ATR-corrected (where applicable).

a strong acid like sulfuric acid can have unwanted side-effects on the film/substrate, SEM images were taken after the reaction. Figure 7.7a shows an exemplary image of a p(GMA-DEGDVE) sample after acid exposure. Aside from strong charging effects due to the non-conductive substrate (bright areas in the image), the surface is covered with small dot-like features. Likely, the acid treatment had led to the formation of holes in the iCVD film. The EDX spectrum of this sample (Figure 7.7b) shows the absence of sodium (Na) while sulfur is still present, indicating a successful conversion of the film. A quantitative analysis of the spectrum yields a sulfur fraction of 2%

(see inset). From this data, a rough estimate about the sulfonation conversion efficiency can be made. Assuming a GMA homopolymer (as it was not possible to determine the DEGDVE content), the carbon/oxygen/sulfur ratios would yield a conversion rate of about 40%. However, this value is likely only a lower limit; as the EDX spectrum probes most of the sample thickness, carbon and oxygen content will also show some contribution from the PET substrate as well as from carbon contamination.

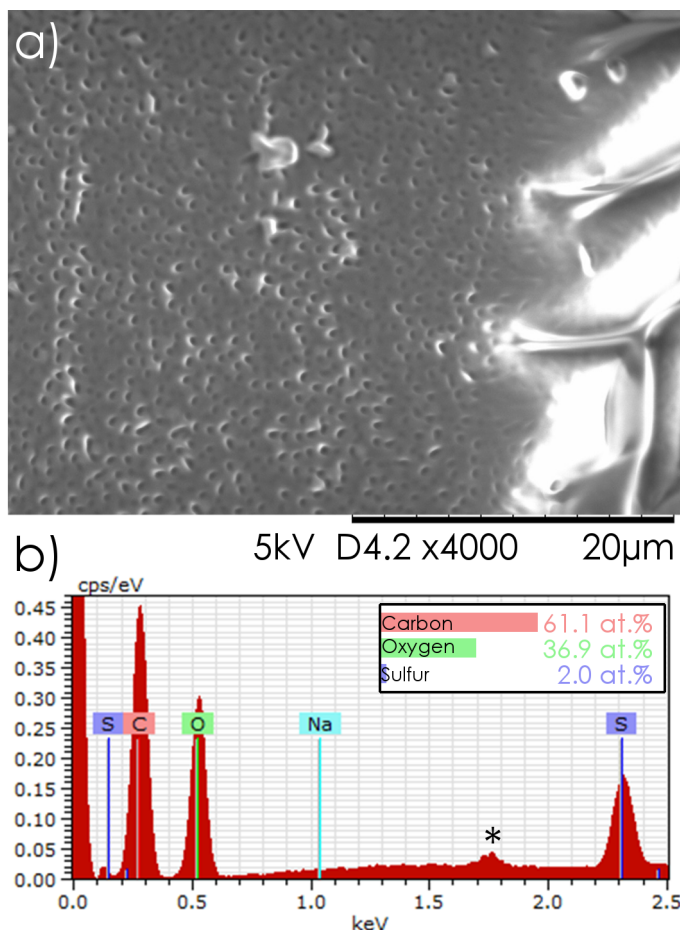


Figure 7.7: a) SEM image of a p(GMA-DEGDVE) coating on a PET substrate after sulfonation and ion exchange in 1 M sulfuric acid. b) EDX spectrum of the sample, evidencing the successful conversion of the salt to the acid state (as sodium is not detected). The inset shows a quantitative compositional analysis of the spectrum. Peaks stemming from a silicon powder contamination are indicated by an asterisk.

**Conductivity measurements.** Polymer electrolyte membranes are commonly tested either directly in fuel cell systems or separately in a conductivity cell. However, this requires rather thick polymer



films (with tens of micrometers in thickness), which are not feasible to deposit with a research iCVD reactor. For this reason, thinner films are usually investigated instead, requiring more specialized experimental setups. As iCVD polymers can easily be prepared on different surfaces, this raises an interesting option: instead of preparing free-standing films, which are then contacted mechanically by the measurement electrodes, one can directly deposit the polymers on an electrode array. In this context, printed circuit boards (PCBs) are an interesting option as they are highly customizable and are cheaply available (an example is shown in the inset of Figure 7.8a). Electrodes with a varying spacing allow for conductivity measurements as a function of electrode separation distance, which can be useful to detect the influence of local defects (as they interfere with the otherwise linear relationship according to Ohm's law). Also, from the rough, polymeric substrate of the PCB one can expect improved adhesion between iCVD film and PCB, thus minimizing the delamination problem. While this was confirmed in the sulfonation experiments (data not shown), another issue arose during measurements. For this, samples are usually inserted into water, in order to hydrate the sulfonated films prior measurement (*cf.* Figure 7.8b). However, measurements turned out to be surprisingly unstable (data not shown). SEM images of repeatedly water-exposed samples revealed structural damage at the polymer-electrode interfaces (*cf.* Figure 7.8a). The gold-coated copper electrodes have a height of about 30  $\mu\text{m}$ , which is much larger than the polymer thickness (approx. 1  $\mu\text{m}$ ). This difference makes the so important interface susceptible for defects, the SEM image showing creasing and ruptures in the iCVD layer on top of the electrodes (marked by arrows).

To avoid this issue, thin gold electrodes were evaporated on PET substrates instead (*cf.* Figure 7.8c). These electrodes had a thickness of just 50 nm and retained the advantages of using a flexible substrate. For measurements, electrodes feature broader pads at their top, at which they can be connected by toothless alligator clips (*cf.* Figure 7.8d). While this concept did function in principle, the tedious and costly preparation process makes also this approach not feasible for evaluating a wider spectrum of samples. Thus, these thin gold electrodes were used only complementary to measurements with the BekkTech conductivity cell. In addition, samples were swollen in humidity rather than inserting them directly into water, allowing more time for the swelling process and also allowing the study of the time-dependence of the conductivity during water uptake.

In the following, some preliminary conductivity data are presented for samples measured in humidity. As samples were prepared on nylon substrates, the uncoated substrate was investigated first. In order to exclude any influence of the post-deposition sulfonation reaction, the nylon substrate was put in the solution for 14 hours at 75 °C. In

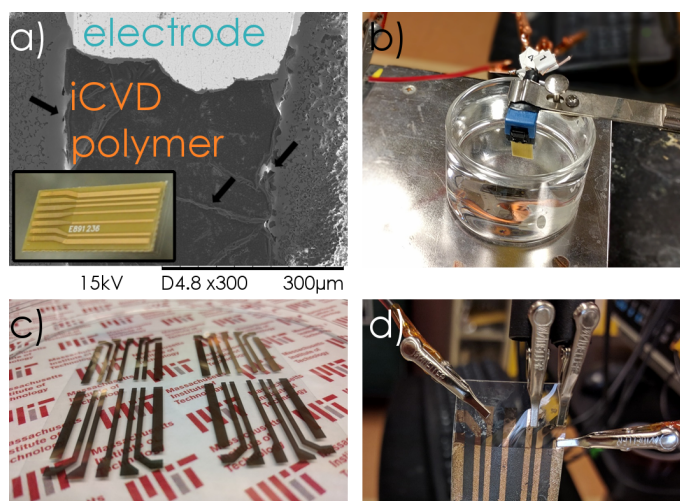


Figure 7.8: a) SEM image of the electrode-polymer interface on a PCB after sulfonation. The inset depicts a photograph of the full PCB, with an iCVD film covering the right part of the board. Arrows mark several defects at the polymer/electrode interface. b) EIS measurement setup in water. c) Gold electrodes evaporated on PET substrates. d) 4-point EIS measurement of a sulfonated iCVD film prepared on a PET substrate with a gold electrode array.

Figure 7.9a, changes in nylon conductivity as a function of time are depicted, as determined from electrochemical impedance spectroscopy measurements in saturated humidity. While the sample does show some increase in conductivity over time (as the nylon substrate takes up water), the nylon remains overall highly resistive. This is a good indication that the nylon substrate was not strongly affected by the sulfonation process, allowing coating and substrate to be distinguished in the EIS measurements. In Figure 7.9b, the Nyquist plot of a representative impedance spectrum is shown (i. e., x- and y-axis depict the real and imaginary part of the impedance, respectively). The data feature most prominently a semicircle, corresponding to an equivalent circuit of a capacitance and a resistance in parallel. For practical reasons, an imperfect capacitance is usually considered, modeled by a constant phase element (CPE). While there is another, smaller semicircle noted at higher  $Z_{\text{real}}$  values, it can be neglected in the data evaluation; the membrane conductivity is calculated from the measured resistance, i. e. the intersection with the x-axis.

When evaluating sulfonated iCVD polymers deposited on nylon, a different behavior is observed. Impedance spectra for a p(GMA-EGDMA) film with 55 % GMA content (cf. Figure 12 for the FTIR data) show a pronounced inductive behavior at high frequencies (above 10 kHz), which transits into a resistive/capacitive behavior at lower frequencies (for an exemplary data set, cf. Figure 7.10a). For the eval-



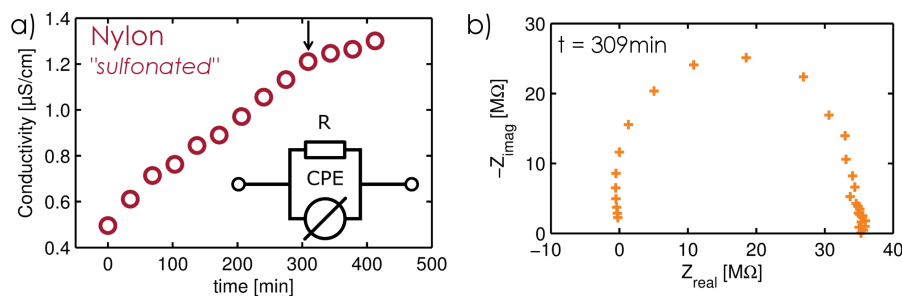


Figure 7.9: a) Changes in ionic conductivity for an uncoated nylon membrane, which was kept in the sulfonation reaction solution for 14 hours (at 75 °C) prior measurement. b) Nyquist plot depicting the impedance spectrum for a selected data point (marked with an arrow in a) The data were collected in a closed system at saturated humidity.

uation of the polymer electrolyte membrane, only the low frequency regime (below 20 kHz) is typically considered.<sup>20–22</sup> A detailed view of this regime is provided in Figure 7.10b. The data feature a first intersection with the x-axis around 47.3 k $\Omega$ , corresponding to ohmic losses, followed by two semicircles and another intersection with the real axis at frequencies lower than 1 Hz. The data can be fitted reasonably well by an equivalent circuit depicted in the inset. Most importantly, the membrane (i.e. iCVD film) resistance can be determined from the intersection at higher frequencies (around 10 kHz).<sup>22–24</sup>

The two parallel RCs, on the other hand, could not be unambiguously interpreted but might be related to double layer formation or transport phenomena. In Figure 7.10c, impedance spectra at selected times are depicted, evidencing a shift of the total spectrum towards lower x-values. This means that the membrane resistance decreases gradually as the hydration level increases in the films. As the hydrated state is necessary for the dissociation of protons from the sulfonic acid groups, this behavior is expected. In Figure 7.10d, membrane conductivities are plotted as a function of time. Please note that these values are calculated with the thickness of the dry iCVD layers as the swollen thicknesses were experimentally not accessible. Therefore, values represent an upper estimate of the true conductivity. The data show conductivity values of about 100 mS/cm, which is very promising for future experiments. As the curve does not show a saturation behavior, the apparent conductivity increase might be in fact related to further water uptake. As a constant thickness is assumed in the conductivity calculation, thickness changes induced by swelling are left unaccounted for. Nevertheless, this thickness increase should not surpass 100%, meaning that the true membrane conductivity should still be in the order of 10 to 100 mS/cm. For comparison, also data for a polymer cross-linked with DVB are shown. While the slightly increased

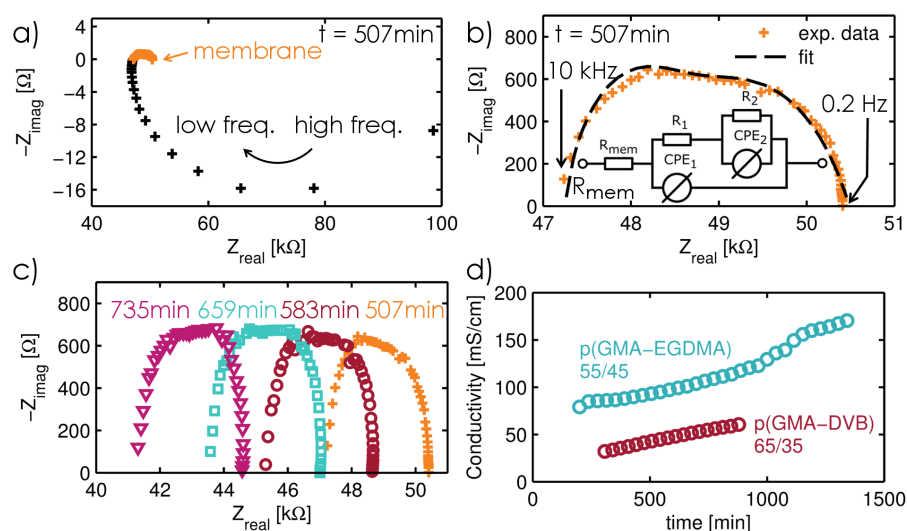


Figure 7.10: Electrochemical impedance spectroscopy data of a p(GMA-EGDMA) sample with 55% GMA content. The data were collected in a closed system at saturated humidity. a) Nyquist plot of the full impedance spectrum collected after 507 seconds, depicting setup and membrane contributions. b) Nyquist plot of the membrane data. The inset depicts the equivalent circuit used in the fits. c) Selected impedance spectra depicting the change in impedance over time. d) Changes in conductivity of the iCVD film as a function of time. For comparison, data for a p(GMA-DVB) film with 65% GMA content are also shown. Please note that conductivity values are calculated with the dry, as-deposited film thickness.

GMA content (65 compared to 55%) suggests higher conductivities, data show actually the opposite behavior. A possible reason might be that DVB, in contrast to EGDMA, is highly rigid, possibly limiting chain rearrangement and charge transport.

## 7.6 Conclusion

The possibility to employ initiated Chemical Vapor Deposition in the preparation of sulfonated proton conductive materials was investigated. Co-polymers of glycidyl methacrylate were prepared by iCVD for subsequent sulfonation. For this, different cross-linkers and co-monomers were evaluated. While it was possible to sulfonate vapor-deposited polymers, delamination and other structural instabilities were commonly encountered in the films during the reaction. Exchanging the rigid silicon substrates with flexible polymeric ones (such as PET or nylon) did significantly enhance the film stability on the substrate. The increased surface area (due to roughness) and the

flexibility of the support decrease the stress at the iCVD polymer/substrate interface when films turn hydrophilic (and thus start swelling) during sulfonation. Preliminary data from conductivity measurements by electrochemical impedance spectroscopy show promising values, with samples reaching conductivity values in the order of 10 to 100 mS/cm. While the experimental conditions do not yet allow for the deposition of thicker membranes within reasonable time/costs, such membranes could be interesting for small-scale applications such as in enzyme fuel cells. In a next step, the proton conductivities of such membranes need to be investigated as a function of polymer composition and further improvements in deposition speed and polymer stability need to be made. Ultimately, the goal will be to test these polymers in a demonstrational power device.

## 7.7 References

- (1) V. Mehta and J. S. Cooper *Journal of Power Sources* **2003**, *114*, 32–53, DOI: 10.1016/S0378-7753(02)00542-6.
- (2) V. Neburchilov, J. Martin, H. Wang, and J. Zhang *Journal of Power Sources* **2007**, *169*, 221–238, DOI: 10.1016/j.jpowsour.2007.03.044.
- (3) S. J. Peighambaridoust, S. Rowshanzamir, and M. Amjadi *International Journal of Hydrogen Energy* **2010**, *35*, 9349–9384, DOI: 10.1016/j.ijhydene.2010.05.017.
- (4) J. Wu, X. Z. Yuan, J. J. Martin, H. Wang, J. Zhang, J. Shen, S. Wu, and W. Merida *Journal of Power Sources* **2008**, *184*, 104–119, DOI: 10.1016/j.jpowsour.2008.06.006.
- (5) M. A. Hickner, H. Ghassemi, Y. S. Kim, B. R. Einsla, and J. E. McGrath *Chemical Reviews* **2004**, *104*, 4587–4612, DOI: 10.1021/cr020711a.
- (6) D. Poppe, H. Frey, K. D. Kreuer, A. Heinzl, and R. Mülhaupt *Macromolecules* **2002**, *35*, 7936–7941, DOI: 10.1021/ma012198t.
- (7) S. Bose, T. Kuila, T. X. H. Nguyen, N. H. Kim, K.-t. Lau, and J. H. Lee *Progress in Polymer Science* **2011**, *36*, 813–843, DOI: 10.1016/j.progpolymsci.2011.01.003.
- (8) A. M. Coclite, P. Lund, R. Di Mundo, and F. Palumbo *Polymer* **2013**, *54*, 24–30, DOI: 10.1016/j.polymer.2012.11.004.
- (9) C. Ranacher, R. Resel, P. Moni, B. Cermenek, V. Hacker, and A. M. Coclite *Macromolecules* **2015**, *48*, 6177–6185, DOI: 10.1021/acs.macromol.5b01145.
- (10) P. Christian *Thermal stability in proton conductive iCVD polymers*, 9th International Conference on Hot Wire and Initiated Chemical Vapor Deposition, Philadelphia, 2016.

- (11) K. A. Mauritz and R. B. Moore *Chemical Reviews* **2004**, *104*, 4535–4586, DOI: 10.1021/cr0207123.
- (12) W. Lee, A. Shibasaki, K. Saito, K. Sugita, K. Okuyama, and T. Sugo *Journal of The Electrochemical Society* **1996**, *143*, 2795–2799, DOI: 10.1149/1.1837109.
- (13) Y. Buchmüller, A. Wokaun, and L. Gubler *Fuel Cells* **2013**, *13*, 1177–1185, DOI: 10.1002/fuce.201300144.
- (14) R. Bakker, V. Verlaan, C. H. M. van der Werf, J. K. Rath, K. K. Gleason, and R. E. I. Schropp *Surface and Coatings Technology* **2007**, *201*, 9422–9425, DOI: 10.1016/j.surfcoat.2007.03.058.
- (15) K. H. Liland *MethodsX* **2015**, *2*, 135–140, DOI: 10.1016/j.mex.2015.02.009.
- (16) D. Nečas and P. Klapetek *Central European Journal of Physics* **2011**, *10*, 181–188, DOI: 10.2478/s11534-011-0096-2.
- (17) P. Larkin, *Infrared and Raman Spectroscopy: Principles and Spectral Interpretation*; Elsevier: 2011; 239 pp.
- (18) Y. V. Bondar, H. J. Kim, and Y. J. Lim *Journal of Applied Polymer Science* **2007**, *104*, 3256–3260, DOI: 10.1002/app.25887.
- (19) M. Tazreiter, P. Christian, R. Schennach, T. Grießer, and A. M. Coclite *Analytical Methods* **2017**, *9*, 5266–5273, DOI: 10.1039/C7AY01748K.
- (20) S. Asghari, A. Mokmeli, and M. Samavati *International Journal of Hydrogen Energy* **2010**, *35*, 9283–9290, DOI: 10.1016/j.ijhydene.2010.03.069.
- (21) S. Sun, Y. Xiao, D. Liang, Z. Shao, H. Yu, M. Hou, and B. Yi *RSC Advances* **2015**, *5*, 14506–14513, DOI: 10.1039/C4RA14104K.
- (22) B. Feketeföldi, B. Cermenek, C. Spirk, Alex, E. Schenk, C. Grimmer, M. Bodner, M. Koller, V. Ribitsch, and V. Hacker *Journal of Membrane Science & Technology* **2016**, *6*, DOI: 10.4172/2155-9589.1000145.
- (23) J. Zhang, H. Zhang, J. Wu, and J. Zhang In *Pem Fuel Cell Testing and Diagnosis*, Zhang, J., Zhang, H., Wu, J., and Zhang, J., Eds.; Elsevier: Amsterdam, 2013, 143.
- (24) M. Bodner, B. Cermenek, M. Rami, and V. Hacker *Membranes* **2015**, *5*, 888–902, DOI: 10.3390/membranes5040888.

## Part III

### DIRECT COATING OF PHARMACEUTICALS BY ICVD

This section explores the applicability of polymer coatings by iCVD onto thin films of active pharmaceutical ingredients. The effect of the polymer on the solid state and on the release behavior of the drug are studied and also polymer properties are evaluated. The results are reproduced from their respective peer-reviewed publications and have been reformatted to fit the format of this thesis.



# Polymer Encapsulation of an Amorphous Pharmaceutical by initiated Chemical Vapor Deposition for Enhanced Stability

This is an open access article published under a Creative Commons Attribution (CC-BY) License, which permits unrestricted use, distribution and reproduction in any medium, provided the author and source are cited.



ACS APPLIED MATERIALS  
& INTERFACES

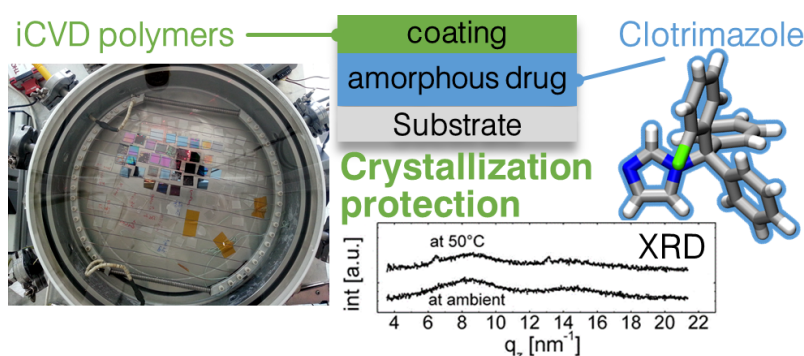
www.acsami.org

## Polymer Encapsulation of an Amorphous Pharmaceutical by initiated Chemical Vapor Deposition for Enhanced Stability

Paul Christian,<sup>†</sup> Heike M.A. Ehmann,<sup>‡</sup> Anna Maria Codite,<sup>†</sup> and Oliver Werzer<sup>\*†‡</sup>

<sup>†</sup>Institute of Solid State Physics, NAWI Graz, Graz University of Technology, 8010 Graz, Austria

<sup>‡</sup>Institute of Pharmaceutical Science, Department of Pharmaceutical Technology, University of Graz, 8010 Graz, Austria



## 8.1 Preface

This work was conducted in close collaboration with Oliver Werzer from the University of Graz, who provided the clotrimazole samples and carried out the X-ray characterization. The author of this thesis performed the polymeric encapsulation by the iCVD method, evaluated the experimental data and wrote the manuscript with assistance of Oliver Werzer. Heike M.A. Ehmann provided optical microscopy data for the samples. Anna Maria Coclite and Oliver Werzer supervised the project. The following text and its illustrations are identical to the published work<sup>1</sup> and are reproduced with permission.

- (1) P. Christian, H. M. Ehmann, A. M. Coclite, and O. Werzer *ACS Applied Materials & Interfaces* **2016**, *8*, 21177–21184, DOI: 10.1021/acsami.6b06015.

## 8.2 Abstract

The usage of amorphous solids in practical applications, such as in medication, is commonly limited by the poor long-term stability of this state, because unwanted crystalline transitions occur. In this study, three different polymeric coatings are investigated for their ability to stabilize amorphous films of the model drug clotrimazole and to protect against thermally induced transitions. For this, drop cast films of clotrimazole are encapsulated by initiated chemical vapor deposition (iCVD), using perfluorodecyl acrylate (PFDA), hydroxyethyl methacrylate (HEMA), and methacrylic acid (MAA). The iCVD technique operates under solvent-free conditions at low temperatures, thus leaving the solid state of the encapsulated layer unaffected. Optical microscopy and X-ray diffraction data reveal that at ambient conditions of about 22 °C, any of these iCVD layers extends the lifetime of the amorphous state significantly. At higher temperatures (50 or 70 °C), the p-PFDA coating is unable to provide protection, while the p-HEMA and p-MAA strongly reduce the crystallization rate. Furthermore, p-HEMA and p-MAA selectively facilitate a preferential alignment of clotrimazole and, interestingly, even suppress crystallization upon a temporary, rapid temperature increase (3 °C/min, up to 150 °C). The results of this study demonstrate how a polymeric coating, synthesized directly on top of an amorphous phase, can act as a stabilizing agent against crystalline transitions, which makes this approach interesting for a variety of applications.

## 8.3 Introduction

Poor solubility and low bioavailability are major concerns in the formulation of several drug systems, limiting or even prohibiting their usage in practical application. Several approaches are known to overcome this limitation, among which particle size reduction is likely the most commonly used.<sup>1</sup> Besides this, the usage of the amorphous solid state is particularly appealing to the pharmaceutical formulation of poorly soluble drugs, because this state promises easier dissolution compared with the crystalline form(s).<sup>2-4</sup> In the amorphous state, enhanced surface accessibility exists and lattice energies are absent, thus resulting in excess free energy.<sup>5</sup> This means that the energetic barriers that molecules have to overcome in order to participate in the solubilization process are relatively low compared with those of molecules within the highly structured arrangements of a crystal. Experimental and theoretical studies have demonstrated this difference for some systems, including indomethacin<sup>6,7</sup> and ritonavir.<sup>8</sup> However, a significant drawback of the amorphous state is the lack of long time stability, which often results in undesired or unpredictable crystalline transition(s) over time. This makes drug formulations with amorphous



active pharmaceutical ingredients challenging.<sup>9</sup> The most common approach to prevent devitrification is the usage of solid dispersions, where the amorphous active pharmaceutical component (API) is dispersed within a carrier material.<sup>5,10</sup> While the definition comprises several different types of solid dispersions, it is mostly used to describe binary systems consisting of amorphous APIs within a polymeric carrier. Such systems aim to increase the glass transition temperature of the drug system because above this point enhanced molecular mobility, and thus crystallization, is facilitated.<sup>11</sup> Additionally, molecular interactions (e.g., hydrogen bonding)<sup>12</sup> or local entrapment within the matrix material can further stabilize the amorphous state.<sup>13</sup>

However, stabilization of the amorphous state through interface interactions is not limited to full encapsulation. Just the presence of a solid substrate may readily allow for enhanced stability. In the case of thin paracetamol films supported on silica surfaces, this provides stabilization up to an hour.<sup>14</sup> For racemic ibuprofen on glass surfaces, crystallization requires more than 2 weeks, while cellulose surfaces lead to crystallite formation already within a day.<sup>15</sup> As new formulation strategies are under development, personalized medicine might benefit from such amorphous states because the shelf life might not be the limiting parameter for successful application. Surfaces are not only capable of stabilizing amorphous states but have also the potential to facilitate crystallization into specific polymorphs or with distinct crystallographic orientations (texture). For instance, poly(3-hexylthiophene) (P3HT) assembles on a potassium 4-bromobenzoate substrate in an “edge-on” orientation.<sup>16</sup> Single crystal surfaces induce a directed growth, which results, for instance, in para-sexiphenyl needles aligning along certain direction on gold or copper crystals.<sup>17,18</sup> Similarly, the crystallographic orientation of caffeine needles on mica surfaces reflects the pseudo-3-fold symmetry of a complex mica sheet.<sup>19,20</sup> Defined crystal growth is of high importance because polymorphic structures as well as morphologies have a tremendous impact on the physicochemical properties of a material. For drugs or pharmaceutically relevant molecules, properties such as dissolution behavior, bioavailability, and shelf life stability are of main concern. Polymorph adjustments can, for instance, induce strong changes in the drug release profile as observed in the case of chloramphenicol palmitate, in which polymorph B yields a 6 times higher maximum human plasma concentration than polymorph A.<sup>21</sup> The crystallization time is another key parameter for successful application because longer production times result in more costly products. Faster crystallization rates may be facilitated by providing additional nucleation sites, such as by seeding, or by the presence of a surface in general.<sup>22</sup> Even a combination of epitaxial growth and enhanced crystallization rates was just recently demonstrated to be effective for a carbamazepine/iminostilbene mixture.<sup>23</sup>

Clotrimazole is commonly used in the treatment of fungal infections,<sup>24</sup> but potential application in malaria treatment<sup>25</sup> is also under research. In this study, clotrimazole is chosen as the model substance because amorphous films are easily accessible from simple solution processes such as spin coating or drop casting.<sup>26</sup> Such a system might readily be employed in different dosage forms, such as in patches for parenteral or sublingual application. Additionally, the usage of solution processes in the film preparation allows also for coprocessing clotrimazole with polymeric materials like polystyrene. This results in a solid state solution, exhibiting a strongly retarded drug release.<sup>27</sup> In general, amorphous clotrimazole films persist for several days on storage under ambient conditions. Enhanced crystallization rates result, for instance, from heat treatment or solvent vapor annealing, which lead to a variation in the crystallite morphology but leave the polymorphic form unaffected; extended spherulitic type growth, dendritic growth, or extended bar shape crystallites were observed.<sup>26</sup> In terms of practical application, such morphology alterations often result in different dissolution behavior.

Coatings of solid state drug formulations are commonly prepared by solution processes such as spray coating.<sup>28</sup> Such an approach works well for systems that do not change properties as they come into contact with solvents. However, because many drug formulations are designed to perform in aqueous environments (e. g., tablets), the application of solvents is usually limited. A solvent-free method that also allows the coating of such dosage forms is chemical vapor deposition (CVD). With this technique, polymers of defined chemical composition can be synthesized directly at, for instance, tablet surfaces. In principle, this method is applicable to any surface so that even liquid matter can be coated.<sup>29</sup> A recently developed variation of this process is initiated CVD (iCVD).<sup>30</sup> In this, primary radicals are created by thermal fragmentation of an initiator molecule (e. g., a peroxide with a labile O–O bond) at a heated filament.<sup>31</sup> The introduction of an initiator molecule lowers the energy required for radical generation so that polymerization can be performed even at low filament (usually in the range 150–300 °C) and substrate temperatures (usually below 60 °C). In turn, this promotes selective chemistry because the radicals react exclusively with the vinyl bonds of a monomer, creating an initiator-monomer radical, which itself is capable of reacting with another monomer unit. The process is propagated along chain growth until a radical site is terminated by either another initiator molecule or another active chain.<sup>32,33</sup> In recent years, this process enabled coatings with tailored properties, including thermal<sup>34</sup> or pH-responsiveness,<sup>35</sup> encapsulation,<sup>36</sup> and swellability,<sup>37</sup> among many more.

In this work, three different polymer compositions were deposited by iCVD on top of amorphous clotrimazole films to study how

the stability of the drug solid state is affected: poly(2-hydroxyethyl methacrylate) [p-HEMA], poly-(methacrylic acid) [p-MAA], and poly(perfluorodecyl acrylate) [p-PFDA]. Both p-HEMA and p-MAA are of interest in drug formulation because they bring distinct functionalities with them, possibly allowing for drug release only in a certain environment (e. g., acidic in the stomach). While p-MAA exhibits pH-responsiveness, p-HEMA forms a hydrogel. This means that the mesh size will increase in an aqueous environment, which should lead to enhanced drug dissolution behavior in turn. p-PFDA was chosen as a contrast to the other polymers. It exhibits crystallinity itself and is highly hydrophobic, which should, in turn, make it a perfect encapsulation, preventing any water uptake (hydrate formation can be a problem for many drugs). For practical application, also the biocompatibility of such materials has to be considered. While biocompatibility has been demonstrated for both p-HEMA<sup>38,39</sup> and p-MAA<sup>40</sup> in several cases, there is no data for the biocompatibility of p-PFDA in literature (to our knowledge). Anyway, thorough testing will be necessary for all the compounds before such a polymer system can be used in actual medication. These polymeric encapsulation layers confine the drug film, which is then unable to crystallize at the solid-air interface. As a consequence, the coating layer introduces another solid-solid boundary. By employing investigation techniques such as optical microscopy, X-ray diffraction, or *ex situ* and *in situ* thermal treatment, the impact of these coatings on the amorphous films is studied along with how the film stability and the eventual crystallization is affected.

## 8.4 Materials and Methods

Pharmaceutical grade clotrimazole (IUPAC name 1-[(2-chlorophenyl)-(diphenyl)methyl]-1H-imidazole) was purchased from Gatt-Koller GmbH (Austria) and used without further purification. For sample preparation, a clotrimazole-tetrahydrofuran solution (Aldrich, Germany) of 60 mg/g (0.15 mol/L) was prepared. As substrates, conventional glass slides (Carl Roth GmbH+Co.KG, Germany) of 2.5 cm<sup>2</sup> × 2.5 cm<sup>2</sup> size were sonicated in an acetone bath for 15 min, subsequently rinsed with 2-propanol and finally dried under a nitrogen stream. For sample preparation, 100 μL of the solution was drop cast onto the substrates, leveled precisely horizontally. Additionally, the samples were covered by a Petri dish, allowing for a slower and more controlled solvent evaporation, which resulted in reproducible, high quality films.

Polymer coatings of 22-hydroxyethyl methacrylate (HEMA, 97 %, Aldrich, Germany), 1H,1H,2H,2H-perfluorodecyl acrylate (PFDA, 97 %, Aldrich, Germany), and methacrylic acid (MAA, 99 %, Aldrich, Germany) (Figure 8.1) were deposited in a custom-built iCVD cham-

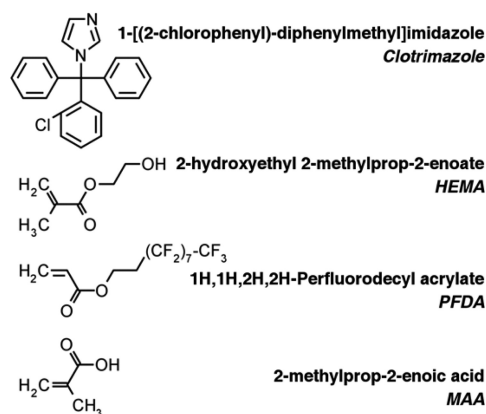


Figure 8.1: Structural formulas of clotrimazole and the monomers used in the iCVD process, together with the corresponding names.

ber, using tert-butyl peroxide (TBPO, 98 %, Aldrich, Germany) as initiator. The individual polymers are denoted as p-HEMA, p-MAA, and p-PFDA from here on. (A more detailed description is provided in the Supporting Information 8.11.) Additionally, ethylene glycol dimethacrylate (EGDMA, 98 %, Aldrich, Germany) was employed as cross-linking agent for p-MAA and p-HEMA. For all samples, the same coating thickness of 200 nm was deposited.

The crystalline sample properties were investigated with a PANalytical Empyrean X-ray diffractometer, equipped with a copper sealed tube (wavelength  $\lambda = 0.154$  nm), a Göbbel mirror, various slits, and a PIXcel<sup>3D</sup> solid state detector. The angular scans ( $\theta/2\theta$ ) are represented in the scattering vector ( $q_z$ ) notation, whereby  $q_z = 4\pi \cdot \sin(\theta)/\lambda$ . Such a representation allows for a direct comparison of measurements taken at other wavelengths. The index  $z$  denotes that only net-planes parallel to the substrate surface are evaluated in these particular measurements (“specular scans”). The diffuse scattering from the amorphous glass substrate is subtracted prior plotting.

To study the effect of temperature on the crystallization behavior, samples were subject to *ex situ* and *in situ* heating. *Ex situ* isothermal annealing was performed in standard ovens at 50 and 70 °C/min, respectively, under ambient atmosphere. *In situ* temperature-dependent X-ray diffraction measurements were performed using a DHS900 heating stage (Anton-Paar, Austria). Individual samples were heated to 170 °C, using a heating rate of 3 °C/min.

Optical images were taken on an AxioVert polarization microscope (Zeiss, Germany) with a high resolution camera. For some samples, the topographic information was recorded by a FlexAFM (Nanosurf, Switzerland) equipped with an EasyScan 2 controller. All measurements were taken in noncontact mode using Tap300 cantilevers (Bud-

getSensors, Bulgaria). The data were processed and depicted using the software package Gwyddion.<sup>41</sup>

## 8.5 Results

**Pristine Clotrimazole Films.** Clotrimazole solutions were drop cast onto glass substrates, forming homogeneous liquid layers. Upon solvent evaporation, a solid film of several micrometers height is established in about 5 min. Such films are initially completely transparent (thus, optical data are omitted), indicating that the amorphous state is present. The X-ray diffraction exhibits, indeed, no Bragg peaks but two broad humps around  $q_z \approx 8$  and  $15 \text{ nm}^{-1}$  (see Figure 8.2), indicative for low order within this film.

On ambient storage, the diffraction pattern changes significantly within 4 h. Multiple peaks have emerged, with the most prominent being located between  $q_z = 6$  and  $7 \text{ nm}^{-1}$ . This means that the clotrimazole film has (at least partially) crystallized. A comparison with theoretical powder spectra data shows agreement with the triclinic form of clotrimazole, with lattice parameters  $a = 8.76 \text{ \AA}$ ,  $b = 10.55 \text{ \AA}$ ,  $c = 10.61 \text{ \AA}$ ,  $\alpha = 114.1^\circ$ ,  $\beta = 96.96^\circ$ , and  $\gamma = 97.54^\circ$ .<sup>42</sup> Because the peak intensities do not follow those of an ideal powder, a slight texture (i. e., favorable contact planes parallel to the surface) is present. Additional peaks are noted at  $q_z = 8.25, 10.04, 14.30, 15.40,$  and  $18.34 \text{ nm}^{-1}$ , which are unexplained by the triclinic form. Because there are still two amorphous humps in the pattern, full crystallization was not achieved within the 48 h storage at ambient conditions.

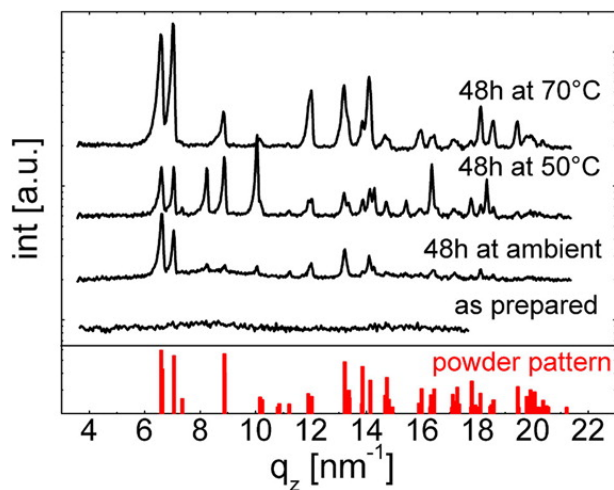


Figure 8.2: X-ray diffraction scans of an as-prepared clotrimazole film and films stored at different temperatures. The red bars indicate positions and the intensities of an ideal powder.

The coexistence of both crystalline and amorphous clotrimazole is also apparent in the optical micrograph (see Figure 8.3a). Several densely packed spherulites correspond to crystals. Within these spherulites, the color varies, likely the result of deviating thicknesses or differences in the crystal contact planes. Remaining portions of the "as-prepared" film are found. While this confirms amorphous fraction, the amount was small. Eventually, another 12-24 h storage would transfer such a partially crystalline film into a solely crystalline one.

Full crystallization results within 48 h when a film is stored at a higher temperature (50 °C). The micrograph exhibits exclusively crystalline regions with two distinct morphologies (see Figure 8.3b): first bold, colorful structures branching from common centers and second, pale looking structures with random distribution. Transparent (amorphous) film portions are absent, meaning that likely all material was crystalline. In the limit of the experiment, this agrees with the X-ray scan, in which amorphous humps are absent (see Figure 8.2). The Bragg peak positions remained the same, although a variation in the relative intensities is noted. Peaks characteristic for the triclinic polymorph exhibit here a powder-like intensity distribution, that is, a common contact plane with the substrate is missing. But also the peaks of the unknown phase are more intense, suggesting that more crystals exist in this phase.

Sample treatment at 70 °C for 48 h resulted mainly in pale spherulitic structures (see Figure 8.3c). The absence of colorful features in the optical micrograph suggests similar thicknesses for these structures. Like the previous samples, the diffraction pattern displays peaks typical for the triclinic form, while peaks of the unknown phase have disappeared. Amorphous humps are also absent in this pattern; thus (in the limit of the experiment) full crystallization results for samples stored at 70 °C within 48 h.

**iCVD Coatings on Amorphous Films.** Amorphous clotrimazole films supported on glass substrates were coated with p-HEMA, p-MAA, or p-PFDA layers. After the iCVD deposition, the encapsulated clotrimazole remained in the amorphous state for all the samples. These samples were stored either at ambient, 50 °C, or 70 °C, for 48 h each. Then optical micrographs (Figure 8.4) and X-ray diffraction patterns (Figure 8.5) were collected. For a p-HEMA coating, two dominant features are noted. First, a strong surface wrinkling is evident. Visual inspection during the iCVD process shows that films turn opaque already within short deposition times, that is, at thin coating layer thicknesses. This means that surface wrinkling develops at early deposition stages, whereby the increase in roughness (wrinkles) causes the opaque appearance. The second interesting aspect is that for 48 h storage, the majority of the clotrimazole film remained amorphous, which appears *greyish* in the image. Only some crystals

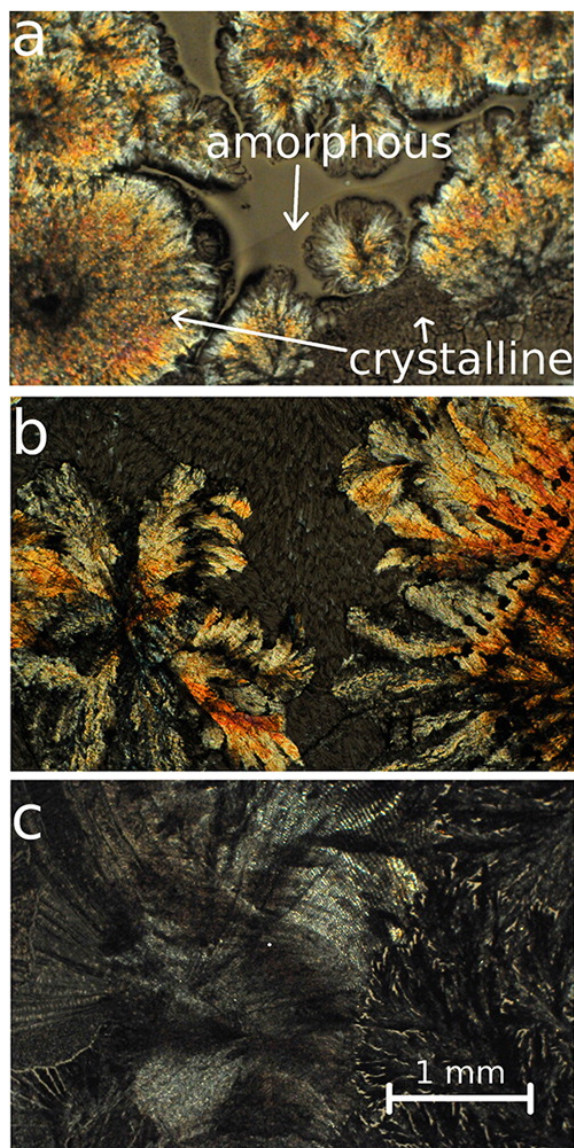


Figure 8.3: Optical micrographs of pristine clotrimazole films 48 h after preparation, stored at ambient temperature (a), 50 °C (b), or 70 °C (c). Arrows indicate crystalline regions as well as amorphous fractions of clotrimazole.

were present (bright areas in the image). Please note that this image does not reflect the statistic nature of the entire sample, that is, the crystalline fraction is overrepresented in this image compared with the entire sample. This agrees with the corresponding diffraction scan, which displays two amorphous humps but not Bragg peaks. Because X-ray scans generally contain integral information on a sample (and thus are a good statistical estimate), the total number of clotrimazole crystals in the sample is likely very small.



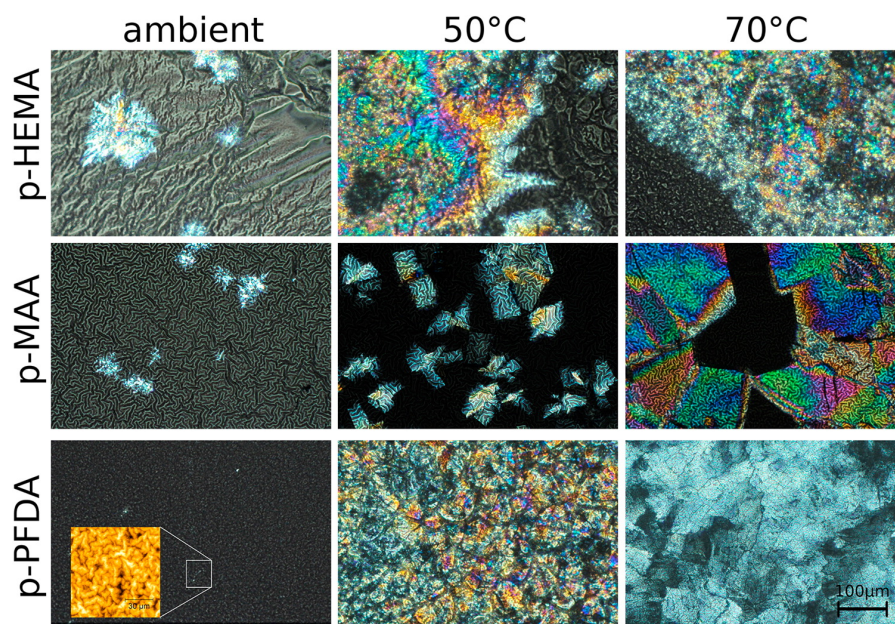


Figure 8.4: Various clotrimazole-iCVD samples stored for 48 h at different temperatures. The inset of the p-PFDA sample displays an AFM height image of the surface.

Using storage temperatures of 50 or 70 °C, the crystalline fractions enlarged (Figure 8.4, top row). These crystals show more defined shapes (note that the apparent “fuzzy” surface of the crystalline regions is in fact the wrinkled polymeric top layer). The crystalline regions appear similar in shape for both samples but the number of crystals is lower when stored at 50 °C. This agrees with the X-ray results (Figure 8.5), which show diffraction from triclinic clotrimazole as well as scattering from amorphous fractions. Two dominant peaks are noted for both samples, located at  $q_z = 6.5 \text{ nm}^{-1}$  and  $13 \text{ nm}^{-1}$ , meaning that these samples are textured. A closer inspection shows that each peak is in fact a convolution of two separate peaks (see Supporting Information 8.11), which correspond to distinct crystallographic planes, that is, the crystals contact the substrate/polymer coating preferentially along the (001) and (010) planes. On account of the low crystallinity, other peaks are absent in the 50 °C.

Samples with a p-MAA coating show a similar qualitative behavior, although differing quantitatively. The different morphologies of the samples after storage at different temperatures for 48 h appear in the optical images (Figure 8.4, middle row). The p-MAA coating exhibits surface wrinkling (with shorter periodicity in the wrinkles compared with the p-HEMA layer), as most evident for the sample stored at ambient. The underlying clotrimazole film remained largely in an amorphous state (*greyish* area), with only some crystals being present (brighter areas in the micrograph). Accordingly, the X-ray scan (Fig-



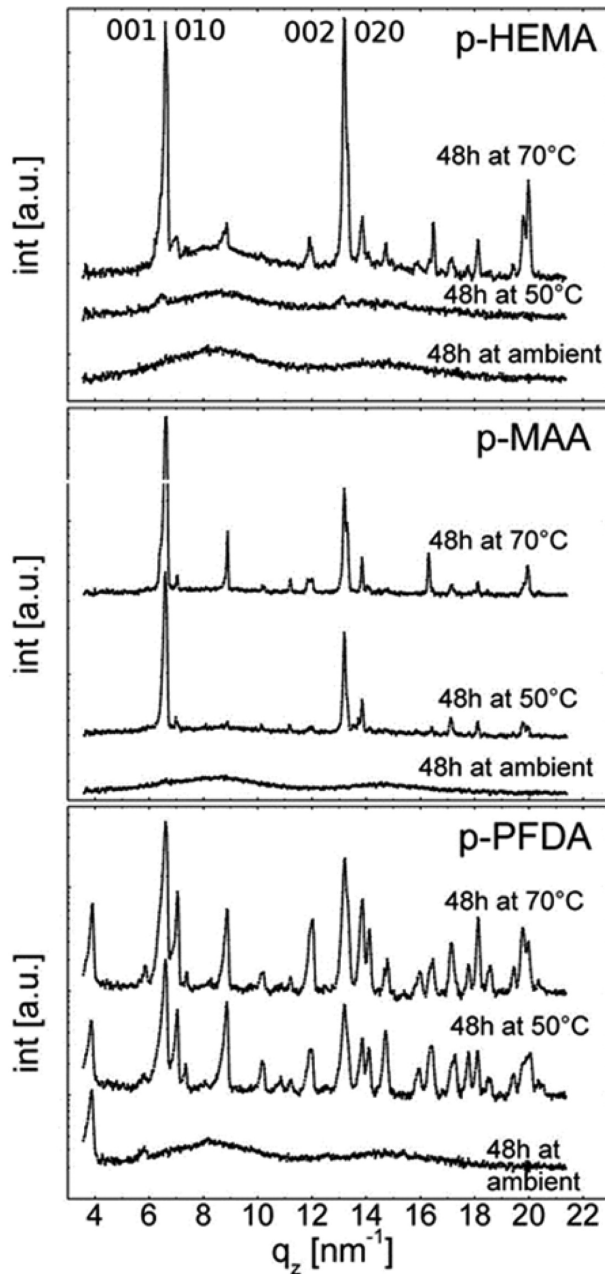


Figure 8.5: X-ray diffraction scans of clotrimazole encapsulated with different polymers after storage at different conditions. Images share a common abscissa for sake of comparability.

ure 8.5) shows solely diffraction from amorphous clotrimazole, meaning that the amount of crystals is small.

Upon 50 °C storage, a larger fraction of clotrimazole crystallized, with the shape of the individual crystals being plate-like. The strong double peak in the X-ray diffraction pattern at  $q_z = 6.5 \text{ nm}^{-1}$  (and higher order reflections), corresponding to the [001] and [010] orientation, means that two preferred contact planes exist between clotri-

mazole and the p-MAA coating. Optical and diffraction data show that only a small fraction remained amorphous. For storage temperatures of 70 °C, the situation remains similar, only the number and size of crystals being larger.

The clotrimazole crystallization changes drastically when encapsulated by p-PFDA. After deposition, the samples retain their transparent appearance (see Figure 4, bottom left). An AFM image (inset in Figure 8.4, bottom left) shows a sample surface after being stored for 48 h at ambient, which clearly hosts wrinkles. However, compared with the other samples, the wrinkles are of much smaller lengths and heights. This sample also lacks crystalline clotrimazole, demonstrating the capability of p-PFDA coating of preventing (or at least retarding) clotrimazole crystallization under ambient conditions. The X-ray diffraction pattern in Figure 8.5 features two peaks and two broad humps. The sharp peaks located at  $q_z = 3.86$  and  $5.79 \text{ nm}^{-1}$  are higher order reflections of the lamellar packing with the fluorine groups of the p-PFDA ( $d$ -spacing  $\approx 3.25 \text{ nm}$ ) exhibiting parallel stacking onto the sample.<sup>43</sup> The two broad humps are solely attributed to amorphous clotrimazole.

Upon storage at higher temperatures (50 or 70 °C), the amorphous clotrimazole transfers into the crystal state. The optical data shows the formation of extended plate-like crystallites similar to the p-MAA sample. The X-ray pattern, however, reveals the absence of a defined clotrimazole contact plane when coated with p-PFDA. The diffraction pattern resembles more that of an ideal powder, in which any order in respect to the substrate surface is completely absent.

**In Situ Heating of Amorphous Films.** To follow the structural evolution on temperature change, clotrimazole layers with and without polymeric encapsulation were investigated using *in situ* X-ray diffraction experiments. The evolution of the diffraction patterns as a function of temperature is summarized in Figure 8.6 for the various samples. For a bare clotrimazole layer, that is, without coating, the diffraction data contains initially information from the amorphous film. A moderate elevation of the temperature had no impact. Reaching 108 °C, crystallization was initiated and the (001)/(010) double peak started to evolve at  $q_z = 6.57 \text{ nm}^{-1}$ . The peak intensity increased steadily up to 148 °C, meaning that the amount of crystals is likewise increasing. Though hardly visible, also other peaks emerged, for example, at  $q_z = 7.0 \text{ nm}^{-1}$ , meaning also crystals with other contact planes start to grow, similar to the behavior observed in isothermal heat treatments. Exceeding 150 °C, the intensities decreased on account of clotrimazole melting. It is noteworthy that the amorphous state prevails on rapid cooling ( $>50 \text{ °C/min}$ ), so that crystallization experiments can eventually be repeated.

Samples hosting polymer coatings of p-HEMA or p-MAA showed different temperature responses. Over the course of the experiments,

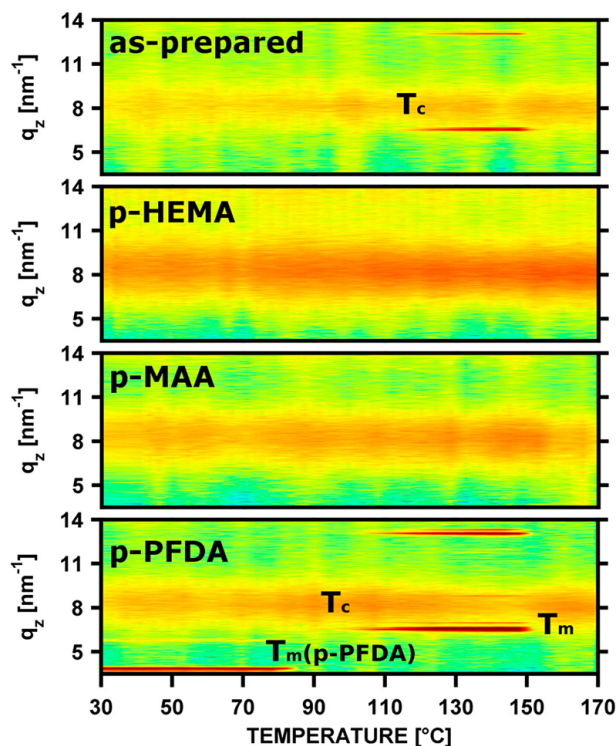


Figure 8.6: *In situ* X-ray diffraction scans of amorphous clotrimazole films, encapsulated by iCVD layers, at different temperatures.  $T_c$  and  $T_m$  denote the onset of clotrimazole crystallization and melting, respectively.  $T_{m(p\text{-PFDA})}$  denotes melting of the p-PFDA lamella.

sharp peaks, as present for the pristine clotrimazole, were absent and only the broad amorphous humps persisted. The polymeric coating thus fully suppresses clotrimazole crystallization for short temperature increases up to the melting point of crystalline clotrimazole, that is, 150 °C.

The initial pattern of the clotrimazole–p-PFDA sample contains two sharp peaks at  $q_z = 3.86$  and  $5.79 \text{ nm}^{-1}$ , characteristic of the p-FDA lamella order, as well as the amorphous clotrimazole hump. This pattern prevails unaffected until 80 °C, at which the two peaks disappeared. At this temperature p-PFDA melts. On a further temperature increase to 92 °C, the (001) double peak of clotrimazole at  $q_z = 6.57 \text{ nm}^{-1}$  emerges. This crystallization onset temperature is significant lower compared with the unprotected sample. On further heating, more material crystallized as evident by the higher peak intensity. Besides the strong (001) peak, there are also other peaks present, meaning that also crystallization in arbitrary directions took place and thus, a powder-like behavior resulted, with no (or only a slight) texture. At a temperature of 150 °C, the crystalline clotrimazole melts, which agrees with the uncoated sample.

## 8.6 Discussion

Clotrimazole consists of four rings joined together and is of rather asymmetric and bulky shape (Figure 8.1), which generally results in slower crystallization dynamics. Thin clotrimazole films require more than 48 h to transit from an amorphous into a crystalline state, at least when stored in ambient conditions and hosted on glass. In comparison, amorphous phenytoin thin films require only some minutes until the first crystals start forming.<sup>44</sup> Nevertheless, the clotrimazole crystallization rate increases as elevated storage temperatures are employed; high temperatures facilitate in general diffusion of molecules both on interfaces and in the bulk. Already at 50 °C, which is about 1/3 of the melting temperature, significantly more crystals develop. The better diffusion capabilities allow molecules to adapt faster to adjacent molecules, thus fostering nuclei formation or adsorption at crystalline sites. The optical microscopy shows spherulitic structures with growth from arbitrary directions (confirmed by X-ray experiments), that is, neither the organic-glass nor the solid-air interface can dictate selective growth from specific contact planes. The presence of spherulite centers mean common crystal initiation sites are present. These sites, however, are unable to grow into larger crystals. This is also likely caused by limited diffusion in the solid state, and thus diffusion limited growth mode of branching spherulitic arms is expected.

The amorphous clotrimazole state is robust and persists throughout the iCVD deposition. In addition, clotrimazole does not sublime under moderate vacuum conditions and the substrate temperature of 30 °C used. Similarly, other drugs like indomethacin or phenytoin can be encapsulated by this route, while other active pharmaceutical ingredients like caffeine, paracetamol, or ibuprofen are prone to sublimation. In general, the iCVD process performs well in a wide range of different temperatures and pressures, which might enable using these encapsulations also for such volatile materials.

The encapsulation of the amorphous drug exhibits surface wrinkling in the polymeric layer. The p-HEMA layer resulted in pronounced wrinkles of several micrometers extension. p-MAA produces less pronounced wrinkles, while wrinkles in p-PFDA coating are much smaller, which (compared with the other cases) seems negligible. Often, wrinkling is a result of two materials having different physicochemical properties. Especially differences in elastic moduli ( $E$ ) of a “substrate” (here the clotrimazole layer) and the coating explain wrinkling. Depending on the theory for calculation, the wrinkling amplitude ( $A$ ) might follow  $A \approx E_1/3$ .<sup>45</sup> From this, it is estimated that p-HEMA is the softest material while p-PFDA is the stiffest, with the  $E$  of p-MAA being between these two. This assumption is also in agreement with literature data on such films, reporting

an elastic modulus of 183 MPa for p-HEMA and one of 8.2 GPa for p-PFDA.<sup>46,47</sup> A test shows that such wrinkling is absent in coatings of crystalline clotrimazole layers (an example is shown in the Supporting Information 8.11). After heating such samples to the melting point of clotrimazole (150 °C), wrinkles formed again. Surprisingly, cooling or a subsequent crystallization did not change the morphology of surface wrinkles. This means that surface “relaxation” deformed the surface, but crystallization does not cause additional strain so that wrinkling remained unchanged. As will be shown elsewhere, the size of the wrinkling structures also correlates with the thickness of the clotrimazole layer between the substrate and the iCVD layers. For sake of faster dissolution, wrinkled surfaces might be favorable because the accessible surface areas are larger compared with a flat surface. Especially the usage of p-HEMA with its capability to swell in an aqueous environment might allow for very controlled release.

The deposition of coating layers on top of an amorphous clotrimazole film results in an alteration of the clotrimazole crystallization. While uncoated samples crystallize within 48 h, coated samples stored at ambient conditions remain amorphous significantly longer. p-PFDA coatings did not show any indication of clotrimazole crystallization and only a very small number of crystals formed under p-HEMA and p-MAA coatings. The reason for this behavior cannot unambiguously be identified. However, the exchange of the solid-air interface by another solid-solid interface (i. e., clotrimazole–iCVD coating) strongly hinders the molecular movement at this interface. This means that the probability of nuclei formation and thus also of crystal growth drastically reduces. The drug molecules remain longer in their respective spatial positions, and the amorphous state prevails.

At temperatures higher than ambient, the iCVD layers cannot fully suppress crystallization. Interestingly, the p-PFDA layer shows protection at ambient temperatures, but it is unable to prevent crystallization at 50 or 70 °C. Also a rapid heat increase causes the amorphous clotrimazole to crystallize. Because p-PFDA surfaces are strongly hydrophobic and oleophobic,<sup>48</sup> most substances prevent contact, meaning surface diffusion eases because solid-solid interface interaction strengths are small. Furthermore, the formation of various crystallographic orientations means that crystallization in arbitrary directions takes place, which agrees with the assumption of poor interactions. It can be concluded that p-PFDA coatings result in clotrimazole films behaving similar to an uncoated sample, with similar crystallization times and undirected growth.

In contrast, p-HEMA and p-MAA layers are more effective in suppressing crystallization, which, independent of the storage temperatures, provides large amounts of amorphous clotrimazole even after 48 h storage. Noteworthy, they prevent clotrimazole crystallization even through brief heat treatments up to the melting point

of crystalline clotrimazole. This is of high practical interest, since, for instance, sterilizing processes often need heat treatments, which puts amorphous drug formulations at risk of crystallization. The pH-responsiveness of p-MAA or the hydrogel properties of p-HEMA would possibly allow for an encapsulation design with an environment-sensitive or retarded release, respectively. Also the usage of these polymers as matrix material for drug loading is possible. For practical application, thin film administration routes (such as buccally or sublingually) seem to be the natural choice, given the sample design used in this study. But also whole tablets can be encapsulated by the iCVD technique, making this technique broadly applicable. Whether the polymer should be part of the final drug formulation has to be decided on a case to case basis, requiring additional testing of biocompatibility, permeability, and chemical and physical stability of the polymer. Eventually, slower heating ramps, that is, less than 3 °C/min, would allow induction of crystallization also in these samples in one heat run.

p-HEMA or p-MAA layers result in a more defined crystallization compared with the other samples. Clotrimazole crystals align prefer-

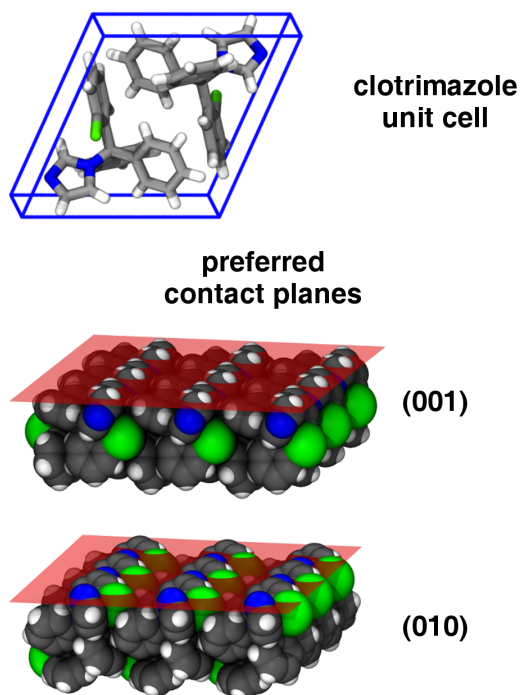


Figure 8.7: Molecular packing in the clotrimazole unit cell (top) and the two preferred molecular contact planes between clotrimazole crystals and the p-HEMA and p-MAA encapsulation layers (bottom); the structures are illustrated with the software package VMD.<sup>49</sup>

entially along two specific crystallographic planes with the polymer/substrate interface, as illustrated in Figure 8.7. In the (001) orientation, the contact at the solid–solid interface is mostly facilitated by the apolar C–H groups, with the polarizable chloric unit embedded within the bulk. Nevertheless, also some polar interactions with the –OH groups of the polymers might be present in this configuration, because the nitrogen in the imidazole ring (i. e., the hydrogen bond acceptor side) is in close proximity to the interface. The polar interaction becomes more dominant in the (010) assembly, since there the hydrogen bond acceptor sides (and the chloric unit) are directly exposed at the interface. The presence of the two preferred crystallographic orientations in clotrimazole means that the molecules near the polymer–drug interface need to adapt their conformation (rotation and translation) in order to adsorb or physisorb at this interface. Because this is time-consuming, nucleation or condensation at lattice sites is less likely to occur, extending therefore the lifespan of the amorphous phase. This agrees with the observation that elevated temperatures accelerate crystal growth within such films.

## 8.7 Conclusion

The solid state transition from amorphous to crystalline clotrimazole films can be strongly altered by modifying the drug-air interface through a polymer encapsulation. The use of a solvent-free process (i. e., iCVD) in the deposition of the polymer layer circumvents any risk of solvent-induced solid state transitions in the drug or dissolution. Three different iCVD encapsulating layers were investigated: p-PFDA, p-MAA, and p-HEMA. Each of these layers stabilized the drug in its amorphous state. At higher temperatures, the protection failed in the case of p-PFDA, while both the p-HEMA and the p-MAA encapsulations reduced the crystallization rate significantly. Furthermore, the chemical composition of the polymer layers also enables selective growth so that clotrimazole crystallites contact the polymer layers along the (001) and (010) planes, on account of both apolar interaction forces and hydrogen bonding. Suppressing crystallization upon a rapid temperature increase makes this encapsulation interesting for application relevant processes such as sterilization, where high temperatures are only briefly required. While this study is limited to only three different polymers, the general applicability of such an iCVD encapsulating layer to drug molecules motivates this approach for other polymeric compositions, which might then enable further tuning of the crystallization behavior.

## 8.8 Author Information

### Corresponding Author

\*E-mail: oliver.werzer@uni-graz.at.

### Notes

The authors declare no competing financial interest.

## 8.9 Acknowledgments

The work was funded by the Austrian Science Fund (FWF) [Grant P25541-N19]. The authors thank the NAWI Graz for support. Part of the research was supported by a Marie Curie International Incoming Fellowship (Project 626889) within the 7th European Community Framework Programme.

## 8.10 References

- (1) F. Kesisoglou, S. Panmai, and Y. Wu *Advanced Drug Delivery Reviews* **2007**, *59*, 631–644, DOI: 10.1016/j.addr.2007.05.003.
- (2) B. C. Hancock and M. Parks *Pharmaceutical Research* **2000**, *17*, 397–404, DOI: 10.1023/A:1007516718048.
- (3) L. Yu *Advanced Drug Delivery Reviews* **2001**, *48*, 27–42, DOI: 10.1016/S0169-409X(01)00098-9.
- (4) N. J. Babu and A. Nangia *Crystal Growth & Design* **2011**, *11*, 2662–2679, DOI: 10.1021/cg200492w.
- (5) A. M. Kaushal, P. Gupta, and A. K. Bansal *Critical Reviews in Therapeutic Drug Carrier Systems* **2004**, *21*, 133–193, DOI: 10.1615/CritRevTherDrugCarrierSyst.v21.i3.10.
- (6) H. Imaizumi, N. Nambu, and T. Nagai *Chemical & Pharmaceutical Bulletin* **1980**, *28*, 2565–2569, DOI: 10.1248/cpb.28.2565.
- (7) S. B. Murdande, M. J. Pikal, R. M. Shanker, and R. H. Bogner *Journal of Pharmaceutical Sciences* **2010**, *99*, 1254–1264, DOI: 10.1002/jps.21903.
- (8) D. Law, E. A. Schmitt, K. C. Marsh, E. A. Everitt, W. Wang, J. J. Fort, S. L. Krill, and Y. Qiu *Journal of Pharmaceutical Sciences* **2004**, *93*, 563–570, DOI: 10.1002/jps.10566.
- (9) B. C. Hancock and G. Zografi *Journal of Pharmaceutical Sciences* **1997**, *86*, 1–12, DOI: 10.1021/js9601896.
- (10) G. Van den Mooter *Drug Discovery Today: Technologies* **2012**, *9*, e79–e85, DOI: 10.1016/j.ddtec.2011.10.002.



- (11) M. Yoshioka, B. C. Hancock, and G. Zografi *Journal of Pharmaceutical Sciences* **1994**, *83*, 1700–1705, DOI: 10.1002/jps.2600831211.
- (12) L. S. Taylor and G. Zografi *Pharmaceutical Research* **1997**, *14*, 1691–1698, DOI: 10.1023/A:1012167410376.
- (13) V. B. Pokharkar, L. P. Mandpe, M. N. Padamwar, A. A. Ambike, K. R. Mahadik, and A. Paradkar *Powder Technology* **2006**, *167*, 20–25, DOI: 10.1016/j.powtec.2006.05.012.
- (14) H. M. A. Ehmman and O. Werzer *Crystal Growth & Design* **2014**, *14*, 3680–3684, DOI: 10.1021/cg500573e.
- (15) T. Kellner, H. M. A. Ehmman, S. Schrank, B. Kunert, A. Zimmer, E. Roblegg, and O. Werzer *Molecular Pharmaceutics* **2014**, *11*, 4084–4091, DOI: 10.1021/mp500264e.
- (16) M. Brinkmann *Journal of Polymer Science Part B: Polymer Physics* **2011**, *49*, 1218–1233, DOI: 10.1002/polb.22310.
- (17) T. Haber, S. Muellegger, A. Winkler, and R. Resel *Physical Review B* **2006**, *74*, 045419, DOI: 10.1103/PhysRevB.74.045419.
- (18) M. Oehzelt, L. Grill, S. Berkebile, G. Koller, F. P. Netzer, and M. G. Ramsey *ChemPhysChem* **2007**, *8*, 1707–1712, DOI: 10.1002/cphc.200700357.
- (19) C. Röthel, M. Radziown, R. Resel, A. Zimmer, C. Simbrunner, and O. Werzer *Crystal Growth & Design* **2015**, *15*, 4563–4570, DOI: 10.1021/acs.cgd.5b00833.
- (20) O. Werzer, B. Kunert, E. Roblegg, A. Zimmer, M. Oehzelt, and R. Resel *Crystal Growth & Design* **2013**, *13*, 1322–1328, DOI: 10.1021/cg301812m.
- (21) A. J. Aguiar, J. Krc, A. W. Kinkel, and J. C. Samyn *Journal of Pharmaceutical Sciences* **1967**, *56*, 847–853, DOI: 10.1002/jps.2600560712.
- (22) Y. Diao, A. S. Myerson, T. A. Hatton, and B. L. Trout *Langmuir* **2011**, *27*, 5324–5334, DOI: 10.1021/la104351k.
- (23) P. Christian, C. Röthel, M. Tazreiter, A. Zimmer, I. Salzmann, R. Resel, and O. Werzer *Crystal Growth & Design* **2016**, *16*, 2771–2778, DOI: 10.1021/acs.cgd.6b00090.
- (24) P. R. Sawyer, R. N. Brogden, K. M. Pinder, T. M. Speight, and G. S. Avery *Drugs* **1975**, *9*, 424–447, DOI: 10.2165/00003495-197509060-00003.
- (25) N. T. Huy, K. Kamei, Y. Kondo, S. Serada, K. Eanaori, R. Takano, K. Tajima, and S. Hara *Journal of Biochemistry* **2002**, *131*, 437–444.

- (26) H. M. A. Ehmman, A. Zimmer, E. Roblegg, and O. Werzer *Crystal Growth & Design* **2014**, *14*, 1386–1391, DOI: 10.1021/cg401859p.
- (27) H. M. A. Ehmman, S. Winter, T. Griesser, R. Keimel, S. Schrank, A. Zimmer, and O. Werzer *Pharmaceutical Research* **2014**, *31*, 2708–2715, DOI: 10.1007/s11095-014-1368-5.
- (28) M.-I. Ré *Drying Technology* **2006**, *24*, 433–446, DOI: 10.1080/07373930600611877.
- (29) L. C. Bradley and M. Gupta *Langmuir* **2012**, *28*, 10276–10280, DOI: 10.1021/la301170a.
- (30) A. M. Coclite, R. M. Howden, D. C. Borrelli, C. D. Petruczuk, R. Yang, J. L. Yagüe, A. Ugur, N. Chen, S. Lee, W. J. Jo, A. Liu, X. Wang, and K. K. Gleason *Advanced Materials* **2013**, *25*, 5392–5423, DOI: 10.1002/adma.201301878.
- (31) Y. Mao and K. K. Gleason *Langmuir* **2004**, *20*, 2484–2488, DOI: 10.1021/la0359427.
- (32) K. K. S. Lau and K. K. Gleason *Macromolecules* **2006**, *39*, 3695–3703, DOI: 10.1021/ma0601621.
- (33) K. K. S. Lau and K. K. Gleason *Macromolecules* **2006**, *39*, 3688–3694, DOI: 10.1021/ma0601619.
- (34) S. J. P. McInnes, E. J. Szili, S. A. Al-Bataineh, R. B. Vasani, J. Xu, M. E. Alf, K. K. Gleason, R. D. Short, and N. H. Voelcker *Langmuir* **2016**, *32*, 301–308, DOI: 10.1021/acs.langmuir.5b03794.
- (35) K. K. S. Lau and K. K. Gleason *Surface and Coatings Technology* **2007**, *201*, 9189–9194, DOI: 10.1016/j.surfcoat.2007.04.045.
- (36) K. K. S. Lau and K. K. Gleason *Advanced Materials* **2006**, *18*, 1972–1977, DOI: 10.1002/adma.200600896.
- (37) N. Marí-Buyé, S. O’Shaughnessy, C. Colominas, C. E. Semino, K. K. Gleason, and S. Borrós *Advanced Functional Materials* **2009**, *19*, 1276–1286, DOI: 10.1002/adfm.200801561.
- (38) R. K. Bose and K. K. S. Lau *Chemical Vapor Deposition* **2009**, *15*, 150–155, DOI: 10.1002/cvde.200806748.
- (39) G.-H. Hsiue, J.-A. Guu, and C.-C. Cheng *Biomaterials* **2001**, *22*, 1763–1769, DOI: 10.1016/S0142-9612(00)00336-7.
- (40) S. K. Bajpai and S. Singh *Reactive and Functional Polymers* **2006**, *66*, 431–440, DOI: 10.1016/j.reactfunctpolym.2005.09.003.
- (41) D. Nečas and P. Klapetek *Central European Journal of Physics* **2011**, *10*, 181–188, DOI: 10.2478/s11534-011-0096-2.

- (42) H. Song and H.-S. Shin *Acta Crystallographica Section C Crystal Structure Communications* **1998**, *54*, 1675–1677, DOI: 10.1107/S0108270198006386.
- (43) A. M. Coclite, Y. Shi, and K. K. Gleason *Advanced Functional Materials* **2012**, *22*, 2167–2176, DOI: 10.1002/adfm.201103035.
- (44) H. M. A. Ehmman, T. Kellner, and O. Werzer *CrystEngComm* **2014**, *16*, 4950–4954, DOI: 10.1039/C4CE00424H.
- (45) N. Bowden, S. Brittain, A. G. Evans, J. W. Hutchinson, and G. M. Whitesides *Nature* **1998**, *393*, 146–149, DOI: 10.1038/30193.
- (46) J. Yin, J. L. Yagüe, D. Eggenpieler, K. K. Gleason, and M. C. Boyce *Advanced Materials* **2012**, *24*, 5441–5446, DOI: 10.1002/adma.201201937.
- (47) H. Sojoudi, G. H. McKinley, and K. K. Gleason *Materials Horizons* **2014**, *2*, 91–99, DOI: 10.1039/C4MH00162A.
- (48) A. M. Coclite, Y. Shi, and K. K. Gleason *Advanced Materials* **2012**, *24*, 4534–4539, DOI: 10.1002/adma.201200682.
- (49) W. Humphrey, A. Dalke, and K. Schulten *Journal of Molecular Graphics* **1996**, *14*, 33–38, DOI: 10.1016/0263-7855(96)00018-5.

## 8.11 Supporting Information

### iCVD setup

Polymerization by initiated chemical vapor deposition (iCVD) is performed in custom-made vacuum reactor. The cylindrical chamber (height 5.5 cm, diameter 36 cm) is pumped by a Duo 5M rotary vane pump (Pfeiffer Vacuum, Germany) and the process pressure is regulated by a throttle valve (MKS Instruments, USA). A removable quartz glass lid allows for *in situ* thickness control via laser interferometry (He-Ne laser with  $\lambda = 633$  nm, Thorlabs, USA). The chamber houses a resistively heated filament array of 12 parallel nickel-chromium wires (Goodfellow, UK), which are mounted 2.5 cm above the reactor floor. The substrate temperature is regulated by an Accel 500 LC heater/chiller (Thermo Fisher Scientific, USA) to  $\pm 2$  °C, as monitored by type K thermocouples (Omega Engineering, USA). The monomers are stored in glass jars at constant temperatures (PFDA and EGDMA at 80 °C, HEMA at 75 °C and MAA at 70 °C) and can be flown into the reactor through a heated mixing line (held at 90 °C). Both initiator and nitrogen enter separately the chamber at ambient temperature. The individual flow rates were manually set by needle valves (Swagelok, USA) or mass flow controllers (MKS Instruments, USA). The individual process parameters used in this work are stated in Table S8.1.

Table S8.1: Deposition parameters for the individual polymer coatings. The flow rates of the monomers ( $F_{\text{mono}}$ ), crosslinker ( $F_{\text{EGDMA}}$ ), the initiator ( $F_{\text{TBPO}}$ ) and nitrogen ( $F_{\text{N}_2}$ ) are summarized together with the filament ( $T_{\text{fil}}$ ) and substrate ( $T_{\text{sub}}$ ) temperatures. During deposition, the pressure ( $p$ ) was constant.

	p-HEMA	p-MAA	p-PFDA
$F_{\text{mono}}$ [sccm]	$0.75 \pm 0.05$	$0.80 \pm 0.05$	$0.15 \pm 0.03$
$F_{\text{EGDMA}}$ [sccm]	$0.03 \pm 0.05$	$0.03 \pm 0.01$	–
$F_{\text{TBPO}}$ [sccm]	$0.80 \pm 0.05$	$0.80 \pm 0.05$	$0.80 \pm 0.05$
$F_{\text{N}_2}$ [sccm]	$3.0 \pm 0.1$	$3.0 \pm 0.1$	$6.0 \pm 0.1$
$T_{\text{fil}}$ [°C]	$310 \pm 10$	$240 \pm 10$	$240 \pm 10$
$T_{\text{sub}}$ [°C]	$30 \pm 2$	$25 \pm 2$	$30 \pm 2$
$p$ [mTorr]	$350 \pm 10$	$500 \pm 10$	$800 \pm 10$

### Clotrimazole double peak

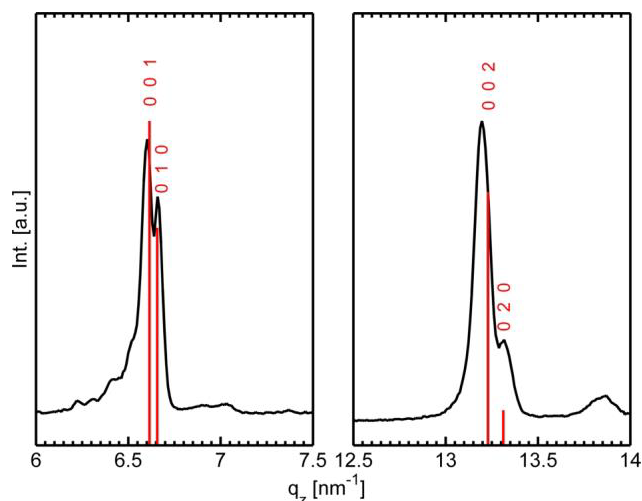


Figure S8.8: Image section of the X-ray diffraction pattern of clotrimazole, encapsulated by p-HEMA, after 24 h storage at 70 °C. The red bars indicate the positions and the intensities of the (001), (010) and higher order reflections of an ideal clotrimazole powder.

### Crystalline clotrimazole layers

For the identification of the wrinkling effect, a crystalline sample of clotrimazole was prepared. On this crystalline sample, a 200 nm p-HEMA layer was deposited (Figure S8.9, left) which results in a surface structure that is dominated by the underlying clotrimazole crystals. On heating to 160 °C, slightly above the melting temperature of clotrimazole ( $T_m = 150$  °C), all crystals disappeared but the formation of wrinkles is clearly visible (Figure S8.9, middle). After storing this sample at 70 °C for 48 h, crystallization is again observed, but different to the initial film, surface wrinkling prevails.

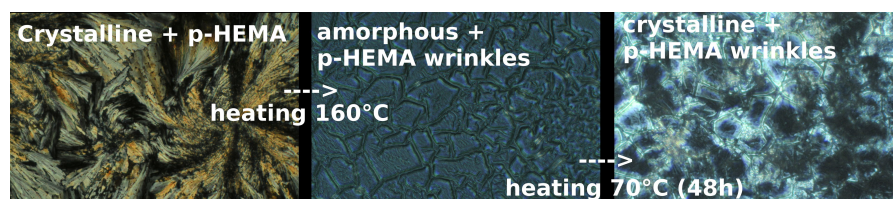


Figure S8.9: Crystalline clotrimazole coated with a p-HEMA layer (left), the same sample heated above 160 °C and rapidly cooled to room temperature (middle) and the sample stored at 70 °C for another 48 h.



# Wrinkle Formation in a Polymeric Drug Coating Deposited via initiated Chemical Vapor Deposition

Soft Matter



PAPER

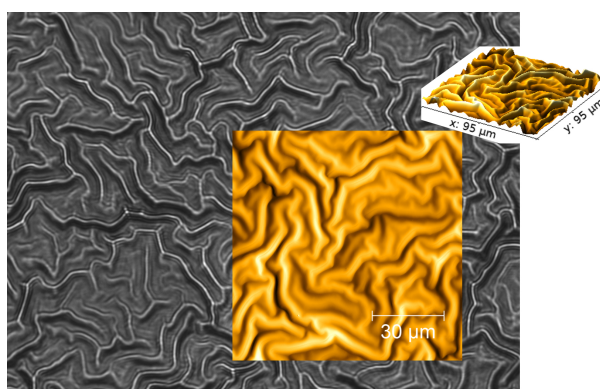
[View Article Online](#)  
[View Journal](#) | [View Issue](#)



Cite this: *Soft Matter*, 2016, 12, 9501

Wrinkle formation in a polymeric drug coating deposited via initiated chemical vapor deposition†

Paul Christian,<sup>a</sup> Heike M. A. Ehmman,<sup>bc</sup> Oliver Werzer<sup>bc</sup> and Anna Maria Coclite<sup>\*bc</sup>



## 9.1 Preface

This work was conducted in close collaboration with Oliver Werzer from the University of Graz, who provided the clotrimazole samples. The author of this thesis performed the polymer synthesis by the iCVD method, evaluated the experimental data and wrote the manuscript with assistance of Oliver Werzer. Heike M.A. Ehmman provided atomic force micrographs of the samples. Anna Maria Coclite and Oliver Werzer supervised the project. The following text and its illustrations are identical to the published work<sup>1</sup> and are reproduced with permission.

- (1) P. Christian, H. M. A. Ehmman, O. Werzer, and A. M. Coclite *Soft Matter* **2016**, 12, 9501–9508, DOI: 10.1039/C6SM01919F.

## 9.2 Abstract

Polymer encapsulation of drugs is conventionally used as a strategy for controlled delivery and enhanced stability. In this work, a novel encapsulation approach is demonstrated, in which the organic molecule clotrimazole is enclosed into wrinkles of defined sizes. Having defined wrinkles at the drug/encapsulant interface, the contact between the encapsulating polymer and the drug can be improved. In addition, this can also allow for some control on the drug delivery as the available surface area changes with the wrinkle size. For this purpose, thin films of clotrimazole were deposited onto silica substrates and were then encapsulated by crosslinked poly(2-hydroxyethyl methacrylate) (pHEMA) via initiated chemical vapor deposition (iCVD). The thickness and the solid state (crystalline or amorphous) of the clotrimazole layer were varied so that the conditions under which surface wrinkles emerge can be determined. A (critical) clotrimazole thickness of 76.6 nm was found necessary to induce wrinkles, whereby the wrinkle size is directly proportional to the thickness of the amorphous clotrimazole. When the pHEMA was deposited on top of crystalline clotrimazole instead, wrinkling was absent. The wrinkling effect can be understood in terms of elastic mismatch between the relatively rigid pHEMA film and the drug layer. In the case of amorphous clotrimazole, the relatively soft drug layer causes a large mismatch resulting in a sufficient driving force for wrinkle formation. Instead, the increased elastic modulus of crystalline clotrimazole reduces the elastic mismatch between drug and polymer, so that wrinkles do not form.

## 9.3 Introduction

Encapsulating drugs with synthetic polymers has several important roles: it creates a diffusion membrane around medications for release in adjustable time-scales;<sup>1,2</sup> it protects the drug during the administration (e. g. from acidic environment in the oral route); it enhances the drug stability on storage. This is generally achieved by biocompatible polymer/drug composite layers or by dispersing the drug itself within a soluble or insoluble polymer matrix, thus forming a solid-state dispersion or solution.<sup>3,4</sup>

The recently developed initiated chemical vapor deposition (iCVD) allows the preparation of thin polymer coatings on nearly any surface, including delicate substrates such as liquid layers,<sup>5</sup> paper,<sup>6</sup> organic films<sup>7</sup> or drug molecular layers.<sup>8</sup> iCVD polymerization works in a wide range of environmental conditions, among the mild vacuum and low substrate temperatures, allowing even the direct deposition onto delicate drug formulations which are easily altered by solution-based polymer coating processes.<sup>9</sup> The iCVD process follows the mechanisms of conventional radical polymerization,<sup>10,11</sup> Radicals are cre-

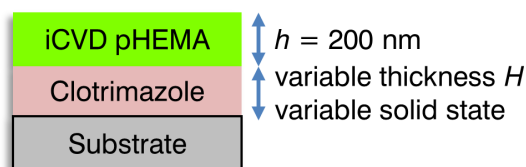


ated in the vapor phase upon thermal decomposition of an initiator molecule, often a peroxide, by selectively breaking the labile oxygen-oxygen bond at temperatures in the range 250-350 °C. The monomer remains unaffected by these temperatures and gets adsorbed on a substrate held at moderate temperatures (ambient to 60 °C). There, radicals can react with the vinyl bonds of the monomer molecules from the vapor phase, resulting in the formation of heavier initiator-monomer fragments. Subsequently, growth proceeds by attaching additional monomer units to the chain until it is terminated by another radical or unsaturated chain.<sup>12</sup> Further details on this iCVD polymerization mechanism can be found in recent reviews.<sup>9,13</sup>

It has been demonstrated that engineered three-dimensional wrinkles bind the coating intimately to its substrate.<sup>14</sup> When a solid thin film is deposited onto a liquid and forms wrinkles, the liquid seeks to keep the solid-liquid contact by flowing into the wrinkles.<sup>15</sup> In the current study, the encapsulation of a drug molecular layer into a wrinkled, hydrogel-forming layer is investigated. This approach can be applicable for morphology-controlled drug-release, as well as for other practical purposes, including tunability of adhesion,<sup>16,17</sup> wettability<sup>18,19</sup> for microfluidics<sup>20</sup> or optical coatings (anti-reflection layers). In particular, keeping the surface chemistry unchanged while varying the morphology in a controlled manner can be beneficial for studies of properties like wettability or crystal growth as a function of the interface morphology. Among three-dimensional surface morphologies, wrinkled surfaces have recently attracted a great deal of attention. Since Bowden's experiments in 1998,<sup>21</sup> many groups have investigated different routes to prepare defined surface wrinkles, both from the experimental and the theoretical point of view. Most often, wrinkles on a surface are obtained when a compressive stress is generated between a coating layer and a substrate due to the expansion mismatch of the two materials.<sup>22</sup>

Ordered wrinkling has already been demonstrated by the deposition of a cross-linked poly(2-hydroxyethyl methacrylate) (pHEMA) layer onto PDMS substrates by iCVD.<sup>23</sup> This resulted in the formation of two-dimensional herringbone patterns by the sequential release of the biaxially stretched PDMS. In this current work, another approach is demonstrated to fabricate wrinkles of various sizes. For this, clotrimazole was encapsulated by crosslinked pHEMA via iCVD. Clotrimazole is commonly used in the treatment of fungal disease,<sup>24</sup> but is also evaluated for therapies of malaria.<sup>25</sup> In this study, clotrimazole is used as a model substance as it is stable under mild vacuum conditions (required in our iCVD process) and remains amorphous at a solid substrate for a prolonged period prior and after fabrications, in contrast to other molecules which rapidly transit to a more stable crystalline form.<sup>26</sup> Furthermore, its excellent solubility in organic solvents allows simple but defined film preparation by spin coating. Various films of

different thicknesses were prepared, functioning effectively as a spacing layer between the iCVD pHEMA coatings and the rigid silicon substrate, as depicted in Scheme 9.1. The pHEMA polymer belongs to the category of hydrogels, as it shows a fast response to wet environments. The presence of absorbed water in the polymer network induces a reversible change in thickness from unswollen to the swollen state and vice versa. Encapsulating clotrimazole in a pHEMA hydrogel presumably enables the polymer coating to act as diffusion barrier in the dry, unswollen state while allowing for a drug delivery when swollen. For this, also the biocompatibility of pHEMA, which was demonstrated already in several cases, plays an important role.<sup>27,28</sup> In this work, the impact of the drug layer thickness and of its solid state (i. e. crystalline vs. amorphous) on the wrinkling process was studied. Many studies on wrinkles are based on depositing a hard skin layer on soft substrate and varying the thickness of the skin layer.<sup>29–31</sup> When the skin layer is thick enough, wrinkles form as a result of the elastic mismatch between the rigid film and the soft substrate.<sup>32</sup> In this work, a different approach was chosen: the thickness and the solid state of the clotrimazole layer were varied in order to control wrinkle formation (Scheme 9.1).



Scheme 9.1: Schematic of the sample structure, indicating the variables (thickness and solid state of the clotrimazole layer) whose impact on the wrinkling process is evaluated.

#### 9.4 Materials and methods

Pharmaceutical grade clotrimazole was purchased from Gatt-Koller GmbH (Austria) and used without further treatment. Tetrahydrofuran (THF) of spectrophotometric grade was purchased from Sigma-Aldrich (Germany). Solutions of clotrimazole in THF were prepared in various solute concentrations, ranging from  $1.7 \text{ mg g}^{-1}$  to  $66.6 \text{ mg g}^{-1}$ , and stirred prior usage. Silicon wafers with defined thermally grown oxide of 150 nm (Siegert Wafers, Germany) were used as substrates. Prior usage, the substrates were cleaned by ten minutes sonication each in acetone and ethanol solution, respectively, rinsed with MilliQ water and finally dried under a nitrogen stream.

Defined clotrimazole layers were prepared by spin coating from the different concentrations using a standard spin coating device (Ingenieurbüro Reinmuth, Germany). The spin time was set to 30 seconds at

a rotation speed of 25 rounds per second. The clotrimazole layer thicknesses were determined by variable angle spectroscopic ellipsometry using a M-2000 ellipsometer (J. A. Woollam, USA). For the layer thickness extraction, the data was modeled as a system consisting of three-layers including bulk silicon, silicon oxide (150 nm) and clotrimazole, using the CompleteEASE software. The optical constants of the silicon crystal and the surface oxide were taken from literature,<sup>33</sup> while the refractive index of the clotrimazole layer were modeled by a Cauchy function.

iCVD layers were deposited using a custom build setup. The samples were housed in a cylindrical vacuum chamber equipped with a throttle valve, controlling the operating pressure to 350 mTorr. The substrate temperature was kept at  $(30 \pm 3)^\circ\text{C}$  by a chiller/heater system (Thermo Scientific Accel 500 LC). The thermal decomposition of the initiator was induced by a filament array of nickel-chromium wires (Goodfellow, UK), heated to  $(320 \pm 5)^\circ\text{C}$ . The hydrophilic monomer 2-hydroxyethyl methacrylate (HEMA, 97%, Aldrich, Germany), the crosslinking agent ethylene glycol dimethacrylate (EGDMA, 98%, Aldrich, Germany) and the initiator tert-butyl peroxide (TBPO, 98%, Aldrich, Germany) were used without further treatment. The two monomers were kept at 75 and 80 °C, respectively, and flown into the reactor through a heated mixing line. The flow rates were adjusted via needle valves. The initiator was kept at ambient temperature and was introduced separately into the chamber. The various samples were coated at constant flow rates: TPBO ( $0.80 \pm 0.02$ ) sccm, HEMA ( $0.75 \pm 0.05$ ) sccm, EGDMA ( $0.04 \pm 0.01$ ) sccm and N<sub>2</sub> ( $3.0 \pm 0.1$ ) sccm. The N<sub>2</sub> was used as patch flow. A nominal layer thickness of 200 nm was deposited on all the samples, monitored *in situ* by laser interferometry (He-Ne Laser with  $\lambda = 633$  nm, Thorlabs, USA). Simultaneous to the deposition of clotrimazole layers, also pristine silicon substrates were coated with cross-linked pHEMA to allow for an easier characterization of the polymer properties.

The chemical composition and structure of the pHEMA layer were evaluated by Fourier transform infrared (FT-IR) spectroscopy (Bruker IFS 66 v/S) in transmission. The atomic composition of the compound (clotrimazole and polymer) and the pristine polymers were determined by X-ray photoelectron spectroscopy (XPS). The spectra were acquired using non-monochromatic M<sub>g</sub> K-alpha radiation (1253 eV). The pass energy was 50 eV for survey scans and 20 eV for high resolution scans. The take-off angle was 55.1°. The analysis of the data were performed using Casa XPS. Morphological studies were conducted by a FlexAFM (Nanosurf, Switzerland) using an EasyScan 2 AFM controller and a Tap190 cantilever (BudgetSensors, Bulgaria). The measurements were performed in non-contact mode so that the amplitude of the cantilever, excited at 190 kHz, was used as the feedback

loop parameter. The individual images were corrected for sample flatness and artifacts with the software package Gwyddion.<sup>34</sup>

## 9.5 Results and discussion

### Amorphous clotrimazole layers on silicon oxide

The deposition of clotrimazole from THF solutions resulted in homogeneous films for solute concentrations ( $c$ ) ranging from  $1.7 \text{ mg mL}^{-1}$  to  $66.6 \text{ mg mL}^{-1}$ . Atomic force microscopy measurements of such films featured little to no surface structures, which is also reflected by a surface roughness (root mean squared, RMS) below  $0.4 \text{ nm}$  (data not shown). As a previous study has shown, this preparation route generally results in (initially) amorphous clotrimazole films, which is also indicated by the absence of a significant surface roughness.<sup>35</sup>

At solute concentrations lower than  $1.7 \text{ mg mL}^{-1}$ , holes started to appear in the spin coated clotrimazole layers as the system had not enough time to form a coherent film or the amount of material is not sufficient for covering the entire sample. Exceeding  $c = 66.6 \text{ mg mL}^{-1}$ , the film quality decreased quickly due to comet structure formation by residual particles of un-dissolved clotrimazole in solution, making the surface inhomogeneous. Therefore, only samples in the concentration range of  $1.7\text{--}66.6 \text{ mg mL}^{-1}$  were studied further. Using a different solvent and/or spin coating conditions, crucial parameters such as solubility and evaporation speed can likely be altered, probably pushing the limits for high quality films to thinner but also to thicker ones.

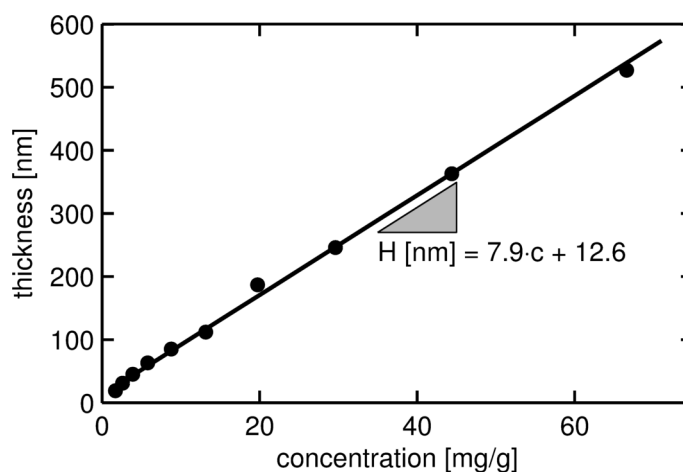


Figure 9.1: Layer thicknesses ( $H$ ) of the clotrimazole films deposited via spin coating from various THF solutions. The thickness has been obtained from ellipsometric measurements.

Ellipsometric measurements of the clotrimazole layers show a variation in layer thickness, ranging from  $19 \text{ nm}$  to  $531 \text{ nm}$  as the solute

concentration is varied from 1.7 to 66.6 mg mL<sup>-1</sup> in the spin coating process (see Figure 9.1). The thicknesses in between those two extremes increase linearly with the clotrimazole concentration. A linear regression fit shows that the layer thickness ( $H$ ) can be described by  $H$  [nm]  $\sim 12.6 + 7.9 \cdot c$ .

When stored under ambient conditions after film fabrication, the appearance and thus the solid state of such films remained unaffected for several hours. This stability allows the subsequent deposition and characterization of polymeric iCVD coatings on top of the amorphous clotrimazole films without the need for other process steps, like heat treatment.

### Characterization of the pristine iCVD pHEMA layer

A crosslinked pHEMA hydrogel was deposited onto a silicon oxide surface by iCVD to analyze the layer properties in the absence of clotrimazole. The ratio of monomer to saturation vapor pressure at the substrate surface can be calculated from the deposition parameters, which yields a HEMA to EGDMA ratio of 2 : 1. The film thickness is determined to 206 nm from the ellipsometry data, with the AFM height image showing a homogeneous surface with a roughness of 1.2 nm (see Figure 9.2, top left). Even if this value is larger than the one of bare silicon oxide surfaces (below 0.3 nm), it is comparable to the typical roughness of solution cast polymer films. This demonstrates that the iCVD process can be utilized to alter the chemical composition of a rigid surface while leaving the roughness (almost) unchanged.

FT-IR measurements were performed to determine the chemical composition of the hydrogel. The FT-IR spectra (ESI 9.9, Figure S9.7) show peaks characteristic for both EGDMA and HEMA monomers: the carbonyl ester absorption (1705-1740 cm<sup>-1</sup>), the methyl and methylene absorption at 2950-2800 cm<sup>-1</sup> and 1200-1000 cm<sup>-1</sup> and C-O absorption (1050-1150 cm<sup>-1</sup>). The characteristic OH band, attributable to the HEMA monomer, is also visible at 3500-3000 cm<sup>-1</sup>. A detailed analysis of the line profile suggests a crosslinker content, i. e. EGDMA content, of (15 ± 1) %, which is in good agreement with the XPS data of the film. The atomic ratio of carbon-to-oxygen calculated from the XPS spectrum was 2.09 : 1, while a ratio of 2.08 : 1 would be expected from the FTIR data. As the sampling depth in XPS experiments is just about 10 nm and the FT-IR samples instead the whole thickness, the good agreement of the C/O ratios determined by these two techniques hints at a very similar bulk and surface composition. Often, a preferential orientation of apolar groups (e. g. methyl groups) at the polymer=air interface or some surface contamination will result in a carbon-enriched surface composition relative to the bulk. In addition, both techniques, i. e. FT-IR and XPS analysis, confirm the retention of the monomeric units of HEMA and EGDMA after the deposition as well as a defined copolymer composition.

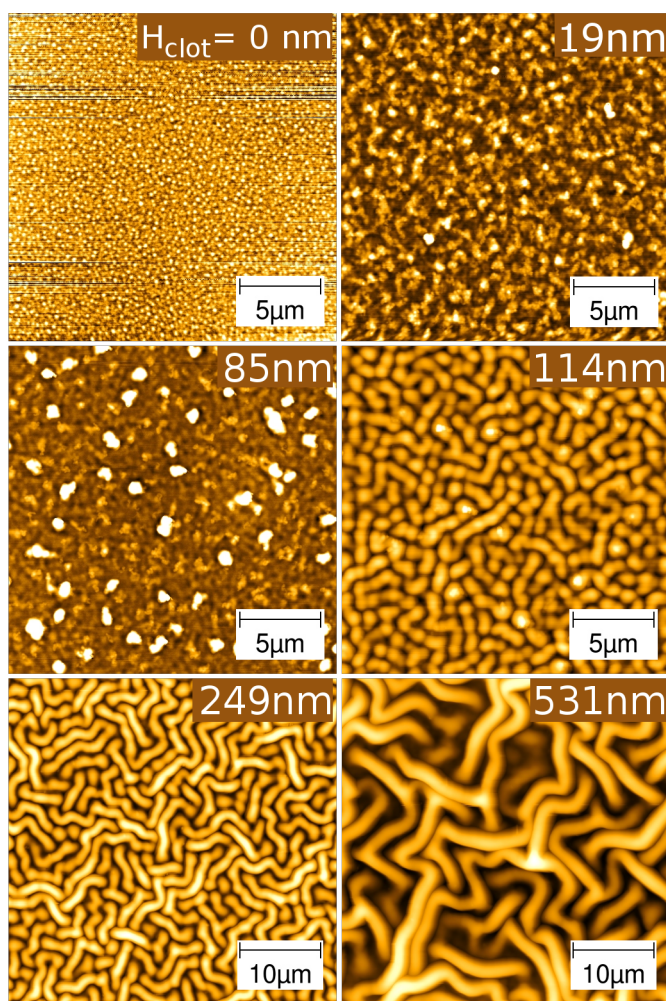


Figure 9.2: AFM height images of pHEMA films ( $h = 206$  nm) coated on top of clotrimazole spacing layers of varying thicknesses  $H$ , as reported in the labels. For comparison, a pHEMA film on the bare silicon oxide substrate is also shown (label “0 nm”). Note that the color scale and the resolution are different for the individual images, as the feature height varies from a few nanometers to microns.

### iCVD coatings on amorphous clotrimazole

The deposition of a crosslinked pHEMA layer onto a rigid bare substrate by the iCVD process resulted in a smooth surface, with the film adhering to the morphology of the substrate. However, when the crosslinked pHEMA is deposited on a relatively soft layer, i. e. on top of amorphous clotrimazole (which acts then as a spacing layer from the actual silicon substrate), the morphology drastically changes (see Figure 9.2 for selected examples, the complete AFM data are provide in the ESI 9.9, Figure S9.8 and S9.9).

Already at a clotrimazole layer thickness of 19 nm, the deposition of pHEMA resulted in a significant increase in surface roughness ( $\sigma_{\text{rms}} = 7$  nm) when compared to either the bare silicon substrate (23 times), the amorphous clotrimazole (18 times) or the pristine pHEMA film on the silicon wafer (6 times). This means that the growth of the pHEMA layer is affected by the presence of the drug spacing layer underneath even when it is just 19 nm thick.

Increasing the thickness of the clotrimazole spacer slightly did not change the film morphology significantly, indeed the roughness of the iCVD surface on top of a 63 nm thick clotrimazole layer was only  $\sigma_{\text{rms}} = 9$  nm, slightly higher than that of thinner spacers. At a spacer thickness of 85 nm, some dots, bigger than other surface areas, are visible. The number of these dots increases with the thickness of the spacing layer (see ESI 9.9) and reaches a maximum at 85 nm.

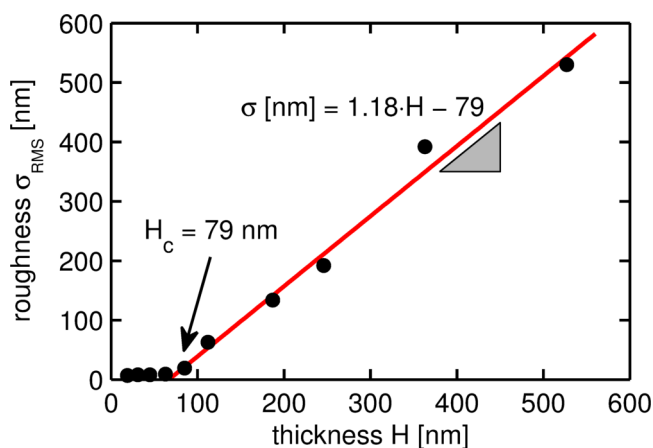


Figure 9.3: Root-mean-square roughness of the crosslinked pHEMA surfaces deposited on top of amorphous clotrimazole layers of different thicknesses. The values are calculated from the AFM data presented in Figure S9.8 (ESI 9.9).

At spacer thickness of 114 nm, a transition from the relatively smooth surface morphologies (except for some dots) to surface wrinkles occurs. Many structures appear dot-like but the structure size being significantly larger when compared to the samples containing thinner drug layers. Besides this, structures with elongated shape but of same width and height as the dot-like structures are observed. The length of these can, however, extend several tens of micrometers. In Figure 9.2, it can be seen that a further increase in spacer thickness results in much larger structures with mostly fibrillar shape instead of the dot-like one. The thickest sample tested, i.e. with a spacer thickness of 531 nm, contains only fibrillar structures, which form a labyrinth-like pattern (Figure 9.2). A preferred orientation of the wrinkles is not observed which is expected as neither the underlying

isotropic silicon oxide layer nor the amorphous clotrimazole layer introduces any directional surface properties.

To gain further information, the surface root mean square roughnesses ( $\sigma_{\text{rms}}$ ) of the various samples were extracted from the AFM height images and the results are summarized in Figure 9.3. The root mean square roughness values represent the deviation from an average (calculated) surface. This means that  $\sigma_{\text{rms}}$  is a good approximation for the peak-to-peak amplitude, i. e. the total variation in structure height. For a spacer thickness below 85 nm, the roughness is nearly independent from the thickness of the clotrimazole layer and consequently, the slope of a linear regression fit is close to zero in this region. For spacer thicknesses larger than 85 nm, the roughness drastically changes with the thickness. The increase in roughness is directly proportional to the spacer thickness, with a slope of 1.18. A critical thickness ( $H_c$ ) can be identified at 79 nm, where the extrapolations of the two linear regressions intercept, i. e. for values below  $H_c$ , the surface roughness is not (or only little) dependent on the spacer thickness while above, the roughness is a function of the distance between the supporting substrate surface and the pHEMA layer. Huang *et al.* reported such a behavior in a similar study.<sup>15</sup> They observed that there is a critical thickness at which interfacial forces and surface stresses assume a dominant role in the appearance of the surface morphology. Below the critical thickness of the spacing layer, the rigidity of the solid film stabilizes the flat morphology against the wrinkled one. Above the critical thickness, the compressive stress acts on the solid film, inducing wrinkling.

Besides the wrinkling amplitude represented by the roughness parameter, the wavelength is a key parameter of such surface wrinkles. Due to the unordered nature of the wrinkling, the radial power spectral density (RPSD) of the AFM micrographs was used in the determination of the characteristic wrinkle wavelengths. The RPSD is the Fourier transform of the radial autocorrelation function, which represents the power of the spatial frequencies and can thus be utilized to reveal periodic structures on a surface. This evaluation provides only reasonable numbers for samples exhibiting some periodicity (i. e. wrinkles), so only data with a spacer thickness of 114 nm and above are considered. At clotrimazole thickness of 114 nm, the wrinkle wavelength is approximately 1100 nm, showing a steady increase up to a maximum of  $\approx 3000$  nm as the spacing layer thickness reaches 531 nm.

There are many studies describing and modeling the appearance of wrinkles and relating their characteristics (e. g. amplitude, wavelength) to some physically meaningful parameters. Having a multi-layer system, a strain relaxation causes wrinkle formation when the individual layers differ in their elastic response (elastic modulus or Young's modulus), whereby most often systems containing a soft sub-



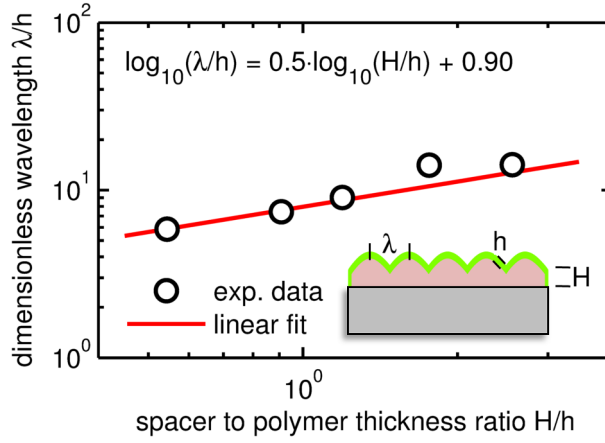


Figure 9.4: Wrinkle wavelength represented in a double logarithmic plot, with normalization for the iCVD polymer thickness  $h$ . The solid line represents a linear fit of the data, with the corresponding equations given in the inset.

strate ( $E_s$ ) and a thin, rigid top layer ( $E_f$ ) are studied.<sup>36</sup> Then the wrinkle wavelength  $l$  can be related to

$$\lambda = 2\pi h \left( \frac{\bar{E}_f}{3\bar{E}_s} \right)^{1/3}, \quad (9.1)$$

whereby  $h$  denotes the thickness of the clotrimazole film. For the validity of this model, the thickness of the substrate has to be significantly larger than that of the film so that small variations of the substrate thickness (i. e. the clotrimazole spacer here) do not influence the forces at the substrate/film interface. However, in the present case, the resulting morphology of the pHEMA thin film is the consequence of the force balance at the polymer-air and the clotrimazole-polymer interface, with the forces at the latter changing with the clotrimazole thickness  $H$ . Therefore, assumptions made for the model in Equation (9.1) are not fulfilled. A model whose assumptions are more similar to our experimental setup regards the case of a stiff film on a compliant substrate of similar thickness.<sup>37</sup> For an incompressible substrate, an analytic expression can be derived:

$$\frac{\lambda}{2\pi h} = \sqrt{\frac{H}{h}} \left( \frac{\bar{E}}{18\bar{E}_s} \right)^{1/6}. \quad (9.2)$$

The wrinkle wavelength is hereby also a function of the square-root of the substrate to film thickness ratio  $H/h$ . This means that from a double logarithmic, normalized plot of the experimental data (i. e.  $\lambda/h$  over  $H/h$ ) the ratio of elastic moduli can be calculated. Equation (9.2) represents then a linear function (see Figure 9.4) where the intercept

with the  $y$ -axis corresponds to  $\log_{10} \left( 2\pi \cdot \left[ \frac{\bar{E}}{18E_s} \right]^{1/6} \right)$ . From this, the elastic modulus ratio of polymer to spacer is derived to 73.

As it is evident from Equations (9.1) and (9.2), the wrinkle wavelength is independent of any pre-straining of the substrate before the deposition. Nevertheless, the formation of wrinkles, in general, requires the presence of a compressive stress prior a relaxation step. In most cases, this is achieved by thermal pre-straining of the sample, which results in the wrinkling after stress release/relaxation. In the present case, thermal pre-strain is inherently present as the substrate temperature is above room temperature during deposition. Further, the clotrimazole layer itself has a strong tendency to de-wet the surface, as observed for thinner films. Having thicker films, the de-wetting is balanced by adjacent molecules resulting in a metastable state. A slight disruption of this state might facilitate de-wetting and thus also wrinkle formation.

### Encapsulation performance

To obtain an estimate of the encapsulation quality of the pHEMA polymer regarding the ability to protect the clotrimazole layer from the environment, XPS investigations were performed after storing the samples for one month under ambient conditions. In all these measurements, signals from the chlorine unit of the clotrimazole were absent, independently on the spacer thickness. Furthermore, no nitrogen was detected (data not shown). This suggests that the clotrimazole is fully buried below the polymeric layer. From all these measurements it can be concluded that the crosslinked pHEMA layer deposited by iCVD performed well in terms of encapsulating the clotrimazole against ambient. The results shown here demonstrate also the advantage of using such deposition technique when compared, for instance, with a solution cast technique.<sup>4</sup> In such solution cast films, the matrix material and the clotrimazole layers formed a solid state solution but the XPS results revealed that a significant amount was hosted at the sample surface. While this may be interesting for a ready drug delivery, the drug molecules are not as well-protected against the environment as in the case of the iCVD encapsulation.

### iCVD on partial crystalline film

There are many ways clotrimazole can be transferred into the crystalline state. The method that works fastest without strong de-wetting of the clotrimazole from the substrate is water solvent vapor annealing.<sup>35</sup> Within a couple of days, an initial amorphous film is fully crystallized. In this work, a thick clotrimazole film of 530 nm thickness was stored in water vapor for two days, resulting in the film being partly transferred into a crystalline state. When the iCVD coating was deposited on top of such a partially crystalline film,

interesting behaviors were observed in optical and atomic force microscopy images. Firstly, the amorphous fraction of the film contains wrinkles (see Figures 9.5a and 9.5b). In the vicinity of the crystal, which appears bright in the polarized optical microscopy image, a depletion zone formed, i. e. clotrimazole molecules diffuse out of the intermediate region, typically addressed as Ostwald ripening. This depletion region shows a steady increase in thickness, as the distance to either crystalline or amorphous regions is getting smaller (interference due to the layer thickness variation results in the visible color gradient). As a result, also the wrinkling structure deviates in size: the structures are less pronounced for areas containing lower amounts of clotrimazole, in accordance with the findings above.

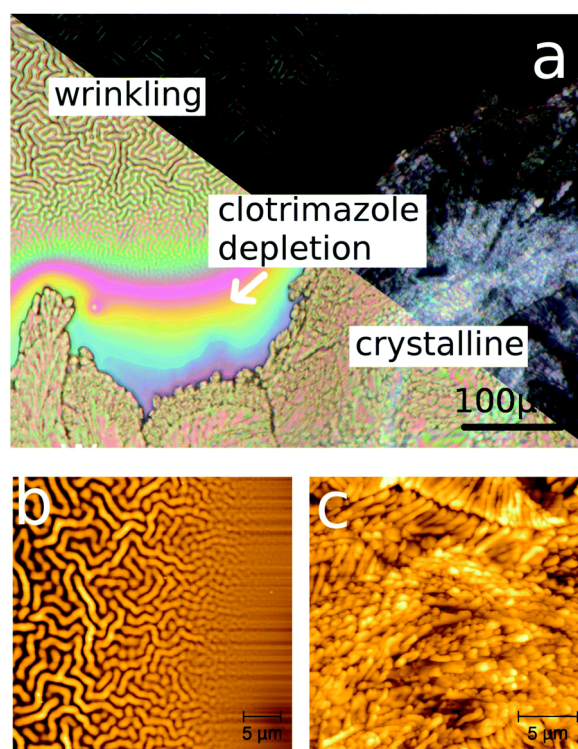


Figure 9.5: (a) Optical microscope image of a partial crystalline clotrimazole film coated with a 200 nm pHEMA layer without (lower left triangle) or with (upper right triangle) the usage of a polarizer. AFM height images of areas containing the spacer either in an amorphous (b) or crystalline (c) state.

Having crystalline clotrimazole on the silica surface results in the surface morphology being dominated by the crystal morphology, despite having a pHEMA layer on top. Surface wrinkling does not occur on these surfaces. In the framework of the wrinkling theory described above, this suggests that the elastic response of clotrimazole and polymer are now nearly identical. Such a behavior might be expected as the crystalline state reduces the degrees of freedom, making the sys-

tem more rigid. As shown elsewhere,<sup>38</sup> wrinkle formation results also for the samples when the crystalline clotrimazole is heated above its melting temperature ( $T_m \sim 150^\circ\text{C}$ ) and subsequently cooled to ambient, since this treatment yields again the amorphous clotrimazole state.

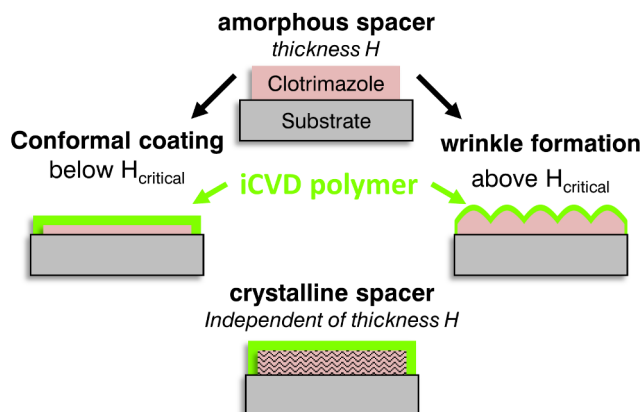


Figure 9.6: Scheme of the sample geometry prior iCVD coating and the assembly after deposition on thin or thick amorphous spacer (middle) and on crystalline clotrimazole (bottom).

## 9.6 Conclusion

The combination of solution processed drug layers and encapsulation by iCVD polymer depositions promises a highly adaptable and reproducible fabrication process whereby the surface morphology tuning might be of interest to fields beyond the pharmaceutical application. While many methods facilitate different sample compositions and preparation methods, the present approach does not require mechanical pre-stressing or heat treatments. In fact, three different responses in the surface were identified to correlate with the clotrimazole properties being present prior deposition (*cf.* Figure 9.6). When the thickness of the clotrimazole/spacer film is below a critical thickness, the iCVD polymer covers the clotrimazole surface with rather conformal layers. Above the critical spacer thickness, the elastic modulus mismatch between the polymer and the drug layer results in strong surface wrinkling. For crystalline spacers, wrinkling is absent and the resulting morphology remains alike the bare crystal surface.

## 9.7 Acknowledgements

The work was funded by the Austrian Science Fund (FWF): [P25541-N19]. The authors want to thank the NAWI Graz for support. Part of the research was supported by a Marie Curie International Incoming Fellowship (project 626889) within the 7th European Community Framework Programme.

## 9.8 References

- (1) F. Siepmann, J. Siepmann, M. Walther, R. J. MacRae, and R. Bodmeier *Journal of Controlled Release* **2008**, *125*, 1–15, DOI: 10.1016/j.jconrel.2007.09.012.
- (2) J. Siepmann and F. Siepmann *International Journal of Pharmaceutics* **2013**, *457*, 437–445, DOI: 10.1016/j.ijpharm.2013.10.010.
- (3) S. Schrank, B. Kann, E. Saurugger, H. Ehmman, O. Werzer, M. Windbergs, B. J. Glasser, A. Zimmer, J. Khinast, and E. Roblegg *Molecular Pharmaceutics* **2014**, *11*, 599–609, DOI: 10.1021/mp4005782.
- (4) H. M. A. Ehmman, S. Winter, T. Griesser, R. Keimel, S. Schrank, A. Zimmer, and O. Werzer *Pharmaceutical Research* **2014**, *31*, 2708–2715, DOI: 10.1007/s11095-014-1368-5.
- (5) L. C. Bradley and M. Gupta *Langmuir* **2012**, *28*, 10276–10280, DOI: 10.1021/la301170a.
- (6) K. K. S. Lau, Y. Mao, H. G. Pryce Lewis, S. K. Murthy, B. D. Olsen, L. S. Loo, and K. K. Gleason *Thin Solid Films* **2006**, *501*, 211–215, DOI: 10.1016/j.tsf.2005.07.208.
- (7) N. Chen, P. Kovacic, R. M. Howden, X. Wang, S. Lee, and K. K. Gleason *Advanced Energy Materials* **2015**, *5*, DOI: 10.1002/aenm.201401442.
- (8) K. K. S. Lau and K. K. Gleason *Macromolecular Bioscience* **2007**, *7*, 429–434, DOI: 10.1002/mabi.200700017.
- (9) A. M. Coclite, R. M. Howden, D. C. Borrelli, C. D. Petruczok, R. Yang, J. L. Yagüe, A. Ugur, N. Chen, S. Lee, W. J. Jo, A. Liu, X. Wang, and K. K. Gleason *Advanced Materials* **2013**, *25*, 5392–5423, DOI: 10.1002/adma.201301878.
- (10) K. K. S. Lau and K. K. Gleason *Macromolecules* **2006**, *39*, 3688–3694, DOI: 10.1021/ma0601619.
- (11) K. K. S. Lau and K. K. Gleason *Macromolecules* **2006**, *39*, 3695–3703, DOI: 10.1021/ma0601621.
- (12) S. H. Baxamusa and K. K. Gleason *Chemical Vapor Deposition* **2008**, *14*, 313–318, DOI: 10.1002/cvde.200806713.

- (13) B. Reeja-Jayan, P. Kovacic, R. Yang, H. Sojoudi, A. Ugur, D. H. Kim, C. D. Petruczok, X. Wang, A. Liu, and K. K. Gleason *Advanced Materials Interfaces* **2014**, *1*, n/a–n/a, DOI: 10.1002/admi.201400117.
- (14) L. R. J. Scarratt, B. S. Hoatson, E. S. Wood, B. S. Hawkett, and C. Neto *ACS Applied Materials & Interfaces* **2016**, *8*, 6743–6750, DOI: 10.1021/acsmi.5b12165.
- (15) R. Huang and Z. Suo *Thin Solid Films* **2003**, *429*, 273–281, DOI: 10.1016/S0040-6090(03)00065-8.
- (16) E. P. Chan, E. J. Smith, R. C. Hayward, and A. J. Crosby *Advanced Materials* **2008**, *20*, 711–716, DOI: 10.1002/adma.200701530.
- (17) S. Vajpayee, K. Khare, S. Yang, C.-Y. Hui, and A. Jagota *Advanced Functional Materials* **2011**, *21*, 547–555, DOI: 10.1002/adfm.201001652.
- (18) S. Yang, K. Khare, and P.-C. Lin *Advanced Functional Materials* **2010**, *20*, 2550–2564, DOI: 10.1002/adfm.201000034.
- (19) C. Bukowsky, J. M. Torres, and B. D. Vogt *Journal of Colloid and Interface Science* **2011**, *354*, 825–831, DOI: 10.1016/j.jcis.2010.11.034.
- (20) T. Ohzono, H. Monobe, K. Shiokawa, M. Fujiwara, and Y. Shimizu *Soft Matter* **2009**, *5*, 4658–4664, DOI: 10.1039/B912235D.
- (21) N. Bowden, S. Brittain, A. G. Evans, J. W. Hutchinson, and G. M. Whitesides *Nature* **1998**, *393*, 146–149, DOI: 10.1038/30193.
- (22) G. Gioia and M. Ortiz In *Advances in Applied Mechanics*, Wu, T. Y. and Hutchinson, J. W., Eds.; Elsevier: 1997; Vol. 33, 119.
- (23) J. Yin, J. L. Yagüe, D. Eggenspieler, K. K. Gleason, and M. C. Boyce *Advanced Materials* **2012**, *24*, 5441–5446, DOI: 10.1002/adma.201201937.
- (24) P. R. Sawyer, R. N. Brogden, K. M. Pinder, T. M. Speight, and G. S. Avery *Drugs* **1975**, *9*, 424–447, DOI: 10.2165/00003495-197509060-00003.
- (25) V. Borhade, S. Pathak, S. Sharma, and V. Patravale *International Journal of Pharmaceutics* **2012**, *431*, 138–148, DOI: 10.1016/j.ijpharm.2011.12.040.
- (26) H. M. A. Ehmman and O. Werzer *Crystal Growth & Design* **2014**, *14*, 3680–3684, DOI: 10.1021/cg500573e.
- (27) R. K. Bose and K. K. S. Lau *Chemical Vapor Deposition* **2009**, *15*, 150–155, DOI: 10.1002/cvde.200806748.

- (28) G.-H. Hsiue, J.-A. Guu, and C.-C. Cheng *Biomaterials* **2001**, *22*, 1763–1769, DOI: 10.1016/S0142-9612(00)00336-7.
- (29) N. Bowden, W. T. S. Huck, K. E. Paul, and G. M. Whitesides *Applied Physics Letters* **1999**, *75*, 2557–2559, DOI: 10.1063/1.125076.
- (30) C. M. Stafford, C. Harrison, K. L. Beers, A. Karim, E. J. Amis, M. R. VanLandingham, H.-C. Kim, W. Volksen, R. D. Miller, and E. E. Simonyi *Nature Materials* **2004**, *3*, 545–550, DOI: 10.1038/nmat1175.
- (31) E. P. Chan and A. J. Crosby *Soft Matter* **2006**, *2*, 324–328, DOI: 10.1039/B515628A.
- (32) J. Genzer and J. Groenewold *Soft Matter* **2006**, *2*, 310–323, DOI: 10.1039/B516741H.
- (33) C. M. Herzinger, B. Johs, W. A. McGahan, J. A. Woollam, and W. Paulson *Journal of Applied Physics* **1998**, *83*, 3323–3336, DOI: 10.1063/1.367101.
- (34) D. Nečas and P. Klapetek *Central European Journal of Physics* **2011**, *10*, 181–188, DOI: 10.2478/s11534-011-0096-2.
- (35) H. M. A. Ehmman, A. Zimmer, E. Roblegg, and O. Werzer *Crystal Growth & Design* **2014**, *14*, 1386–1391, DOI: 10.1021/cg401859p.
- (36) E. Cerda and L. Mahadevan *Physical Review Letters* **2003**, *90*, 074302, DOI: 10.1103/PhysRevLett.90.074302.
- (37) Z. Y. Huang, W. Hong, and Z. Suo *Journal of the Mechanics and Physics of Solids* **2005**, *53*, 2101–2118, DOI: 10.1016/j.jmps.2005.03.007.
- (38) P. Christian, H. M. Ehmman, A. M. Coclite, and O. Werzer *ACS Applied Materials & Interfaces* **2016**, *8*, 21177–21184, DOI: 10.1021/acsmi.6b06015.

## 9.9 Supporting Information

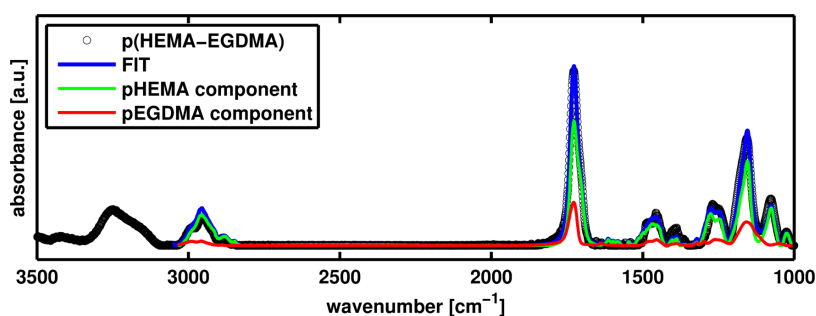


Figure S9.7: FT-IR spectrum of the crosslinked pHEMA layer obtained by iCVD. The experimental data are fitted as a combination of the single component FT-IR spectra. From this, the pHEMA fraction is determined to 85 %.

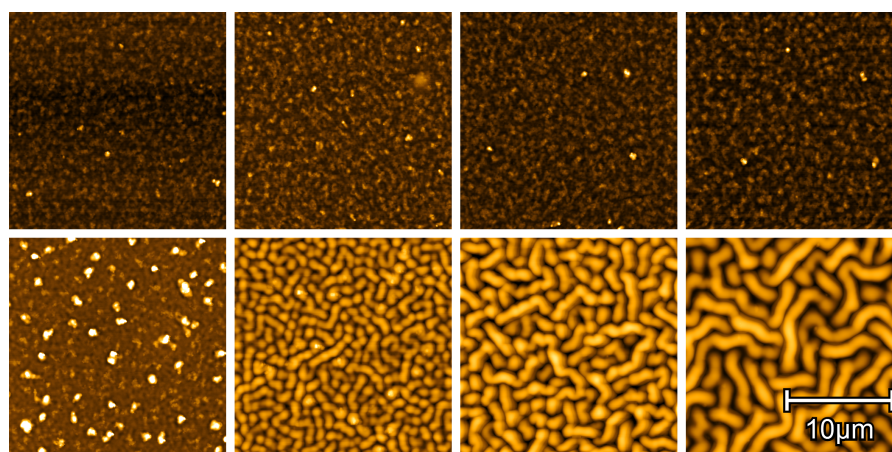


Figure S9.8: AFM height images of pHEMA films (200 nm) coated by iCVD onto amorphous clotrimazole layers of various thickness. Starting on top left and going right, the thicknesses are: 19, 31, 45, 63, 86, 114, 189, 249 nm.

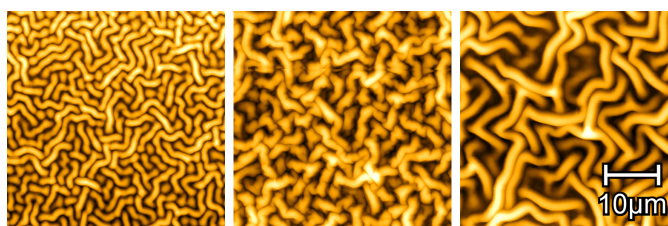


Figure S9.9: AFM height images of iCVD coated amorphous clotrimazole layers of various thickness. Starting from left: 249, 365, 531 nm. (The sample 249 nm is the same as above, but on a different scale for sake of comparability).



# Controlling Indomethacin Release through Vapor-Phase Deposited Hydrogel Films by Adjusting the Cross-linker Density

---

Paul Christian,<sup>¶</sup> Stephan Tumphart,<sup>¶,†</sup> Heike M.A. Ehmman,<sup>†</sup>  
Hans Riegler,<sup>†</sup> Anna Maria Coclite<sup>¶</sup> and Oliver Werzer<sup>†,\*</sup>

<sup>¶</sup> Institute for Solid State Physics, NAWI Graz, Graz University of Technology, 8010 Graz, Austria

<sup>†</sup> Institute of Pharmaceutical Sciences, Department of Pharmaceutical Technology, University of Graz, 8010 Graz, Austria

\* Corresponding author: oliver.werzer@uni-graz.at

## 10.1 Preface

This work was conducted in close collaboration with Oliver Werzer from the University of Graz, who provided the indomethacin samples. The author of this thesis performed the polymer synthesis by the iCVD method. He performed ellipsometry and FTIR analysis of the samples, evaluated the experimental data and wrote the manuscript with assistance of Oliver Werzer. Stephan Tumphart, Heike M.A. Ehmman, Hans Riegler and Oliver Werzer performed the dissolution studies and did the drug characterization. Anna Maria Coclite and Oliver Werzer supervised the project. The manuscript is currently under submission for publication in a peer-reviewed journal.

## 10.2 Abstract

Vapor-phase deposited polymer coatings are applied on thin indomethacin films to modify the drug release. Hydrogel-forming co-polymers of 2-hydroxyethyl methacrylate and ethylene glycol dimethacrylate were prepared directly on top of solution cast indomethacin thin films by initiated Chemical Vapor Deposition (iCVD). This technique allows for solvent-free processing under mild conditions, thus minimizing a potential impact on the pharmaceutical. The drug release behavior, among other properties, was evaluated for polymers of different compositions and at different temperatures. The data show that the release kinetics can be tuned by several orders of

magnitude as the cross-linker fraction is varied in the polymer coating. While uncoated indomethacin films were fully released within an hour, polymer coatings showed gradual liberation over several hours to days. Additional insight is gained from evaluating the experimental dissolution data in the framework of diffusive transport. The results of this study show the potential of iCVD polymers in the field of drug coatings, allowing for tailored release behavior by altering the polymer composition.

### 10.3 Main text

To enhance efficiency of existing medication and to develop new therapeutic options for currently untreatable medical conditions, pharmaceutical research focuses not only on the screening of new active pharmaceutical ingredients (APIs) but also on the exploration of different administration routes and alternative dosage forms. Polymers can assume various crucial functions in drug formulations, providing protection against premature release,<sup>1,2</sup> stabilizing specific solid state forms,<sup>3,4</sup> enabling site-specific drug activity<sup>5,6</sup> or being functionalized themselves by anchoring drugs or proteins directly to their structure (polymer therapeutics)<sup>7</sup>. The drug release from such polymer systems is usually facilitated by either degradation/erosion of the polymer host or by diffusion of the drug; for the latter mechanism, matrix-, reservoir- and hydrogel-based systems are usually differentiated.<sup>8</sup>

In matrix systems, the API is homogeneously dispersed inside a suitable host material such as cellulose<sup>9</sup> or lipids<sup>10</sup>, with the tortuosity of the material determining release kinetics<sup>11</sup>. While hydrogel systems can also be considered matrix systems as they are usually loaded with an API, drug release occurs upon swelling of the hydrogel and is governed by the mesh size of the polymer.<sup>12</sup>

In reservoir systems, on the other hand, a core-shell structure is usually present, with the API being encapsulated by an outer membrane; as such devices can store and then gradually release a larger amount of the drug, they are suitable for internal application as implants.<sup>13</sup> Reservoir systems have mostly been investigated for conventional drug forms such as pellets,<sup>14,15</sup> while less work has been performed on coatings of thin film dosage forms by solution-based methods. However, the preparation of thin pharmaceutical films is of particular interest; dosage forms like patches can allow for perpetual therapeutic action while being easy to apply/remove.<sup>16</sup> When combined with sequential polymer deposition, multilayer devices with different functionalities can even be realized.<sup>17,18</sup>

However, preparing defined and well-separated layers of API and polymers can be quite challenging, especially in the case of thin films. Solution-based techniques commonly applied in the preparation of polymer layers will usually affect the drug as well. While this might

not be a limitation to matrix-type systems where intermixing is desired, such an approach is not well suited for reservoir systems. Even if intermixing is avoided by use of orthogonal solvents, other solvent-drug interactions may still be present which in turn can change the solid-state of the drug. In addition, environmental and health issues might limit excessive use of solvents and residual solvents have to be avoided in the final films.

A solvent-free approach lies in polymer synthesis by initiated Chemical Vapor Deposition (iCVD).<sup>19</sup> This technique allows for the synthesis of polymeric layers directly at an interface while achieving conformality and defined chemical composition even on delicate substrates.<sup>20,21</sup> The iCVD process is based on the mechanism of radical polymerization in solution, with the difference being that all reagents are supplied in their vapor phase form at low reactor pressure (usually held between 10 to 100 Pa). An initiator, usually a peroxide with a labile oxygen–oxygen bond, decomposes thermally at a heated filament (typically 200–300 °C), thus forming radicals. These radicals can then interact with vinyl bonds of monomer units absorbed on the substrate surface, forming a monomer-radical complex. Additional monomer units then attach, facilitating polymer chain growth until being terminated by either another radical or monomer-radical complex. A more detailed description about iCVD in general and the associated mechanisms can be found in literature.<sup>22,23</sup>

Previous applications of iCVD polymers in the field of biomedicine comprise the fabrication of thermo- and pH-responsive drug delivery systems.<sup>24–26</sup> In these cases, delivery was mostly studied in relation to the stimuli-responsive properties of the iCVD coatings but little focus was put on the release kinetics. The latter is of great importance for pharmaceutical dosing, where direct control can enable therapies that are specific to the individual and the situation. For this reason, the present study focuses on how variations in polymer mesh size affect the drug release behavior.

Polymers of 2-hydroxyethyl methacrylate (HEMA) and ethylene glycol dimethacrylate (EGDMA) were deposited by iCVD on top of indomethacin thin films (for the structural formulas and an illustration of the sample structure, see Figure 10.1). Hydrogel-forming polymers based on HEMA are widely studied as drug release platforms in matrix systems.<sup>27–29</sup> This makes HEMA also interesting in the present application as a coating layer for reservoir drug systems; the hydrophilic character facilitates swelling in aqueous environment, which in turn should foster drug release. The addition of EGDMA, a cross-linker, enhances the mechanical stability of the coatings and can be used to control the hydrophilic/-phobic character of the material (and thus, the mesh size and water uptake). The impact of the iCVD coating on the solid-state, the morphology and the dissolution behavior of the indomethacin films is investigated as function

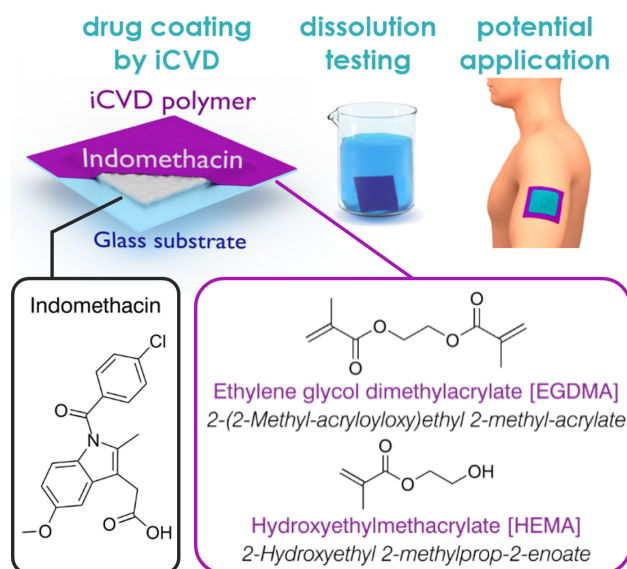


Figure 10.1: Cutaway drawing of the sample structure, depicting indomethacin drug layers on glass substrates, encapsulated by an iCVD polymer layer (top left). To the right, dissolution testing and a potential application of such films as transdermal patches are illustrated. At the bottom, structural formulas of indomethacin and of the iCVD monomers, labeled by their trivial names, are provided. The corresponding abbreviations are stated in square brackets, the IUPAC names in italic letters.

of polymer composition and dissolution media temperature. While amorphous drug formulations can be desirable in applications where enhanced drug release is favorable, this will often result in additional polymer-drug interactions. For instance, polymeric coatings exhibit strong wrinkling when deposited on amorphous API films while such behavior is absent on crystalline films due to a smaller difference in elastic modulus.<sup>30</sup> Also, polymeric coatings can influence solid state transitions of drug layers, both enhancing or retarding crystallization kinetics depending on the drug-polymer interactions.<sup>31</sup> To minimize these and other influences, the focus of the present study is put on polymer encapsulation of crystalline indomethacin films.

#### 10.4 Results

*Indomethacin film characterization.* Homogeneous indomethacin films were obtained by solution casting. Initially, a uniform liquid layer forms on the substrate due to the good wetting properties of THF on glass surfaces. Upon fast solvent removal, homogeneous indomethacin films form. The solid state of such films is amorphous and crys-

talline fractions are neither noted in the optical micrographs nor (more qualitatively) in X-ray diffraction patterns (thus, data are omitted). As film formation occurs quickly due to the high vapor pressure of THF, this leaves little to no time to the individual molecules to adapt an ordered (long range) arrangement, thus the system remains in a metastable amorphous state. While samples will transfer to a crystalline state eventually, neither storage at ambient conditions nor at 50 °C for five consecutive days did change the solid state. Indeed, previous studies on amorphous indomethacin have found induction times between 15 to 50 days when employing temperatures below 60 °C.<sup>32</sup>

However, by casting indomethacin from different solvents or by artificially reducing the solvent evaporation rate (e. g. by covering the sample with a Petri dish), the formation of some crystalline fraction results, which grows into larger domains within a few hours. In addition, some solvents yield distinct crystal structures (polymorphs); for instance, indomethacin crystallizes from ethanol solution in the  $\alpha$ -form (monoclinic)<sup>33</sup> while the  $\gamma$ -form (triclinic) is obtained from ethyl ether.<sup>34</sup> Similarly, this solvent-specific behavior can also be used to transfer amorphous films into specific crystal forms.

In this study, ethanol solvent vapor annealing was used for controlled crystallization. Within 48 hours, samples exposed to ethanol vapor in a sealed container had fully crystallized. Figure 10.2a shows an optical microscopy image of such a sample taken under crossed polarizers, revealing Maltese cross patterns characteristic for spherulitic growth (the patterns are due to birefringence). The size of a single spherulitic domain varies from approximately 200  $\mu\text{m}$  to 850  $\mu\text{m}$ . The crystalline nature of such films is also confirmed by X-ray diffraction (see Figure 10.2b). The specular diffraction pattern exhibits multiple Bragg peaks and the indexation reveals the presence of the indomethacin  $\alpha$ -form<sup>35</sup> (CCDC Nr 201766). The various Bragg peaks present in the pattern indicate that a preferred orientation is absent, i. e. the individual spherulitic branches are also rotated in respect to the substrate normal and the crystallites exhibit a powder-like distribution.

*Polymer deposition onto crystalline drug layers.* The coating of crystalline indomethacin with iCVD polymers leaves the underlying drug layer mostly unaffected and changes in morphology or solid state are not observed. Spherulitic indomethacin domains dominate the optical appearance as the polymer coatings are optically transparent. Thus, samples were investigated by AFM, the data being summarized in Figure 10.3. The uncoated surface exhibits branched, feather-like structures typical for the spherulitic growth of indomethacin crystals. These structures are simply replicated by the polymer coatings grown atop, underlining the conformity of iCVD coatings. Also, changes in the solid state were not detected from XRD scans (data not shown), indicating the gentle nature of the iCVD process.

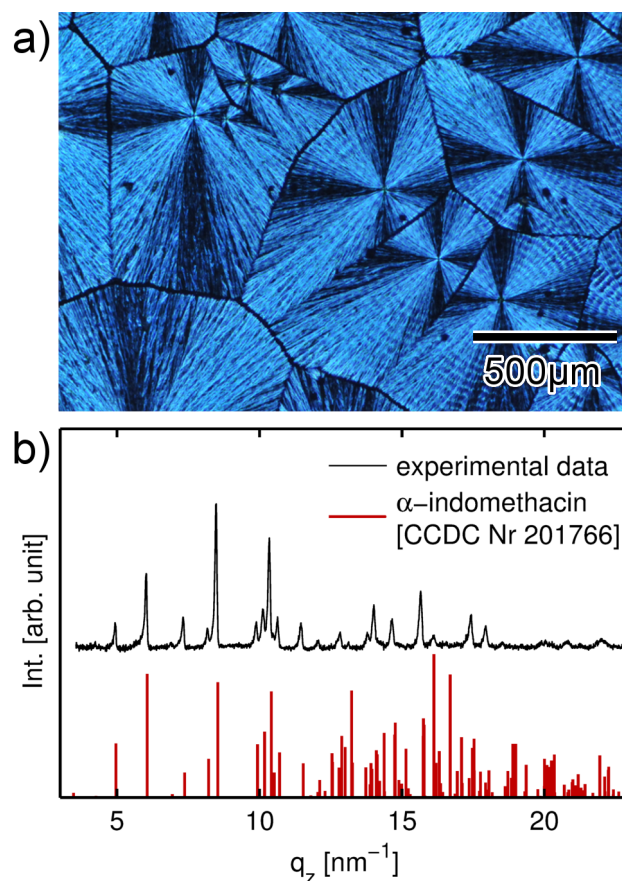


Figure 10.2: (a) Optical microscopy image of an indomethacin sample in the crystalline state after ethanol solvent vapor annealing. The image was taken under crossed polarizers. (b) Specular X-ray diffraction pattern of a solvent-annealed sample and theoretical powder diffraction pattern of the indomethacin  $\alpha$ -polymorph. Please note that experimental data are baseline corrected to remove scattering from the amorphous glass substrate.

A more detailed look at the data in Figure 10.3 reveals that surface features appear smoothed when covered by the polymers, indicating that such structures become slowly buried as the polymer thickness increases during deposition. While this behavior is noted both for the pEGDMA homopolymer and the hydrogel-forming p(HEMA-co-EGDMA) coating, detailed inspection reveals another difference. Graphs of the latter depict a blurred surface, more reminiscent to a measurement artifact than to actual morphology. Likely, this is caused by a softening of the polymer when taking up water from the environment (approx. 25 °C, 70 % humidity), thus forming a hydrogel.<sup>36</sup>

Under dry conditions, the non-polar methyl groups are oriented towards the environment-polymer interface while the polar hydrox-

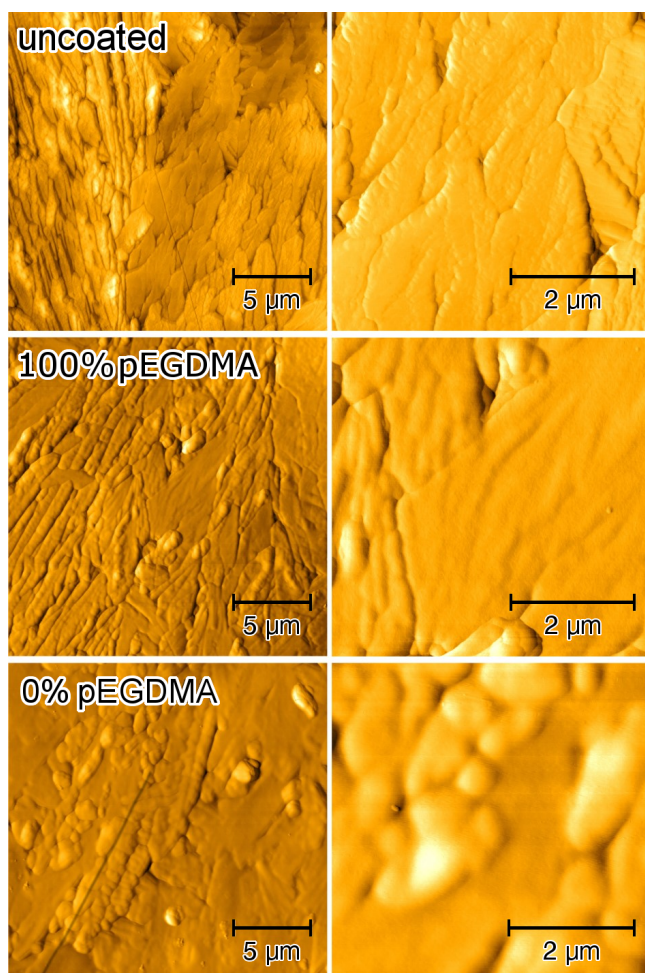


Figure 10.3: AFM micrographs of an uncoated, crystalline indomethacin sample (top) and of samples coated with either a pEGDMA (center) or a p(HEMA-co-EGDMA) polymer layer (bottom). The coating thicknesses are approximately 200 nm. Left column depicts the samples at larger scales, for details refer to the right column.

yethyl are turned inward, with a reversed behavior being observed in the swollen state, thus increasing flexibility.<sup>37</sup>

*Characterization of iCVD coatings on bare substrates.* The deposition of p(HEMA-co-EGDMA) layers onto silica substrates replicates the surface so that morphologies similar to a bare substrate result (Figure S10.8). The chemical composition of the polymers had not impact on the morphology of the films. The polymer layers were prepared at a thickness of about 200 nm. This choice was made based on pre-evaluations and provides the best compromise for the iCVD setup in use in terms of preparation times (deposition rates are typically below 10 nm/min) and the final coating performance. All deposited

polymers were subject to chemical characterization by infrared spectroscopy, allowing the HEMA to EGDMA ratios to be determined (data are shown in Figure S10.9). Three different compositions are exemplarily considered for the dissolution experiments, i. e. the ones with 25 %, 50 % and 100 % EGDMA. It should be noted that with no or little cross-linking, pHEMA exhibits strong water uptake, thus detaching easily from the surface. While such a behavior is undesirable for controlled release, it is potentially useful for targeted drug delivery, especially when combined with stimuli-responsive functionalities. The ability of HEMA copolymers to swell in aqueous environment is crucial for the drug release; uptake of water (or any other liquid) depends strongly on the mesh size of the polymer, which will also strongly influence how drug transport proceeds through the membrane.

To evaluate the swellability of the studied polymers, polymer film thickness was monitored during aqueous swelling by *in situ* ellipsometry. In Figure 10.4a, exemplary swelling curves are depicted for different polymer compositions. The data evidence how swelling is drastically decreased as the cross-linker fraction is increased in the polymer. While a polymer with 27 % EGDMA content exhibits swelling up to 11 %, the EGDMA homopolymer shows a negligible thickness increase when immersed into water. The hydrophobic character of EGDMA paired with strong cross-linking (and physical entanglement) in the polymer prevents water penetration at large so that only imperfections (such as unpolymerized vinyl groups or pinholes) should contribute to water uptake. From the equilibrium swelling degree  $s_{EQ}$ , the mesh size of such polymers can be estimated. For this, the evolution of swelling degree  $s = (d_0 + \Delta d)/d_0$  as a function of time is fitted to an empirical model by

$$s(t) = s_{EQ} \left( 1 - e^{(-k \cdot t^n)} \right), \quad (10.1)$$

with  $d_0$  being the initial (unswollen) polymer thickness,  $k$  being the rate constant and  $n$  being an empirical exponent. This equation is a simple sigmoid function and allows for a more reliable estimation of  $s_{EQ}$  in cases where equilibrium is not reached within the time of the experiment. The average molecular weight between cross-links ( $\overline{M}_c$ ) in the layer is related to the polymer volume fraction at equilibrium  $\phi = d_0/\Delta d = 1/(s_{EQ} - 1)$  by

$$\overline{M}_c = -V_s \rho_{pol} \frac{\left( \frac{1}{\phi} - \frac{\phi}{2} \right)}{\ln(1 - \phi) + \phi + \chi \phi^2}, \quad (10.2)$$

where  $V_s$  denotes the molar volume of the solvent (for water,  $V_{H_2O} = 18.03 \text{ cm}^3/\text{mol}$ ),  $\rho_{pol}$  is the polymer density (for pHEMA<sup>38</sup>,  $\rho_{HEMA} = 1.274 \text{ g/cm}^3$ ) and  $\chi$  is the polymer-solvent interaction parameter. For pHEMA, this interaction parameter was found to be



dependent on  $\phi$ , with  $\phi = 0.320 + 0.904 \cdot \phi$ .<sup>39</sup> Equation (10.2) is a modified form of the Flory-Rehner equation,<sup>40,41</sup> accounting for the case of a surface-attached polymer which is thus restricted to one dimensional swelling.<sup>42</sup> A full derivation of this expression is provided in the supplementary information 10.9. The mesh size  $\xi$  is then given by

$$\xi = l\phi^{-1/3}C_n^{1/2} \left( \frac{2\overline{M}_c}{M_m} \right)^{1/2}, \quad (10.3)$$

with  $l$  referring to the characteristic atomic bond length of the backbone (for C–C,  $l = 0.154$  nm) and  $C_n$  denoting the Flory characteristic ratio (rigidity factor). For pHEMA, literature suggests  $C_n = (6.9 \pm 0.5)$ .

Evaluating experimental swelling data of polymers with different fractions of cross-linker in the framework of Equation (10.3) yields mesh sizes ranging from  $(0.29 \pm 0.01)$  nm for 27 % EGDMA to  $(0.15 \pm 0.01)$  nm for 57 % EGDMA (see Figure 10.4b). For pEGDMA, a theoretical mesh size of  $(0.088 \pm 0.004)$  nm is calculated. Given that the diameter of water is about 0.27 nm,<sup>44</sup> this raises the question how such values have to be interpreted. The theoretical analysis works on the premise of a defect-free, syndiotactic polymer where the local structure is repeated indefinitely throughout the swelling film. In praxis, polymers will often be (at least partially) atactic, displaying physical entanglement and incomplete vinyl conversion, among other defects, so that the mesh size will only be a mean measure of a distributed quantity. This is also evident when comparing the average number of links  $N = 2\overline{M}_c/M_m$ , determined from the swelling studies, to the (theoretical) ratio calculated from the volume fractions,  $N_{\text{theory}} = F_{\text{HEMA}}/F_{\text{EGDMA}}$ .<sup>45</sup> For instance,  $N_{\text{theory}}$  calculates to 2.7 for the sample containing 27 % EGDMA, while the swelling studies determine a value of just 0.5, meaning that the polymer appears (in average) stronger cross-linked than expected from just the composition. This difference is usually attributed to physical entanglement, which is limiting the overall swelling.<sup>45</sup>

*Indomethacin dissolution without coating.* The dissolution behavior of uncoated indomethacin films was studied in a phosphate buffer solution held at 25 °C. Both amorphous and crystalline indomethacin samples were tested, with the individual release profiles being depicted in Figure 10.5. For an as-prepared, amorphous sample, rapid release kinetics are observed. Initially, drug release from the substrate surface proceeds at a constant rate, the slope being 19 %/min. As the released volume fraction surpasses sixty percent, a gradual decrease of the release rate results (elimination phase), until full dissolution is achieved after 30 minutes. In general, dissolution of thin drug layers from a surfaces proceeds at very fast pace as the surface area per volume, which

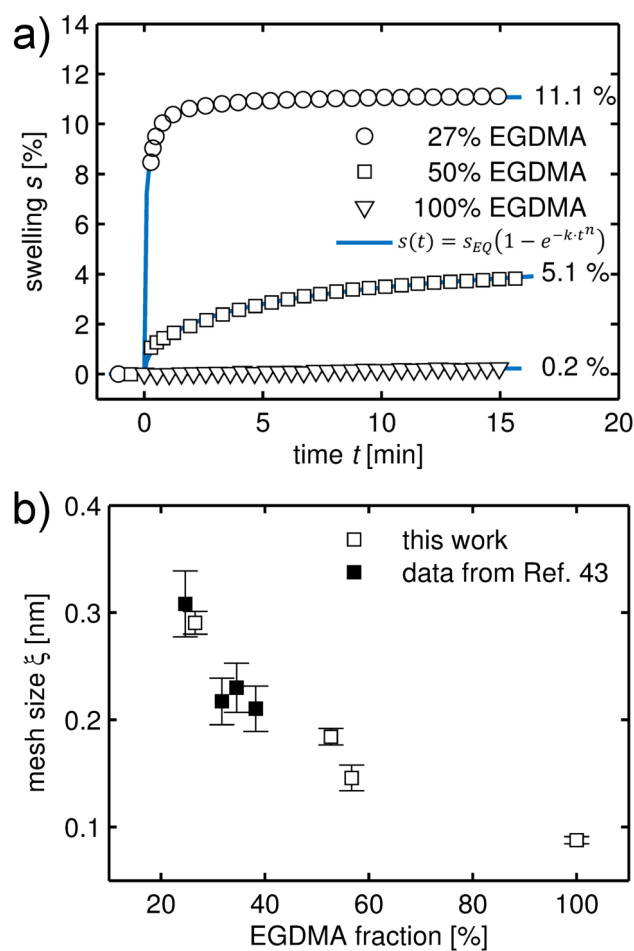


Figure 10.4: (a) Swelling ratios of p(HEMA-co-EGDMA) films with different EGDMA volume fractions (100% refers to the homopolymer) as a function of time, as determined from ellipsometric measurements. Data are fitted by the empirical model provided in Equation (10.1) and labeled with the values of equilibrium swelling  $s_{EQ}$ . (b) Polymer mesh size as a function of EGDMA cross-linker content, calculated from the equilibrium swelling ratio according to equation (3). Data from the present study are plotted with open symbols ( $\square$ ), data from a previous publication<sup>43</sup> are represented by filled symbols ( $\blacksquare$ ).

is directly proportional to the release kinetic, is very large.<sup>46,47</sup> Such a rapid release might be desired in cases where immediate therapeutic action is required. For comparison, amorphous samples were also tested after being stored at 50 °C under ambient atmosphere for five consecutive days. This does not change, at least in the limit of detection, the sample properties (i. e. morphology, solid state). Similar to the as-prepared samples, dissolution experiments reveal a rapid release, again displaying a constant rate at first. The slope of 11 %/min in the

initial release means that indomethacin dissolution is a bit slower in this case and full release results after approximately 45 minutes. While the exact reason for this difference cannot be unambiguously identified within this study, one possible explanation can be amorphous-crystalline phase transitions during dissolution experiments.<sup>48</sup> While such an effect might also be present here, the (overall) fast dissolution rate means that the period for significant crystallization is likely too small. It should also be mentioned that due to the rapid dissolution behavior, error bars are rather large for these data sets. To avoid these issues when testing polymer coated samples, only samples containing crystalline indomethacin were employed.

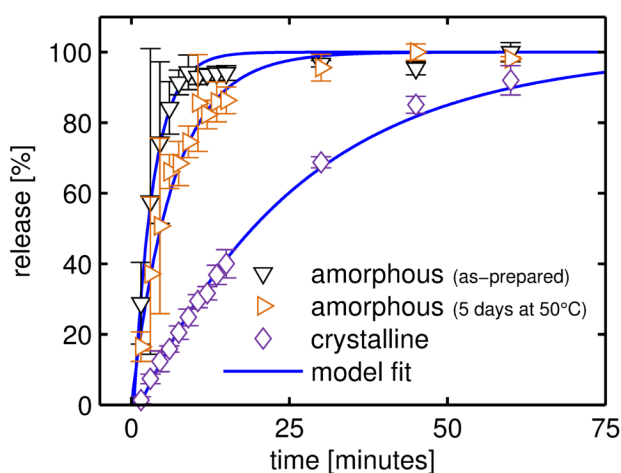


Figure 10.5: Drug release performance of thin indomethacin films in the amorphous (as-prepared and after storage) and the crystalline state. All data has been collected at 25 °C. A detailed description of the model fit is provided in the text (section *data modeling*).

Crystalline indomethacin, on the other hand, displays a significantly slower drug release when compared to its amorphous counterpart. Full dissolution of crystalline samples takes approximately two hours, meaning that a modification of the solid state form allows already some control over the drug release behavior. The slower drug release is the result of an additional energetic barrier that molecules need to overcome in the dissolution process, due to being confined to distinct lattice sites. It should also be mentioned that it was not possible to gain statistically reasonable results with the applied dissolution measurement strategy when increasing the temperature to 37 °C or even 50 °C as the dissolution rates were too high.

*Dissolution of crystalline indomethacin with iCVD polymer coating.* In Figure 10.6, the dissolution profiles of crystalline indomethacin films, coated with different iCVD polymers, are depicted. The dissolution

medium was held at 25 °C and the dissolution profile of the uncoated sample is also shown for comparison. While the release of uncoated indomethacin films from glass substrates proceeds on the time scale of minutes, drug liberation from coated samples occurs over a span of several hours to days. Moreover, distinct release behaviors are noted for the different polymer compositions; as the number of cross-links is increased in the polymer, drug release is increasingly retarded. For example, full indomethacin release takes over 20 hours in the case of a 25 % EGDMA coating, prolonging drug release by a factor of 10 compared to the uncoated film. As the hydrogel character of the polymer coating is reduced by increasing EGDMA fraction, release kinetics are slowed down further. Interestingly, some release is also noted from a sample coated with the EGDMA homopolymer, albeit only a fraction of the other samples is liberated in the same time frame. Despite the high cross-linking degree and little water penetration (compare swelling data in Figure 10.4), the pEGDMA coating allows for some release. This behavior suggests that coating imperfections are mainly responsible for this kind of release; oligomeric portions, pinholes, edge defects and/or partial ablation of the polymer coating may cause such a *leaking release*.

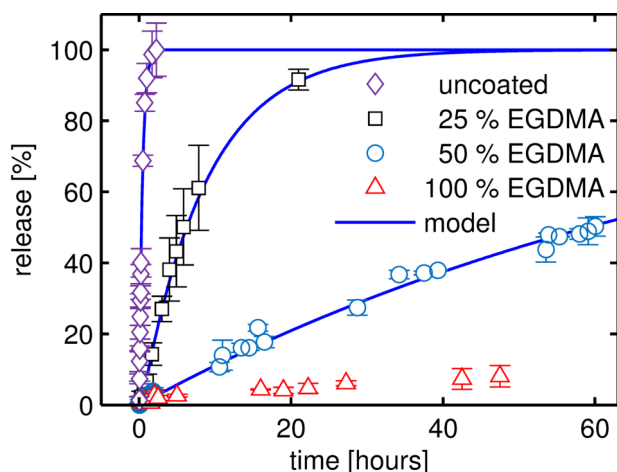


Figure 10.6: Dissolution of various crystalline indomethacin layers with and without iCVD coatings of different composition. All data were measured at a constant temperature of 25 °C and only the first 60 hours of the dissolution processes are depicted.

Therefore, dissolution data for the pEGDMA coating can be regarded as a measure for the integrity and mechanical stability of such coatings. Given that less than 10 % of indomethacin is released over the course of 50 hours, a reasonable quality of these films can be expected. This is also in agreement with the fact that morphological investigations did not reveal any obvious imperfections, as mentioned

previously. Overall, this means that such coatings are very effective in controlling drug release from the model substrate, here a glass surface. A more detailed analysis of release kinetics as function of temperature for the different coatings is provided in the following sections. Temperature dependent release. In general, an increase in temperature means that drug diffusion and thus dissolution processes are accelerated. To test this, dissolution measurements at three different temperatures (25, 37 and 50 °C) were performed, the data being summarized in Figure 10.7. At higher temperatures, faster release kinetics result for all the tested polymer compositions. While higher temperatures lead to significantly accelerated drug liberation, a burst release is not apparent from the present data, indicating that the polymer retains its mechanical integrity for at least some time during the dissolution experiment. The polymer coating with the least amount of EGDMA cross-linker exhibits the fastest release kinetics throughout all the tested temperature regimes. For example, by increasing the temperature to 37 °C (approximately human body temperature), full indomethacin release is achieved almost four times faster through a 25% EGDMA coating than at 25 °C. Increasing the temperature further to 50 °C, the necessary timeframe is reduced to 2.5 hours. At a cross-linker ratio of 50%, a similar behavior is observed, though the time scale for the release is increased to days instead of hours (Figure 10.7b). Also, the improvement in dissolution rate upon a temperature increase to 37 °C is less pronounced; for full release, the required time is reduced from more than nine days (at 25 °C) to 3.8 days. An increase to 50 °C accelerates the dissolution behavior further and full release is observed after approximately 2 days.

A different behavior is observed in the case of the EGDMA homopolymer (Figure 10.7c). At 25 °C, little drug release is observed; even after 10 days, less than a quarter of the total drug loading has been liberated. Increasing the temperature to 37 °C, release kinetics are becoming increasingly similar to the ones recorded for the copolymers. However, full release is again not observed within the time scale of the experiment. As mentioned previously, release in the case of the pEGDMA polymer should be considered being due to polymer imperfections. In particular, increased temperature will cause additional stress between the several interfaces (polymer-drug, polymer-substrate, drug-substrate), which in turn will foster rupture formation and (partial) ablation. This is also evident when looking at the release kinetics at 50 °C; release proceeds even faster than the one of the 50% EGDMA copolymer sample. As the rigidity is increased with the cross-linker content, the difference in elastic modulus between drug and polymer is most pronounced for the EGDMA homopolymer. Further tuning of the iCVD process parameters and polymer properties (composition and comonomer choice) can likely

help to improve the stability, if desired.

*Dissolution data modeling.* Qualitative differences in the dissolution behavior of uncoated and coated indomethacin samples can be directly noted from the curves in Figure 10.5 and Figure 10.7. When a polymeric coating is applied, the drug release rate is significantly reduced, indicating that the coating layer becomes the rate limiting step in the dissolution process. For a more quantitative evaluation, a mathematical model was fitted to the experimental data. While for matrix systems (drug dispersed within a polymer network) the semi-empirical Korsmeyer-Peppas equation<sup>49</sup> is commonly applied, this equation does not necessarily hold for reservoir systems such as the present one. For such systems, an analytic expression can be derived from Fick's law of diffusion under the premise of perfect sink conditions, no or negligible polymer swelling and that drug permeability does not change during the process<sup>50</sup>. For a slab geometry with a non-constant activity source<sup>51</sup>, the released drug fraction  $M_t/M_\infty$  as a function of time  $t$  can be described by

$$\frac{M_t}{M_\infty} = 1 - e^{-\frac{(A \cdot D \cdot P)}{(V \cdot L)t}}. \quad (10.4)$$

Here,  $A$  denotes the total surface area available for release,  $D$  is the drug diffusion coefficient within the membrane,  $P$  is the drug partition coefficient between membrane and reservoir,  $V$  is the volume of the reservoir and  $L$  is the thickness of the coating. As only the diffusion coefficient is dependent on the polymer composition and the other parameters should not vary between samples (within the experimental limits), the exponent of Equation (10.4) can be reduced to an effective release constant  $k$ :

$$\frac{M_t}{M_\infty} = 1 - e^{-k \cdot (t-t_0)}. \quad (10.5)$$

Introducing a time offset  $t_0$  as an additional fit parameter (*lag time*) greatly improved the data modeling, accounting for a dissolution onset different from the start of the experiment (i. e. insertion of the samples into the dissolution medium). The model parameters fitted to the experimental dissolution data are summarized in Table 10.1 for all the samples investigated. In general, a good agreement between the mathematical model and the experimental data is found, as evident from  $R^2$  values close to unity. The exception is the EGDMA homopolymer, which fits the theory the least. This is most evident for data collected at 25 °C, for which the fit yields an  $R^2$  value of just 0.775. This underlines the previously discussed assumption that drug liberation in the case of the EGDMA homopolymer proceeds likely through imperfections in the polymer layer and is not due to diffusive transport as assumed by the model.

Table 10.1: Release constants  $k$  and time offsets  $t_0$  for the different samples at different temperatures as determined from non-linear regression of the experimental release data with the model presented in Equation (10.5). The parameter uncertainty is given as the (fit) standard error,  $R^2$  is the coefficient of determination of the fit.

	$T$ [°C]	$t_0$ [min]	$k$ [ $10^{-3}\text{min}^{-1}$ ]	$R^2$
<b>No coating</b>				
<i>amorphous (as-prepared)</i>	25	$0.39 \pm 0.17$	$320 \pm 5$	0.978
<i>amorphous (heated)</i>	25	–	$156 \pm 5$	0.985
<i>crystalline</i>	25	$1.35 \pm 0.14$	$38.9 \pm 0.9$	0.998
	25	$20.2 \pm 1.4$	$2.0 \pm 0.1$	0.995
25 % EGDMA	37	$5.75 \pm 0.16$	$5.58 \pm 0.04$	0.988
	50	$3.1 \pm 0.5$	$21.5 \pm 0.8$	0.995
	25	–	$0.196 \pm 0.002$	0.995
50 % EGDMA	37	$1.4 \pm 0.4$	$0.388 \pm 0.006$	0.995
	50	–	$1.19 \pm 0.04$	0.982
	25	–	$0.030 \pm 0.004$	0.775
100 % EGDMA	37	–	$0.180 \pm 0.005$	0.986
	50	$6.2 \pm 1.7$	$3.0 \pm 0.2$	0.932

From the fit parameters in Table 10.1 it is also evident that the time offset  $t_0$  is mostly relevant for the samples covered by a 25 % EGDMA coating. As these samples also exhibit the highest degree of swelling of the polymers tested, a causal connection might be suspected. At 25 °C, a time offset of approximately 20 minutes is determined, while equilibrium swelling is reached in about ten minutes (*cf.* Figure 10.4a) For coatings of higher EGDMA content, this difference might not be observable as drug release proceeds much slower in general while equilibrium swelling does not take significantly longer. The release constant  $k$  decreases by an order of magnitude between the different samples, with the uncoated samples showing the fastest release ( $k = (38.9 \pm 0.9) 10^{-3}\text{min}^{-1}$ ) and the EGDMA homopolymer the slowest ( $k = (0.030 \pm 0.004) 10^{-3}\text{min}^{-1}$ ) at 25 °C. Increasing the temperature to 37 °C doubles the release constant and an approximate fourfold increase is observed when dissolution is performed at 50 °C. While release constants are available at only three different temperatures, the data appear to follow an Arrhenius-like behavior. This is somewhat expected as, for example, temperature-dependent solvent diffusion in polymer systems is usually predicted by an Arrhenius term (Vrentas-Duda model).<sup>52</sup> Anyway, the results indicate that different

release behaviors are accessible by tuning the cross-linker fraction in the p(HEMA-*co*-EGDMA) polymer, so that coatings can be tailored to the therapeutic action required. It should be noted that without any or little cross-linking, a pHEMA polymer exhibits strong water uptake and detaches easily from the surface. This means such films are unstable under aqueous conditions, which might be undesirable for controlled release. The rapid removal of the coating layer exposes the drug layer directly to the dissolution media, and a rather immediate therapeutic action might follow, as indicated by the fast release observed in Figure 10.7c. In summary, different drug release behaviors were achieved by depositing iCVD polymers on top of thin crystalline films of indomethacin, with the release time frames spanning several orders of magnitude. The vapor-based polymer synthesis method allows for direct preparation of the coating atop the drug layer, ensuring a defined drug-polymer interface and minimizing the risk of any drug alteration often encountered in solution based processes. The p(HEMA-*co*-EGDMA) polymer coatings showed hydrogel formation when the cross-linker fraction is low, while little to no water permeation was observed for the hydrophobic EGDMA homopolymer. Likewise, drug liberation proceeded the fastest for coatings with low EGDMA content, with release rates being reduced as the EGDMA content increases. The ability to adjust the release behavior can enable individual therapeutic actions; short term pain relief might necessitate a large therapeutic input while chronic problems (e. g. rheumatic disorder) could make use of retarded drug liberation by means of small but continuous dosage, as provided from thin film patches.



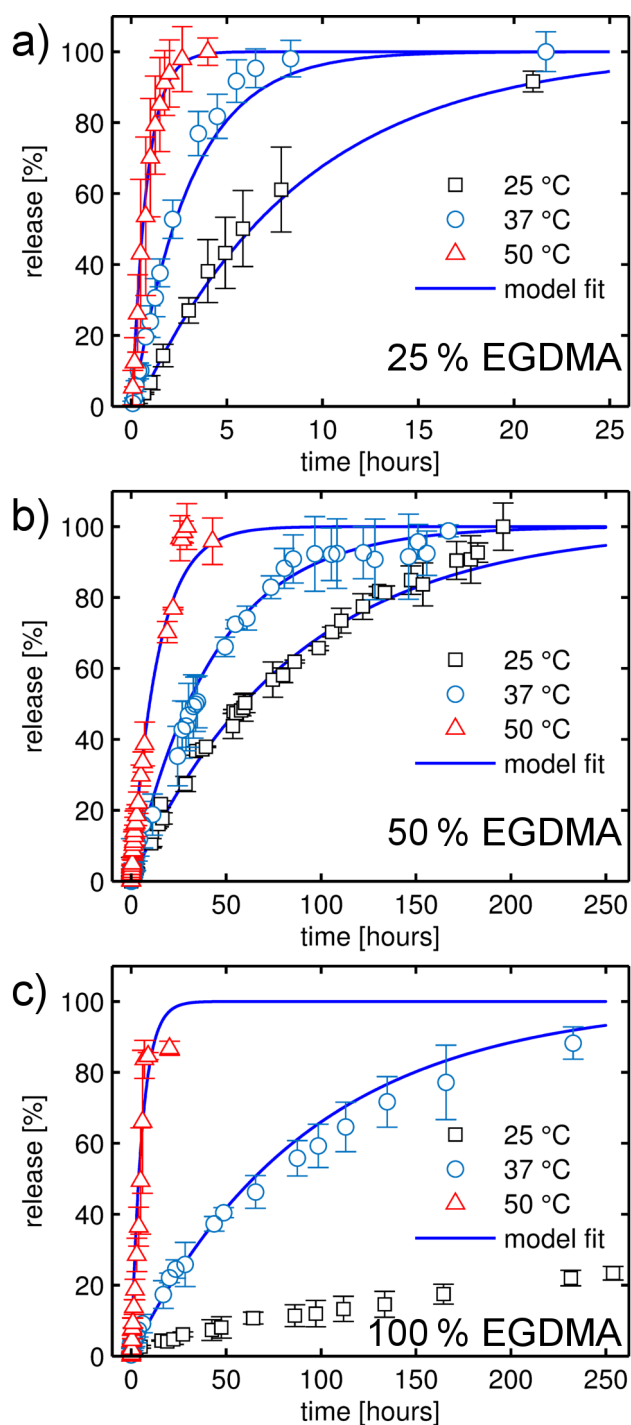


Figure 10.7: Temperature-dependent dissolution profiles of indomethacin samples coated with different p(HEMA-co-EGDMA) films. Release dynamics are depicted at three different temperatures (25, 37 and 50 °C for polymer coatings consisting either of 25 (a), 50 (b) or 100 % (c) EGDMA. Fits to the experimental data by equation (5) are indicated by solid, blue lines. Please note that graph (a) features a much shorter time frame than graphs (b,c).

## 10.5 Methods

*Preparation of thin Indomethacin layers.* Pharmaceutical grade indomethacin powder was purchased from Sigma-Aldrich (Germany) and used without further purification. Samples of indomethacin were prepared via drop casting on conventional microscopy glass slides (Roth, Germany). For this, indomethacin was dissolved in tetrahydrofuran (Sigma-Aldrich, Germany) at a solute concentration of 1 wt%, with the resulting solution being kept stirred prior usage. The substrates were cut to  $2.5 \times 2.5 \text{ cm}^2$  pieces and cleaned in acetone and ethanol, respectively, and finally purged with a nitrogen stream. The substrates were carefully leveled before placing 200  $\mu\text{L}$  of solution on the surface, which results in a homogeneous drop spread with full surface coverage. After solvent evaporation, homogeneous amorphous films are obtained. For the preparation of crystalline indomethacin films, amorphous samples were then exposed to an ethanol solvent vapor (solvent annealing<sup>53</sup>), which resulted in the entire film being transferred into a crystalline state within 24 hours.

*Preparation of drug coatings by initiated Chemical Vapor Deposition (iCVD).* Polymer coatings were prepared on the crystalline indomethacin samples by iCVD of the monomer 2-hydroxyethyl methacrylate (HEMA, purity 97%, Aldrich, Germany) and the cross-linker ethylene glycol dimethacrylate (EGDMA, purity 98%, Aldrich, Germany), using tert-butyl peroxide (TBPO, purity 98%, Aldrich, Germany) as initiator. For all the depositions, the substrate temperature was  $(28 \pm 1)^\circ\text{C}$ , the working pressure was 47 Pa and the filament temperature was  $(200 \pm 5)^\circ\text{C}$ . The TBPO flow rate was set to 0.80 sccm and a Nitrogen patch flow of 3 to 4 sccm was applied. By adjusting the monomer to cross-linker flow ratios, different polymer compositions were achieved (for compositional analysis, please refer to the supplementary information 10.9). The p(HEMA-co-EGDMA) polymers are labeled by their cross-linker volume fraction (EGDMA fraction), with 100% denoting the EGDMA homopolymer. For polymer characterization, pristine silicon wafers with a native oxide (Siegert Wafers, Germany) were coated in addition. For all samples, a nominal coating thickness of 200 nm was deposited (monitored *in situ* by laser interferometry).

*Polymer thickness characterization and swelling studies.* Spectroscopic ellipsometric data were collected at three incidence angles (65, 70 and  $75^\circ$ ) on a Woollam M-2000 ellipsometer (J.A. Woollam Co., USA) in the wavelength range between 370 and 1000 nm. For swelling experiments, the ellipsometer was equipped with a liquid cell attachment and measurements were performed at an incidence angle of  $75^\circ$ . Experimental data were fitted in the CompleteEASE<sup>®</sup> software to a model consisting of bulk silicon, a native silicon oxide layer (1.7 nm) and a transparent Cauchy layer accounting for the polymer coating.

In swelling experiments, the Cauchy layer is representing thickness and optical properties of the swollen polymer matrix and the ambient medium is set to water in the model.

*Morphological and structural investigation of Indomethacin films.* Morphological characterization was performed on a standard AxioVert 40 ZEISS optical microscope equipped with polarizers. A FlexAFM atomic force microscope (Nanosurf, Switzerland), equipped with an Easyscan 2 controller, was used in non-contact mode using a TAP 300 cantilever (Budget sensors, Bulgaria). Data and image processing were performed using the freely available software package *Gwyddion*<sup>54</sup>. Crystallographic properties were probed on a PANalytical Empyrean reflectometer in  $\theta/\theta$  geometry (specular scans). The setup was equipped with a copper sealed tube (Cu  $K\alpha$ , wavelength  $\lambda = 0.154$  nm), various slits and masks as well as a Pixel3D detector. Data are presented in scattering vector notation which calculates as  $q_z = 4 \cdot \pi \cdot \sin(\theta)$ .

*Thin film dissolution testing.* Time-resolved drug release studies were performed in a non-standard dissolution experiment as the standard apparatus is unable to evaluate samples containing very low drug loads. Instead, an adapted system was employed. Indomethacin samples (on glass substrates) were placed in a cylindrical, sealed glass vessel containing 50 mL of 0.2 molar  $\text{KH}_2\text{PO}_4$  phosphate buffer as dissolution media, adjusted to pH 5.8 with sodium hydroxide. The pH is slightly above the range of healthy and clean skin, representing more realistically the environment of potential patients' skin.<sup>55</sup> The indomethacin concentration in solution was probed at certain times by measuring the absorption at a wavelength of 321 nm with a nanophotometer (Implen, Germany). For this, 1 mL solution was taken from the vessel and placed in a quartz cuvette for the measurement. Thereafter, the solution was fed back to the system to keep the medium volume overall constant. Data points are given as the average of four samples, improving statistics and thus accounting for small differences in drug/polymer film quality during preparation.

## 10.6 Acknowledgment

The work was funded by the Austrian Science Fund (FWF): [P25541-N19]. The authors want to thank the BioTechMed Graz. Part of the research was supported by funding from the European Research Council (ERC) under the European Union's Horizon 2020 research and innovation programme (grant agreement 715403).

## 10.7 Author contributions

P.C. performed the polymer synthesis and characterization, analyzed the data and wrote the paper. A.M.C. and O.W. supervised the project and wrote the paper. S.T., H.M.A.E., H.R. and O.W. performed dissolution studies and drug characterization.

## 10.8 References

- (1) H. Häbel, H. Andersson, A. Olsson, E. Olsson, A. Larsson, and A. Särkkä *Journal of Controlled Release* **2016**, *222*, 151–158, DOI: 10.1016/j.jconrel.2015.12.011.
- (2) R. Banerjee, S. Maiti, D. Dey, and D. Dhara *Journal of Colloid and Interface Science* **2016**, *462*, 176–182, DOI: 10.1016/j.jcis.2015.09.068.
- (3) Y. C. Ng, Z. Yang, W. J. McAuley, and S. Qi *European Journal of Pharmaceutics and Biopharmaceutics* **2013**, *84*, 555–565, DOI: 10.1016/j.ejpb.2013.01.008.
- (4) L. Yu *Advanced Drug Delivery Reviews* **2001**, *48*, 27–42, DOI: 10.1016/S0169-409X(01)00098-9.
- (5) R. Cheng, F. Meng, C. Deng, H.-A. Klok, and Z. Zhong *Biomaterials* **2013**, *34*, 3647–3657, DOI: 10.1016/j.biomaterials.2013.01.084.
- (6) K. Ulbrich, K. Holá, V. Šubr, A. Bakandritsos, J. Tuček, and R. Zbořil *Chemical Reviews* **2016**, *116*, 5338–5431, DOI: 10.1021/acs.chemrev.5b00589.
- (7) R. Haag and F. Kratz *Angewandte Chemie International Edition* **2006**, *45*, 1198–1215, DOI: 10.1002/anie.200502113.
- (8) M. W. Tibbitt, J. E. Dahlman, and R. Langer *Journal of the American Chemical Society* **2016**, *138*, 704–717, DOI: 10.1021/jacs.5b09974.
- (9) H. Valo, S. Arola, P. Laaksonen, M. Torkkeli, L. Peltonen, M. B. Linder, R. Serimaa, S. Kuga, J. Hirvonen, and T. Laaksonen *European Journal of Pharmaceutical Sciences* **2013**, *50*, 69–77, DOI: 10.1016/j.ejps.2013.02.023.
- (10) R. H. Müller, K. Mäder, and S. Gohla *European Journal of Pharmaceutics and Biopharmaceutics* **2000**, *50*, 161–177, DOI: 10.1016/S0939-6411(00)00087-4.
- (11) T. Kellner, H. M. A. Ehmman, S. Schrank, B. Kunert, A. Zimmer, E. Roblegg, and O. Werzer *Molecular Pharmaceutics* **2014**, *11*, 4084–4091, DOI: 10.1021/mp500264e.
- (12) C. S. Brazel and N. A. Peppas *Polymer* **1999**, *40*, 3383–3398, DOI: 10.1016/S0032-3861(98)00546-1.

- (13) C. L. Stevenson, J. T. Santini, and R. Langer *Advanced Drug Delivery Reviews* **2012**, *64*, 1590–1602, DOI: 10.1016/j.addr.2012.02.005.
- (14) P. Borgquist, G. Zackrisson, B. Nilsson, and A. Axelsson *Journal of Controlled Release* **2002**, *80*, 229–245, DOI: 10.1016/S0168-3659(02)00033-0.
- (15) S. Muschert, F. Siepmann, B. Leclercq, B. Carlin, and J. Siepmann *Journal of Controlled Release* **2009**, *135*, 71–79, DOI: 10.1016/j.jconrel.2008.12.003.
- (16) M. S. G. Nandagopal, R. Antony, S. Rangabhashiyam, N. Sreekumar, and N. Selvaraju *Microsystem Technologies* **2014**, *20*, 1249–1272, DOI: 10.1007/s00542-014-2233-5.
- (17) K. C. Wood, J. Q. Boedicker, D. M. Lynn, and P. T. Hammond *Langmuir* **2005**, *21*, 1603–1609, DOI: 10.1021/la0476480.
- (18) A. N. Zelikin *ACS Nano* **2010**, *4*, 2494–2509, DOI: 10.1021/nn100634r.
- (19) K. K. S. Lau, Y. Mao, H. G. Pryce Lewis, S. K. Murthy, B. D. Olsen, L. S. Loo, and K. K. Gleason *Thin Solid Films* **2006**, *501*, 211–215, DOI: 10.1016/j.tsf.2005.07.208.
- (20) L. C. Bradley and M. Gupta *Langmuir* **2012**, *28*, 10276–10280, DOI: 10.1021/la301170a.
- (21) S. H. Baxamusa and K. K. Gleason *Chemical Vapor Deposition* **2008**, *14*, 313–318, DOI: 10.1002/cvde.200806713.
- (22) K. K. Gleason, *CVD Polymers: Fabrication of Organic Surfaces and Devices*; John Wiley & Sons: Weinheim, Germany, 2015; 484 pp.
- (23) A. M. Coclite, R. M. Howden, D. C. Borrelli, C. D. Petruczok, R. Yang, J. L. Yagüe, A. Ugur, N. Chen, S. Lee, W. J. Jo, A. Liu, X. Wang, and K. K. Gleason *Advanced Materials* **2013**, *25*, 5392–5423, DOI: 10.1002/adma.201301878.
- (24) K. K. S. Lau and K. K. Gleason *Macromolecular Bioscience* **2007**, *7*, 429–434, DOI: 10.1002/mabi.200700017.
- (25) S. J. P. McInnes, E. J. Szili, S. A. Al-Bataineh, R. B. Vasani, J. Xu, M. E. Alf, K. K. Gleason, R. D. Short, and N. H. Voelcker *Langmuir* **2016**, *32*, 301–308, DOI: 10.1021/acs.langmuir.5b03794.
- (26) A. Perrotta, O. Werzer, and A. M. Coclite *Advanced Engineering Materials*, n/a–n/a, DOI: 10.1002/adem.201700639.
- (27) A. S. Hoffman *Advanced Drug Delivery Reviews* **2012**, *64*, Supplement, 18–23, DOI: 10.1016/j.addr.2012.09.010.
- (28) S. R. Lustig and N. A. Peppas *Journal of Applied Polymer Science* **1988**, *36*, 735–747, DOI: 10.1002/app.1988.070360401.

- (29) G.-H. Hsiue, J.-A. Guu, and C.-C. Cheng *Biomaterials* **2001**, *22*, 1763–1769, DOI: 10.1016/S0142-9612(00)00336-7.
- (30) P. Christian, H. M. A. Ehmman, O. Werzer, and A. M. Coclite *Soft Matter* **2016**, *12*, 9501–9508, DOI: 10.1039/C6SM01919F.
- (31) P. Christian, H. M. Ehmman, A. M. Coclite, and O. Werzer *ACS Applied Materials & Interfaces* **2016**, *8*, 21177–21184, DOI: 10.1021/acsami.6b06015.
- (32) V. Andronis and G. Zografu *Journal of Non-Crystalline Solids* **2000**, *271*, 236–248, DOI: 10.1016/S0022-3093(00)00107-1.
- (33) H. Yamamoto *Chemical & Pharmaceutical Bulletin* **1968**, *16*, 17–19, DOI: 10.1248/cpb.16.17.
- (34) N. Kaneniwa, M. Otsuka, and T. Hayashi *Chemical & Pharmaceutical Bulletin* **1985**, *33*, 3447–3455, DOI: 10.1248/cpb.33.3447.
- (35) X. Chen, K. R. Morris, U. J. Griesser, S. R. Byrn, and J. G. Stowell *Journal of the American Chemical Society* **2002**, *124*, 15012–15019, DOI: 10.1021/ja017662o.
- (36) G. Mabilieu, I. C. Stancu, T. Honoré, G. Legeay, C. Cincu, M. F. Baslé, and D. Chappard *Journal of Biomedical Materials Research Part A* **2006**, *77A*, 35–42, DOI: 10.1002/jbm.a.30618.
- (37) J. Lukáš, R. N. S. Sodhi, and M. V. Sefton *Journal of Colloid and Interface Science* **1995**, *174*, 421–427, DOI: 10.1006/jcis.1995.1410.
- (38) O. Wichterle and R. Chromeček *Journal of Polymer Science Part C: Polymer Symposia* **1967**, *16*, 4677–4686, DOI: 10.1002/polc.5070160844.
- (39) J. Janáček and J. Hasa *Collection of Czechoslovak Chemical Communications* **1966**, *31*, 2186–2201, DOI: 10.1135/cccc19662186.
- (40) P. J. Flory and J. Rehner *The Journal of Chemical Physics* **1943**, *11*, 521–526, DOI: 10.1063/1.1723792.
- (41) P. J. Flory *The Journal of Chemical Physics* **1950**, *18*, 108–111, DOI: 10.1063/1.1747424.
- (42) R. Toomey, D. Freidank, and J. Rühle *Macromolecules* **2004**, *37*, 882–887, DOI: 10.1021/ma034737v.
- (43) K. Unger, R. Resel, and A. M. Coclite *Macromolecular Chemistry and Physics* **2016**, *217*, 2372–2379, DOI: 10.1002/macp.201600271.
- (44) Y. Zhang and Z. Xu *American Mineralogist* **2015**, *80*, 670–675, DOI: 10.2138/am-1995-7-807.

- (45) N. A. Peppas, H. J. Moynihan, and L. M. Lucht *Journal of Biomedical Materials Research* **1985**, *19*, 397–411, DOI: 10.1002/jbm.820190405.
- (46) O. Werzer, R. Baumgartner, M. Zawodzki, and E. Roblegg *Molecular Pharmaceutics* **2014**, *11*, 610–616, DOI: 10.1021/mp4006479.
- (47) C. Röthel, H. M. A. Ehmman, R. Baumgartner, D. Reischl, and O. Werzer *CrystEngComm* **2016**, *18*, 588–595, DOI: 10.1039/C5CE01889G.
- (48) D. E. Alonzo, G. G. Z. Zhang, D. Zhou, Y. Gao, and L. S. Taylor *Pharmaceutical Research* **2010**, *27*, 608–618, DOI: 10.1007/s11095-009-0021-1.
- (49) R. W. Korsmeyer, R. Gurny, E. Doelker, P. Buri, and N. A. Peppas *International Journal of Pharmaceutics* **1983**, *15*, 25–35, DOI: 10.1016/0378-5173(83)90064-9.
- (50) J. Siepman and F. Siepman *International Journal of Pharmaceutics* **2008**, *364*, 328–343, DOI: 10.1016/j.ijpharm.2008.09.004.
- (51) J. Siepman and N. A. Peppas *Advanced Drug Delivery Reviews* **2012**, *64*, Supplement, 163–174, DOI: 10.1016/j.addr.2012.09.028.
- (52) J. S. Vrentas and C. M. Vrentas *Journal of Polymer Science Part B: Polymer Physics* **1993**, *31*, 69–76, DOI: 10.1002/polb.1993.090310109.
- (53) H. M. A. Ehmman, A. Zimmer, E. Roblegg, and O. Werzer *Crystal Growth & Design* **2014**, *14*, 1386–1391, DOI: 10.1021/cg401859p.
- (54) D. Nečas and P. Klapetek *Central European Journal of Physics* **2011**, *10*, 181–188, DOI: 10.2478/s11534-011-0096-2.
- (55) H. Lambers, S. Piessens, A. Bloem, H. Pronk, and P. Finkel *International Journal of Cosmetic Science* **2006**, *28*, 359–370, DOI: 10.1111/j.1467-2494.2006.00344.x.

## 10.9 Supporting Information

### POLYMER MORPHOLOGY ON SILICON

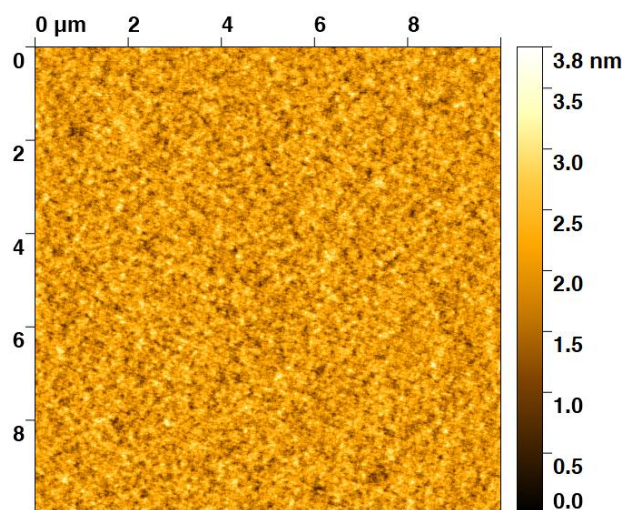


Figure S10.8: Atomic force micrograph of a p(HEMA-*co*-EGDMA) sample prepared on silicon. The EGDMA volume fraction is 25 %. The root mean squared roughness is 0.4 nm.

### POLYMER COMPOSITIONAL ANALYSIS

For the analysis of the polymer composition, iCVD polymers were deposited on single crystal silicon wafers. Fourier transform infrared spectroscopy (FT-IR) was then performed in transmission mode on a Bruker IFS 66v/s spectrometer. The experimental spectra were baseline correction by a custom routine written in R, utilizing routines provided in the baseline package.<sup>1</sup> The polymer composition was determined by treating the baseline-corrected experimental spectra as a linear combination of the constituting homopolymers, weighted by scaling factors (the fit parameters) for their respective volume fraction. A more detailed explanation of the applicability of this method in the analysis of thin polymer films is given elsewhere.<sup>2</sup> In Figure S10.9, the experimental spectra of two polymer compositions are provided. The compositional analysis reveals that the p(HEMA-*co*-EGDMA) polymers contain 25 % (a), respectively 50 % (b) EGDMA. The theoretical spectra from the fit are found in good agreement with the experimental data. The absence of a pronounced peak at  $1620\text{ cm}^{-1}$  indicates that most vinyl bond are converted in the iCVD process (in the detection limit), i. e. the films are strongly cross-linked.



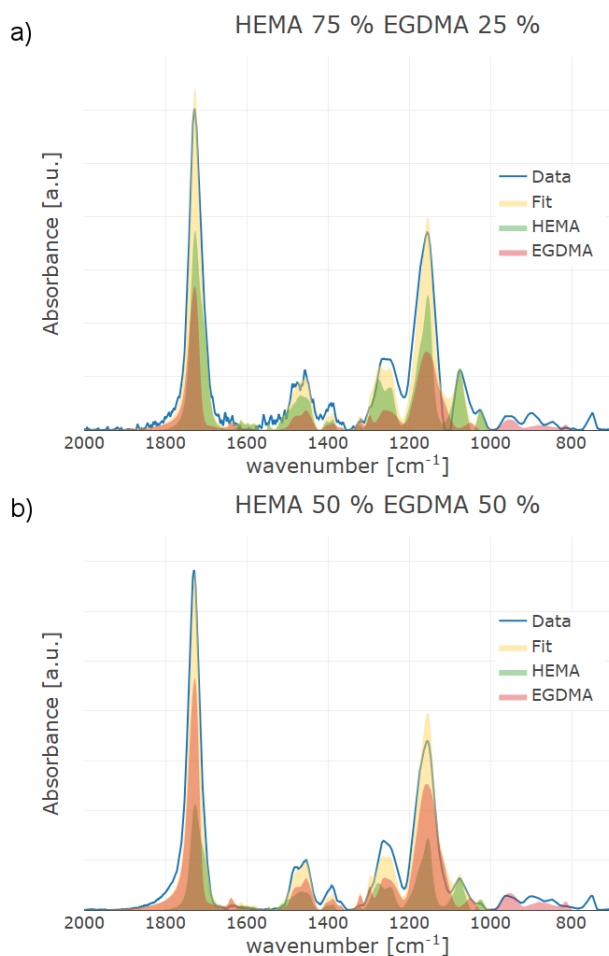


Figure S10.9: Exemplary analysis of the FT-IR spectra of two different iCVD polymers. The experimental spectra are evaluated as a linear combination of the homopolymer spectra of HEMA and EGDMA, respectively.

## SWELLING THEORY

The derivation presented here follows the original work of Flory,<sup>3,4</sup> with the adaptations Toomey *et al.*<sup>5</sup> introduced for the one-dimensional case.

The Gibbs free energy change upon swelling a system in a pure solvent can be described by two terms; the free energy of mixing  $\Delta G_{\text{mix}}$  and the elastic free energy  $\Delta G_{\text{el}}$ , describing the expansion of the network structure

$$\Delta G = \Delta G_{\text{mix}} + \Delta G_{\text{el}}. \quad (\text{S10.6})$$

According to the Flory-Huggins theory, the free energy of mixing can be described by

$$\Delta G_{\text{mix}} = RT(n_1 \ln(\phi_1) + \chi n_1 \phi_2), \quad (\text{S10.7})$$

where  $n_1$  denotes the molar number of solvent molecules occupying volume fraction  $\phi_1$ ,  $\phi_2$  is the polymer volume fraction and  $\chi$  denotes the Flory-Huggins polymer-solvent interaction parameter. Note that this equation does not contain a term for the molar number of polymer molecules  $n_2$ , as a network structure does not include single molecules and thus  $n_2$  is equated to zero.

For a linear deformation of factor  $\alpha$ , the free energy is described by

$$\Delta G_{\text{el}} = d \cdot RT \frac{\nu_e}{2} (a^2 - 1 - \ln(\alpha)), \quad (\text{S10.8})$$

with  $d$  corresponding to the number of dimensions in which swelling occurs and  $\nu_e$  denoting the effective molar number of chains in the polymer network.

When swelling reaches the thermodynamic equilibrium, the change in Gibbs free energy becomes zero ( $d\Delta G = 0$ ), meaning that difference in chemical potential  $\mu$  has to become zero as well:

$$\Delta G = \sum_i \mu_i dN_i, \quad (\text{S10.9})$$

$$\begin{aligned} \mu_1 - \mu_1^0 &= \left( \frac{\partial \Delta G}{\partial n_1} \right)_{T,p} dN_1 = \\ &= dN_1 \left[ \underbrace{\left( \frac{\partial \Delta G_{\text{mix}}}{\partial n_1} \right)}_{\text{Part I}} + \underbrace{\left( \frac{\partial \Delta G_{\text{el}}}{\partial \alpha} \right) \left( \frac{\partial \alpha}{\partial n_1} \right)}_{\text{Part II}} \right] = 0, \end{aligned} \quad (\text{S10.10})$$

### Part I

The polymer volume fraction  $\phi_2$  is the ratio of initial volume  $V_0$  to the swollen volume

$$\phi_2(n_1) = \frac{V_0}{V_0 + \nu_1 n_1} \quad (\text{S10.11})$$

with  $\nu_1$  denoting the molar volume of the solvent. Therefore, evaluating part I of Equation (S10.10) and utilizing  $\phi_1 + \phi_2 = 1$ , one obtains

$$\left( \frac{\partial G_{\text{mix}}}{\partial n_1} \right) = RT [\ln(1 - \phi_2) + \phi_2 + \chi \phi_2^2]. \quad (\text{S10.12})$$

### Part II

Taking the derivative of  $\Delta G_{\text{el}}$  with respect to  $\alpha$ , one obtains

$$\left( \frac{\partial G_{\text{el}}}{\partial \alpha} \right) = d \cdot RT \frac{\nu_e}{2} \left( 2\alpha - \frac{1}{\alpha} \right). \quad (\text{S10.13})$$

The partial derivative of  $\alpha$  with respect to  $n_1$  depends on the number of swelling dimension. For three-dimensional isotropic swelling, the inverse of the swollen volume fraction corresponds to the cube of the

deformation factor, i. e.  $\alpha_{3D}^3 = \frac{1}{\phi_2}$ . For the one-dimensional case,  $\alpha_{1D} = \frac{1}{\phi_2}$  accordingly. Together with Equation (S10.11), the derivative reads

$$1D \text{ case} \quad \left( \frac{\partial \alpha_{1D}}{\partial n_1} \right) = \frac{\nu_1}{V_0} \quad (\text{S10.14})$$

$$3D \text{ case} \quad \left( \frac{\partial \alpha_{3D}}{\partial n_1} \right) = \frac{1}{3} \frac{\nu_1}{V_0} \alpha^{-2}. \quad (\text{S10.15})$$

### Thermodynamic equilibrium

Evaluating Equation (S10.10) with Equations (S10.12) to (S10.15), one obtains

#### 1-Dimensional swelling

$$0 = dN_1 \cdot RT \left[ \ln(1 - \phi_2) + \phi_2 + \chi \phi_2^2 + \frac{\nu_e \nu_1}{2 V_0} \left( 2\alpha_{1D} - \frac{1}{\alpha_{1D}} \right) \right]. \quad (\text{S10.16})$$

#### 3-Dimensional swelling

$$0 = dN_1 \cdot RT \left[ \ln(1 - \phi_2) + \phi_2 + \chi \phi_2^2 + \frac{\nu_e \nu_1}{2 V_0} \left( \frac{2}{\alpha_{3D}} - \left( \frac{1}{\alpha_{3D}} \right)^3 \right) \right] \quad (\text{S10.17})$$

Rearranging the equations and expressing  $\alpha_x$  as function of  $\phi_2$ , one obtains

#### 1-Dimensional swelling

$$M_c = -\nu_1 \rho_{\text{pol}} \left[ \frac{\left( \frac{1}{\phi_2} - \frac{\phi_2}{2} \right)}{\ln(1 - \phi_2) + \phi_2 + \chi \phi_2^2} \right] \quad (\text{S10.18})$$

#### 3-Dimensional swelling

$$M_c = -\nu_1 \rho_{\text{pol}} \left[ \frac{\left( \phi_2^{1/3} - \frac{\phi_2}{2} \right)}{\ln(1 - \phi_2) + \phi_2 + \chi \phi_2^2} \right], \quad (\text{S10.19})$$

by introducing the average molecular weight between cross-links  $M_c = \frac{V_0}{\nu_e} \rho_{\text{pol}}$ , with  $\rho_{\text{pol}}$  denoting the polymer density.

**REFERENCES**

- (1) K. H. Liland *MethodsX* **2015**, *2*, 135–140, DOI: 10.1016/j.mex.2015.02.009.
- (2) M. Tazreiter, P. Christian, R. Schennach, T. Grießer, and A. M. Coclite *Analytical Methods* **2017**, *9*, 5266–5273, DOI: 10.1039/C7AY01748K.
- (3) P. J. Flory *The Journal of Chemical Physics* **1950**, *18*, 108–111, DOI: 10.1063/1.1747424.
- (4) P. J. Flory, *Principles of Polymer Chemistry*; The George Fisher Baker Non-Resident Lectureship in Chemistry at Cornell University; Cornell University Press: Ithaca, NY, 1953; 688 pp.
- (5) R. Toomey, D. Freidank, and J. Rühle *Macromolecules* **2004**, *37*, 882–887, DOI: 10.1021/ma034737v.

## Conclusion and Outlook

---

Initial studies of proton conductive iCVD polymers had shown very promising properties for a system of a perfluorinated compound and methacrylic acid. However, further characterization within the framework of this thesis revealed several shortcomings of such materials, rendering their applicability to real systems questionable. In particular, usage in fuel cell applications will be limited by thermal stability issues. The liquid crystalline character of the perfluorinated compound does not persist above 75 °C, which is even below temperatures typically employed in low-temperature fuel cell systems. Also, the conductive group is prone to anhydride formation, which makes methacrylic acid unsuitable for such systems. For this reason, an entirely different concept has been explored.

The preparation of sulfonated polymers was attempted by iCVD, which necessitated a post-deposition modification. Similar membranes have previously been attempted by other researchers utilizing rather complicated and expensive radiation grafting, requiring several processing steps. With iCVD, it was possible to directly synthesize a cross-linked polymer, which could be sulfonated in a single post-deposition step. The resulting material seems promising in terms of conductivity but studies are still at an early stage. Further investigations have to be carried out to evaluate thermal and mechanical stability of such films and the synthesis steps have yet to be optimized. Nevertheless, this material seems promising for future applications and might allow for direct deposition of sulfonated films on complicated substrates.

Another aspect of this thesis concerned the encapsulation of pharmaceuticals by thin polymer films synthesized by iCVD. In this context, polymer-drug interactions have been evaluated on different systems. In an initial study, the effect of the polymer coating on the solid state of the drug clotrimazole has been investigated. Evaluating different polymer chemistries, it was possible to demonstrate a suppression of clotrimazole crystallization even at elevated temperatures. Such a behavior might be helpful for ensuring an acceptable shelf-life of formulations containing active pharmaceutical ingredients in the amorphous (i. e. meta-stable) state.

In a separate study, thin film drug reservoir systems were investigated. For this, a hydrogel layer was deposited on the active pharmaceutical ingredient indomethacin via iCVD. By changing the polymer composition, the mesh-size of the hydrogel could be varied which, in

turn, led to a change in the drug release behavior. With the promising results of this model system, a possible next step could be the preparation of a more application focused thin film dosage form such as dermal patches or oral drug strips.

When envisaging a commercial product, regulatory approval seems to be a major concern. Little has been published so far on the biocompatibility of iCVD polymers and more testing will be required in this field. While compatibility is often assumed from the known properties of the involved compounds, this is not necessarily true for iCVD synthesis. In particular, one has to be careful about potential monomer/initiator inclusion which can be harmful in their unpolymerized form. However, the versatility of iCVD is also deemed a huge strength in this context; processing conditions can be adapted fairly easily so that polymer properties are likely to be improved by further parameter tuning.

As initiated Chemical Vapor Deposition is still a rather “young” technique and is not highly standardized yet, also further advances in reactor design and handling can be expected. While a sound theoretical framework exists for the processes involved in iCVD polymerization, it is often quite difficult to relate theory to experiment in a meaningful way. Thermal gradients within the system and large reactor volumes seem to be mainly responsible for these discrepancies. In particular, thermal insulation of the whole iCVD system is assumed to be largely beneficial. In current systems, the reactor body is usually exposed to ambient temperatures. As most parts are made of metal, this results in large thermal gradients between the heated monomer lines, the substrate and the reactor body. An improved reactor design might also ease the usage of less volatile monomers, thus broadening the variety of compounds available for iCVD polymerization.

# List of publications

---

## ARTICLES

- (1) P. Christian and A. M. Coclite *Thin Solid Films* **2017**, *635*, 3–8, DOI: 10.1016/j.tsf.2017.01.023.
- (2) P. Christian and A. M. Coclite *Beilstein Journal of Nanotechnology* **2017**, *8*, 933–942, DOI: 10.3762/bjnano.8.95.
- (3) A. O. F. Jones, C. Röthel, R. Lassnig, O. N. Bedoya-Martínez, P. Christian, I. Salzmänn, B. Kunert, A. Winkler, and R. Resel **2017**, DOI: 10.1039/C7CE00227K.
- (4) J. Pilz, A. Perrotta, P. Christian, M. Tazreiter, R. Resel, G. Leising, T. Griesser, and A. M. Coclite *Journal of Vacuum Science & Technology A: Vacuum, Surfaces, and Films* **2017**, *36*, 01A109, DOI: 10.1116/1.5003334.
- (5) B. Schrode, B. Bodak, H. Riegler, A. Zimmer, P. Christian, and O. Werzer *ACS Omega* **2017**, *2*, 5582–5590, DOI: 10.1021/acsomega.7b00783.
- (6) M. Tazreiter, P. Christian, R. Schennach, T. Griebler, and A. M. Coclite *Analytical Methods* **2017**, *9*, 5266–5273, DOI: 10.1039/C7AY01748K.
- (7) P. Christian, H. M. A. Ehmann, O. Werzer, and A. M. Coclite *Soft Matter* **2016**, *12*, 9501–9508, DOI: 10.1039/C6SM01919F.
- (8) P. Christian, H. M. Ehmann, A. M. Coclite, and O. Werzer *ACS Applied Materials & Interfaces* **2016**, *8*, 21177–21184, DOI: 10.1021/acsam.6b06015.
- (9) P. Christian, C. Röthel, M. Tazreiter, A. Zimmer, I. Salzmänn, R. Resel, and O. Werzer *Crystal Growth & Design* **2016**, *16*, 2771–2778, DOI: 10.1021/acs.cgd.6b00090.
- (10) O. Kettner, A. Pein, G. Trimmel, P. Christian, C. Röthel, I. Salzmänn, R. Resel, G. Lakhwani, F. Lombeck, M. Sommer, and B. Friedel *Synthetic Metals* **2016**, *220*, 162–173, DOI: 10.1016/j.synthmet.2016.06.010.
- (11) D. Reischl, C. Röthel, P. Christian, E. Roblegg, H. M. A. Ehmann, I. Salzmänn, and O. Werzer *Crystal Growth & Design* **2015**, *15*, 4687–4693, DOI: 10.1021/acs.cgd.5b01002.

## ORAL PRESENTATIONS

- (1) *Fluorinated Copolymer Membranes via initiated Chemical Vapor Deposition*, THERMEC'2016, Graz, 2016.
- (2) *Application, Characterization and Synthesis of Polymers from initiated Chemical Vapor Deposition*, Advanced Materials Day, Graz, 2016.
- (3) *Thermal stability in proton conductive iCVD polymers*, 9<sup>th</sup> International Conference on Hot Wire and Initiated Chemical Vapor Deposition, Philadelphia, 2016.

## POSTERS

- (1) *Crystallization of Carbamazepine in Proximity to its Precursor Iminostilbene and a Silica Surface*, NESY workshop, Graz, 2016.
- (2) *Fluorinated Copolymers by initiated Chemical Vapor Deposition*, Advanced Materials Day, Graz, 2015.
- (3) *Proton Conductive Polymers via iCVD*, 7<sup>th</sup> School on Organic Electronics, Como, 2015.
- (4) *Structural Analysis of Proton Conductive Polymers synthesized by initiated Chemical Vapor Deposition*, NESY-Winterschool, Altaussee, 2015.



## Colophon

This document was typeset using the typographical look-and-feel `classicthesis` developed by André Miede. The style was inspired by Robert Bringhurst's seminal book on typography "*The Elements of Typographic Style*". `classicthesis` is available for both  $\LaTeX$  and  $\text{LyX}$ :

<https://bitbucket.org/amiede/classicthesis/>

*Final Version* as of January 31, 2018 (`classicthesis` version 4.4).